The Fluid Dynamics of Nascent Biofilms

NICOLA ELLEN FARTHING (M.PHYS. (HONS))

PH.D

University of York

MATHEMATICS AND PHYSICS

APRIL 2019

ABSTRACT

Bacteria are often found in surface associated structures called biofilms, composed of individual bacterial cells along with various extra-cellular components. They are a leading cause of antibiotic resistant infections and are a global issue. In this thesis, the focus is on the very early stages of biofilm formation and, in particular, the effect of bacterial motility on biofilm formation is investigated. Various microscopy techniques are used to determine that surface attached bacteria maintain moving flagella, which induce a flow around the bacteria. The flow due to such surface-attached bacteria has not previously been reported. In this thesis, holographic microscopy is used to determine the shape of the flow. The flow is found to be different when cells are exposed to a lactam analogue (which is thought to disrupt biofilm formation by interfering with cell-cell communication). In this thesis, a suggested explanation for this change in flow is an increase in flagellar reversal rate when the cells are exposed to the lactam analogue compared to a control set is presented. A simple model of the surface-attached cell with a motile flagellum is developed to capture the key elements of the flow. This simple model relies on singularity solutions to the Stokes equations and has low computational expenditure. This ease of computation allows the simulation of multiple cells so that the effect of the cells' induced flow on cell-cell communication can be investigated. Particle dispersion is found to be enhanced in the presence of simulated cells with the control reversal rate in comparison to those with the lactam reversal rate. This suggests that one effect of the lactam analogue is to lessen the transport of cell-cell communication molecules.

CONTENTS

LIST OF TABLES

LIST OF FIGURES

In motion irresistible,
In substance incompressible,
A tiny little minnow swims along the line of flow.
Now cutting out all verbosity,
And neglecting all viscosity,
The faster its velocity,
The faster it'll go.
(Author unknown)

ACKNOWLEDGMENTS

I would like to offer thanks to my supervisors Martin Bees and Laurence Wilson for their critical advice, support and patience. I'd also like to thank the bio-soft matter group and my TAP members for their input on the direction of the project.

I have so much gratitude for my incredible friends and office mates. Rachel, thanks for being such a calming influence. Sarah and Siobhan you know this thesis would never have happened without the Infinity Girls and all the gin we shared. Last but definitely not least; Katie you have been simply indispensable!

I'd definitely need to thank my amazing family. You never once thought I wouldn't be able to do this even when I adamantly told you I couldn't. Thanks for listening when I needed to rant and being a sanctuary when I didn't. Ben, thanks for for Bandi, all the wine and for never letting me quit. I blame this thesis on you - or dedicate it to you, whatever.

My advice for anyone starting out on a PhD can be summed up with two quotes from The Hitchhikers Guide to the Galaxy (which I'm sure my Uncle will appreciate immensely). The first is 'I think the problem, to be quite honest with you, is that you've never actually known what the question is'. This reminds you to take a step back sometimes and get perspective. The second is critical and something I wish I'd remembered more:

'Don't Panic'

AUTHOR'S DECLARATION

I declare that the work in this thesis was carried out in accordance with the requirements of the University's Regulations and Code of Practice for Research Degree Programmes and that it has not been submitted for any other academic award. Except where indicated by specific reference in the text, the work is the candidate's own work. Work done in collaboration with, or with the assistance of, others, is indicated as such. Any views expressed in the thesis are those of the author.

SIGNED: .... DATE: ....

PRELIMINARIES

"If you don't like bacteria, you're on the wrong planet"

Stewart Brand

1.1 Introduction

The best estimate for the number of bacteria on this planet is approximately 1 nonillion (10^{30}), a billion times the number of stars in the sky [1]. Of these nonillion bacteria, it is estimated that over 95% are found in surface-associated structures called biofilms. Being so ubiquitous, these biofilms can be advantageous with various uses [2–4], but they can also be disadvantageous causing serious infections and even death [5–7]. The pervasive nature of biofilms has led to an increasing interest in the factors governing their formation and a need to further understand the mechanisms involved.

In this thesis, the early stages of biofilm formation are investigated to obtain increased understanding on how biofilm growth may be controlled. Using both experimental techniques and mathematical models, the motility of individual 'seed' cells is investigated and an exploration on how such motility may affect later biofilm stages is explored. The impact of hydrodynamic interactions (from external flows and bacterial motility) on the early stages of biofilm formation is little understood. In this thesis, a range of

experimental techniques, including a novel application of holographic microscopy, were used to obtain information on the 3D field induced by surface-associated bacteria. Models of low computational expenditure based on singularity solutions to the Stokes equations were used to capture the dominant characteristics of this experimentally derived flow. The low computational expense means that these models are an extremely useful tool to investigate multi-cell effects that are difficult to understand experimentally. Examples of multi-cell systems are presented in this thesis to show the applicability of the model and further understand the role of cell induced fluid dynamics on flagellar and tracer dynamics. Results from this thesis provide a foundation for developing techniques to either promote or prevent biofilms.

1.2 *Pseudomonas aeruginosa*

Throughout this project, the main organism of study is *Pseudomonas aeruginosa*; a gram-negative, rod-shaped bacterium, which is approximately $1-5$ μm in length and $0.5-1.0$ μm in width [8]. *P. aeruginosa* are generally aerobic, although they can respire anaerobically if necessary. Described as one of the most abundant organisms on earth [9], *P. aeruginosa* is ubiquitous and has been found to survive in soil, faeces, water, plants, animals and humans [10]. *P. aeruginosa* is often called an 'opportunistic' human pathogen because, although it is pathogenic, it rarely infects healthy individuals. It is, instead, more commonly found in individuals with compromised immune systems. For example, *P. aeruginosa* is a key pathogen causing complications for patients with cystic fibrosis [11] and has even been cited as a factor in as many as 90% of cystic fibrosis deaths [12]. On the other hand, *P. aeruginosa* does have some positive attributes. For example, it can be used for pollution control [13] because it is able to degrade aromatic hydrocarbons, which are by-products of petroleum industries. It is also a very important soil bacterium [8] helping to fix nutrients.

Its prevalence was likely instrumental in the early identification of *P. aeruginosa*. As early as 1884, Carle Gessard published 'On the Blue and Green Coloration that Appears on Bandages' [14] identifying *P. aeruginosa* as a unique species and referencing the pigment produced by *P. aeruginosa*. The name *Pseudomonas* was coined by German botanist Walter Migula in 1894 [15] to label a group of organisms he described as 'cells with polar organs of motility'. It has been suggested that the name came from the bacteria's resemblance to a group of aquatic organisms called 'monas' (see figure 1.1).
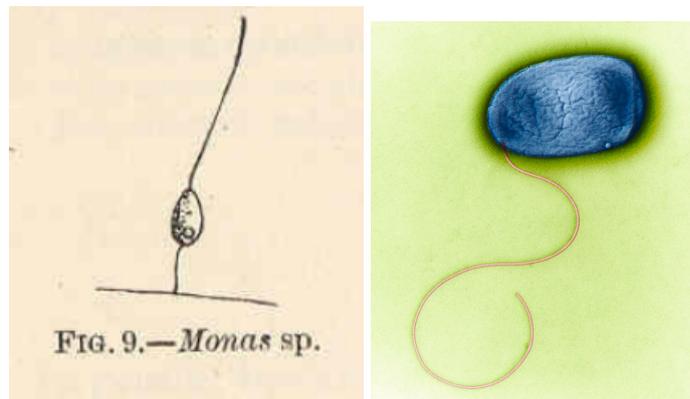
FIGURE 1.1.
On the left is an illustration of the aquatic 'monas' from which the name *Pseudomonas* is thought to be derived. This image is from the 1773 work by Müller [17]. For comparison a colour-enhanced, tunneling electron microscopy image of *P. aeruginosa* is shown on the right. This image was taken from https://fineartamerica.com/featured/1-pseudomonas-aeruginosa-tem-eye-of-science.html.

The etymology of the of *aeruginosa* it better understood. Deriving from the Latin *aerūgõ* meaning 'copper rust', the name refers to the blue/green colouration of the colonies [16].

P. aeruginosa was chosen as the test organism for this project primarily because it is a common laboratory organism which readily forms biofilms. As such, there is an abundance of literature on growth protocols *etc*. Furthermore, since *P. aeruginosa* cells are motile with a single polar flagellum (see fig 1.2), they are perfect for motility investigations and a relatively simple cell to model. Both the pathogenic nature and uses of *P. aeruginosa*, detailed previously, mean it is important to understand more about how it forms biofilms and such is the aim of this project. However, since many bacterial species display motility and form biofilms, it is hoped that conclusions drawn within this project may be widely extended to other bacterial species and to multi-species biofilms. Like many other bacterial species, *P. aeruginosa* is also surface motile by means of a type IV pili [18]. These appendages allow the bacteria to move on a surface and a thought to be important in biofilm formation/ surface attachment but are not focused on in this thesis.
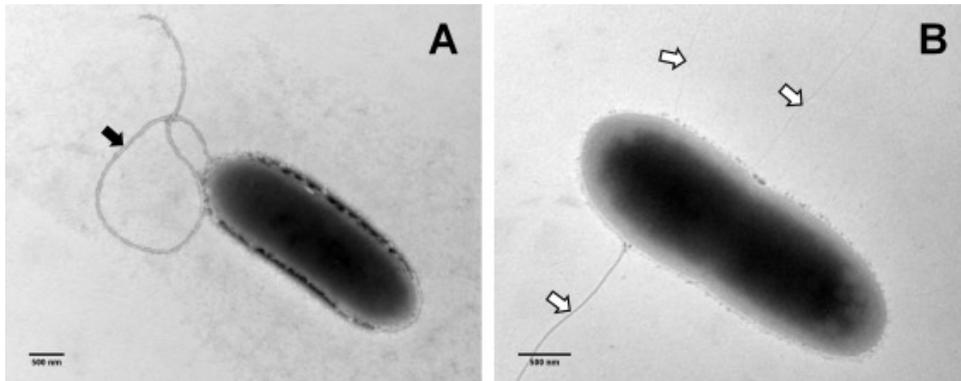
FIGURE 1.2. Transmission electron microscopy observations of *P. aeruginosa* PA01. Black arrow (A) indicates the polar flagellum of a cell while the white arrows (B) show type IV pili. Image taken directly from [18].

1.3 Swimming cells

1.3.1 Modes of bacterial swimming

Possibly the most well known bacterial motility is the 'run-and-tumble' motion typical of *Escherichia. coli*. The peritrichously flagellated organisms swim by rotating their helical flagella counterclockwise (CCW). The flagella, rotating in this way, form a bundle behind the cell body and propel the bacterium forward. This forward swimming is known as a 'run' and is a highly directionally persistent motion [19]. When one or several of the flagella reverse rotation direction and begin rotating clockwise (CW), the flagellar bundle comes apart and the cell body reorientates with little translation. This reorientation event is termed a 'tumble'. Bacteria are known to respond to gravity, chemical and light gradients (called gyrotaxis, chemotaxis and phototaxis respectively), by controlling the frequency with which they tumble. This run-and-tumble motility (see figure 1.3a) is a balance between the organisms efficiently spreading and effectively sampling and responding to their environment.

Other bacterial species only have a single flagellum that moves the cell body either from the front or from the rear. This again corresponds to a 'run'. Often, when these flagella reverse, the cells simply reverse their direction (see figure 1.3b). This 'run-reverse' motility is often found in marine bacteria such as *Pseudoalteromonas haloplanktis* [20]. This kind of motility relies on fluid instabilities/ Brownian motion to allow the cell to effectively sample the environment.
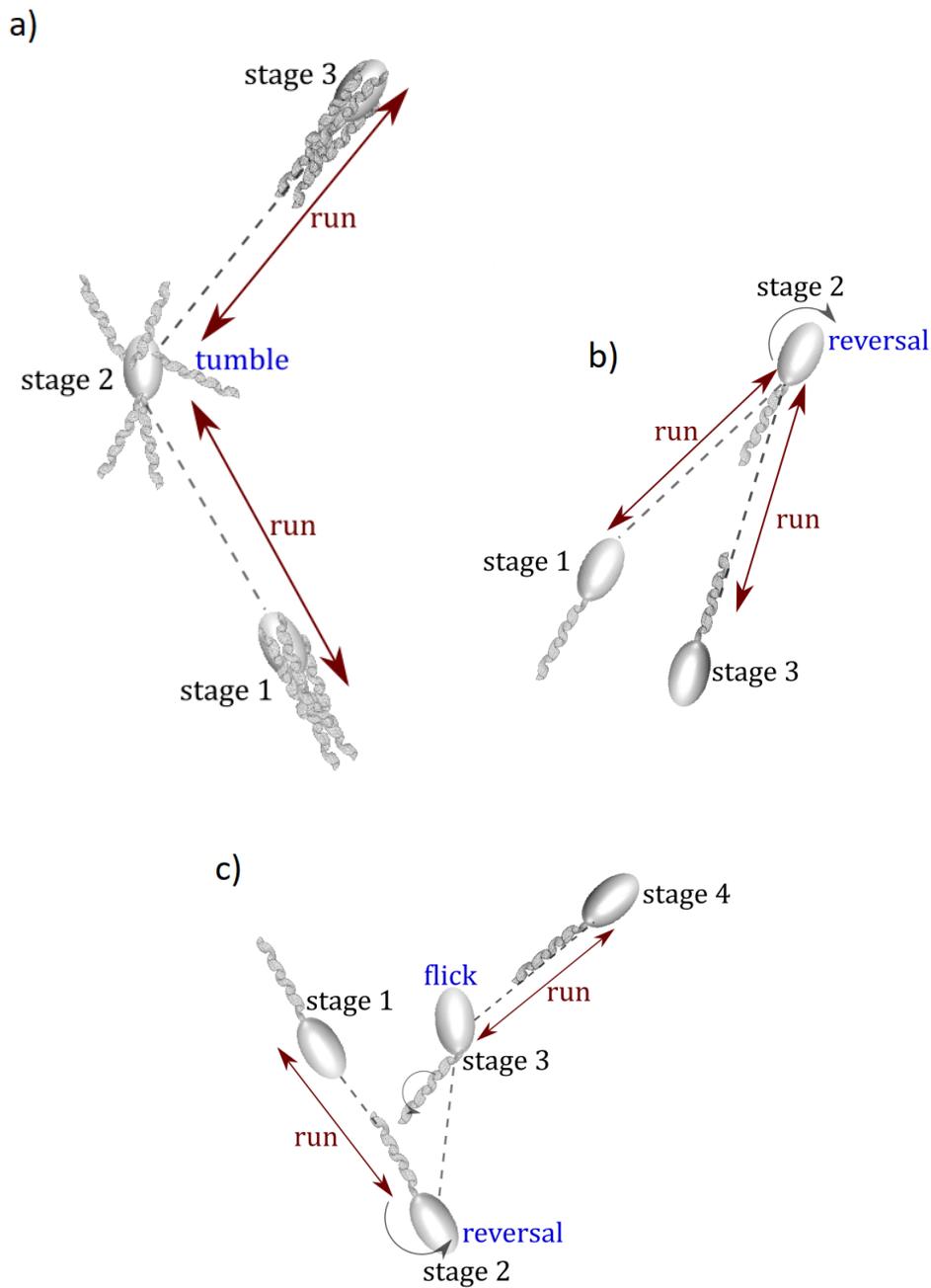
FIGURE 1.3. The motility archetypes of free-swimming bacteria in liquid media. a) the run and tumble motility typical in multi-flagellated bacteria. b) the run-reverse motility common to many marine bacteria [19]. c) the run-reverse-flick motility observed in *P. aeruginosa*.
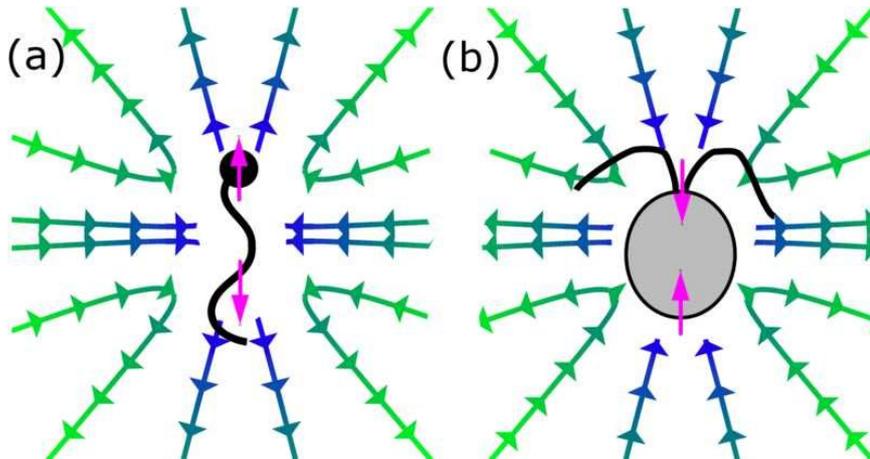
FIGURE 1.4. The flow streamlines induced around Stokeslet dipole singularities.
a) the pusher dipole typically used to model flagellated bacteria. b) the
puller dipole commonly associated with flagellated algal cells. Figure taken
directly from [22].

P. aeruginosa swim using a 'run-reverse-flick' motility (see figure 1.3c), whereby the cells
re-orientate themselves by 'flicking' their flagella. This increases their sampling of the
environment.

1.3.2 Freely swimming cells

Many theoretical models for free swimming bacterial cells utilise what is known as a
Stokeslet dipole singularity (equation (1.17)). The justification is that the drag on the
body acts as a point force of strength **F** moving through a fluid, which results in an
induced flow field of what is known as a Stokeslet (equation 1.16). This is balanced by
the flagellar thrust of equal strength, resulting in a 'pusher' dipole (see figure 1.4a) [21**?**
]. If, instead, the flagella pull the cell body, the dipole is a 'puller' type (see figure 1.4b).
This puller type dipole is commonly associated with flagellated algal cells that use their
flagella to 'breaststroke' swim. Theoretically, both of these fields decay with the square
of the distance from the cell, but until recently this was never experimentally verified.
The reason for this was essentially that the bacteria moved too quickly for the field to be
evaluated. Then, in 2010, the field around free swimming algal cells (slightly larger and
slower than bacteria) was determined using tracking microscopes and fluid velocimetry
[23, 24]. These algal cells were assumed to produce a 'puller' dipole singularity in the far
field. The experiments revealed that this model was valid at large distances from the cell
(≥ 7 body lengths). However, closer to the cell the field was much different. Instead of

the dipole, it was found that the time-averaged field was better approximated by three Stokeslet model [23].

In 2011, Drescher *et al.* [23] used cell tracking and velocimetry to determine the field around swimming *Escherichia coli* bacterial cells. Since the bacterial cells are smaller than the algal cells, and induced a smaller field, noise was more of an issue in this experiment. By time-averaging and averaging over 10^4 cells, the field was found to agree well with the dipole model provided the cell was $> 50 \mu m$ from a no-slip boundary. The collected data was only in 2D but the field was assumed to be axially symmetric. It should be noted that, although *E. coli* are peritrichously flagellated, the field was analysed when the cells were in a 'run' and so the flagella were bundled behind the cell. Although the flow around swimming *P. aeruginosa* cells has not been explicitly investigated, the similarity of *P. aeruginosa* body shape to that of *E. coli*, and the bundling of the *E. coli* flagella, suggests the field around *P. aeruginosa* is also dipolar. However, the 'run-reverse-flick' motion of *P. aeruginosa* implies that a reversal in flagellar rotation would correspond to a transition between 'pusher' and 'puller' dipoles. More information on the singularities discussed here is given in section 1.5.1.

Another key difference between pusher and puller cells is the impact of the flagellar hook [25]. The flagellar hook is a flexible connector between the flagellar motor (which uses a proton motor force to rotate - thus rotating the flagellum) and the more rigid, helical flagellar filament. Both pushers and pullers have the flagellar hook but, as can be seen in figure 1.5, the directions of the forces acting on the hook are different. In puller cells, the hook is under tension and so is stable. However, for pusher cells, the hook is under compression, which can lead to buckling instabilities and is the cause of 'flicks' [26]. This hook will be important for the simple model presented in chapter 5.

1.3.3 Cells swimming close to a boundary

It is reasonable to expect that the interaction with surfaces affects the flow induced around cells and it is common to utilize the method of images to determine this effect [27–30]. The method of images is detailed in section 1.5.8. The effect of this interaction is observable in a change of bacterial swimming behaviour near surfaces. The 'pusher' type swimmers have been seen to follow anticlockwise (when viewed from above) circular trajectories when near a stress-free boundary and clockwise circles when near a no-slip surface [21, 31–35]. As the cell becomes closer to no-slip boundaries, the circles have been observed to become smaller [21] and the cells swim slower [33]. This leads to an
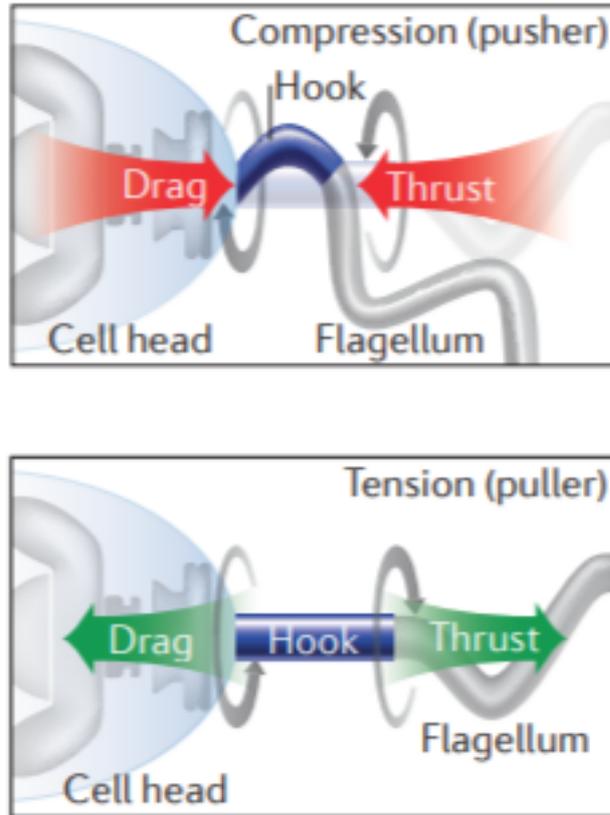
FIGURE 1.5. The forces acting on the flagellar hook for pusher/ puller cells
[25]. The hook in 'puller' type cells is under tension resulting in fewer
instabilities. In contrast, the hook is under compression in 'pusher' type
cells and so flagellar buckling is more common.

aggregation of cells near the surface, increasing the possibility of attachment, which is
thought to have implications in biofilm formation.

The field induced around bacteria near a no-slip surface was obtained by Drescher *et
al* [36] following a similar technique as that used to determine the free-swimming field.
Close to a no-slip boundary ($< 6\mu$m) the dipole model was found to slightly overestimate
the flow due to a swimming bacterial cell with noise found to have decreased importance.
Again this result was 2D extrapolated to 3D by the assumption of axial symmetry. In
the same paper, the effect of long-range hydrodynamic interactions was investigated by
considering the change in direction of one bacterium (modelled as dipoles) due to another.
They found that for a bacteria with a cell body approximately 3μm long, hydrodynamic
interactions only dominated over noise within 3.3μm from the cell. This suggests that
hydrodynamic interactions have little effect over ranges of the order of the cell body.

To determine whether this result is also true for cell-surface hydrodynamics, Drescher *et al.* considered the angle of approach of a cell to a no-slip surface [**?**]. For the cell to escape from the surface, the swimming velocity component perpendicular to the surface needed to exceed the attraction from the hydrodynamic image. For *E. coli* cells the escape angle was determined to be $< 11°$. By considering the distance at which the hydrodynamic torque barrier from the image is approximately equal to diffusion, the escape height can be found. From this, they determined that hydrodynamic interactions were negligible at distances greater than a cell length from the surface.

1.3.4 Surface attached cells

The obvious importance to biofilm formation has meant that surface attached cells are of increasing interest and various modes of surface motility have been identified. On no-slip surfaces, *P. aeruginosa* has been shown to attach via its flagellum or short cell-body axis and remain motile causing the cell body to spin [37]. Many bacteria, including *P. aeruginosa* also have appendages called pili protruding around the whole cell body which are thought, not only to aid in attaching the cell body to the surface, but are also involved in other forms of surface motility. On no-slip surfaces, these pili are thought to be used in what is known as gliding motility where the cells are attached to the surface via their long axis and move over a surface smoothly [38]. On softer surfaces (such as agar), these pili are thought to let the cell twitch where the cells 'crawl' along surfaces.

There is little known about the flows induced by surface motility of bacterial cells. In 2008, Cisneros *et al.* investigated the flows induced by *Bacillus subtilis* cells trapped between a no-slip and a stress-free surface [39]. Using particle tracking of tracer beads, they obtained a 2D flow field showing circulation around the cell. In this situation, molecules would be trapped around the cell but with multiple cells large scale transport has been seen. As biofilms are known to rely on cell communication via quorum sensing molecules, this has obvious implications to biofilm formation. In this case, the thin film of fluid trapping the bacteria also ensured that all tracer beads remained within the focal plane and so were able to be tracked. However, boundary conditions in this experiment are different to those focused on in this project and the peritrichously flagellated nature of *B. subtilis* means that the results of this data are not directly transferable to the modelling of the mono-flagellated *P. aeruginosa*.

The flow induced by a bacterial cell in the half-space of being attached to a no-slip

surface has not been directly investigated since the 3D nature of such an arrangement is not conducive to standard bright field imaging. However, in 2004 Darnton *et al* investigated the transport of tracer beads over a carpet of surface attached bacteria [40]. Here, a number bacteria were artificially attached to a no-slip surface. They were then covered in media containing tracer beads and the motion of the beads was imaged from above. The beads indicated a considerably enhanced flow close to the carpet of bacteria compared to far away. Although in 2D, this experiment indicates that the flow induced by surface attached cells is significant and worthy of further investigation.

1.4   An Introduction to biofilms

Biofilms are ubiquitous and can be found on almost every immersed surface in natural aqueous environments [41]. Being so prevalent, biofilms have been observed for millennia but it was the assiduous Antonie van Leeuwenhoek who first suspected they consisted of microbes. In 1684 Leeuwenhoek wrote a report to the Royal Society of London in which he claimed that 'The number of these animalcules in the scurf of a man's teeth are so many that I believe they exceed the number of men in a kingdom'. Here, he identifies dental plaque to be made up of microbes, which he calls 'animalcules' (from the Latin 'animalculum' = tiny animal), in what is considered the first scientific report on biofilms [42].

These biofilms can form on solid surfaces (also known as no-slip surfaces in reference to the boundary conditions involved) or liquid/air interface surfaces (called stress-free surfaces), and often present as 'slime'. In this thesis, the focus is primarily on biofilms forming on solid surfaces since these are often the most problematic. They are made up of cells suspended in 'glue' produced by the cells themselves. Although in this thesis the key focus is on single-species bacterial biofilms, in nature biofilms can be made up of a mixture of different bacterial, algal or fungal species.

In this section, the motivation for studying biofilms is discussed along with the stages of their formation, the role of cell motility in the formation and the role of cell-cell communication in their growth. A general outline of previous attempts at modelling biofilms is also provided to give context to the new approach of this project.

1.4.1 Motivation

In recent years, it has become increasingly apparent that biofilms are the dominating lifestyle of bacteria in natural environments. In fact, though planktonic bacteria are frequently studied in the lab, free bacteria are relatively rare in nature [43]. Being both advantageous and detrimental, biofilms impact the economy, the environment and healthcare. On the one hand, biofilms in food processing plants have been estimated to cost the US economy $78 billion in one year alone [44]. In medical circles, biofilms are of paramount importance since The European Centre for Disease Prevention and Control (ECDC) (2007) stated that "every year some 3 million people in European Union countries catch an infectious disease associated with healthcare and that around 50,000 die as a result." About $60 - 70\%$ of these infections are associated with some type of implanted medical device [45], many of which are due to biofilm growth on the device. These kinds of infections on devices are not only prevalent, they are also pervasive and are increasingly difficult to treat [46]. At present, biofilms are often treated with antibiotics (with varying degrees of success). The 'glue' component of biofilms acts as a barrier to protect the cells from antibiotics, decreasing the effectiveness of antibiotics against biofilms and increasing the chance of resistance. Therefore, one of the key motivations for studying biofilms is to develop a safe and effective method of treating biofilm that is an alternative to antibiotics.

Biofilms, however, are not always bad. Common in wastewater treatment plants, biofilms are used to extract organic material from water [47]. One interesting new use for biofilms is to exploit their biocementation properties. Here, certain biofilms that promote mineral deposition are used to protect stone structures such as building, monuments and statues [48]. They also have applications in the biofuel industry [49], can be used to protect plants from diseases [50] and can help to stabilize the human microbiome [51]. The expensive, and often deadly, nature of the nocuous biofilms has led to a keen interest in developing methods to inhibit biofilm formation [52–54]. In this project, the aim is to develop an increased understanding of the early biofilm stage. This means that biofilm formation can be controlled so that the detrimental biofilms are minimized and the beneficial ones can be exploited.

1.4.2 Quorum Sensing

Quorum sensing (QS) is the general term given to the communication system between individual bacterial cells via signal molecules called auto-inducers (AI). QS is generally cell-density dependent and is predominantly known as a bacterial communication system, although it is now known to be employed by some eukaryotes [55, 56]. This communication allows the community to collectively act as one, serving all individuals by increasing survival rates and the population as a whole by ensuring multiple phenotypes proliferate [57]. This communication system is crucial in biofilm formation and has been found to play a particularly important role in the initiation of later biofilm stages such as the production of the 'glue' [58]. The general mechanism for this collective co-ordination is a system of signaling molecules fitting into a feedback loop that controls gene expression. The AIs are produced by each individual in isolation at a constant rate when the cell is exposed to constant conditions [57]. This means that, as the density of cells increases, so does the concentration of AIs. AIs in the surrounding fluid then bind to receptors on the individual bacterium stimulating certain genes to be expressed and an increase in the production of AIs per cell.

In *P. aeruginosa*, there are at least three of these positive feedback signaling loops which are linked [59]. The LasI/LasR system is viewed as the primary system. LasI is a protein which catalyzes the synthesis of the AI $3O\text{-}C_{12}\text{-HSL}$, which in turn binds to the transcriptional regulator LasR. This binding activates LasR which then up-regulates the secondary, RhlI/RhlR, system. Here the AI is $C_4\text{-HSL}$ and it is the gene expression stimulated by this system that is thought to be important in biofilm formation [57]. The third system is called the Pseudomonas Quinolone Signal (PQS). This system is significantly less understood but is thought to be involved in how the cell colony reacts to environmental stress [57].

1.4.3 Biofilm Formation

In this thesis, the majority of biofilm/motility investigations have been conducted using *P. aeruginosa* strain PA01. This is a common laboratory strain and so there is a wealth of literature on its biofilm formation. Conventionally, biofilm formation is considered to pass through five distinct phases (see figure 1.6), with full maturation being reached after approximately 9 days for PA01 [60]. The first of these stages is the initial attachment of planktonic cells, with cells observed to attach either via the cell pole or via the polar

Planktonic cell

Flagellum
attached cell

Short axis
attached cell

Long axis
attached cell

1a: Reversible attachment -
cells transition from plancktonic to
attached via flagella, short body axis or
long body axis. During this stage, the
cells can leave the surface.

Long axis
attached cell

1b: Irreversible attachment -
cells are attached via their long
body axis. During this stage, the
cells cannot leave the surface.

Motility of cell
downregulated

2: Cluster formation -
small aggregations of cells are seen on
the surface. No EM is seen at this
stage and motility is downregulated.

Extracellular Matrix (EM)

Non-motile cell

3: EM produced-
The concentration of cells on the
surface is sufficent for QSM to stimulate
the production of EM. The biofilm is now
distinct from a surface-associate colony.

Extracellular Matrix (EM)

Non-motile cell

4: Structures develop -
The biofilm forms projections into
the bulk fluid to exploit nutrients etc.
The biofilm now appears thicker than
in previous stages.

Cell with motility
upregulated

Non-motile cell

Extracellular Matrix (EM)

5: Maturation and dispersion -
Openings develop within the biofilm
from which motile bacterial cells
are released and dispersed into
the bulk fluid.

FIGURE 1.6.
A schematic showing the five key stages of biofilm formation as detailed in
[60]. For PA01, the full cycle takes approximately 9 days at room tempera-
ture. Here the EM is shown in gray.
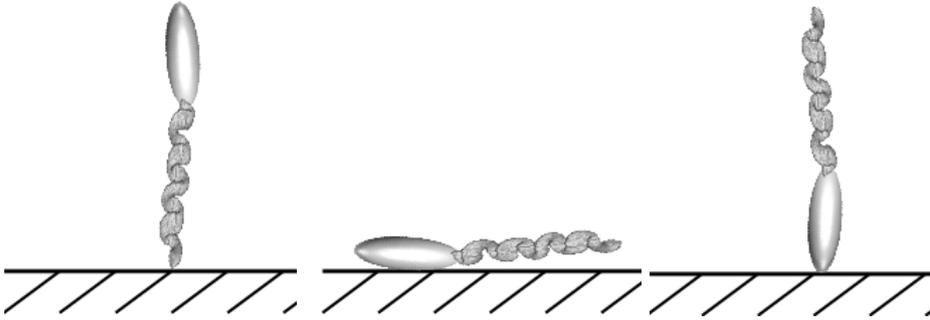
FIGURE 1.7. The three modes of surface attachment

The various motile modes of PA01 no-slip surface attachment. From left to right are schematics of flagella attached, long-axis body attached and short-axis body attached cells. Both the flagella and short-axis body attached modes of attachment manifest in spinning cell bodies when imaged with bright field microscopy. The long-axis body attached mode is indistinguishable from non-motile cells on the surface unless fluid motion is observed, ie. using tracer beads.

flagellum (see figure (1.7). This stage is usually observed for the first eight hours of growth and has been found to be highly dependent on flagellar motility [37, 60]. During this stage, the attachment is reversible and cells are often seen to detach from the surface. Some cells however, are observed to become attached via their cell body and all cells that progress to the second phase of attachment are observed to have transitioned into the body-attached stage. The three distinct modes of surface attachment may be seen in figure 1.7.

The second stage of development is when the cells are irreversibly attached and begin to form cell clusters on the surface [60]. It is not yet fully understood whether these cluster are formed from primarily daughter cells, cells recruited from the bulk fluid, cells migrating on the surface or a combination of multiple mechanisms. During this stage, motility is down-regulated and the LasI/LasR QS system has been observed to activate [42]. It is thought that the activation of this system stimulates certain genes controlling the cell-associated and extracellular virulence of *P. aeruginosa* to be expressed [61]. These factors include motility, adhesion (e.g. pili) and compounds produced by the cell. However, in 2014 Siryaporn *et al* [62] determined that the mechanical stimulus of surface attachment along with this chemical stimulus was required for virulence.
The activation of the LasI/LasR system, as discussed in the previous section, also stimulates the second RhlI/RhlR system to activate. This activation characterises the third stage of biofilm formation in which the extracellular matrix (EM) is produced and the cell

clusters begin to thicken to be $> 10 \ \mu$m in depth [60]. The EM (previously described in this chapter as 'glue'), also known as the extracellular polymeric substance (EPS) since it consists of various biopolymers, has various roles in biofilm formation and growth. Perhaps key amongst these is to act as a protective barrier against background flows that might remove cells from the surface [9], and act as a barrier to any antimicrobials in the surrounding fluid. The presence of EPS has been found to increase the resistance of cells to antimicrobials by a factor of between 100 and 1000 [46, 63]. On top of this, the EPS also acts as a scaffold for the 3D biofilm structure, holds the cells in close proximity for cell-cell communication and retains all nutrients (e.g. from lysed cells). The increased interest in biofilms has, not surprisingly, led to an increased concern in the precise constituents making up the matrix. Sometimes called the 'dark matter of biofilms' [64], research into the components of the EPS has been hindered by the fact that there is so much variation in the make-up of EPS. The matrix can vary greatly depending on species, shear, temperature and nutrients [65]. Regardless of the specific makeup, the EM is the distinguishing characteristic of a biofilm and makes them one of the most successful life forms on earth [66].

The fourth biofilm stage occurs after approximately 6 days of growth and it characterised by the biofilm reaching its maximum thickness ($\approx 100 \ \mu$m depending on conditions) [60]. This 3D structure allows the extraction of oxygen and nutrients from the bulk fluid via diffusion.

After 9 days, the biofilm reaches its final stage - dispersion. Openings in the cell clusters develop from which motile cells disperse into the bulk fluid [60]. These openings are thought to allow the diffusion of nutrients and other agents through the biofilm [67]. Throughout the stages of biofilm formation, the ratio of EPS to cells in the biofilm steadily increases so that by this final stage, the biofilm is approximately $80 - 85\%$ EPS (by volume) [41].

For this thesis, the main focus is on the first stage of biofilm formation and the role that motility in this early stage may have on the progression to the later stages. As such, the first two quorum sensing systems (LasI/LasR and RhlI/ RhlR) are of most relevance, since these are the systems involved in early stage biofilm formation [42, 60].

1.4.4 Role of motility in biofilm formation

It has previously been observed that motile cells are more effective at forming biofilms [68–71] and O'Toole and Kolter [37] determined that *P. aeruginosa* mutants defective in either flagella or type IV pili were poor at forming biofilms. The pili-defective mutants

attached to the surface at a similar rate to wild-type but did not form the clusters of the second biofilm stage. This suggests that the twitching motility associated with pili (where cells use pili to 'crawl' across a surface) may be important in this stage of biofilm formation.

The flagellar defective mutants, on the other hand, were less likely to attach to the surface in the first place. This result is supported by a similar investigation by Sauer [60] and is indicative of the importance of flagella in the initial attachment phase. It is not clear, however, whether it is flagella-driven motility or the presence of the flagella themselves that is of importance. It has also not been investigated whether the flagella are important only in causing initial attachment or whether they are also important in the maintenance of surface attachment leading to the later biofilm stages. In this thesis, the effect of flagella-induced flows on the surface is investigated and the impact this has on progression to later stages of biofilm formation is discussed. In chapter 4, experimental evidence is presented that suggests the first biofilm stage is more complex than previously thought and may need to be subdivided.

1.4.5 Effect of lactam analogue on biofilms

Some life forms have evolved mechanisms to prevent colonisation by microbes, and one way in which they do this is by producing quorum sensor inhibitors (QSIs). Using various mechanisms, these QSIs block the production or action of QS molecules and prevent biofilms from being established. One particularly effective group of such inhibitors in a family of halogenated furanones derived from a marine algae *Delisea pulchra* [72]. The shape of these furanones suggests that they act as competitive inhibitors for bacterial QS molecules [57]. This means that the furanones, having a similar shape to the QS molecules, attach to the QS receptor binding sites and therefore the QS molecules are unable to attach.

QSIs are of interest as a potential new way of preventing bacterial biofilm infections. At present, most bacterial infections are treated by antibiotics. This has two disadvantages. The first is that antibiotics typically have a low level of specificity meaning they can cause problems relating to a diminished microbiome. The second issue, of increasing relevance, is the fact that bacteria can become resistant to antibiotics. In a 2014 report on global public health, the World Health Organisation (WHO) reported that in many regions the resistant proportion of three bacterial species (*Escherichia coli*, *Klebsiella pneumoniae* and *Staphylococcus aureus*) to commonly used antimicrobials was over 50%

FIGURE 1.8.

a) Photograph of a *Delisea pulchra*. It grows to approximately 60mm in height and is found on exposed coral reefs. Image taken from http://www.nswmarineguide.com/species/plocamium-angustum. b) Marine anti-fouling field trial, arrow shows rod impregnated with the *Delisea pulchra* derived furanones compared to control rods. Created by BioSignal Ltd (https://asknature.org/idea/biosignal-products-formerly)

[73]. Since most antibiotics kill cells, there is a great selective pressure to develop a resistance to the toxin [57]. At present, there are very few alternatives to antibiotics but the antibiotics themselves are becoming increasingly ineffective. Dr Margaret Chan, director-general of WHO claimed that if antibiotics do become totally ineffective, it will mean 'an end to modern medicine as we know it. Things as common as Strep throat or a child's grazed knee could once again kill' [73].

A treatment derived from QSIs could combat both the issue of low specificity and that of resistance. A treatment of this form would not kill cells, but would prevent them forming biofilms. Thus, it would be safe to the microbiome and there would be a significant reduction in the selective pressure for resistance. This would mean that any such treatment would have a substantial lifespan of efficacy.

As part of the investigation into whether the flow induced by surface-attached cells has any ramifications on biofilm formation, the effect of a candidate anti-biofilm compound from Unilever, on the flow is investigated. This anti-biofilm compound is a furanone-derived lactam analogue obtained from *D. pulchra*. It is believed that this lactam analogue is a QSI [70] but it is not known whether it also has an effect on cell motility. This investigation will aim to establish whether this suspected QSI impacts motility.

1.4.6 Outline of methods used to model biofilms

As discussed previously, biofilms (even single-species) are incredibly complex systems. Modelling is an indispensable tool for investigating such abstruse systems and the problem has been approached in various ways. One of the earliest such models is a (comparatively) simple, one dimensional, continuum approach, first applied to biofilms in 1980 [74, 75]. These types of models tend to focus on quasi-steady-state growth of the biofilm, predicting dynamics within the biofilm and biofilm thickness by considering conservation principles. Often used to model biofuel reactor systems, these models are able to predict how the biofilm state depends on available nutrients, reactor layout, growth rates of the microbes and assumed detachment mechanisms. A key use of these types of models was to establish the importance of microbe growth rate on detachment, which is crucial in biofuel reactors [76]. However, since these models require input parameters (the growth rate at a certain nutrient level, for example), they rely heavily on experimental data and any predictions are only as accurate as the inputted values. The 1D descriptors also fail to model early stages of biofilm formation so are of limited use when investigating conditions necessary for a biofilm to form. Also, being one-dimensional, these models are unable to capture the three-dimensional nature of a biofilm.

Another common method for modelling biofilms is the cellular automaton (CA) approach, which evolved from Conway's game of life [77]. Here, the surface is divided into a regular grid that can be in one of a finite number of states. The state of each element in the grid at the discrete timestep, t, is a function of the states of elements surrounding it at time $t-1$. A clear advantage of CA models is that they can capture complex multi-dimensional phenomenon despite being relatively simple. In particular, 3D structures that have been observed in experiments have been replicated using CA [78]. This simplicity means multiple simulations with various parameters (changing nutrient uptake rates, for example) can be performed relatively fast [79]. CA also allows for the model to tackle multispecies biofilms [80], cell-cell communication and decision-based biological rules [81, 82]. This form of biofilm modelling also has the advantage that the simulated biofilms can be 'grown' from nothing. One of the key results from CA models is the relative importance of the different parameters in biofilm growth. In particular, small variations in nutrient concentration has been found to dramatically alter the structure of the developing biofilm [83]. However, the necessity of specifying the grid has led to the criticism that the biofilm is limited in its growth to pre-specified directions [84]. Furthermore, the rules used to determine the state of each element can

seem arbitrary and sometimes have little experimental grounding [85].

A third class of model, often directly compared to CA models, is individual-based models (IbM), sometimes called agent-based models [85, 86]. Here the cells are modelled with a particular geometry, such as spheres which have varying volumes, masses and growth parameters. Each of these cell units can grow by consuming surrounding substrate and divide when a threshold volume is reached [87]. In this way, the individual nature of the cells is linked to equations balancing production, consumption and diffusion of the substrate [88]. Thus IbM are a hybrid discrete-continuous class of model. The spreading mechanism in IbM means growth may be continuous in all directions, overcoming one of the limitations of CA. However, IbM are typically more computationally expensive than standard CA models. The often-used hard sphere model for cell also poses a problem since evidence suggests that cells change their shape depending on conditions [89]. However, the IbM do offer a way to build chance and randomness into biofilm models and in fact the main results of IbM have been randomized 3D biofilm structures that reflect what is seen in experiments [90].

1.5 Modelling physical aspects of flow

1.5.1 Stokes flow

Many investigations into the flow produced by bacterial cells start with the assumption that the flow may be described by the Stokes equations. The Stokes equations are derived from the Navier-Stokes equations.

$$\nabla \cdot \mathbf{v} = 0 \tag{1.1}$$

$$\rho \left(\frac{\partial \mathbf{v}}{\partial t} + \mathbf{v} \cdot \nabla \mathbf{v} \right) = -\nabla P_r + \mu \nabla^2, \mathbf{v} + \rho \mathbf{f}, \tag{1.2}$$

here, $\mathbf{v}$ is the fluid velocity, ρ is the density, P_r is the pressure, μ is the dynamic viscosity and $\mathbf{f}$ describes any external forces on the fluid.

These Navier-Stokes equation are obtained by considering the conservation of mass and momentum [91**?**]. Equation (1.1) is known as the incompressibility condition and, as the name suggests, stipulates that the fluid in unable to be compressed, while equation (1.2) is the conservation of momentum equation.

The above Navier-Stokes equations effectively capture the dynamics of all incompressible Newtonian fluids but are nonlinear and as such can be extremely difficult,

if not impossible, to solve analytically. A common approach to this is by taking 'limiting' realms and analyzing the fluid dynamics. The realm that is of most relevance when studying the dynamics of micro-swimmers is the low-Reynolds number realm. The Reynolds number is obtained by non-dimensionalising equation (1.2). In a co-ordinate system of x_1, x_2, x_3, lengths are non-dimensionalised using a characteristic length L and velocities non-dimensionalised using a characteristic velocity U. The non-dimensional time is $\bar{t} = tU/L$, the non-dimensional pressure is $\bar{P}_r = P_r L/\mu U$ and $\bar{\nabla} = \frac{\partial}{\partial \bar{x}_i L} + \frac{\partial}{\partial \bar{x}_j L} + \frac{\partial}{\partial \bar{x}_k L}$. Applying this non-dimensionalisation to equation (1.2) gives

$$\frac{\partial U \bar{\mathbf{v}}}{\partial \bar{t} L/U} + \frac{U^2}{L} \bar{\mathbf{v}} \cdot \bar{\nabla} \bar{\mathbf{v}} = \frac{-1}{\rho L^2} \bar{\nabla} \bar{P}_r \mu U + \frac{\mu}{\rho L^2} \bar{\nabla}^2 \bar{\mathbf{v}} U, \tag{1.3}$$

which, after collection of terms and a division by U^2/L, gives

$$\frac{\partial \bar{\mathbf{v}}}{\partial \tau} + \bar{\mathbf{v}} \cdot \bar{\nabla} \bar{\mathbf{v}} = -\frac{\mu}{\rho U L} \bar{\nabla} \bar{P}_r + \frac{\mu}{\rho U L} \bar{\nabla}^2 \bar{\mathbf{v}}. \tag{1.4}$$

The final term in this equation is known as the viscous term and determines the effect of viscosity on the flow. The parameter in front of this term is $\mu U L/\rho$ and is the inverse of the Reynolds number. Therefore, the Reynolds number, Re, may be written as

$$\text{Re} = \rho U L/\mu. \tag{1.5}$$

In the limiting case where $\text{Re} \to 0$, $1/\text{Re} \to \infty$ and the viscous term dominates. Dropping the bars for clarity equation (1.4) can be written as

$$Re\left(\frac{\delta \mathbf{v}}{\delta t} + \mathbf{v} \cdot \nabla \mathbf{v}\right) = -\nabla P_r \nabla^2 \mathbf{v}, \tag{1.6}$$

Taking $\text{Re} = 0$ and considering external forces, $\mathbf{f}$, allows equations equation (1.2) and equation (1.1) to be written as

$$-\nabla P + \mu \nabla^2 \mathbf{v} = -\rho \mathbf{f} \tag{1.7}$$

$$\nabla \cdot \mathbf{v} = 0. \tag{1.8}$$

These are known as the Stokes equations and are the basis for many micro-swimmer models.

1.5.2 Diffusion

Motivated by QSM and the lactam analogue, diffusion is involved in this thesis. In 1827, a Scottish botanist named Robert Brown was looking at a suspension of some

pollen grains under a microscope [92]. He noticed that minute particles ejected from the grains were moving in the water for no explicable reason. He repeated the observation with non-organic matter to establish that it was a physical phenomenon rather than an organic one. It wasn't until a century later that the physics involved in the motion was understood and named Brownian motion. Originating from thermal fluctuations in the surrounding fluid, Brownian motion is the motion of particles (such as the pollen particles) due to collisions with the molecules in the fluid they are in. Assuming the fluid is homogeneous, the mean induced particle velocity is zero but the variance is non-zero [93]. The equipartition principle is used to assume that, if a particle is moving in three dimensions, on average the kinetic energy is split equally between the three dimensions. Using this principle for the kinetic energy, the speed of the particle per translational degree of freedom can be determined as

$$U_p = +\sqrt{\frac{k_B T}{m}}, \tag{1.9}$$

where k_B is the Boltzmann constant, T is the absolute temperature and m is the particle's mass. The subsequent motion of a spherical particle can be written as

$$\frac{d}{dt}(mU) = -\frac{1}{2}\rho C_D \pi A^2 U^2, \tag{1.10}$$

where A is the particle's radius and C_D is the drag coefficient for a sphere. In low-Reynolds number flow, there is an analytical solution for the drag coefficient such that

$$C_D = \frac{24}{\text{Re}}. \tag{1.11}$$

Therefore, if the characteristic length scale in the Reynolds number is taken as the diameter of the sphere, the force balance for a sphere in low-Reynolds number flow can be written as

$$m\frac{dU_p}{dt} = -6\pi\mu A U_p. \tag{1.12}$$

This can then be integrated to give

$$U_p(t) = U_{p0}\exp(-t/t_r) \tag{1.13}$$

where U_0 is the particle velocity at $t = 0$ and $t_r = m/(6\pi\mu A)$. The parameter t_r can be considered as the timescale over which the particle returns to rest after a collision and can be used to determine the distance traveled after a collision $\Delta x_s = \frac{\sqrt{mkT}}{6\pi\mu A}$. Therefore,

the particle undergoes a random walk of step time τ and step size Δx_s. The three dimensional diffusion coefficient of the particle can then be written as

$$Di = \frac{\Delta x_s{}^2}{t_r} = \frac{kT}{6\pi\mu A}.$$

(1.14)

In 1997, Dusenbury investigated at what organism size Brownian motion was important [94]. He determined that, for organisms of a radius greater than 0.6 μm Brownian motion is obscured by active swimming. Therefore, it is expected that Brownian motion will be obscured when *P. aeruginosa* is actively swimming.

1.5.3 Pèclet number

Many biofilms form in flow environments, whether they be external flows or due to the individual microbes. Therefore, it is of importance to this thesis which flows dominate over diffusion. Named after the French physicist Jean Claude Eugene Pèclet, the Pèclet number, Pe, is defined as

$$\text{Pe} = \frac{LU_c}{D},$$

(1.15)

where L is the characteristic length scale of the system and U_c is the characteristic velocity of the flow [91]. This dimensionless parameter gives the ratio of advective versus diffusive transport rates and is useful for understanding the importance of Brownian motion in a problem. Small Pe corresponds to fast diffusion over a weak flow while a large Pe indicates strong flows over a weak diffusion. Therefore, large Pe is expected for the work in this thesis.

1.5.4 Stokeslet singularity

Imagine a quiescent, low-Reynolds number flow with a single point force within it. The flow produced by this point force must satisfy the Stokes equations previously, equation (1.7) and equation (1.8), everywhere in the field except at the exact point force location, where the flow will be singular. This fundamental solution was first obtained by Oseen [?]. In 1953, Hancock gave it its common name [?], a Stokeslet, and it has since been indispensable in the modelling of microhydrodynamics. The velocity profile produced by this Stokeslet decays with 1/distance from the initial point force location. The flow shape can be seen in figure 1.9, and may be described by equation (1.16) below [27],

$$\mathbf{u}^s(F;\mathbf{r};\mathbf{P}) = \frac{F}{8\pi\mu}\left(\frac{\mathbf{P}}{r} + \frac{(\mathbf{r}\cdot\mathbf{P})\mathbf{r}}{r^3}\right),$$

(1.16)
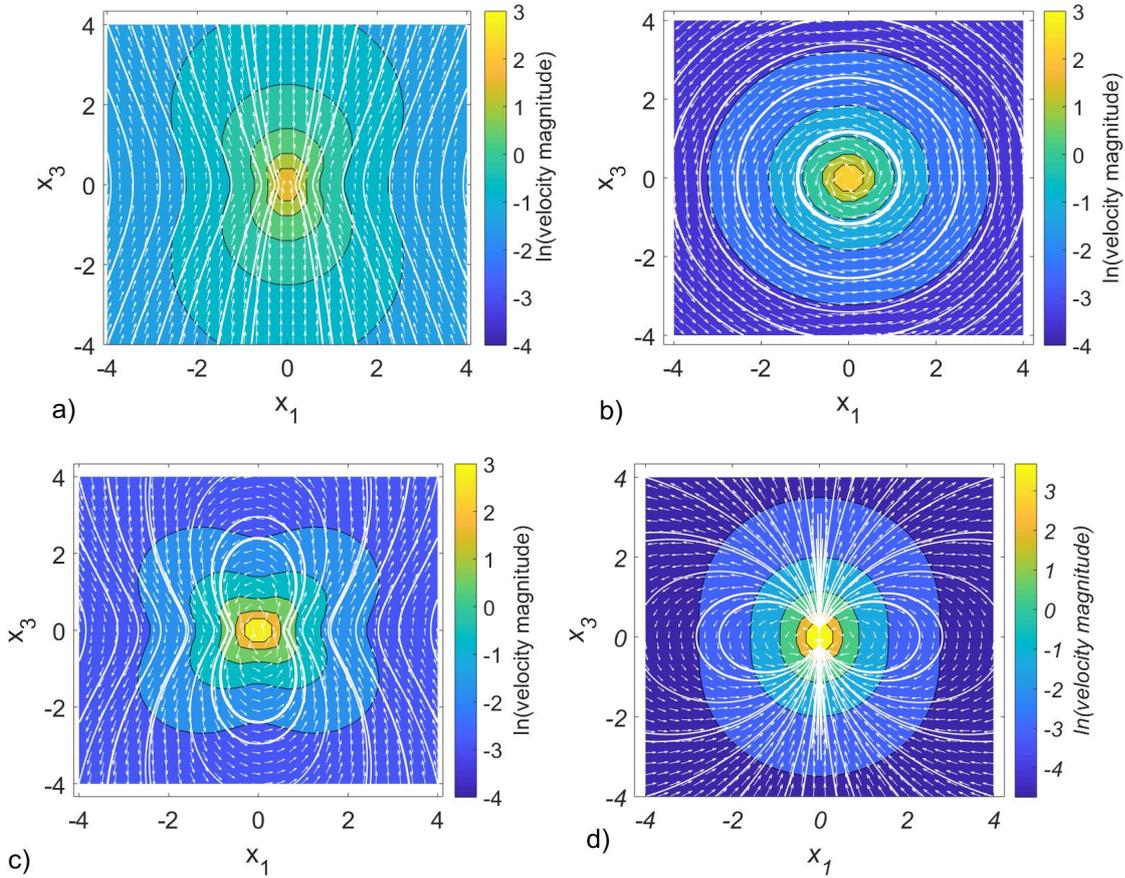
FIGURE 1.9. Singularity flow fields

The fields due to singularities in Stokes flow. a) the field of a Stokeslet at the point $(0,0,0)$ pointing in the direction $(0,0,1)$. The relative velocity magnitude $\times r$ are shown by arrows. b) the field of a rotlet at $(0,0,0)$. In this case the Stokeslet direction or $\mathbf{P}$ is again $(0,0,1)$ and the gradient direction, $\mathbf{d} = (1,0,0,)$. The relative velocity magnitude $\times r^2$ is indicated by the arrows. c) the field of a Stokes dipole with the same $\mathbf{P}$ and $\mathbf{d}$ as in the rotlet. Again the relative velocity magnitude $\times r^2$ is shown by arrows. d) the field of a source doublet with, again, the same $\mathbf{P}$. Arrows are the velocity $\times r^3$. For all fields, i_1, i_2, i_3 denote the axes and are analogous to the x_1, x_2 and x_3 directions.

where $\mathbf{r}$ denotes the vector between the point in the field to be investigated from the point force position, $r = |\mathbf{r}|$, F is the strength of the Stokeslet and $\mathbf{P}$ is the direction of the Stokeslet.

This singularity is important to this thesis since it can be used to model the force on the fluid due to a tethered, moving flagellum.

1.5.5 Stokes-doublet singularity

The linearity of the above Stokes equations, equation (1.7) and equation (1.8), means that any linear combination or derivative of the Stokeslet solution equation (1.16) is also a solution to the Stokes equations. Thus higher order singularity solutions to equation (1.7) and equation (1.8) can be constructed.

Taking the derivative of equation (1.16) in a given direction results in a velocity field that decays with the square of distance from the initial singularity point (figure 1.9). Termed a Stokes-doublet singularity solution, this field is given by

$$\mathbf{u}^{sd}(D;\mathbf{r};\mathbf{d};\mathbf{P}) = \frac{D}{8\pi\mu}\left(\left[\frac{(\mathbf{d}\cdot\mathbf{r})\mathbf{P}-(\mathbf{P}\cdot\mathbf{r})\mathbf{d}-(\mathbf{d}\cdot\mathbf{P})\mathbf{r}}{r^3}+\frac{3(\mathbf{P}\cdot\mathbf{r})(\mathbf{d}\cdot\mathbf{r})\mathbf{r}}{r^5}\right]\right), \tag{1.17}$$

where D characterises the stokes doublet strength and $\mathbf{d}$ is the direction of the derivative.

1.5.6 Rotlet singularity

The Stokes-doublet singularity solution may be decomposed into symmetric and asymmetric terms. Batchelor termed the symmetric term a stresslet [**?**]. The anti-symmetric term may be thought of as the flow due to a point torque in the flow. This rotlet term (alternatively called the couplet), produces a velocity field given by

$$\mathbf{u}^{r}(\Omega;\mathbf{r};\mathbf{P}) = \Omega\frac{\mathbf{P}\times\mathbf{r}}{r^3}, \tag{1.18}$$

where Ω is the rotlet strength and the flow can be seen in figure 1.9. This singularity is of particular relevance to the thesis since it can be used to capture the rotational component of flagellar motion.

1.5.7 Source doublet singularity

Setting $P = 0$ in equation (1.7) we obtain Laplace's equation [**?**], from which we can obtain singular potential flow solutions to the Stokes equation (1.7) and equation (1.8). For this thesis, one of these solutions is of particular interest; that is, the source-doublet or dipole solution. This singularity may be envisioned as a source/sink singularity producing a velocity field as seen in figure 1.9. The velocity profile for this field can by found by applying the negative Laplacian to equation (1.16) resulting in equation (1.19).

$$\mathbf{u}^{d}(E;\mathbf{r};\mathbf{P}) = \frac{E}{8\pi\mu}\left(\left[-\frac{\mathbf{P}}{r^3}+\frac{3(\mathbf{r}\cdot\mathbf{P})\mathbf{r}}{r^5}\right]\right), \tag{1.19}$$

where E indicates the strength of the source-doublet.

1.5.8 Image system of a Stokeslet

The flow described by equation (1.16) gives the flow due to a point force in an infinite, quiescent fluid. However, biofilms, by their very nature, are not in infinite fluids. Instead, much of the work in this thesis will involve modelling cells near/on a no-slip boundary. In order to account for the effect of the boundary, it is common to use what is known as the 'method of images'. Initially used in electrostatics, suitable 'image singularities' are placed at an 'image point' so that the no-slip plane is equidistant from both the initial singularity point and the image singularity (see figure 1.10). The type and strength of singularities at the image point are chosen to satisfy the no-slip boundary conditions. The appropriate image system for a Stokeslet singularity near a no-slip boundary (increasingly called a Blakelet), was derived by Blake in 1971 [95]. To simplify the analysis, the first step is to place an equal but opposite Stokeslet at the image point. The vector $\mathbf{R} = (R_1, R_2, R_3)$ defines a point in the field from the image singularity point. Therefore, similar to equation (1.16), the field due to the Stokeslet image, $\mathbf{u}^{s*}(F; \mathbf{R}; \mathbf{P})$, may be written as

$$\mathbf{u}^{s*}(F; \mathbf{R}; \mathbf{P}) = \frac{-F}{8\pi\mu}\left(\frac{\mathbf{P}}{R} + \frac{(\mathbf{R}\cdot\mathbf{P})\mathbf{R}}{R^3}\right) + \mathbf{w}^s(\mathbf{R}; \mathbf{P}), \tag{1.20}$$

where $R = |\mathbf{R}|$ and $\mathbf{w}^s(F; \mathbf{R}; \mathbf{P})$ represents the extra singularities necessary to satisfy the no-slip boundary condition. If the boundary is taken at $x_3 = 0$ for simplicity (i.e. all the points where $r_3 = 0$), then for an initial Stokeslet aligned parallel to the boundary, the tangential velocities of $\mathbf{w}^s(\mathbf{R}; \mathbf{P})$ at the boundary must be zero but the normal velocity is not. On the other hand, if the initial Stokeslet is aligned perpendicular to the boundary the tangential velocities of $\mathbf{w}^s(\mathbf{R}; \mathbf{P})$ at the boundary must be non-zero and the normal velocity is zero. A Fourier transform can be used to determine the appropriate form of $\mathbf{w}^s$ dependent on the Stokeslet direction. In 2008, Ainley *et al* also obtained the corresponding result by balancing co-efficients of boundary velocities [30] and in 2012 Spagnolie and Lauga approached the problem from a different set of 'tilt' vectors [27]. All approaches obtain the result that $\mathbf{w}^s$ has potential dipole and source doublet components. In this thesis, the later formulation was chosen as it clearly identifies the angle of the Stokeslet to the plane θ (see figure 1.10). Using this formulation, the total image system for a Stokeslet may be written as

$$\mathbf{u}^{s*}(F; \mathbf{R}; \mathbf{P}) = \cos(\theta)\Big(-\mathbf{u}^s(F; \mathbf{R}; \mathbf{P}_\phi) + 2h\mathbf{u}^{sd}(\mathbf{F}; \mathbf{R}; \mathbf{P}_\phi; \hat{\mathbf{z}}) - 2h^2\mathbf{u}^d(F; \mathbf{R}; \mathbf{P}_\phi)\Big)$$

$$+ \sin(\theta)\Big(-\mathbf{u}^s(F; \mathbf{R}; \hat{\mathbf{z}}) - 2h\mathbf{u}^{sd}(F; \mathbf{R}; \hat{\mathbf{z}}; \hat{\mathbf{z}}) + 2h^2\mathbf{u}^d(F; \mathbf{R}; \hat{\mathbf{z}})\Big), \tag{1.21}$$
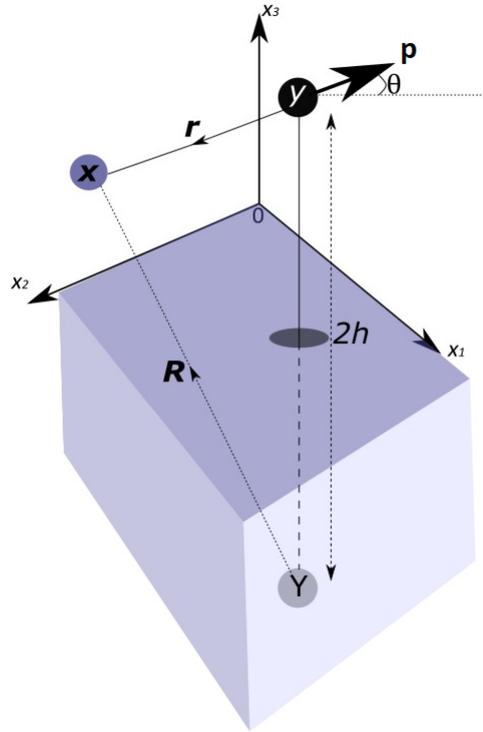
FIGURE 1.10.
A schematic of the initial singularity position, **y**, and its image point, **Y**. Vectors **r** and **R** are vectors from the initial singularity point and the image point to a point in the field, **x**, respectively. The initial singularity is a distance h above the no-slip surface (the $x_3 = 0$ plane), and has a direction **P**. The vector **P** makes an angle θ to the horizontal.

where ϕ is the projection angle of **p** onto the $x_1 - x_2$ plane (see figure 1.10), $\mathbf{P}_\phi = \big(\cos(\phi), \sin(\phi), 0\big)$, $\hat{\mathbf{z}} = (0, 0, 1)$ and h is the height of the Stokeslet above the boundary.

1.5.9   Image system of a rotlet

Similarly, the image system for a rotlet was derived by Blake and Chwang in 1973 [28] and has been re-obtained or rewritten in many ways since. In this case, components of the rotating flow normal to the wall are exactly balanced by an equal and opposite rotlet at the image point but components parallel to the wall require additional terms. For this project, the vector formulation of the rotlet image system fully derived in [27] is used. As in the Stokeslet image system detailed previously, the rotlet image system is dependent on the 'tilt' angle of the singularity to the image surface. The total tilted rotlet image
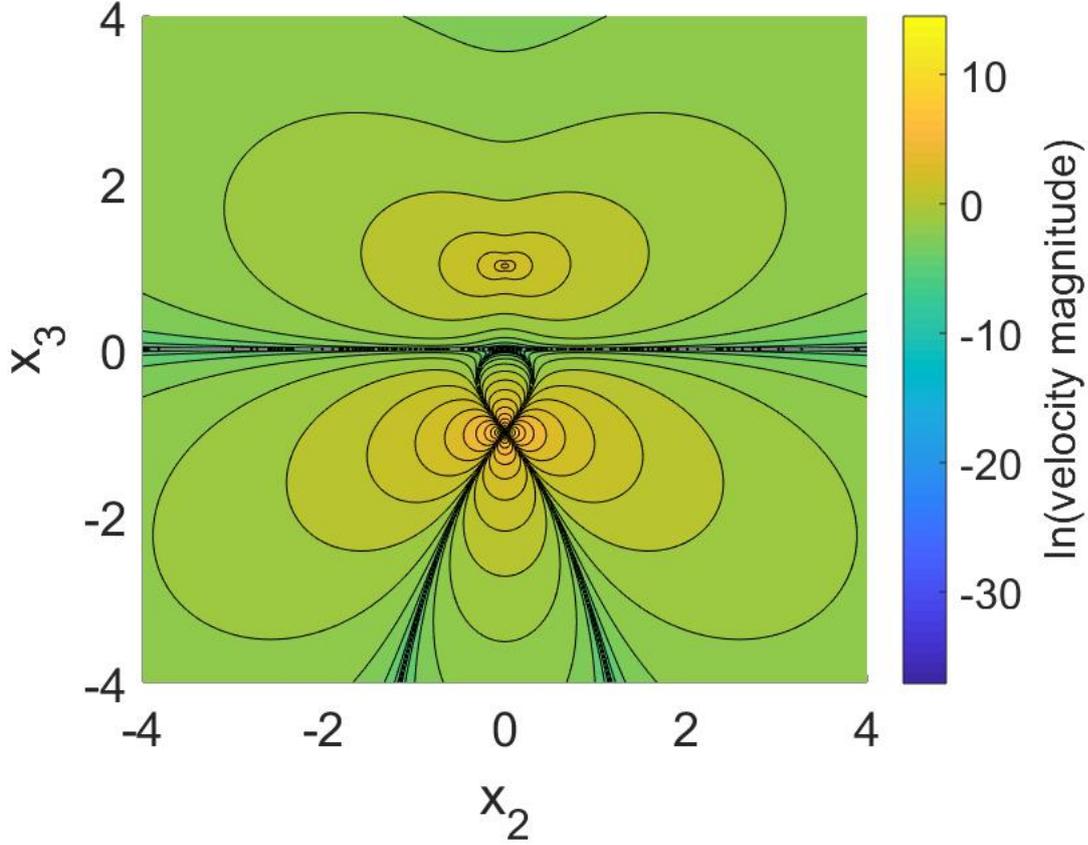
FIGURE 1.11.
    The flow induced by a Stokeslet at the point $(0,0,1)$ in the direction (010) interacting with its image. The no-slip boundary is the x_1, x_2 plane. The field can been seen to drop to zero at the boundary to within numerical precision.

system can be written as

$$\mathbf{u}^{r*}(\Omega;\mathbf{R};\mathbf{P}) = \cos(\theta)\big(-\mathbf{u}^r(\Omega;\mathbf{R};\mathbf{P}_\phi) + 2h\mathbf{u}^d(\Omega;\mathbf{R};\mathbf{P}_\phi^\perp) - \mathbf{u}^{sd}(\Omega;\mathbf{R};\mathbf{P}_\phi^\perp;\hat{\mathbf{z}}) - \mathbf{u}^{sd}(\Omega;\mathbf{R};\hat{\mathbf{z}};\mathbf{P}_\phi^\perp)\big)$$
$$- \sin(\theta)\mathbf{u}^r(\Omega;\mathbf{R};\hat{\mathbf{z}}),$$

(1.22)

where $\mathbf{P}_\phi^\perp = (-\sin(\phi), \cos(\phi), 0)$.

1.6 Swimming cells

There have been various attempts to capture the flow due to motile cells. Within this thesis, a model for the flow induced around a surface-attached cell with a moving

27
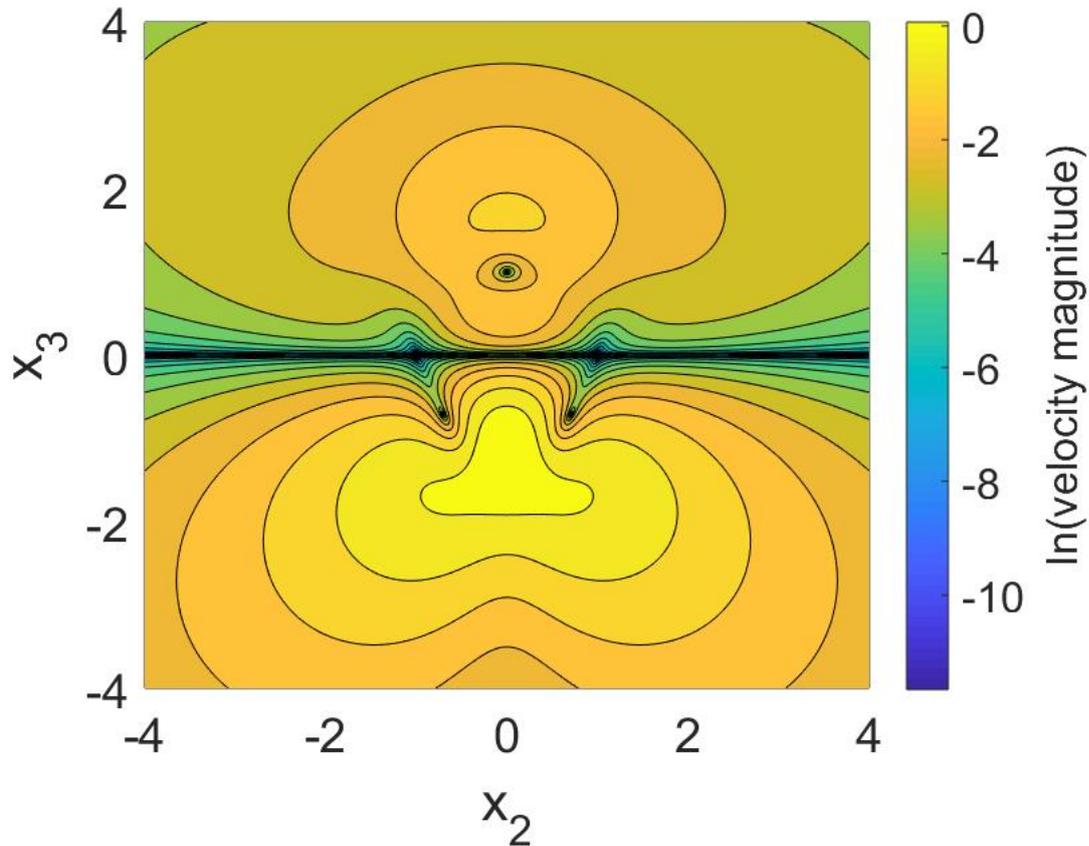
FIGURE 1.12.
  The flow induced by a rotlet at the point $(0, 0, 1)$ interacting with its image.
  The no-slip boundary is the x_1, x_2 plane. The field can been seen to drop to
  zero at the boundary to within numerical precision.

flagellum is developed. For context as to how the this model fits into the literature, here
a brief overview of previous models for motile cells is presented.

1.6.1 Modelling swimming cells far from boundaries

The increasing interest in bacterial motility and its impacts on virulence, biofilm for-
mation and other phenomena has, unsurprisingly, led to an increase of methods for
modelling bacterial motility. The complex and often challenging nature of experimenta-
tion in the area of bacterial motility means that models can often be an invaluable tool
of investigating different aspects of this area. Of particular interest for this project are
those models used to determine the flow induced by swimming bacteria.

Models of swimming bacteria may be broadly classified into two categories: those that incorporate detailed aspects of bacterial geometry and minimal models. The first category encompasses those models which use boundary conditions to model the particular bacterial geometry to a greater or lesser degree. An early example of this was Taylor's swimming sheet described in 1951 [96]. This was one of the simplest geometric models where a swimming bacterium was modelled as a 2D sheet with small amplitude travelling waves propagating along it. By solving the Stokes equations with no-slip boundary conditions on the sheet, Taylor obtained the flow induced by the travelling wave deformation and hence, the velocity of the sheet's motion [21].

The seminal work by Taylor triggered a rush of work on micro-swimmers [97] but was limited in applicability in that the wave amplitudes were assumed to be small whereas real flagella undergo large-amplitude deformations [21]. Resistive Force Theory (RFT) proposed by Gray and Hancock in 1955 [98] and the closely related Slender-Body Theory (SBT) were suggested as possible improvements. They argued that, assuming the radius of curvature of the flagellar deformation was large compared to the radius of the flagellum, the flagellum could be modelled as a series of straight cylinders. Then, by replacing the cylinders with suitable singularity solutions to the Stokes equations, the tangential and normal forces exerted by the cylinders can be found to be proportional to the respective centerline velocities. The total force and thus the flow induced can be obtained by integrating over the whole flagellum. A relatively simple formalization, RFT has been extensively utilised to model various elements of flagellar propulsion [99–101].

RFT is able to capture various aspects of flagellar motility [102] but is only valid for thin filaments and so fails to capture the flow decay observed in experiment. This is especially true when there is a comparatively large cell body [102]. Another failure of RFT is that the different elements are hydro-dynamically uncoupled from each other. The improvement on RFT, SBT, was first proposed by Hancock in 1953 [103]. The idea is to place a series of singularity solutions to the Stokes equations along the centerline of the filament and solve for the flow. A natural extension of RFT, the full solution is approximated by a series of logarithmically small terms [21]. Since used to investigate a wide range of scenarios [104, 105], SBT is still one of the most widely used tools available for modelling flagellar propulsion.

Minimal models, on the other hand, attempt to capture the key aspects of bacterial

motion and induced flow in the simplest way to avoid computational expenditure and make the key mechanisms clear. These types of models are often employed to look at interactions between multiple bacteria or populations. For example, Hernandez-Ortiz *et al.* used a minimal model to investigate the collective motion of bacteria [106]. In their model, the complexities of each individual bacterium were ignored and the far-field flow induced by their swimming was modelled using three point source solutions to the Stokes equations. Using this model, the dynamics of whole populations in various environments were simulated and they were able to reproduce swirls and collective behaviour that had been reported previously.

A further method is the Boundary Element Method (BEM). For this approach, boundary conditions on a mesh of nodes on the surface of an object are used to determine boundary values rather than values for the whole space. This method is often applied to micro-hydrodynamics by fixing the no-slip boundary conditions on the surface of the cell. In this way, individual helical flagella can be modelled [107, 108] along with more complex geometries such as multiple flagella and body shapes [109]. This method has been shown to replicate experimental results [108] but can be computationally expensive. However, symmetries in the geometry can be used to reduce the computational expenditure of the technique [110].

A further way of reducing the computational expenditure of BEM is to replace the singular kernel at the nodes with a regularized form so as to reduce the number of nodes required. This is the technique used in the method of regularized Stokeslets [110]. Here the objective is to determine the forces on a body by determining the appropriate forces on a mesh of nodes over the body to satisfy boundary conditions. However, in this case, the forces are applied over a small ball that vary smoothly from a maximum at the centre to zero on the surface [111]. By removing the singularities and 'spreading' the nodes, fewer nodes are needed and the computational difficulty associated with singularity points is removed.

1.6.2 Modelling swimming cells close to boundaries

Models of a swimming bacterium near a solid boundary date back to 1965 when Reynolds investigated the swimming of a infinite waving sheet near a no-slip boundary [112]. Since then, SBT and RFT have been adapted to consider the presence of a boundary [28, 113] and have been used to investigate flagellar motion near boundaries to great effect [114].

Such models capture the altered flow due to the boundary provided the flagellar distance from the wall is much greater than the flagellum radius [115].

BEM has been applied successfully to swimmers near a wall [116] and was also a useful tool in investigating the effect of cell geometry on near-surface motility [109, 117]. In 2005, Goto *et al* used a boundary element method to explain how the singly flagellated bacterium *Vibrio alginolyticus* was observed to begin swimming in circles near a no-slip surface. Their results indicate that the motion is influenced by the pitching angle of the cell and the rotational direction of the flagellum. This phenomenon of circular trajectories near a surface has been observed in many bacterial species including *E. coli* [21]. This circular motion was shown to be a purely hydrodynamical effect by Lauga *et al.* [21] who used RFT to model a bacterium with a helical flagellum and a spherical body.

1.6.3 Modelling surface attached cells

In 2017, Martindale and Fu also used a centreline distribution of regularized Stokeslets along with a mean field approximation to investigate the flow due to what they called a 'flagellar forest' [118]. The helical flagellum is attached to a no-slip boundary and the rotation rate is imposed. However, in this case the helix is held at some 'tilt' angle to the boundary rather than perpendicular to it. First they look at the time-averaged volumetric flow through a plane near the flagella for various fixed flagellar tilt angles relative to the no-slip boundary, using both left and right-handed flagella with various polymorphic forms. This word 'polymorphic' refers to the different shapes the flagella can adopt. The flagella can curve within the helix or be tighter/looser wound within the helix. They found that the pumping magnitude greatly depended on the polymorphic form but for each form the greatest pumping was when the tilt angle was 45°. Also of note, they found that reversing the handedness simply reversed the direction of the pumping but the magnitude was the same. This result would be expected with the reversibility of flow at low Reynolds numbers.

Martindale and Fu then selected one 'normal' and one 'curly' polymorphic forms which had helical pitches of $2.233 \mu m$ and $1.361 \mu m$ respectively. These were the most commonly found polymorphisms in experiment [40]. The 'normal' form is left-handed and would therefore be associated with the 'run' in the standard run-reverse of *P. aeruginosa*. Conversely, the 'curly' form is right-handed and so corresponds to the 'reverse'. To study their 'flagellar forest', they assume all the flagella are identical with the same tilt angle and feel the same background flow from all other flagella along with its own image flow.

They are, therefore, ignoring all biological fluctuations for their mean-field approach since all flagella are considered identical. What is interesting is that they see stable, self consistent arrangements for the 'normal' flagellum when it is made to rotate clockwise but not when it is rotated anticlockwise. The reverse is seen for the 'curly' flagellum. They also found that the self-sustaining angle was dependent on the rotation rate and the distance between the flagella.

This paper is limited in that all flagella are held constant but it is an interesting way of studying a large array of detailed flagella. The high degree of accuracy available from the complex models such as SBT and the method of regularized Stokeslets comes at a high computational cost. Often, this means that such models are limited to investigating the interaction between a small number of flagella. However, many interesting biological systems involve multiple interacting flagella. One such example is the fluid transport by bacterial carpets that was experimentally investigated by Darnton *et al.* [40] in 2004. Here multiple bacteria were tethered via their cell bodies to a no-slip surface with their motile flagella freely rotating. This bacterial carpet arrangement has a very high number of interacting flagellum and so is not amenable to the computationally expensive method of flagella modelling previously discussed. Instead, in 2010, Uchida and Golestanian [119] developed a minimal model to describe the carpet. In place of substrate-attached cells with free flagella, they looked at an array of 'rotors' consisting of spherical beads, of radius a, that were only allowed to move in circular trajectories, of radius b, which were parallel to, and some distance, h, above, the no-slip plane that represented the substrate.

The bead is assumed to drag fluid behind it as it moves whilst also pumping fluid radially. The radial pumping is modelled by the Blake-Oseen tensor, (the tensor associated with a Stokeslet and its image system for a no-slip boundary) [95]. Using their rotor model and periodic boundary conditions, the velocity field at each timestep was determined using a Fourier transform. They then define a force angle, δ, that is analogous to the β term in the simple model developed in this thesis (see chapter 4), in that it shows the ratio between the force in the radial or tangential directions, or, equivalently, the ratio of the Stokeslet to rotlet strengths.

They are eventually left with a phase equation giving the circular angle of each flagellum and solve this on a grid using the Euler method. If $\delta = 0$, all the fluid is being pumped radially and is driven by the flow of others (ie no rotlet). In this case, the random phase of the initial conditions lead to topological defects which eventually coarsen

into global synchronization. This global synchronization is the end state for $0 < \delta \leq 40°$ When $\delta = 90°$, the rotor is driven by an active torque and they found that the system became disordered. In this situation, the flow due to the rotor is perpendicular to its arm and a neighboring rotor tends to align with flow. However, since every pair of rotors cannot align like this, the system becomes randomly orientated. When $40° < \delta < 90°$, they observed self-proliferating spiral waves around a defect and the direction of the spiral depended on whether the defect was positive or negative.

Whilst this model shows the power of a simplified approach to modelling multi-flagella systems and shows some interesting δ-dependent dynamics, the fact that the beads are constrained to a 2D trajectory is a definite limitation. It should also be noted that the species used in the this experiment was *S. marcescens*, which is a multi- flagellated cell and so in the bacterial carpets study the assumption that $b, h \ll$ flagella separation may not be valid. However, the questions asked in this paper about transport due to surface attached bacteria has obvious implications for biofilm formation.

SBT has also been applied the flow due to bacterial cells on a surface. In 2018, Buchmann *et al.* [120] investigated just such a scenario by studying the flow around two helical flagella tethered with fixed orientation to a no-slip surface. The helical flagella were modelled using a centreline distribution of regularized Stokeslets with their associated no-slip boundary conditions. Buchmann *et al.* specify the kinematics of the helices and so solve for the necessary forces. It should be noted that in this work they follow the Cortez *et al.* [29] method to apply the image system. By plotting the field due to two tethered helices compared to two in free space, the effect of the wall can be seen. The team also defined the helical pitch and compare the pitch angle to the thrust generated by a single one of their tethered flagella. They find that with the wall conditions applied, their model provided good agreement to experimental data, although this is not quantified.

Once they had established a level of confidence in their model, they began investigating the effect of the phase difference between two flagella and the distance between them on the velocity field, the thrust the produced, the power necessary to maintain their constant velocity and their mixing effect. They found that two helices do not pump twice as much fluid as a single flagellum attached to a no-slip plane, nor is the thrust twice as large. This suggests that in situations where the aim is to pump fluid or create thrust, there is an optimal distance between flagella where they effectively don't 'compete' for

fluid to pump. However, optimal mixing of the fluid around two flagella is obtained if the flagella are placed close together and rotated out of phase. The mixing was identified as a key phenomenon many years previously when Berg and Purcell [121] investigated the link between the diffusion constant and bacterial appendage-induced stirring.

This investigation into mixing asks some interesting questions about what might be the 'goal' of biological situations where multiple flagella are close to a boundary. For example, does mixing aid in the cells obtaining nutrients or aid intercellular communication? However, it is limited not only in its computational complexity but also in the constraint that the flagellar kinematics are imposed. This fixing limits the parallels between the simulations and experimental data since flagellar in most scenarios can change position.

1.7 Experimental methods

1.7.1 Culturing cells

In this project, the majority of cells are grown in liquid culture so that flagellar motility may be fully investigated. The standard protocol for growing liquid cultures was followed so that results obtained can be compared to those from the literature. First, a saturated culture was grown by inoculating 10ml of Lysogeny Broth (LB) (see appendix B with a crystal from frozen stock and incubated overnight at 33° C with shaking at 150rpm. *P. aeruginosa* grows in a temperature range of between 4 and 42°C but best between 25 and 37° C [122]. Therefore, the cells were grown at 33° C. The shaking is required to ensure mixing. LB is nutritionally rich and the culture was allowed to grow until saturation to ensure a large population. However, at saturation the cells are nutrient-limited and as a result become less motile. It has been found that cell motility is maximal during the exponential stage of growth (where cells are dividing exponentially) [123]. At this stage in their growth, there is a large number of highly motile cells and it is this exponential culture that is widely used for bacterial motility experiments. To grow the exponential culture, 10ml of Tryptone Broth (TB) (see appendix B) was inoculated with 10μl of the saturated culture and incubated at 33° C with shaking at 150rpm until the culture reached OD_{600} of 0.6 (approximately after 5 hours). An identical protocol was used to grow *E. coli* cells.

1.7.2 Staining cells for fluorescence imaging

The flagella of bacterial cells are not visible using the standard bright field set up used to image the cell bodies themselves. This is because, although the flagella can be many microns long, they are approximately 20nm in diameter [124]. Therefore, in order to visualise the motion of flagella, the flagella themselves were labelled with a fluorescent dye and imaged using epi-fluorescence microscopy.

In order to do this, specially adapted strains of the bacteria were used. In the case of *P.aeruginosa* the fluorescence strain was PA14 and for *E.coli* the strain was HCB1737. These strains have been genetically adapted so that what is known as a sulfhyfryl group is accessible on the flagellar filament by cysteine substitution. The result of this is that a commercially available Alexa Fluor maleimide dye binds to the flagellar filament. When the dye is excited by a certain wavelength of light, it emits a separate wavelength which can be imaged to determine the location of the flagellar filament.

To bind the dye to the flagella, a slightly adapted version of the dying protocol from [124] was followed. First the cells were grown as described previously in LB and then to an OD_{600} of 0.6 in TB. 2ml of this sample was then transferred to an eppendorf and centrifuged at 5000rpm for 5 minutes. After this time, the supernatent was gently removed with a pipette and discarded. The pellet that remained was re-suspended in 2ml of motility buffer (MB) (see appendix B) by gentle shaking. This process was repeated twice but after the third time in the centrifuge, the pellet was re-suspended in $20\mu l$ of Alexa Fluor malemide dye that had previously been dissolved in dimethylsufoxide (DMSO). When imaging the flagella of PA14 the Alexa Fluor C_5 488 malemide dye was used which differed from the Alexa Fluor C_5 647 malemide dye used for HCB1737 only in the wavelength needed to excite it. Once the pellet had been re-suspended in the dye, the eppendorf was kept away from the light for 45 minutes for the dye to bind. After this, 2ml of fresh MB was added to the eppendorf and the sample was again centrifuged 3 times with fresh MB added after each time. The resultant sample was kept away from the light to prevent bleaching of the dye and could be diluted to suit the experiment.

1.7.3 Bright field microscopy

1.7.3.1 History of light microscopy

Bright field microscopy can be thought of as the most basic type of microscopy, where lenses are used to produced an enlarged image of an object. Lenses are not new. In fact, since even a simple droplet of water can be used to magnify, they can be said to predate mankind. It is often assumed that the groundbreaking work of Leeuwenhoek and his 'animalcules' in the seventeenth century was a direct result of the invention of the compound microscope [125] (the predecessor of today's bright field microscopy, made up of two or more lenses in sequence). In fact, much of Leeuwenhoek's work relied on single lenses which have been traced back over 2000 years. Some of the earliest writings on magnification were by Lucius Annaeus Seneca (ca. 4 B.C - 65 A.D) when he remarked on the magnifying properties of water-filled glass spheres [126]. Since Seneca, various forms of lens were used as magnifiers and as early as the eleventh century, Vikings were making optically perfect paraboloids from quartz [127]. Although a matter of debate, the development of the first truly compound microscope is often attributed to Dutch spectacle makers Hans and Zacharias Janssen in the early seventeenth century [128]. Although the compound microscope continued to evolve, it wasn't until the nineteenth century that the physics involved began to be understood.

1.7.3.2 Standard bright field optical set-up

In the simplest possible terms, a lens is a curved piece of glass that bends any rays of light passing through it. Depending on the shape of the lens, the rays may be bent so that two rays originating at different positions are bent towards or away from each other. To produce an enlarged image of an object, rays interacting with the object must be passed through a lens which causes them to diverge. A simple compound microscope will use two lenses in series. The first, the objective lens, is above the specimen and the second, the ocular lens, is close to the observer [129]. Many compound microscopes also have a condenser lens which acts to concentrate light from the light source to increase the number of rays that pass through the specimen. For the experiments in this thesis, a Nikon ECLIPSE Ti microscope was used. Although based on the same principles as the simple compound microscope, this is an inverted microscope, meaning the objective lens is below the sample stage and the specimen is viewed from below. In this set up, rays from the light source pass through the condenser and into the specimen. From there they

pass into the objective lens which produces a magnified image of the specimen below the objective. Two mirrors then reflect this image towards the eyepiece where is is further magnified, before reaching the observer. In order to record images, a camera can replace the observer (see figure 1.13).

Depending on the experiment, lenses offering different magnification may be chosen. For this thesis, a 20× lens was used when the aim was to image many cells at one time and a 60× oil immersion lens was used for when fine detail of the specimen was desired. The immersion oil is used at higher magnifications to refractive index-match the sample chamber and the lens. This is necessary since the higher magnifications have a smaller aperture and so allow in less light. Therefore, the oil is necessary to minimise light losses due to total internal reflection.

It is also important to choose an appropriate level of light from the incident source. Too low and there will not be sufficient enough light to produce a clear image but too much could saturate the picture. This light level depends on the objective used since a higher magnification lens will have a smaller aperture and so will allow less light through. Therefore, the light level for higher magnification is generally greater.

Once the magnified image has been produced, there are also variables within the camera/recording software that can be controlled to optimize the output. The Area of Interest (AOI) can be varied to change the area of the sample that is imaged. A larger area produces more data but also increases the storage size of any images. The gain varies the sensitivity of the camera to light while the black level specifies the minimum dark level. The frame rate can also be changed and this defines how many images are recorded per second. In order to capture the detail of fast changing specimens (e.g. bacterial flagella rotating at 50Hz), a greater frame rate would be required than for slower specimens. However, there is a balance since for each frame rate, there is a maximum exposure time that the camera can accommodate. The exposure time dictates the length of time over which each image is recorded. A low exposure time limits the number of photons that reach the detector per exposure and therefore may limit the detail of the image. For the majority of the experiments in this thesis, the frame rate was set at 100 fps which is sufficient to capture flagellar motion but still allows for a relatively long exposure time if desired.
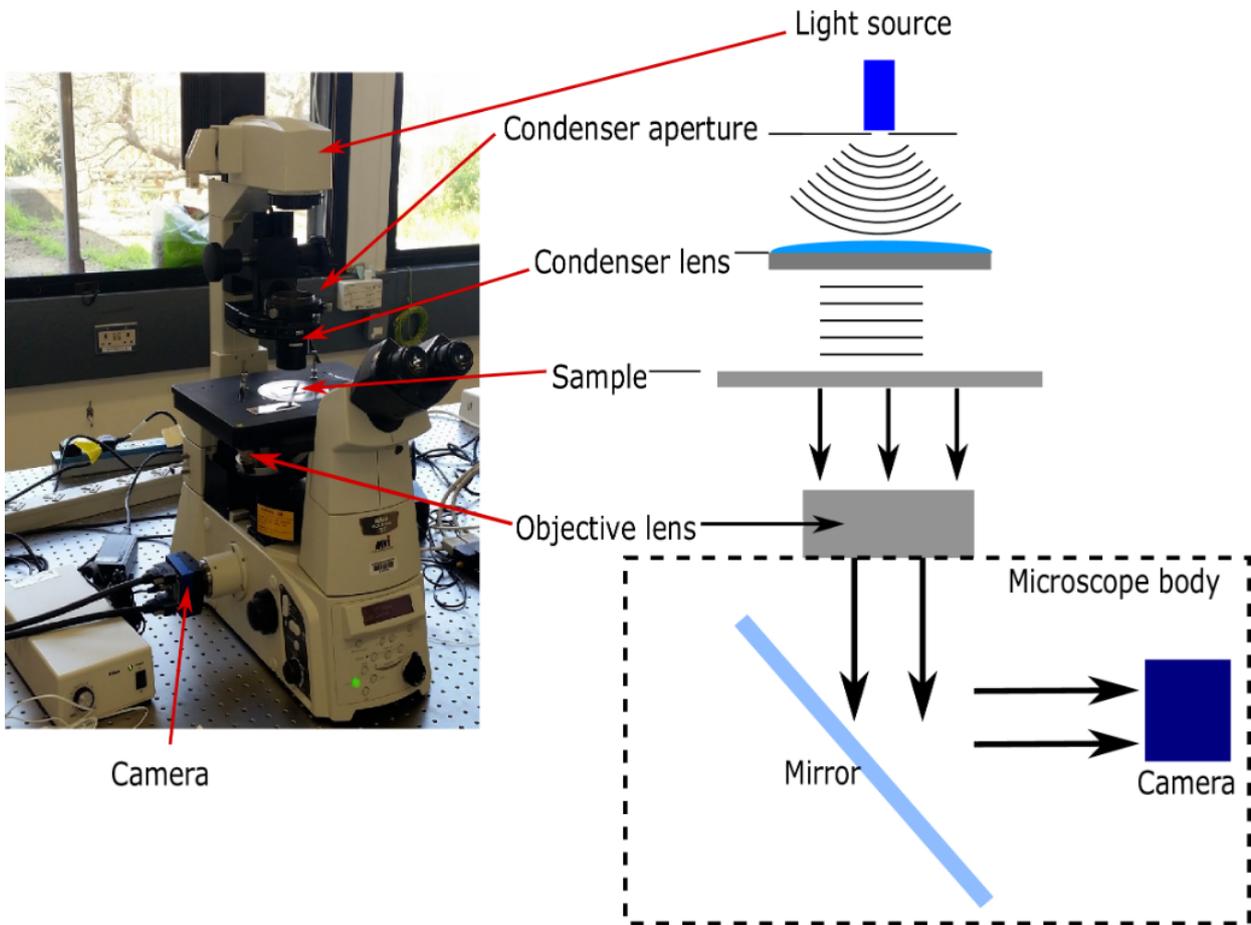
FIGURE 1.13.
The bright field optical set-up on the Nikon ECLIPSE T*i*. Key features identified on the photograph and corresponding ray diagram showing the path of light through the microscope. Figure adapted from [130].

1.7.4 Holographic microscopy

1.7.4.1 History of holography

Being a form of electromagnetic radiation, light can be thought of as a wave with amplitude and phase (see fig 1.14). Most conventional ways of imaging (CCD cameras, photographs, the human eye, etc.) work by forming a picture out of different intensities of light transmitted through different areas of the object. This is how standard bright field microscopy works but it means that only the squared amplitude of the light is recorded and any information about phase is lost. The result of this is that 3D information is condensed down into a 2D image. Holography is a technique which uses both the amplitude
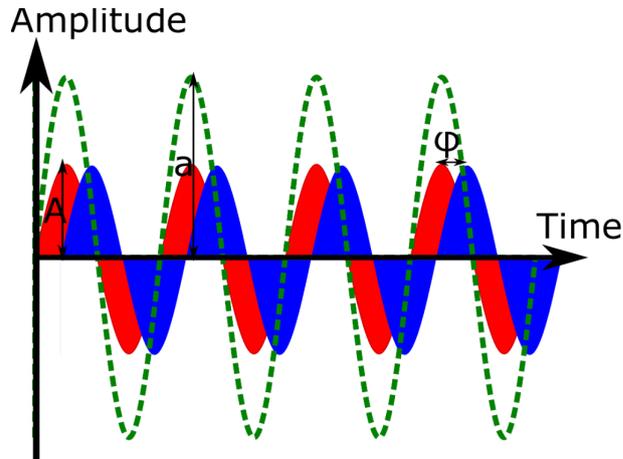
FIGURE 1.14.

The amplitude and phase of three different waves are shown. The red and blue waves are the same amplitude (A) but are out of phase by ϕ. The green wave is the same phase as the red wave but has a larger amplitude a. Standard microscopy utilizes only the amplitude whereas both amplitude and phase are used in holographic imaging.

and phase of the wave to allow 3D data to be extracted on a microscopic scale. Since the phase information is retained, the path of the wave can in principle be traced back to its source [130] and any objects along the path can be imaged.

More than half a century ago, Gabor first proposed the idea of holography as a way of increasing the resolving power of electron lenses, which were limited by issues associated with spherical aberration [131]. Gabor's setup used no lenses and had limited applications because of the impractical method of image reconstruction. Electrons, much like light, can be considered as either a particle or a wave (the analogous particle in light is known as a photon). The similar properties of electrons and light means that the early holography work was easily applicable to light. The optical holography technique commonly used today was pioneered in the 1980s when authors such as Fink and Stocker [132–135] stabilized the system and others began recording the information digitally using CCD cameras [136]. For this project, optical imaging is used because live samples are to be imaged.

1.7.4.2 Standard holographic set-up

There are various methods for holographic imaging that all use essentially the same physics. Differences arise in the specifics of the holographic arrangement and in particular the method of wave reconstruction. Here, the method used is Digital Inline Holographic Microscopy (DIHM) since it is one of the simplest techniques [130]. Whether photons or electrons are used, the source must be coherent since the 3D imaging relies on extracting phase information from interference patterns. Plane waves of wavelength λ, from the source, illuminate the object. Light that hits the object is scattered and is called the 'object wave' [130]. This interacts with light that did not encounter the object (the 'reference wave') and produces an interference pattern on the sensor (see figure 1.15) [136]. This pattern manifests as a series of light and dark fringes centering around the position of the object in the plane parallel to the sensor and corresponding to constructive or destructive interference, respectively. These fringes depend on the relative phase of the object wave to the reference wave and so vary depending on the difference in optical path length between the object and reference waves. If the incident illumination is modelled as the plane wave

$$\mathbf{A}_{ref}(\boldsymbol{\iota}, z_f) = U_0(\boldsymbol{\iota}) e^{ikz_f} \hat{\boldsymbol{\zeta}}_0, \tag{1.23}$$

where $A_{ref}(\boldsymbol{\iota}, z_f)$ is the complex amplitude of the incident light, $\boldsymbol{\iota}$ is the position in the focal plane, z_f is the distance from the focal plane, $U_0(\boldsymbol{\iota})$ is the transverse amplitude profile, k is the wave number (dependant on the refractive index) and $\hat{\boldsymbol{\zeta}}_0$ is the polarization [137]. The wave scattered by the sample can then be written as

$$\mathbf{A}_{scat}(\boldsymbol{\iota}, z_f) = A_{ref}(\boldsymbol{\iota}, z_f) \hat{\boldsymbol{\zeta}}(\boldsymbol{\iota}, z_f), \tag{1.24}$$

with $\mathbf{A}_{scat}(\boldsymbol{\iota}, z_f)$ being the complex amplitude of the scattered light and $\hat{\boldsymbol{\zeta}}(\boldsymbol{\iota}, z_f)$ the spatially varying polarisation. Since intensity of a wave is proportional to the square of the amplitude, the intensity recorded at the sensor may be written as

$$I = |\mathbf{A}_{ref} + \mathbf{A}_{scat}|^2 = U_0^2(\boldsymbol{\iota}) + 2\Re\left[U_0(\boldsymbol{\iota}) A_{scat}(\boldsymbol{\iota}, 0) \hat{\boldsymbol{\zeta}}_0^* \cdot \hat{\boldsymbol{\zeta}}(\boldsymbol{\iota}, 0)\right] + |A_{scat}(\boldsymbol{\iota}, 0)|^2. \tag{1.25}$$

Assuming that the object's height above the focal plane is greater than the object's size, the geometric rotation of scattered polarization is small. Therefore, the normalised hologram of an optically isotropic sample. $b(\boldsymbol{\iota})$, may be written as

$$b(\boldsymbol{\iota}) \approx 1 + 2\Re\left[E_R(\boldsymbol{\iota}, 0)\right] + |E_R(\boldsymbol{\iota}, 0)|^2, \tag{1.26}$$

where $E_R(\iota, z) = A_{scat}(\iota, z)/U_0(\iota)$ is the reduced scattered field. From this, the $3D$ position of objects in the sample can be identified.

For this thesis, two different light sources were used with similar DIHM setups. Both were based on the standard bright field microscopy set-up (see figure 1.13) with the distinction being the light source [130]. In the first (figure 1.15) an LED is used as the coherent light source, which has a wavelength of 660nm. Here, the LED is placed above the condenser lens with the condenser aperture almost fully closed to result in a point source of collimated light. This gives the desired plane coherent plane waves incident on the sample. The second set-up uses a laser of wavelength 642nm coupled to a single-mode optical fibre. In this case, since the laser has higher intensity and is already collimated, the condenser lens is not needed and the laser fibre is held directly above the sample (see figure 1.15). In both cases, the optimum focal plane is just outside the sample (approximately $5 - 10\mu$m above or below the chamber). This simplifies the method of extracting data from the entire sample volume.

Choosing between the two different light sources is a matter of the depth of required imaging. The LED, has a lower coherence than the laser. This limits the deviation that the scattered wave can take from the reference wave for the diffraction pattern to still be formed. Essentially, this means that the LED can only be used to image relatively shallow samples (approximately 50μm in this case), whereas the laser can image much deeper (hundreds of microns). The ability of the laser to image greater sample depths is both a blessing and a curse. Although a large volume of data can be collected simultaneously, any artifacts on the sample surface or dust crossing the optical path is also imaged. This means that in general, laser holographic data is more noisy than that collected using an LED. Not only does this introduce errors in the data extraction, it also means it is more difficult to collect the data since determining the appropriate focal plane can be challenging. Therefore, for this project, when an imaging depth of $< 50\mu$m was required, the LED holographic set-up was used and the laser set-up was only selected when imaging greater sample depths.
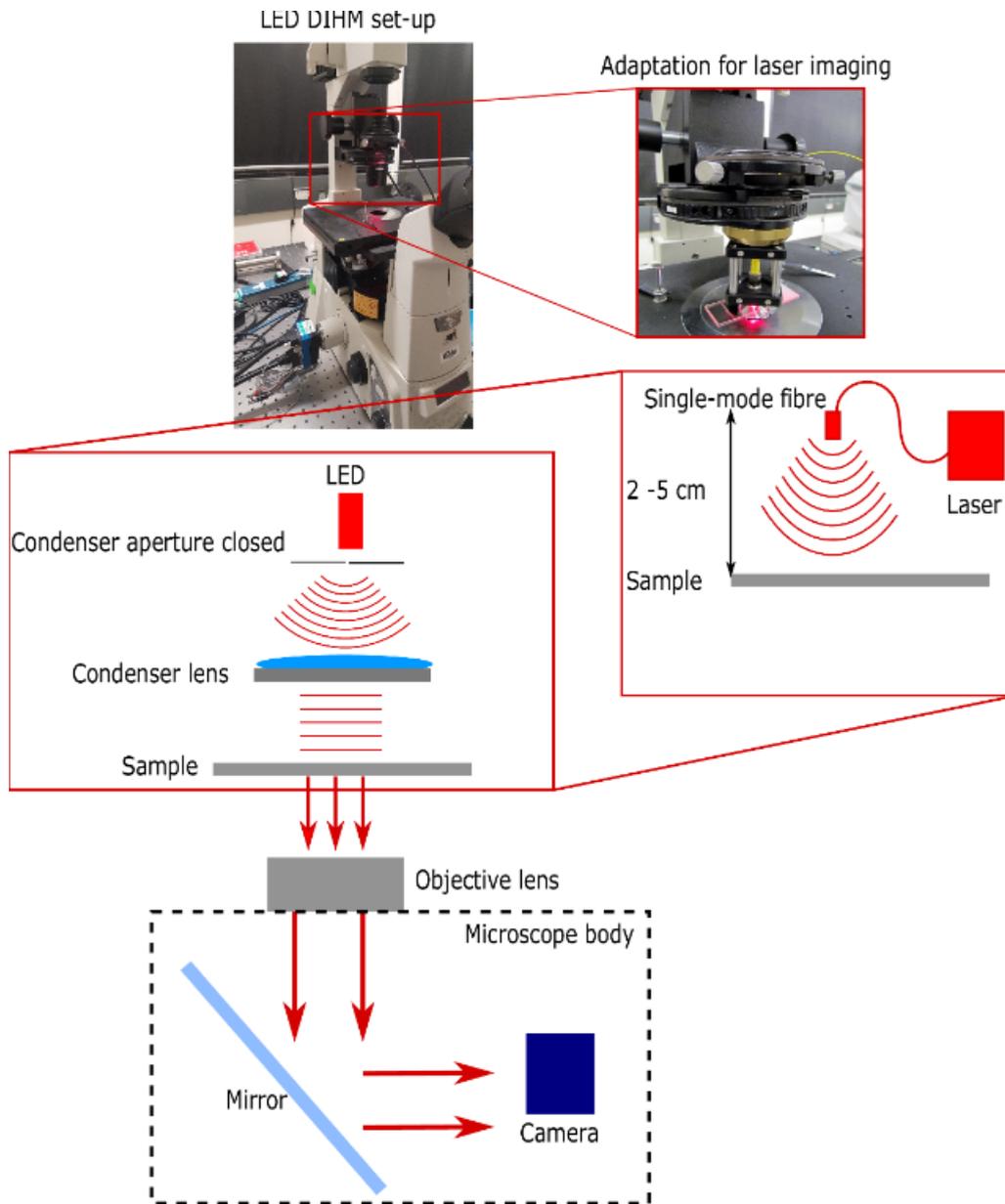
FIGURE 1.15.

The setup for DIHM is much the same as that for bright field, using the same microscope. This figure shows the adaptations for DIHM using either an LED or a laser as the light source. The photographs show the change in setup for the two options and the ray diagrams below them show the change in light path. Adapted from [130].

1.7.5   Fluorescence imaging arrangement

1.7.5.1   History of fluorescence microscopy

The first description of fluorescence is generally attributed to Sir Frederik William Herschel in 1845 when he commented that a solution of quinine, although colourless and transparent, produced a "vivid and beautiful celestial blue colour" in certain lights [138]. Here, he was describing the phenomenon of quinine solutions emitting blue light when excited by ultraviolet light from the sun. The first fluorescent microscopes began to appear a few decades later and began to be used to image living samples using incident light of specific wavelengths. The precursor to the fluorescence microscopy used today were developed by Ellinger and Hirt who treated samples to have a fluorescent source within the organism. Today, organisms can be generically adapted to form a binding site to which fluorescent molecules can attach so as to selectively image desired areas of a sample.

1.7.5.2   Standard fluorescence microscopy set-up

The specificity of wavelengths necessary to induce fluorescence is due to the discreet energy bands of the electronic states of the dye [139]. When a photon of the appropriate incident light is absorbed by the dye, electrons orbiting the atom are excited to a higher energy level. De-excitation occurs when a photon of light is emitted. The emitted photons are the recorded fluorescence and have a longer wavelength than those from the incident light. The phenomenon is known as the 'Stokes shift' and is a result of energy loss.

For the fluorescence experiments in this thesis, the epifluorescence microscope set-up was used. In this set-up, a single lens, placed beneath the sample is used as both the condenser and the objective. This can be achieved by a simple adaptation of the microscope used for both the bright-field and holographic imaging (see figure 1.16). The key element of fluorescence microscopy is filter cube containing a dichroic beam splitter. As the name suggests, this cube splits light according to its wavelength. In this case, it reflects the shorter wavelengths (the wavelengths to excite the dye) onto the sample while simultaneously transmitting longer wavelengths (those emitted from the sample) to the detector (see figure 1.16. For this work, the 488 malemide dye was illuminated with a mercury lamp and the 647 dye was illuminated with a 642nm laser diode.
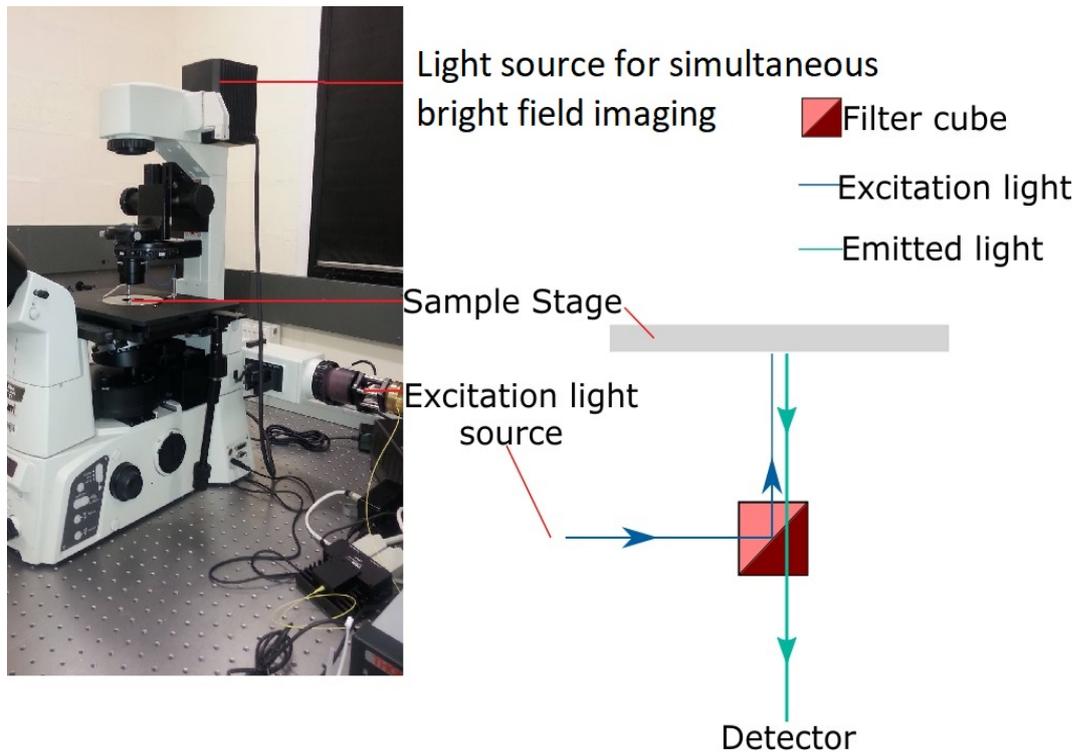
FIGURE 1.16.
The set-up for fluorescence imaging is an adaptation to the standard bright-field set-up. The microscope in fluorescence image configuration is shown along with a simple ray diagram showing the path of light to the sample and on to the detector.

1.8 Summary of thesis

An observation that apparently immobile, surface-attached bacterial cells could maintain a moving flagellum first stimulated the inquiries presented in this thesis. In particular, this thesis aims to answer whether the fluid dynamics of this surface attached motility may have any implication on biofilm formation. In addition, the effect of a known biofilm inhibitor (a lactam analogue - see chapter 2 for more information) on the fluid dynamics is investigated. This thesis aims to answer whether the lactam analogue impacts the fluid dynamics and thereby providing evidence that the fluid dynamics associated with the particular mode of surface-attached motility may be important in biofilm formation.

In chapter 2 of this thesis, freely swimming cells are exposed to the lactam analogue to determine any impact of the lactam on cell motility. Holographic microscopy was used

to track the freely swimming cells in 3D and statistical testing was used to determine any differences in motility characteristics between cells exposed to lactam and those in a control sample set.

Chapter 3 is a presentation of two novel uses of holography to exemplify the strength of the microscopy method. The first method is an investigation into the impact of viscosity on the swimming of bacterial cells and how holography can aid in the identification of different methods of motility. The second use is to test whether the noise associated with determining the 3D location of objects within a sample may be lessened by utilising a two-colour holographic set up.

Holographic microscopy is again used in chapter 4 to determine the fluid flow around a surface-attached cell with a motile flagellum. This novel process of obtaining a 3D flow field from holographic data is discussed in detail. The main questions addressed in this chapter are whether the flow around these surface attached cells may be captured using holography and whether cells exposed to the lactam analogue produce a different flow to those in a control sample.

Being a very complex and dynamic system, it was difficult to investigate the impact of the previously discussed flow field on biofilm formation. Therefore, in chapter 5, a simple model of the flow field was developed. The aim was to design a model that would be computationally inexpensive but would capture the key elements of the experimentally derived flow. The idea was that, using such a model, the dynamics of multi-cell systems could be explored which would be difficult to study experimentally. In chapter 5, the dynamics of the single-cell model system are investigated and compared to the experimental results obtained in chapter 4.

In chapter 6, the simple model derived in chapter 5 is used to study multi-cellular systems. The aim here was to show the advantages of the computationally inexpensive model in that a range of systems may be studied comparatively quickly. Of particular focus in this chapter is the way in which multiple model cells interact as this can inform possible explanations as to why the cells may remain motile while surface attached in the manner discussed in this thesis. Also shown in this chapter is an investigation into the flow of multiple cells on the transport of various particles. Here the primary question was does the lactam analogue alter the transport of particles and is this a way in which

the lactam acts to inhibit biofilm formation?

Chapter 7 exemplifies the diverse uses of the simple model developed in chapter 5 by using it to study the flagella of multi-flagellated cells. Data from the model is compared to experimentally derived data to provide verification in the accuracy of the model. More possible uses for the model are discussed in chapter 8 along with suggestions on how this work could be extended.

TRANSITION TO SURFACE ATTACHMENT

"Get your facts first, then you can distort them as you please."

Mark Twain

2.1 Introduction

There are two key experimental aims of this thesis and both involve flagellar motility of bacterial cells. The primary aim is to understand the implications of flagellar motility on the formation of bacterial biofilms. This links to the second experimental aim, which is to determine whether the lactam analogue supplied by Unilever (a biofilm inhibitor) affects cell motility and whether this may be a mechanism by which the biofilms are inhibited. To address these aims, the cells' motility when free swimming is compared to the motility when near a no-slip surface to identify the effects of the surface. These results are compared to data from cells in a similar environment but exposed to the lactam analogue to determine if the lactam alters the swimming of free/ near surface cells. The importance of this experiment is to evaluate whether the lactam in itself affects the free cells and this is the root of its anti-biofilm properties. If not, it suggests that the lactam interferes with a surface-associated cell mechanism that leads to biofilm formation e.g. quorum sensing.

This chapter contains a detailed account of the holographic microscopy technique used to obtain 3D motility data of swimming cells and how this can be used to understand

the effects of the surface and the lactam analogue.

2.2   Effect of lactam on freely swimming cells

Although the effect of the lactam analogue, supplied by Unilever, on biofilm formation has been previously investigated, little is known of its effect on bacterial motility. Currently, the analogue is thought to interfere with the quorum sensing systems that are necessary for biofilm formation (see section 1.9.3.2). The working theory is that, since a change in motility is observed during biofilm formation, the lactam analogue may have an effect on the motility of surface attached cells by disrupting the quorum sensing systems. If this is the case, the analogue would be expected to have no effect on the motility of free swimming cells, since these cells are not exposed to sufficient QS molecules to stimulate the system. In this section, this theory is tested by investigating the effect of the lactam analogue on the motility of free swimming cells and that of cells near (but not attached to) a surface.

2.2.1   Data collection

All cells in these experiments were imaged in motility buffer (MB), the protocol for which may be found in appendix B. The motivation for this choice of buffer is two-fold. Firstly, as the name suggests, the low nutrient content of MB encourages cell motility and therefore the number of motile cells is maximized. Secondly, it facilitates fluorescence imaging as the dying process must be done in MB since there is minimal risk of components of the media interacting with the dye. The method for sample preparation was the same for both the free-swimming and near-surface experiments, with the only difference being the chamber the sample was imaged in.

2.2.1.1   Lactam stock solution

The lactam analogue was supplied from Unilever in powdered form and stored in a $-20°C$ freezer. The protocol for preparing the working stock solution was adapted from that provided by Unilever. The molecular weight of the compound was 432g/mol so to make a 50mM stock solution 21.6mg of the compound was added to 1ml of deionised water (DI) and vortex mixed. This was then diluted $3:100$ with MB and vortex mixed. The result is a 1500μM stock solution in MB. This stock solution is used immediately

since precipitation was observed if the solution was kept for more than approximately 24 hours.

2.2.1.2   Sample preparation

When imaging bacterial motility, there is a fine balance to be struck between imaging a low enough concentration of cells such that they do not frequently interact whilst also imaging a high enough concentration such that sufficient data is collected. Having a dilute enough concentration of cells so that all the individual bacteria may be considered as independent has been termed the dilute limit. For this project, 50μl of PA01 exponential culture was added to 950μl of MB in a sterile eppendorf tube to create the control sample. The lactam analogue sample was similarly prepared by combining 50μl of PA01 exponential culture to 200μl of the 1500μm lactam stock solution and 750μl of MB. Both samples were shaken gently to mix and imaged immediately in a chamber slide.

2.2.1.3   Chamber slide preparation

The chamber slides for imaging free swimming cells were prepared by first using UV glue to attach two 22×26 mm coverslips to a 76×26 mm glass slide. The two coverslips were glued approximately 22mm apart and a continuous line of glue was used to ensure there were no gaps from which the sample could escape (see figure 2.1). The glue was allowed to dry under a UV lamp for 10 minutes. Once dry, a 22×50 mm coverslip was attached over the cap between the two smaller coverslips, again using a continuous line of UV glue (see figure 2.1). This was then allowed to dry for a further 10 minutes under a UV lamp and the chambers were stored wrapped in lens paper to prevent artifacts on on the glass. When the sample was to be imaged, the capillary effect was used to fill the chamber with the liquid sample. This capillary action is the phenomenon where liquid is observed to be 'pulled' into a small volume (the chamber in the slide) and is due to action of liquid cohesion, adhesion and surface tension [140]. Once the chamber was filled, both openings of the chamber were sealed with nail varnish to prevent evaporation and leakage. The chamber depth is approximately 230 ± 10 μm based on a sample of 5 chambers.

2.2.2   Imaging set-up

The standard holography image set-up from section 1.9.3.2 was used with the 642 nm laser installed, since this allowed for the whole chamber to be imaged. An area of interest
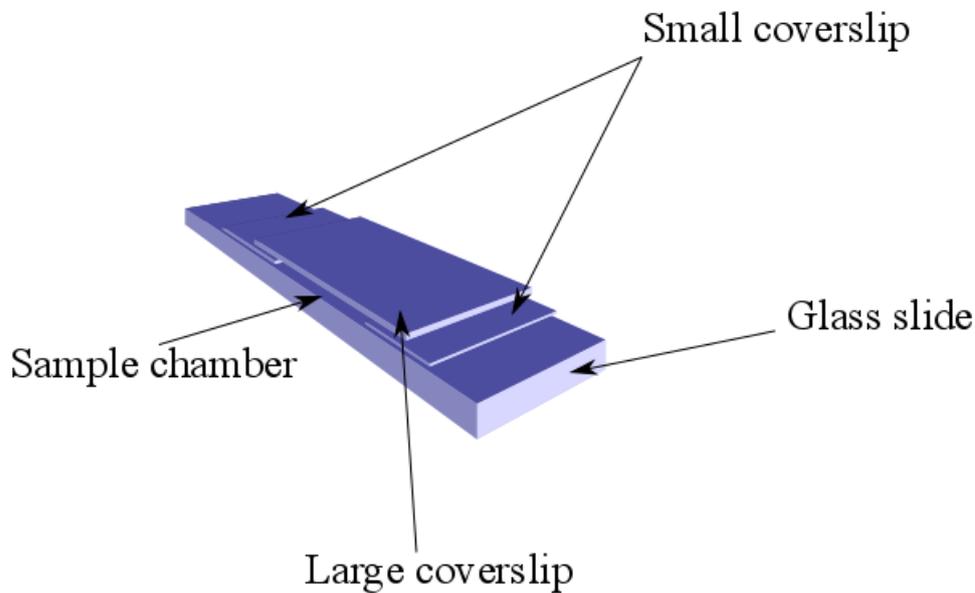
FIGURE 2.1.

The standard chamber slides used to image liquid samples are prepared by using UV glue to attach two coverslips to a glass slide then, after drying, gluing a larger coverslip over the top to create a chamber.

of 1024×1024 μm was set so as to allow a large volume of data to be collected in each recording. To the same end, a 20x lens was used so that multiple tracks of substantial length could be collected in each video. The videos were recorded at a frame rate of 100 Hz and each video had a length of 2000 frames. Videos were then saved in uncompressed .avi format for later processing.

2.2.3 Data analysis

Each of the holographic data videos were treated in much the same way. The positions of objects in each frame are found, and tracks are synthesized from coordinates in neighboring frames. These are then processed with various add-on routines depending on the quantities of interest. Below, the standard protocol for obtaining swimming cell tracks is described.

2.2.3.1   Image pre-processing

Video frames consist of an array (x, y) of light intensity values. The first stage is to obtain a 'background' image of each movie by taking the median pixel value at each position. For the experiments in this project, a temporal median is taken over 20 frames. By diving each pixel in each frame by the corresponding median pixel value, any discrepancies in illumination or artifacts in the optical path etc., can be corrected [141]. To account for dead pixels etc, any pixels in the video with zero intensity are replaced with the median pixel intensity for that location. Figure 2.2 shows a single frame of raw data along with the corresponding 20-frame median and the same frame after the 'background' is removed.

2.2.3.2   Identifying objects

An in-house LabVIEW code was used to extract object locations in each frame of the movies. First, a Rayleigh-Sommerfeld back-propagation method was used to reconstruct the optical field for a single frame, $I_{im}(x, y, z)$ [141]. This requires the refractive index of the sample medium, the magnification, the imaging wavelength, the reconstruction starting point, the number of reconstruction 'z-slices' and the step size between these 'slices' to be inputted. The reconstruction starting point depends on where the focal plane was placed relative to the sample plane during experiments, and the direction of reconstruction can be set to step up or down from the starting point. A bandpass filter can also be applied at this point to attenuate spatial frequencies outside of the range $2\pi/30 - 2\pi$ px^{-1}, enhancing the contrast of objects between $1 - 30$ px in size. Objects are identified using an object localisation scheme based on Gouy phase anomaly [142]. This scheme relies on the fact that, as objects pass through a focal plane, their centers change from being dark to light or vice versa. Therefore, objects are indicated by finding the locations where $\partial I_{im}/\partial z$ is at extrema. To do this, an in-built LabVIEW fast Fourier transform (FFT) is used to construct an 'intensity gradient stack' in the z direction $(I_g(x, y, z))$ using the convolution

$$I_g(x, y, z) = I_{im}(x, y, z) \otimes S_z(x, y, z). \tag{2.1}$$

Here, $S_z(x, y, z)$ is a $3 \times 3 \times 3$ array and is a Sobel-type gradient operator [143]. This gradient stack is then projected down to a single image and a suitable threshold is applied such that objects are represented by bright points (see figure 2.3). This works by setting any pixels within the projected gradient stack that are below the threshold to zero.
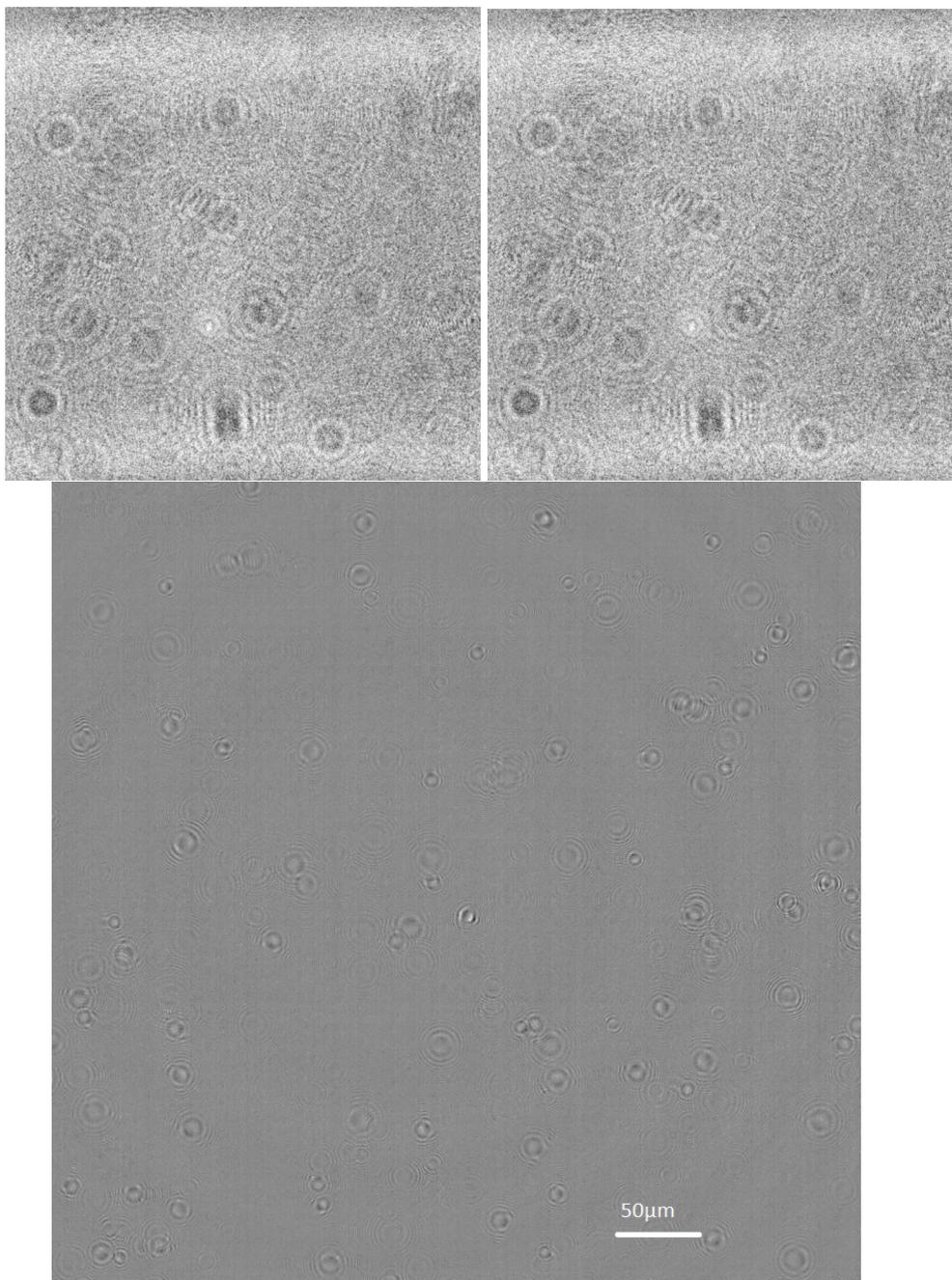
FIGURE 2.2. Top from left to right: a single frame of raw data before processing and the median image of 20 frames of the movie. Bottom: the single frame with the median or 'background' removed buy dividing each pixel of each frame with the corresponding median pixel value. The scale bar indicates 50μm and the three images are of the same AOI. The lower image is shown at a larger scale for clarity. It can be seen that after the background is removed, objects withing the sample are visible.

FIGURE 2.3. A single frame of holographic data projected gradient stack after a suitable threshold is applied. The bright point correspond to objects. This is used to locate locations of objects.

These steps are applied to a single frame of each movie first. This is to determine the appropriate input parameters (step size, number of 'z-slices' etc.) and to determine the appropriate threshold value. Once these have been obtained, the same steps are applied to all frames of the movie. Then, a standard 'particle identification' scheme [144] is used to locate the (x,y) position of any bright points in the projected stack. Next, a column of pixels around the identified bright points in analysed. Although the size of this column can be set, for all the work in this these a 3×3 square of pixels centred on the bright spot is taken. The pixel intensities from this square are then summed to give a value for each bright spot for each of the 'z-slices'. A peak search algorithm is then used to determine at which z this summed intensity is maximised and this value is taken as the z co-ordinate of the object. These are then recorded as text files containing a list of t, x, y, z for all the objects. A single text file (called an 'object file') is produced for each frame of the movie.

2.2.4   Reconstructing tracks

Tracks are constructed using a further, in-house, LabVIEW code. The 'object files' are read in along with track parameters. These parameters are a minimum track length (which specifies how many frames the track is over), the search sphere radius and maximum number of look-back frames. The code works by taking an object found in frame i and looking in frame $i+1$ for an object that is less than the search sphere radius value from the object's position in frame i. If there is a suitable point in frame $i+1$, both points are given the same track number. If multiple points are within the search sphere, the closest is chosen. The maximum number of look-back frames parameter specifies the number of frames for which the object can 'disappear' before the track is terminated. For example, if the maximum number of look-back frames is set to 2, an object in frame $i+2$ could be linked to an object in frame i even if there was not suitable object in frame $i+1$. Allowing the object to 'disappear' for a number of frames accounts for situations where noise or one object passing very close to another results in an object not being identified.

2.2.4.1   Track post processing

Since there is noise associated with the objects' locations, the outputted tracks are often noisy. This noise is especially clear in the z-axis and on slow moving objects. Before analysis of tracks, another in-house LabVIEW code is used to smooth the noise using the freely available Cubic Spline Fit VI. Three dimensional spline-smoothing with a balance parameter is used to smooth the tracks. The balance parameter is a value between 0 and 1 and is the balance between stiffness of fitted curve and fit to the data. If the balance parameter is 0, the fit is equivalent to a linear model and if it is 1 the fit is a cubic spline interpolation. For the data, here the fit parameter $= 0.99$.

Since non-motile cells may obscure the statistics of motile cells, many of the experiments in this thesis require only the swimming cells to be selected. This is done using a final in-house LabVIEW code that calculates the mean squared displacement (MSD) of the objects in each track. For purely diffusive particles, the gradient of log(MSD) is 1 [145]. For purely ballistic particles, the gradient is instead 2. Therefore, for this thesis, and tracks where the gradient is > 1.4 is counted as a swimmer's track. An example track obtained using this protocol is shown in figure 2.4.
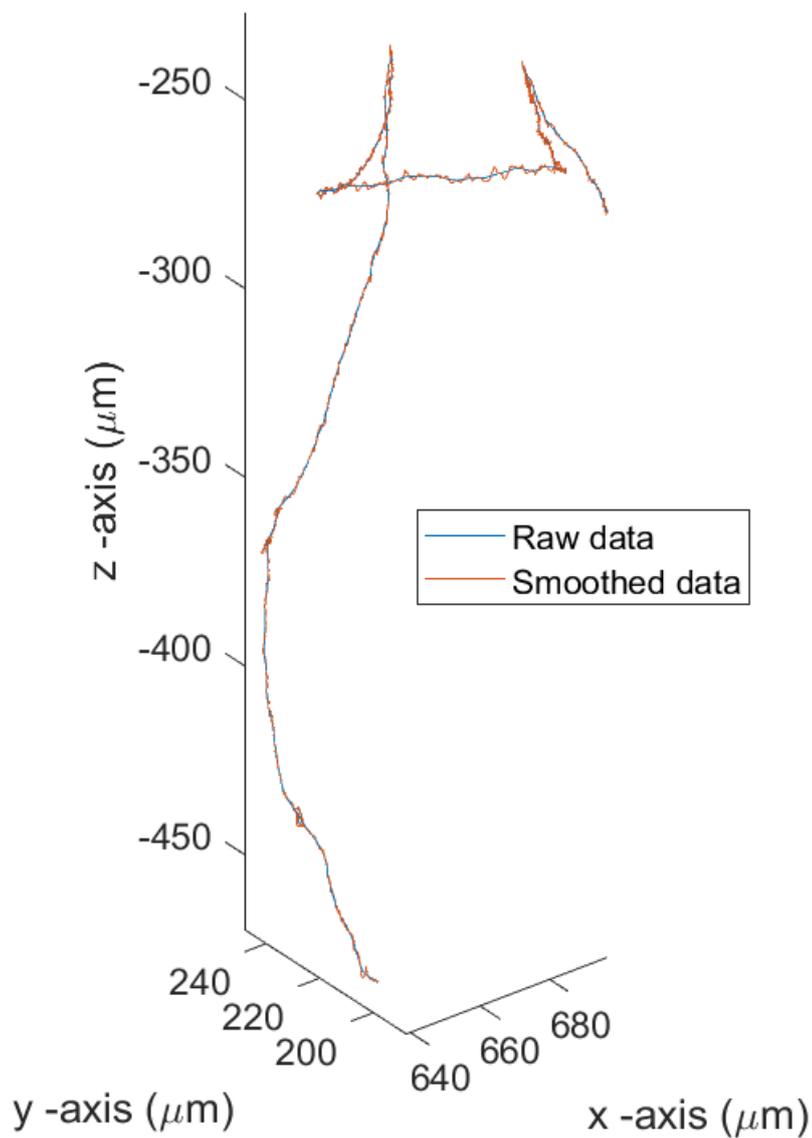
FIGURE 2.4. An example 3D track of a swimming PA01 cell found using reconstruction of holographic data detailed above. Both the smoothed and raw data are shown.

2.2.5 Results

2.2.5.1 Mean speed

Since motility is crucial in biofilm formation [37], there is a suggestion that there may be a link between QSM and motility. It is, therefore, prudent to investigate whether the QSI lactam analogue alters motility. Tracks obtained using the LabVIEW codes were processed using a custom MATLAB code. The code used a forward difference method to determine 'instantaneous' velocity. The vector between the cell position in frame $i + 1$ and frame i is multiplied by the frame rate. The speed is found by taking the magnitude of this velocity vector and the mean speed is found by taking the average of 'instantaneous' speeds over the whole track. This data is used to identify whether the sample with lactam analogue shows any difference from the control sample. Figure 2.5 shows histograms of the mean speeds of tracks in the sample containing the lactam analogue and the control. Throughout this thesis, effort has been made to present data of cells in lactam in blue and those from control in red. The two data sets are of 404 and 497 tracks respectively obtained over 3 days with 3 biological repeats. The mean μ_l and standard deviation σ_l of the mean speeds for the lactam analogue sample are $\mu_l = 34.68~\mu\text{m/s}, \sigma_l = 20.49~\mu\text{m/s}$. The corresponding mean, μ_c, and standard deviation, σ_c, for the control are $\mu_c = 43.98~\mu\text{m/s}, \sigma_c = 21.77~\mu\text{m/s}$. Using Excel's T-test calculator, the two-tailed P value for this data is found to be less that 0.0001, suggesting that there is a significant difference in mean speed between free-swimming cells exposed to lactam and those in the control sample.

2.2.5.2 Frequency of reorientation events per track

The helical flagella of *P. aeruginosa* can rotate either clockwise (CW) or anticlockwise (CCW) and statistically spends equal time in each direction, displaying run-reverse-flick swimming [146]. The cells can use their flagellum to both 'push' and 'pull' themselves through their environment. When running, the cells maintain a constant flagellar rotation direction and move in a smooth line. A reversal of the flagella results in a sharp reorientation event and the cell returns back on itself (with some deviation due to Brownian motion). In some cases, the cells 'pause' (i.e. there is a break in flagellar rotation), before the flagellum begins rotating again in either direction. It is suggested that this 'pause' allows for Brownian motion to cause a large change in angle of the cell's trajectory or a 'turn' [146]. Cells are observed to display longer runs, fewer pauses and shorter pauses as part of a chemotactic response. In order to investigate whether the presence
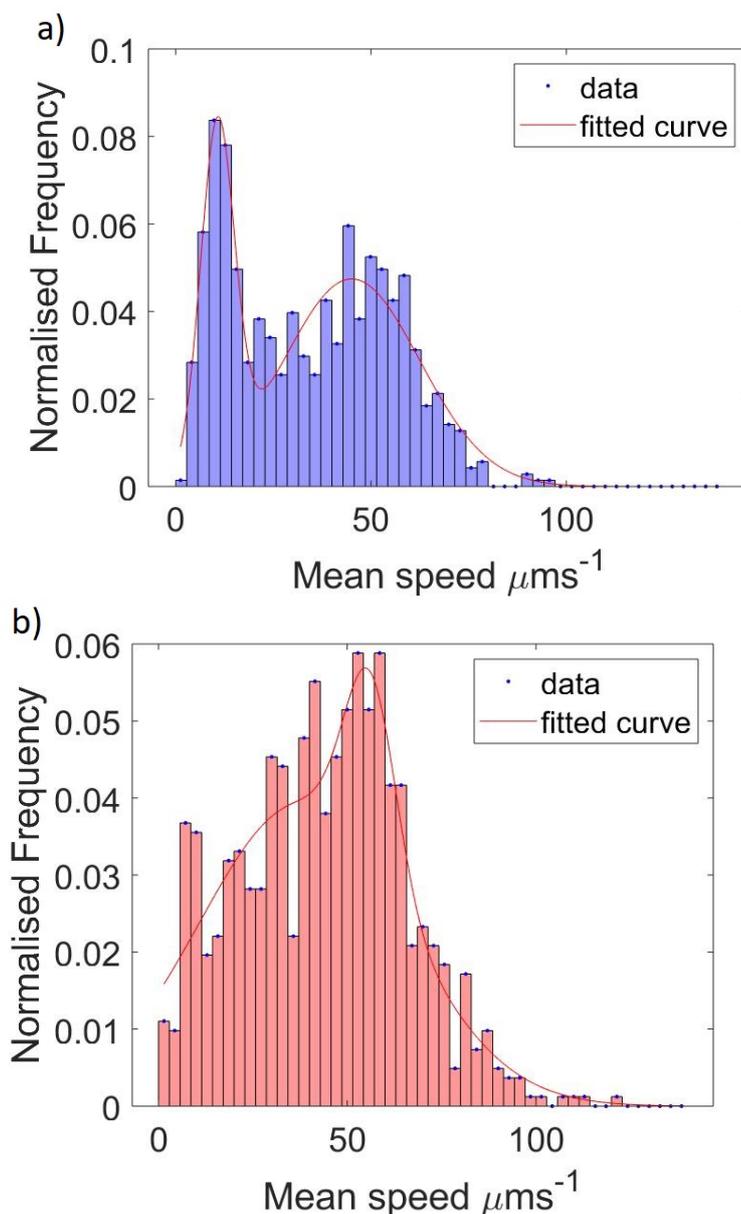
FIGURE 2.5. a) the normalised frequency of each track mean speed in the sample containing the lactam analogue b) the normalised frequency of each track mean speed in the control sample. The fit shown is a two-term Gaussian distribution. The mean μ_l and standard deviation σ_l of the mean speeds for the lactam analogue sample are $\mu_l = 34.68$ μm/s, $\sigma_l = 20.49$ μm/s . The corresponding mean, μ_c, and standard deviation, σ_c, for the control are $\mu_c = 43.98$ μm/s, $\sigma_c = 21.77$ μm/s . Using Excel's T-test calculator, the two-tailed P value for this data is found to be less that 0.0001, suggesting that there is a significant difference in mean speed between free-swimming cells exposed to lactam and those in the control sample.

of the lactam analogue alters the frequency of reorientation events per track, a way of identifying a reorientation event must be constructed.

Using MATLAB, a probability of each point in the track being a reorientation event is determined. Three different ways of determining this probability are tested. Since a reorientation event occurs when the flagellum stops rotating for a time, a slowing of the cell's instantaneous speed ($\dot{x}$) is an indication of a reversal event. A change in the direction of travel is also an indication of a reorientation event. Therefore, we define the probability of a reorientation event at time t to be

$$P_{reorient}(\dot{x}, \xi; t) = 1 - (X(\dot{x}) + \Xi(\xi))/2 \ . \tag{2.2}$$

Here, $X(\dot{x})$ is a function specifying the probability of reversal due to a slowing in speed and $\Xi(\xi)$ is a function giving the probability due to a change in direction of the cell. ξ is the angle between the direction vector of the cell's trajectory at time $t+1$ and that at time t. Both $X(\dot{x})$ and $\Xi(\xi)$ are chosen to be sigmoid functions [147] of the form

$$p(m) = \frac{1}{1 + \exp(A_1(-m + A_2))} \ , \tag{2.3}$$

where m in this case represents either $\dot{x}$ or ξ at time t, A_1 is a parameter affecting the steepness of the curve and A_2 is a parameter specifying the centre of the sigmoid curve. $p(m(t))$ can be any value between 0 and 1. For this thesis, the parameter A_2 for $X(\dot{x})$ is two standard deviations away from the mean speed of the track and A_2 for $\Xi(\xi)$ is $\pi/10$. The three different trial methods for determining a reorientation event simply vary the A_1 parameter in $X(\dot{x})$ and $\Xi(\xi)$. This has the effect of changing how significant a change in speed or direction must be to register in $P_{reorient}(\dot{x}, \xi; t)$. Table 2.1 shows the values of the A_1 parameter for $X(\dot{x})$, $A_{1\dot{x}}$, and the a parameter for $\Xi(\xi)$, $A_{1\xi}$, for the three trial functions $P^1_{reorient}(\dot{x}, \xi; t)$, $P^2_{reorient}(\dot{x}, \xi; t)$ and $P^3_{reorient}(\dot{x}, \xi; t)$. The smaller values of A_1 give a shallower curve and mean that the change in speed or direction has less impact on the probability of a reorientation event. Therefore, $P^1_{reorient}(\dot{x}, \xi; t)$ relies more on a low speed to identify a reorientation, $P^3_{reorient}(\dot{x}, \xi; t)$ relies more on a large change in direction to indicate a reorientation and $P^2_{reorient}(\dot{x}, \xi; t)$ is in between. All the $A_{1\xi}$ values are negative to account for the fact that a large angle should increase the probability of reorientation whilst the values of $A_{1\dot{x}}$ are all positive because a low speed indicates a reorientation.

Figures 2.6 and 2.7 show a track that does not seem to have a reorientation event along

	$A_{1\dot{x}}$	$A_{1\xi}$
$P^1_{reorient}(\dot{x},\xi;t)$	1	-0.001
$P^2_{reorient}(\dot{x},\xi;t)$	0.1	-1
$P^3_{reorient}(\dot{x},\xi;t)$	0.001	-1

Table 2.1: Ratios in trial functions for reorientation identification

with the three trial probability functions for that track and the track's instantaneous speed plot. Since the cell has a fairly constant speed for the whole track, the standard deviation of instantaneous speeds is small. Therefore, two standard deviations below the mean track speed is very close to the mean speed and the speed dips below this 'critical value' at one point in the track. This can be judged by eye not to be a reversal event but $P^1_{reorient}(\dot{x},\xi;t)$, relying heavily on a slowing of speed below the critical value, identifies it as such. This, therefore, suggests that using $P^1_{reorient}(\dot{x},\xi;t)$ is not effective.

On the other hand, figures 2.8 and 2.9 show a track (and associated probability plots) that slows slightly and reorientates with a small angle change. Since a probability > 0.5 is the criterion for identifying a reorientation event, relying most on a change in angle ($P^3_{reorient}(\dot{x},\xi;t)$) does not capture this reorientation event.

Figures 2.10 and 2.11 show a track, the corresponding instantaneous speed profile and three probabilities of reorientation. Again, using a probability > 0.5 as the condition for reorientation, $P^2_{reorient}(\dot{x},\xi;t)$ (relying on speed and angle data), captures the reorientation. Since both $P^1_{reorient}(\dot{x},\xi;t)$ and $P^3_{reorient}(\dot{x},\xi;t)$ fail in identifying reorientations, $P^2_{reorient}(\dot{x},\xi;t)$ will be used for the rest of this thesis.

The accuracy of $P^2_{reorient}(\dot{x},\xi;t)$ in identifying reorientations was tested by using it to find reorientation events in simulated data. From this investigation, $P^2_{reorient}(\dot{x},\xi;t)$ was found to identify reorientation events with an error of 12.03%. This is the error used when analysing the statistics from experiments.

Figure 2.12 shows the normalised frequency of reorientation events in each track for the sample containing the lactam analogue and the control sample. Here, the number of reorientation events per track is shown given that at least one reorientation has been identified in the track. The mean for the lactam analogue sample and control is 3.09 and 2.73 respectively, with the standard deviations being 4.10 and 4.09 respectively. The two-tailed P-value for this data is 0.0189, suggesting that increase in reversals when the cells are exposed to the lactam analogue is significant. On this plot, the fit is exponential
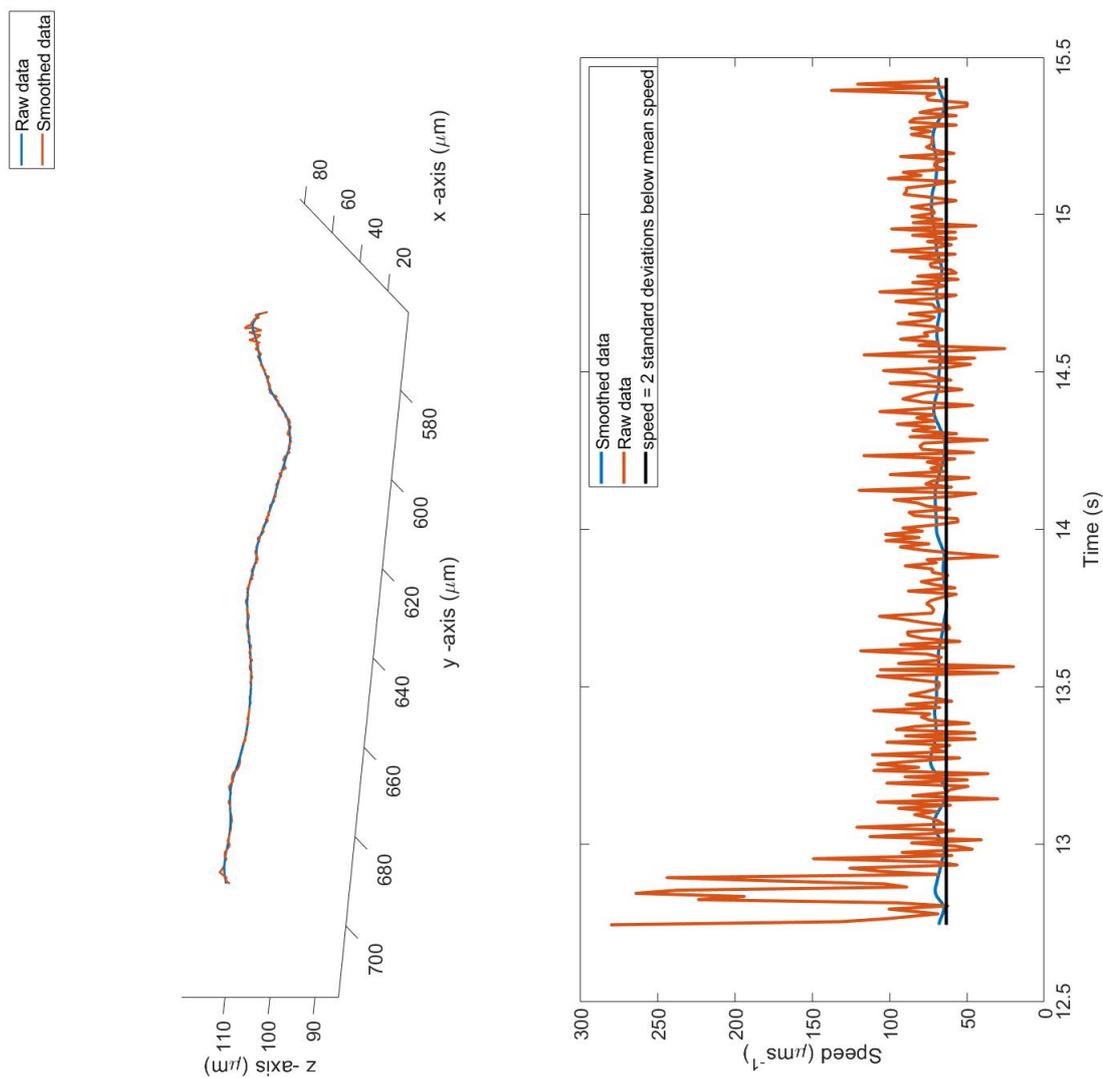
FIGURE 2.6. Top: and example of the raw and smoothed data for a track that has been identified as not having a reversal by eye. Bottom: the raw and smoothed instantaneous speeds of the above track. Also shown is the 'critical speed' used in the speed reversal of the track which is two standard deviations below the mean speed. This track maintains a fairly consistent speed and so the critical speed is close to the mean value.
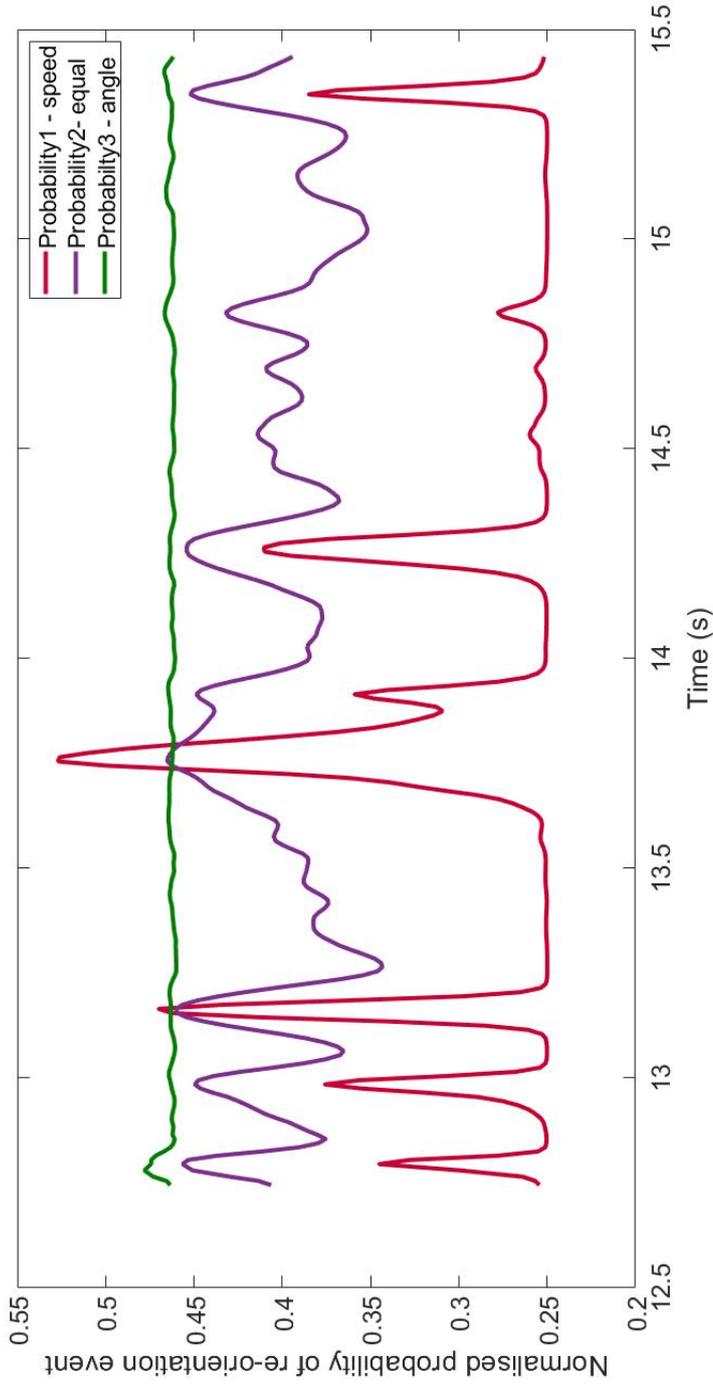
FIGURE 2.7. For the track in 2.6, the instantaneous probability of reversal for the three trial functions is shown. Since a reorientation is recorded when the probability of reorientation is > 0.5, using $P^1_{reorient}(x,\xi;t)$ would falsely identify a reorientation.

61
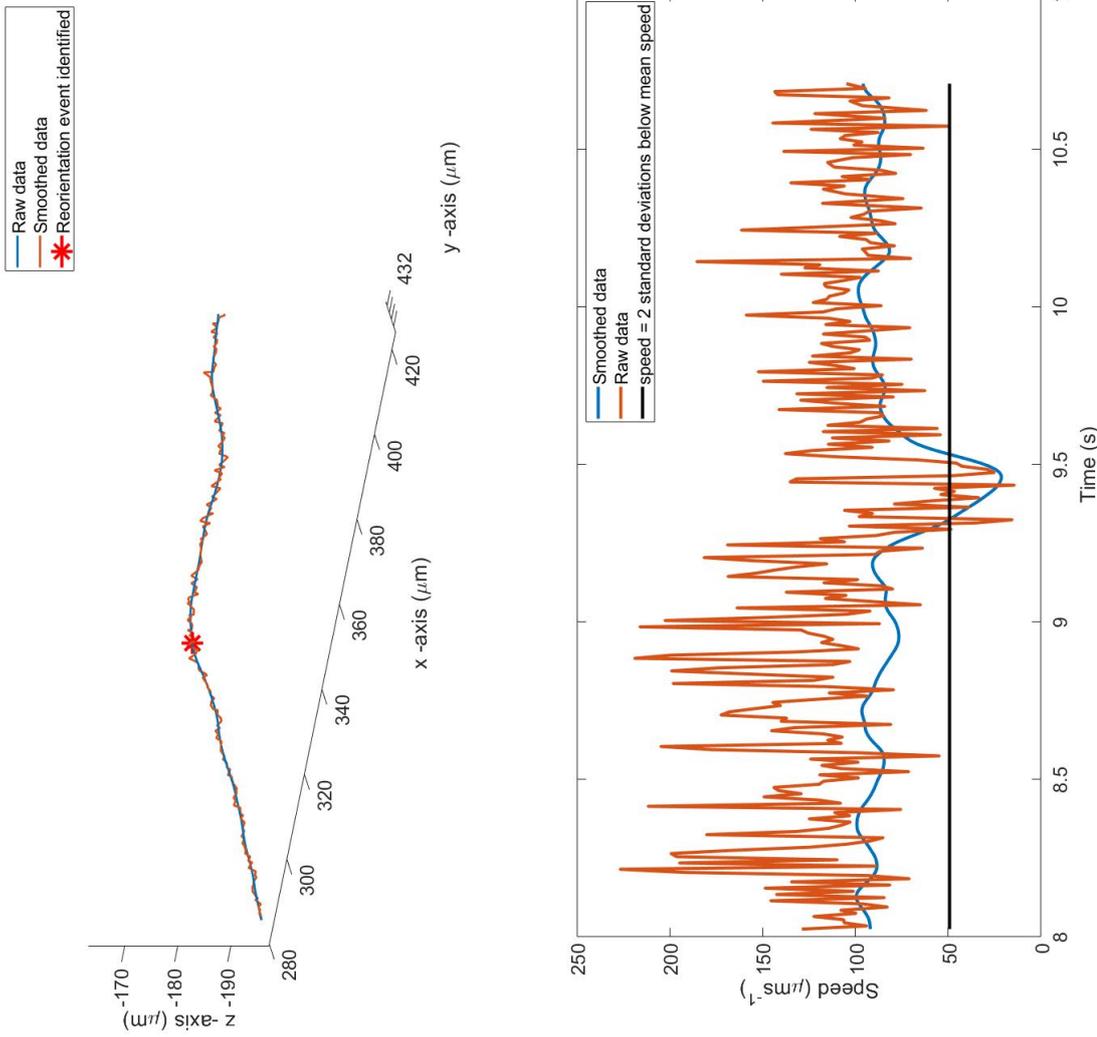
FIGURE 2.8. Top: and example of the raw and smoothed data for a track that has been identified as having a reversal by eye- although the reversal does not result in a large angle change. Bottom: the raw and smoothed instantaneous speeds of the above track. Also shown is the 'critical speed' used in the speed reversal of the track which is two standard deviations below the mean speed. This track shows a point where it drops significantly below the critical value indicating a reorientation event.
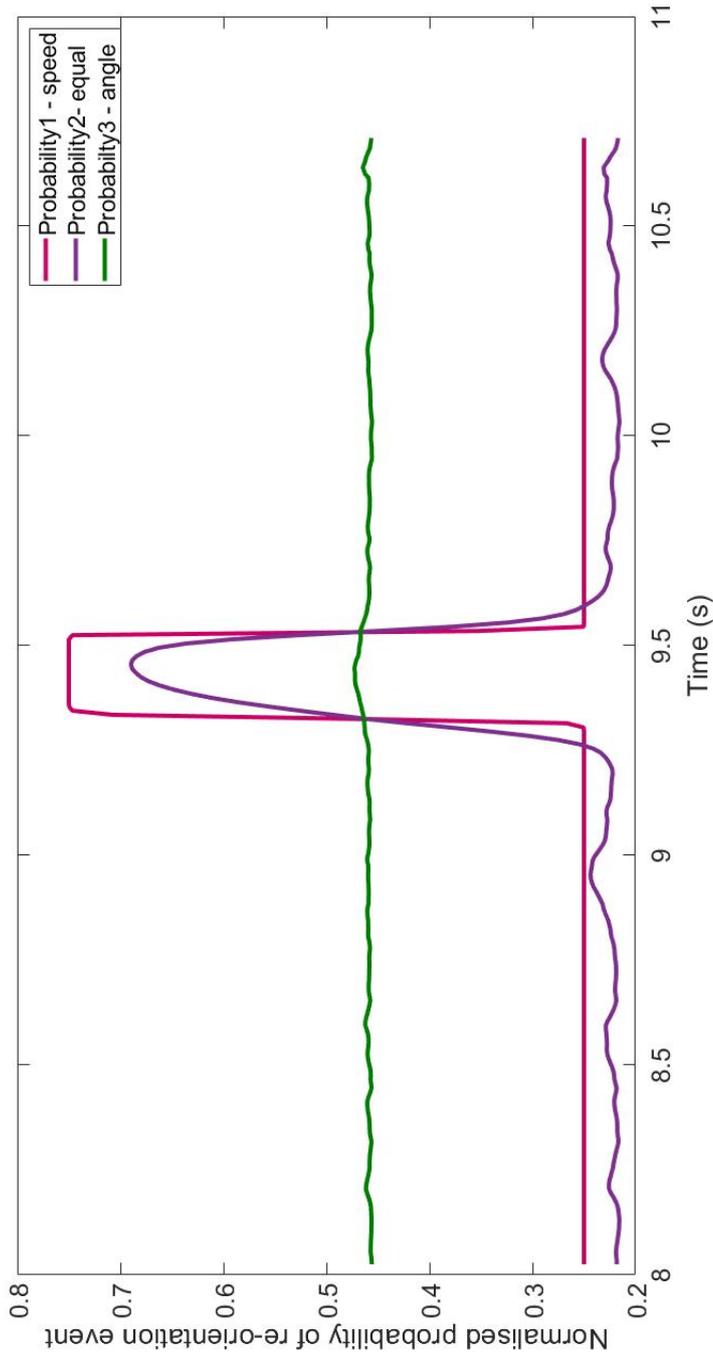
FIGURE 2.9. For the track in 2.8, the instantaneous probability of reversal for the three trial functions is shown. Since a reorientation is recorded when the probability of reorientation is > 0.5, using $P^3_{reorient}(x, \xi; t)$ would not capture the reorientation event suggested by the significant drop in speed.
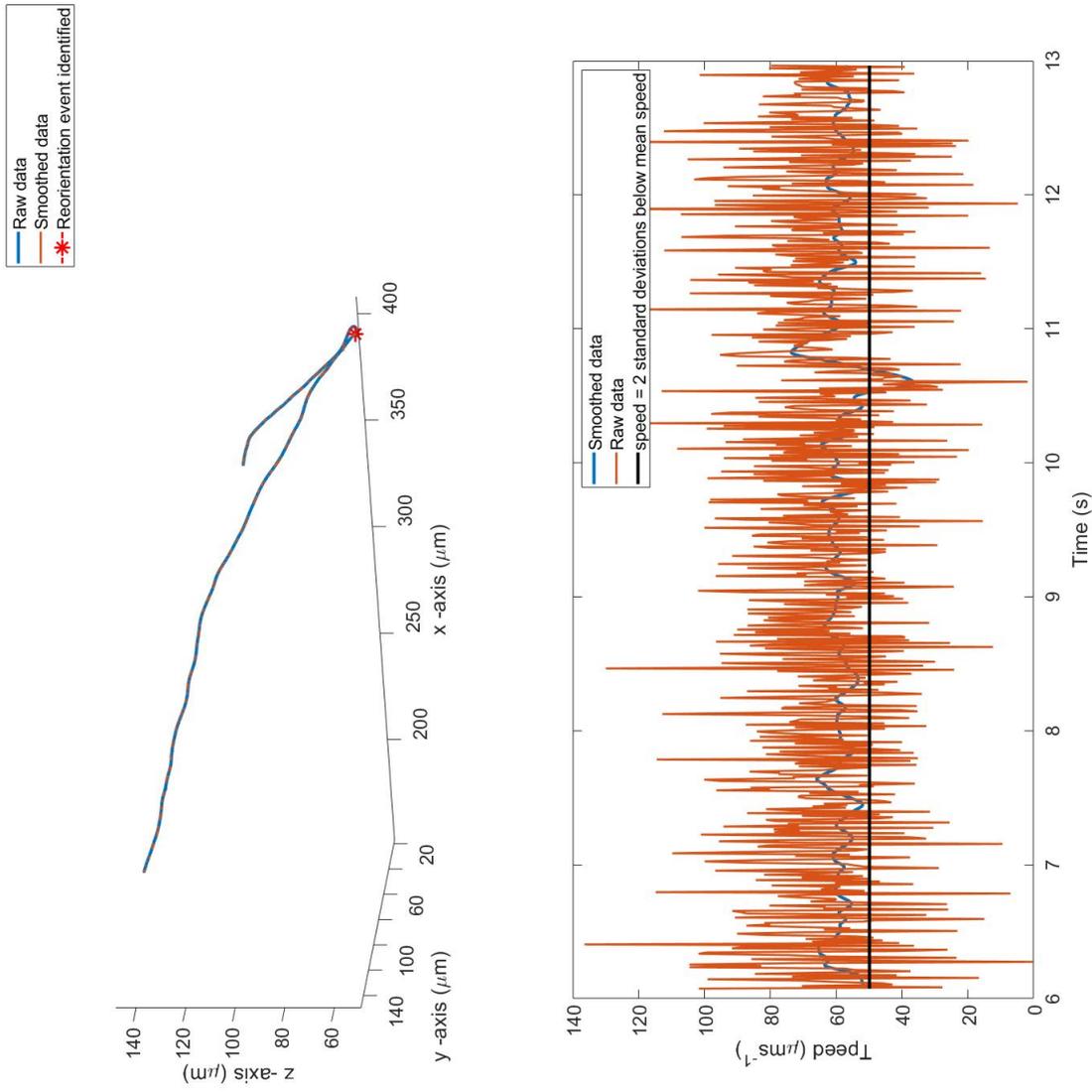
FIGURE 2.10. Top: and example of the raw and smoothed data for a track that has been identified as having a reversal by eye. Bottom: the raw and smoothed instantaneous speeds of the above track. Also shown is the 'critical speed' used in the speed reversal of the track which is two standard deviations below the mean speed. This track shows a point where it drops significantly below the critical value indicating a reorientation event.
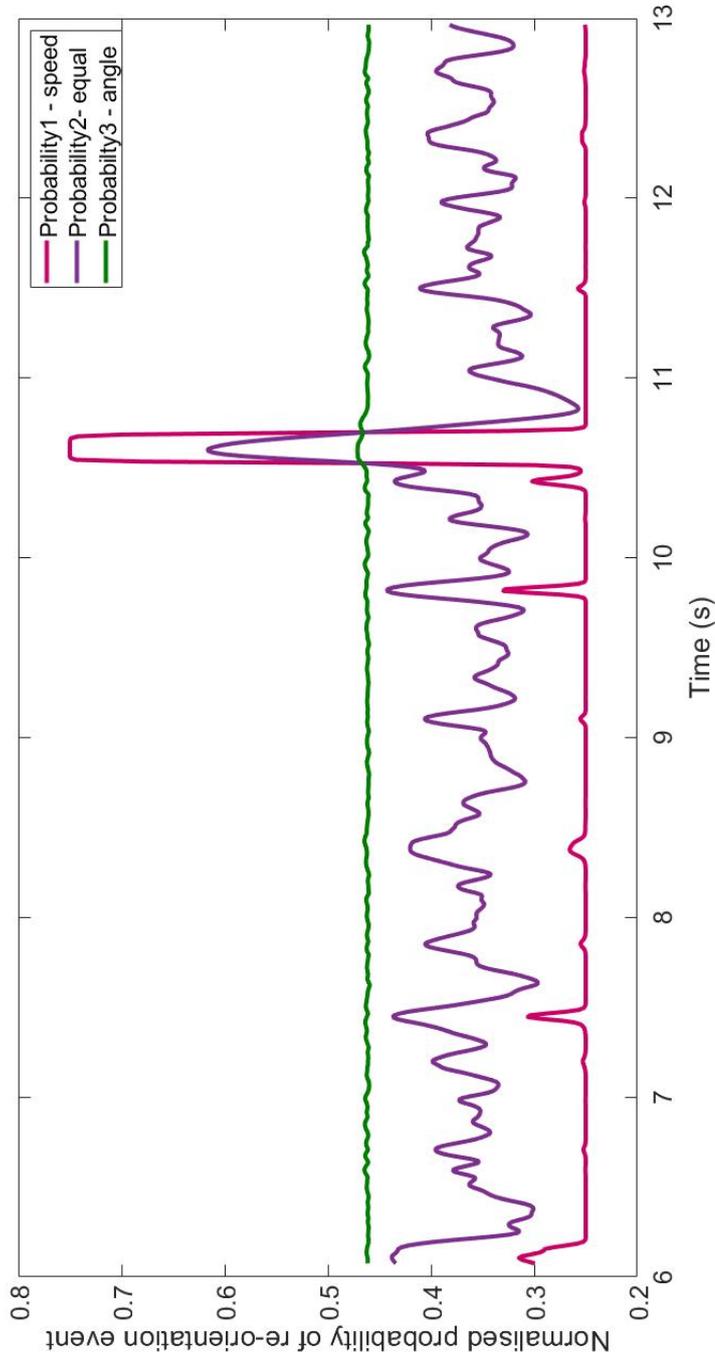
FIGURE 2.11. For the track in 2.10, the instantaneous probability of reversal for the three trial functions is shown. Since a reorientation is recorded when the probability of reorientation is > 0.5, using $P^2_{reorient}(\dot{x}, \xi; t)$ captures the reorientation event identified by eye and will be the function used to identify reorientation events for the rest of this thesis.

and the data is plotted on a log scale to test how well the line fits the data. It can be seen that the fit is good for the data with a low number of reorientation events per track but not so good for those tracks with more reversals.

2.2.5.3 Frequency of reorientation events per second

Since in section 2.2.5.2 there is a possibility that the tracks in the two samples have varying durations depending on the length of time the cell is in the field of view and its swimming speed etc. To account for this, it is also interesting to look at the number of reorientation events per second of track. Figure 2.13 shows the normalised frequency of reorientation events per second of track in the lactam analogue and control samples. This is the number of reorientations in a track divided by the lengths of the track (in seconds) given that a reorientation event is identified in the track. In this case, the mean for the lactam analogue sample and control is 0.76 and 0.58 respectively, with the standard deviations being 0.45 and 0.40 respectively. The two-tailed P-value for this data is less than 0.0001 suggesting that the increase in reorientation events per second when the cells are exposed to the lactam analogue is extremely significant.

2.2.5.4 Run length

A second, linked, characteristic of cell motility is the length of the 'runs'. This gives extra information to the statistics on frequency of reorientations since it shows whether the cells have a constant rate of reorientations or whether there are long periods with no reorientations along with times of frequent reorientations. Figure 2.14 shows the normalised frequency of run lengths (in seconds) for the lactam analogue and control samples. The lengths of the runs were determined by taking the time between reorientation events in the tracks where two or more reorientation events were recorded. The mean for the lactam analogue sample and control is 0.83 and 1.22 respectively, with the standard deviations being 1.49 and 2.01 respectively. Again, the P-value in this case is 0.0265 indicating that the shorter mean run length in the lactam samples is significant.

2.2.6 Discussion

The results here show that the lactam analogue has a clear impact on the free-swimming motility of cells in the regular sample chamber. Along with resulting in a drop in the mean speed of the tracks, the lactam analogue also increases the number of reorientation events of the tracks. This increase in flagellar reversals shown by the reorientation
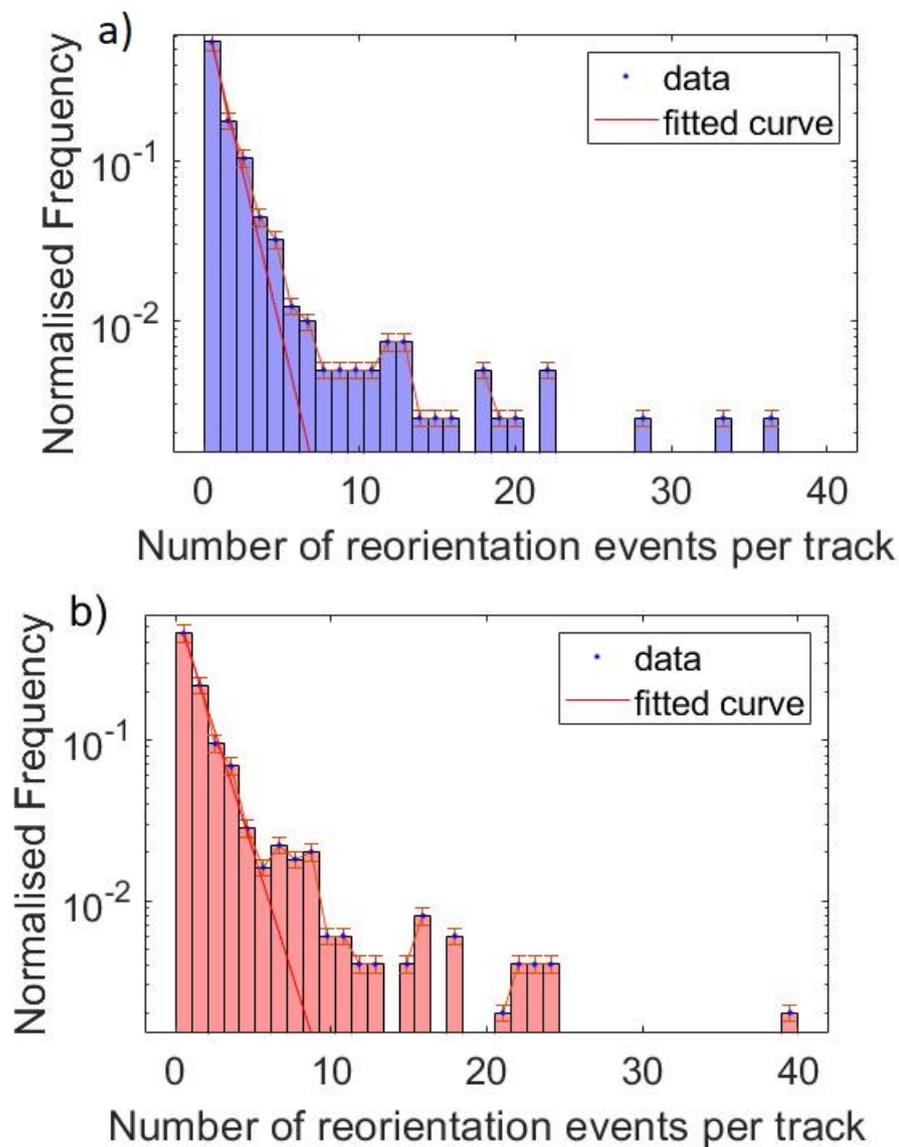
FIGURE 2.12. a) histogram showing the normalised frequency of reorientation events per free-swimming track in the sample containing the lactam analogue and b) that of the control. The fit shown is an exponential. The mean for the lactam analogue sample and control is 3.09 and 2.73 respectively, with the standard deviations being 4.10 and 4.09 respectively. These tracks were imaged in regular sample chambers the two-tailed P-value for this data indicates that the increase in reorientation events in lactam is significant.
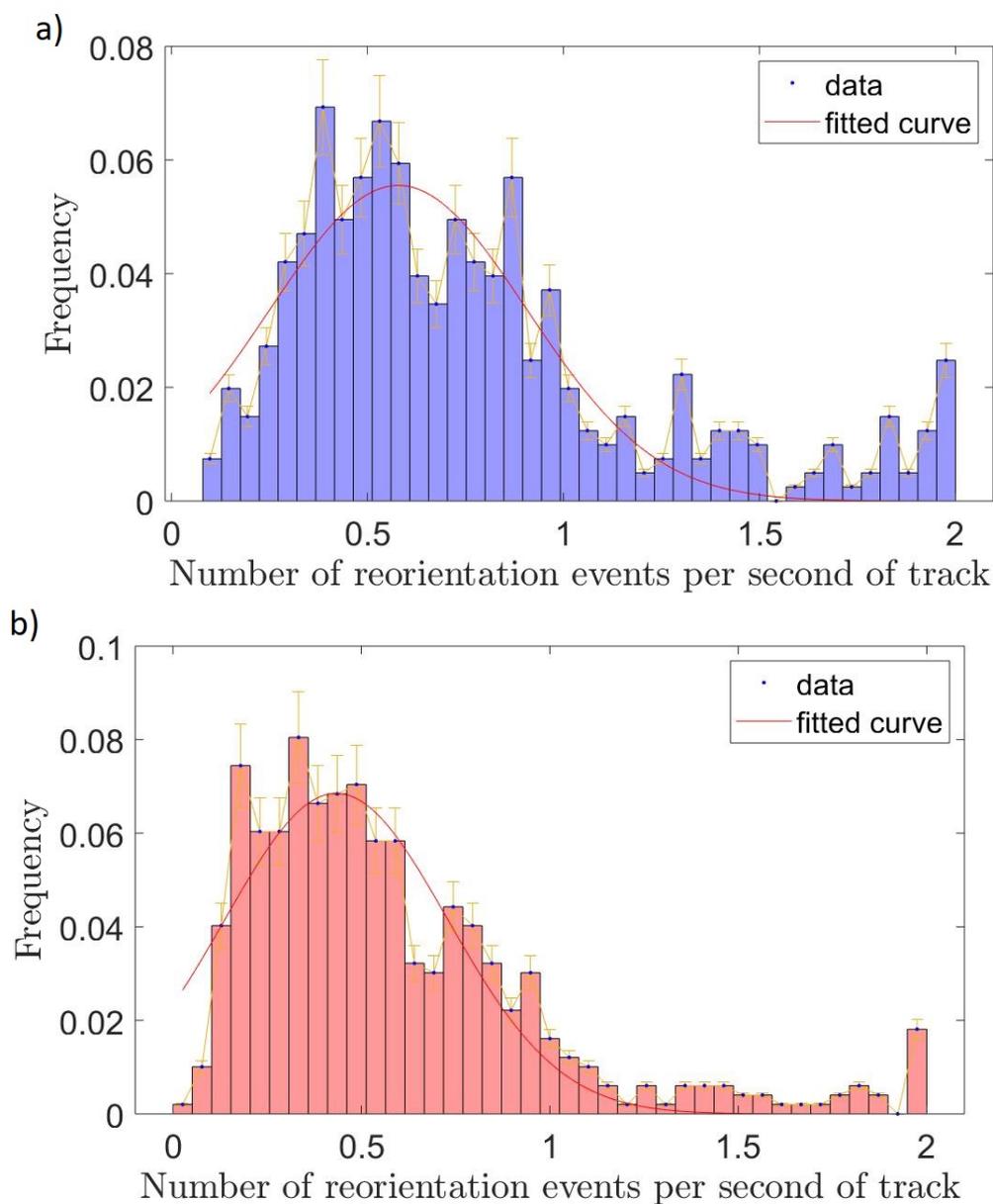
FIGURE 2.13. a) histogram showing the normalised frequency of reorientation events per second of free-swimming tracks in the sample containing the lactam analogue and b) that of the control. The fit shown is a single term Gaussian fit. The mean for the lactam analogue sample and control is 0.76 and 0.58 respectively, with the standard deviations being 0.45 and 0.40 respectively. This data was collected in the regular sample chambers and the P-value suggests the increase in the mean number of reorientation events per second in lactam is significant.
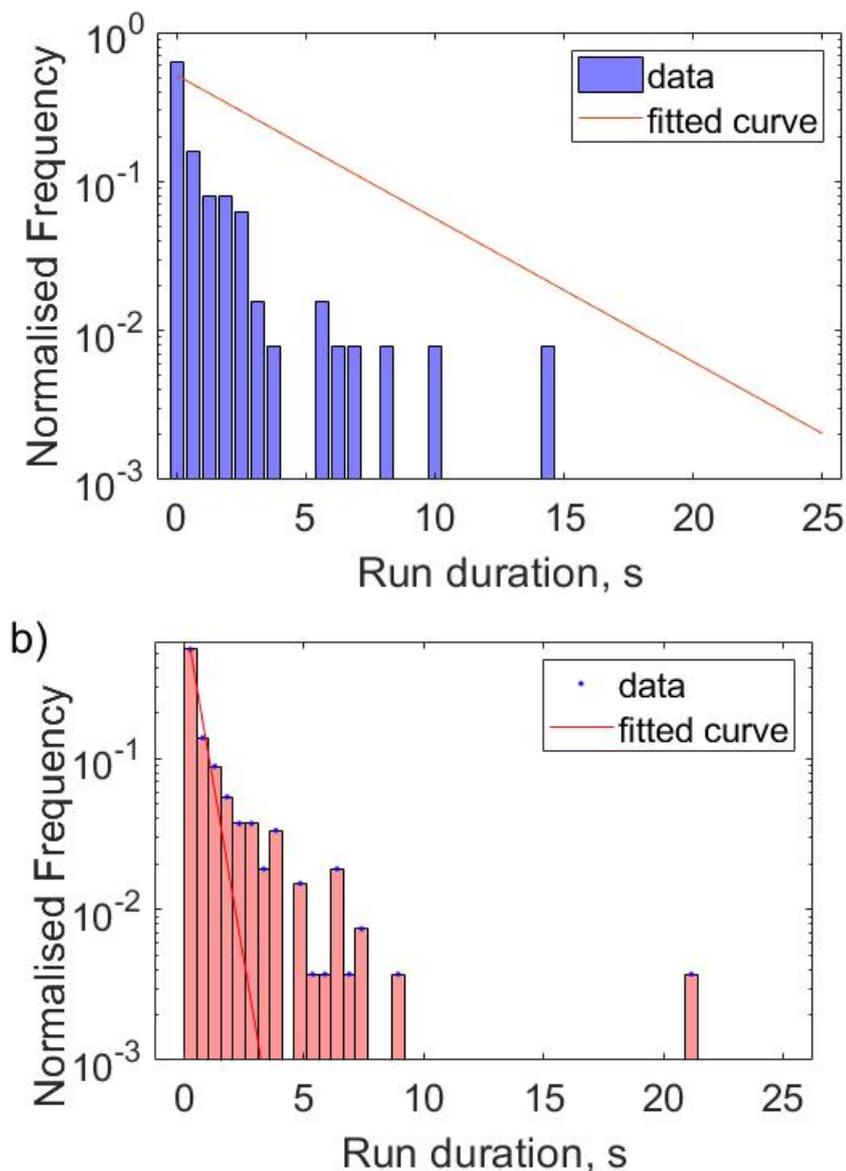
FIGURE 2.14. a) histograms showing the normalised frequency of run durations of free-swimming tracks in the sample containing the lactam analogue and b) that of the control.The fit shown is an exponential. The mean for the lactam analogue sample and control is 0.83s and 1.22s respectively, with the standard deviations being 1.49s and 2.01s respectively. This data was collected in the regular sample chambers and the P-value suggests the increase in the mean number of reorientation events per second in lactam is significant.

events may explain the drop in mean speed as a drop in speed is one of the conditions for a reorientation event to be identified.

It would be interesting to further explore any effect that the lactam might have on cells that were in a growth medium such as TB. This would be useful to identify whether the lactam interferes with any of the growth/division processes and whether daughter cells have a different motility when exposed to the lactam than the parent cells. It would also be interesting to quantify the number of QSMs in the environment to be certain that there is no build up.

2.3   Effect of lactam on swimming cells near a surface

The importance of quorum sensing molecules in biofilm formation, when bacteria are on a surface, suggests that any interference with quorum sensing would only manifest in bacteria on a surface. Here, the effect of the lactam analogue on cells close to a surface was investigated by studying the motility of cells within a shallow chamber. The motivation behind this experiment is to test whether the lactam analogue interferes with cell motility in the near surface limit and, therefore, if the observed reduction in biofilm formation is due to a reduction in ability to surface-attach.

2.3.1   Data collection

Much of the sample preparation and optical set-up for this experiment is the same as used in section 2.2.2. The only distinction is the depth of chamber slide used for imaging. Again, a control sample is compared to that containing lactam analogue and the same method of data collection is used. Therefore, direct comparisons may be made between the data obtained from this experiment and that of the deeper chamber.

2.3.1.1   Shallow chamber slides

The shallow chamber slide for investigating the effect of the lactam analogue on motility near surfaces are approximately 75 ± 5 μm deep (based on a sample of 5 chambers). They are therefore a third of the depth of the deeper chambers and increase the proportion of cells that are affected by the no-slip boundary. The chambers were made by using two pieces of double sided sticking tape to attach a 22×50mm coverslip to a 76×26mm glass
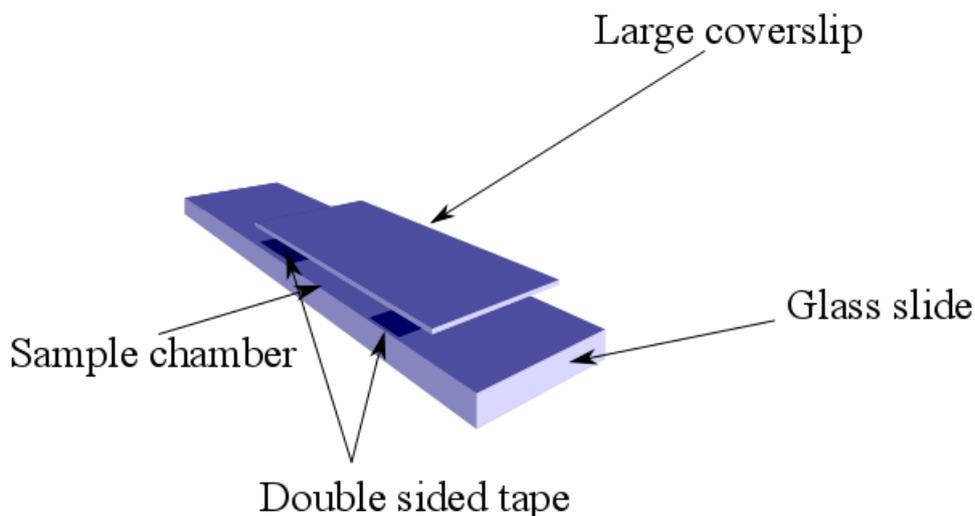
Figure 2.15.
The shallower chamber slides are prepared by using double-sided sticky tape to attach a coverslip to a glass slide, leaving a chamber between.

slide (see figure 2.15). Again the capillary effect was used to fill the chamber with the liquid sample and both ends of the chamber were sealed with nail varnish to prevent evaporation or leakage.

2.3.2   Data analysis

The data was processed and analysed in the same way as that of the freely swimming cells with the same statistics investigated.

2.3.3   Results

2.3.3.1   Mean speed

Figure 2.16 shows a histograms of the mean speeds of tracks in the sample containing the lactam analogue and the control. The two data sets are of 332 and 288 tracks respectively obtained over 3 days. The mean value of the lactam analogue and control samples are 34.67 μm/s and 40.06 μm/s, with the standard deviations 19.34 μm/s and 17.58 μm/s respectively. The two-tailed P-value for this data is 0.0003 indicating that the drop in mean speed is extremely significant. As these cells were imaged in the shallow chambers,

this result shows that the lactam also affects the motility of cells that are influenced hydro-dynamically by no-slip boundaries.

2.3.3.2   Frequency of reorientation events per track

The data on the frequency of reorientation events per track is show in figure 2.17. The mean for the lactam analogue sample and control is 3.49 and 2.22 respectively, with the standard deviations being 2.96 and 4.91 respectively. The two-tailed P-value for this data is 0.0117 indicating that the increase in the number of reorientation events per track is significant. In this case, the cells were imaged in a shallow chamber meaning that an increased proportion of the tracks were near to no-slip boundaries.

2.3.3.3   Frequency of reorientation events per second

Figure 2.18 shows the statistics for the number of reorientation events per second of track given that a reorientation is identified in the track. The mean for the lactam analogue sample and control is 0.74 and 0.54 respectively, with the standard deviations being 0.43 and 0.37 respectively. The two-tailed P-value for this data is less than 0.0001 indicating that the increase in the number of reorientation events per second is significant. In this case, the cells were imaged in a shallow chamber meaning that an increased proportion of the tracks were near to no-slip boundaries.

2.3.3.4   Run length

Figure 2.19 shows histograms of run length (in seconds) for the cells in the lactam and control samples. The mean for the lactam analogue sample and control is 0.89 and 1.36 respectively, with the standard deviations being 1.62 and 2.31 respectively. The two-tailed P-value for this data is less than 0.0387 indicating that the reduction is mean run length is significant. In this case, the cells were imaged in a shallow chamber meaning that an increased proportion of the tracks were near to no-slip boundaries.

2.3.4   Discussion

Here, the motility of cells near a surface and exposed to the lactam analogue is compared to the motility of control near-surface cells. As with the free-swimming cells, there is a clear difference between the two groups suggesting that the lactam does interfere with surface-associated swimming cells. There is a difference between the free-swimming and near surface groups which would be expected due to hydrodynamic interactions with
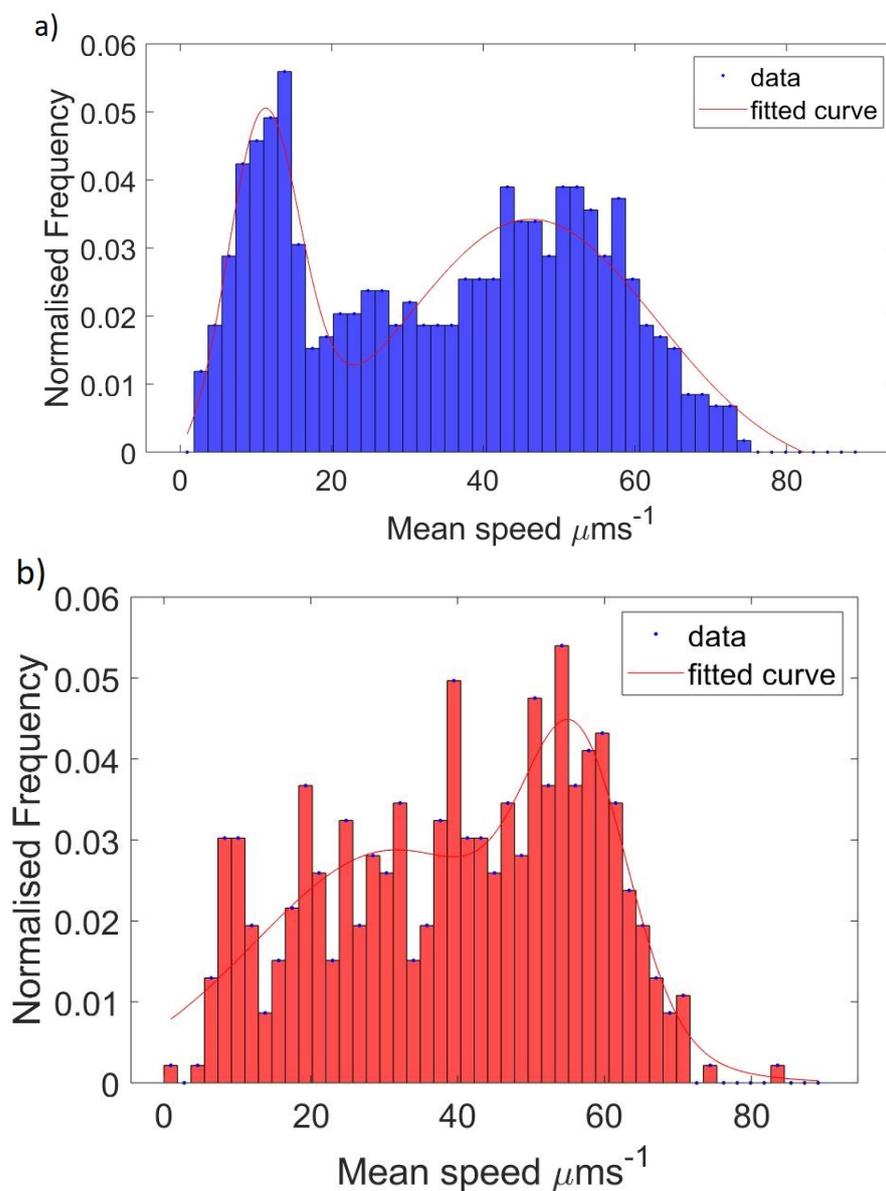
FIGURE 2.16. a) the normalised frequency of each track mean speed for free-swimming cells in the sample containing the lactam analogue and b) the control sample. The fit shown is a two-term Gaussian distribution. The mean value of the lactam analogue and control samples are 34.67 μm/s and 40.06 μm/s, with the standard deviations 19.34 μm/s and 17.58 μm/s respectively. The two-tailed P-value for this data is 0.0003 indicating that the drop in mean speed is extremely significant. In this case, the cells were imaged in a shallow chamber meaning that an increased proportion of the tracks were near to no-slip boundaries.
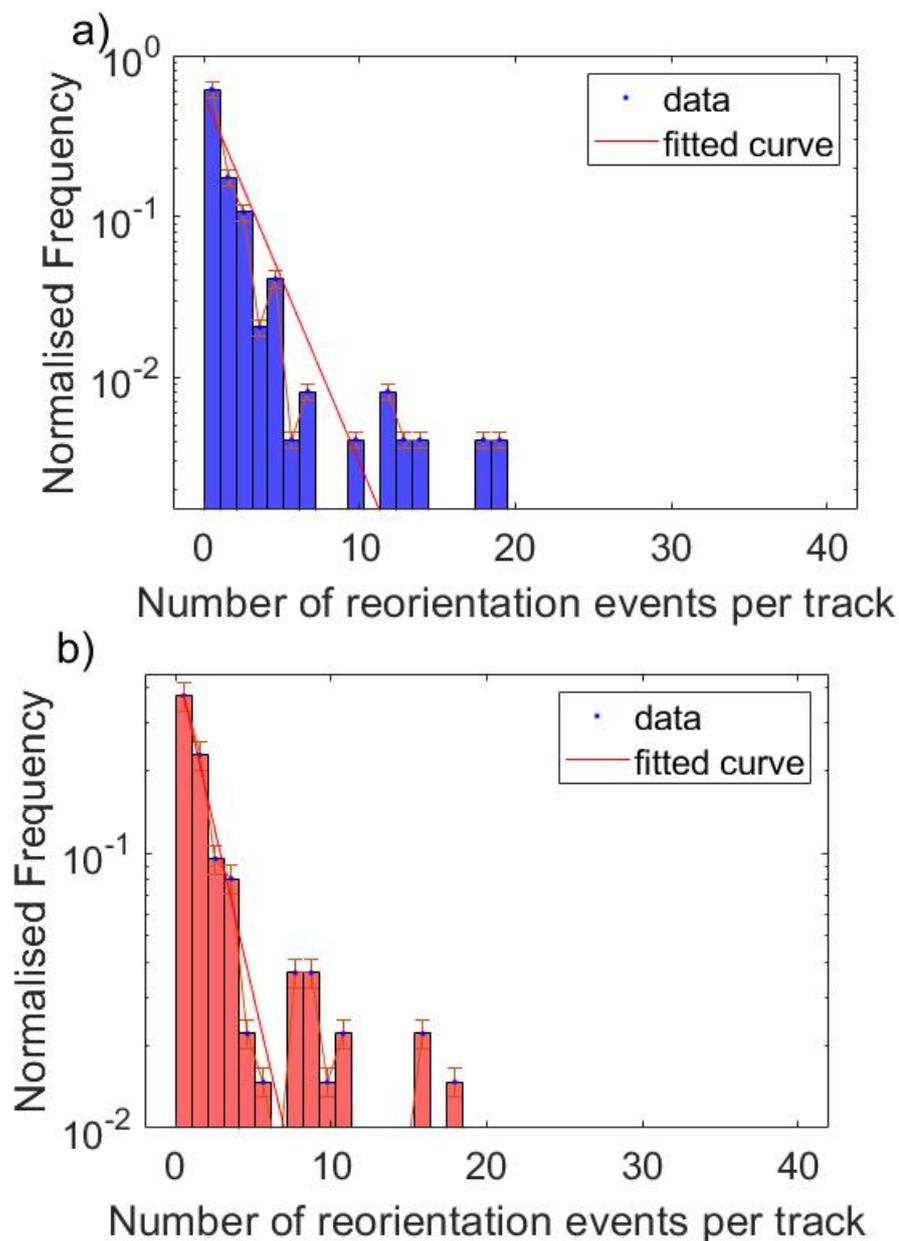
FIGURE 2.17. a) histogram showing the normalised frequency of reorientation events per track in the sample containing the lactam analogue and b) that of the control.The fit shown is an exponential. The mean for the lactam analogue sample and control is 3.49 and 2.22 respectively, with the standard deviations being 2.96 and 4.91 respectively. The two-tailed P-value for this data is 0.0117 indicating that the increase in the number of reorientation events per track is significant. In this case, the cells were imaged in a shallow chamber meaning that an increased proportion of the tracks were near to no-slip boundaries.

a)

b)
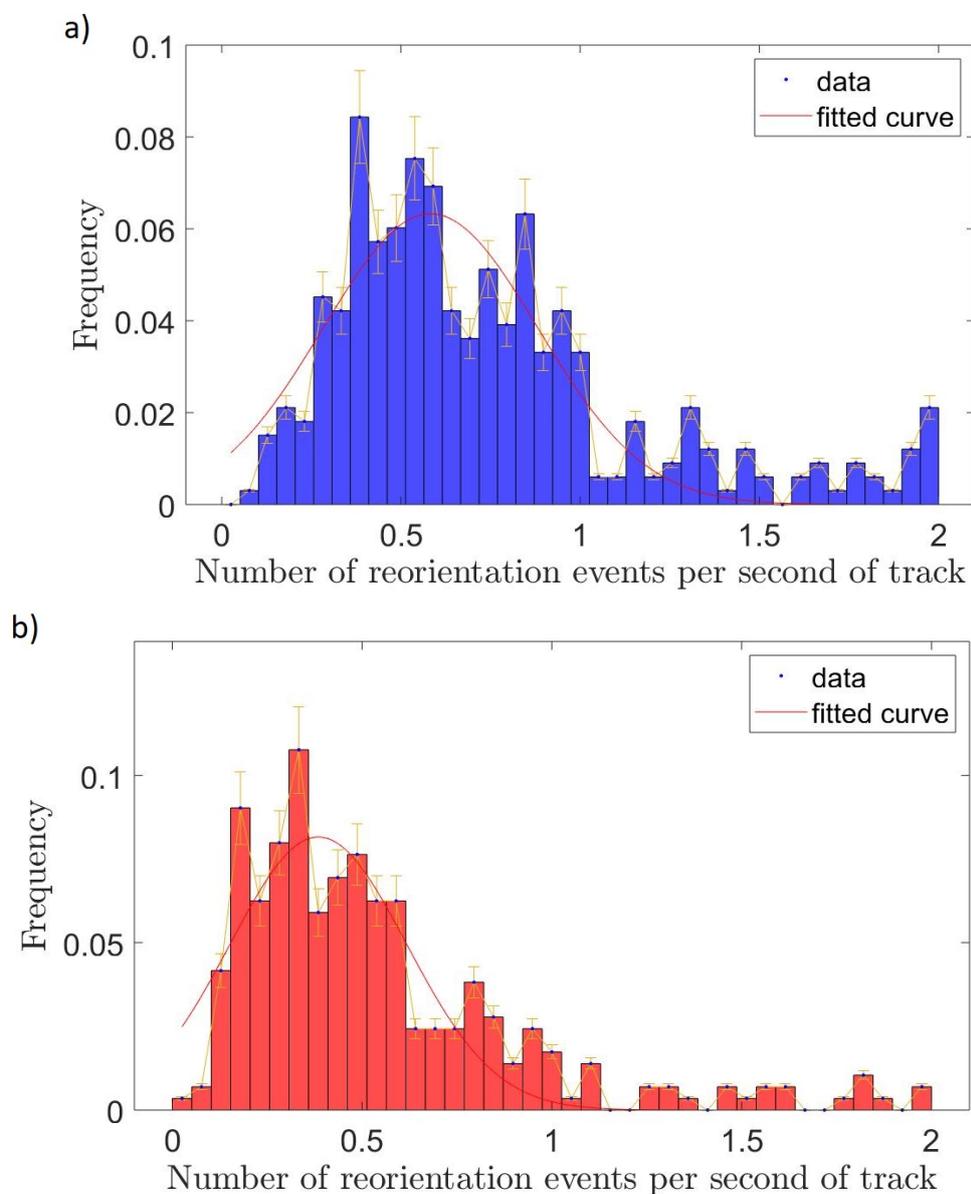
FIGURE 2.18. a) histogram showing the normalised frequency of reorientation events per second in the sample containing the lactam analogue and b) that of the control.The fit shown is a single term Gaussian fit. The mean for the lactam analogue sample and control is 0.74 and 0.54 respectively, with the standard deviations being 0.43 and 0.37 respectively. The two-tailed P-value for this data is less than 0.0001 indicating that the increase in the number of reorientation events per second is significant. In this case, the cells were imaged in a shallow chamber meaning that an increased proportion of the tracks were near to no-slip boundaries.
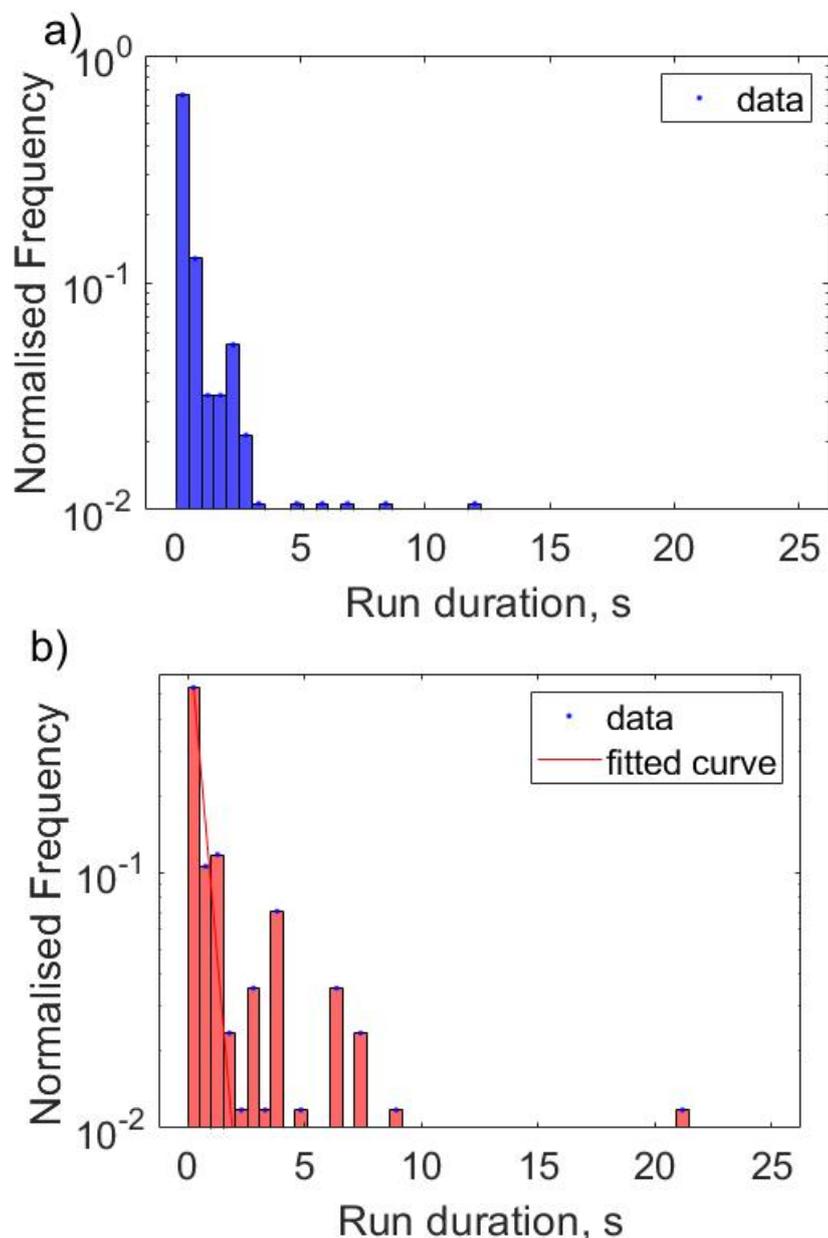
FIGURE 2.19. a) histograms showing the normalised frequency of run durations in the sample containing the lactam analogue and b) that of the control for cells in the shallow imaging chambers.The fit shown is an exponential. The mean for the lactam analogue sample and control is 0.89 and 1.36 respectively, with the standard deviations being 1.62 and 2.31 respectively. The two-tailed P-value for this data is less than 0.0387 indicating that the reduction is mean run length is significant. In this case, the cells were imaged in a shallow chamber meaning that an increased proportion of the tracks were near to no-slip boundaries.

the surface of the sample chamber. Despite this, the general trend of increased reversal and decreased speed when the cells are exposed to lactam in conserved in both types of chamber.

The distribution of run lengths was studied to align with the work in the literature where run length distribution is highlighted as a key characteristic of bacterial motility. Many bacterial species are said to have an exponential distribution of run lengths [19] and the results in this chapter suggest the free-swimming and surface-associated *P. aeruginosa* cells both in the control and lactam samples do not align with this. This suggests that not all bacteria have the same run length distributions. Perhaps this difference could be due to the number of flagella per cell or be due to the different flagella hook/motor systems in the different bacterial species. Bacteria are known to change their run length in response to chemical stimulus to effectively perform chemotaxis [148]. Therefore, if cells in the control were responding to QSM that the lactam cells were unable to, the run length distributions for the two groups would be expected to be different, which aligns with that is seen.

2.4   Chapter conclusions

In this chapter, the effect of the lactam analogue on *P. aeruginosa* cells was investigated. From analysis of instantaneous speeds, tumble frequencies and run durations it was determined that the cells exposed to the lactam analogue show different motility compared to those cells in a control sample. This aligns well with work in the literature. For example, in 2002, Ren *et al* [149] analysed the swimming *Bacillus subtilis* in agar plates when exposed to a furanone derived from *Delisea pulchra* (similar to the lactam analogue used in this thesis). The team found that swimming was significantly reduced, in a concentration dependent manner, when cells were exposed to the furanone. They also found that exposing the cells to the furanone reduced biofilm growth, further evidencing a link between swimming and biofilm formation.

In 2012, de la Fuente-Núñez *et al* identified a novel synthetic cationic peptide which displayed anti-biofilm properties [150]. They found that flagella-dependent swimming motility of PA01 in agar was reduced when cells were exposed to the peptide. Genetic analysis showed that flagellar motility genes were down-regulated in the presence of

the peptide providing further evidence that flagellar motility and biofilm formation are linked.

Work by Glessner *et al* suggests that the *las* and *rhl* quorum sensing systems are involved in the control of twitching motility in *Pseudomonas* [151]. Although twitching motility is a surface-associated effect involving pili, this work shows a clear link between motility and quorum sensing. Similarly, Alavi *et al* analysed the effect of various nanocomposites against multi-drug resistant bacteria. They observed a reduction in quorum sensing and swarming motility providing further evidence that factors altering quorum sensing also impact motility.

Furthermore, in 2015, Yang *et al* studied the swimming motility of the bacterium *Vibrio harveyi* [152]. The group used a mutant that was unable to synthesise AIs and therefore unable to quorum sense. They found that the mutant had significantly reduced swimming motility in agar compared the the wild type. The results in this chapter show that the quorum sensing inhibiting lactam analogue alters the free swimming motility of PA01 cells. This observed change in motility when lactam is present suggests either that the lactam also interrupts the systems involved in motility directly or that the quorum sensing systems have control over the motility systems. The above literature indicates that the latter is not unlikely.

More recently, in 2019, Schniederberend *et al* studied a motile mutant of *P.aeruginosa* that assembled randomly placed flagella [**?**]. They found that this mutation altered biofilm formation along with flagellar rotation at the surface. Their work implicated the signalling messenger cAMP in the control of flagellar rotation. cAMP is known to control many systems in *P.aeruginosa* but its implications on flagellar rotations were previously unknown. Taken in context with these results in the literature, the hypothesis presented in this thesis is that the lactam analogue disrupts the cAMP pathway, thus interfering with flagellar rotation along with biofilm formation. This thesis presents novel insights to the impact of the lactam analogue on the 3D swimming of cells.

NOVEL USES OF HOLOGRAPHY

"To be sure of hitting the target, shoot first, and call whatever you hit the target."

Ashleigh Brilliant

3.1 Introduction

This chapter details two novel uses of holographic microscopy to demonstrate the scope of the technique. The first of these projects is an investigation into the effect of flagellar structure on bacterial swimming. The data from this experiment contributed to the publication [153]. The second project was an investigation into the effect of using two light sources within the holographic set-up to attenuate noise in the data acquisition. The data from this project contributed to the publication [154]. Although the key results from these papers are presented and discussed, all contributions other than holographic data collection on the bacterial cultures was undertaken by collaborators.

3.2 Utilising holographic imaging to study the effect of viscosity and flagellar genetic manipulation

3.2.1 Motivation

The strength of the holographic technique used in this thesis is that the trajectories of a large number of cells may be analysed simultaneously and in 3D. This high throughput method is useful for investigating the effect of changing various parameters on cell motility. In this section experiments investigating the effect of viscosity and flagellar genetic manipulation on motility are detailed. This work was undertaken in collaboration with a team in Germany and their contributions are not discussed in detail [153].

This work was focused on the bacteria *Shewanella putrefaciens* CN-32. Similar in size to the other bacteria studied in this thesis, *S. putrefaciens* is a gram-negative bacterium approximately $2-3\mu$m in length [155]. They are motile by a primary polar flagellum and an addition lateral flagellum and can be found in a variety of aqueous environments [156]. The primary flagellum is approximately $6-7\mu$m long and forms a left hand helix. When the helix rotates clockwise, the flagellum 'pulls' the cell body and a counterclockwise rotation results in the flagellum 'pushing' the cell body. The lateral flagellum is thought to contribute to cell realignment but, for this work, a strain that has had the lateral flagellum deleted genetically was used so as to focus on the effects of the primary flagellum. The flagellar filament is composed of two distinct proteins called flagellins, FlaA and FlaB. The first approximately 17% of the filament (extending from the cell body) is composed almost exclusively of FlaA with FlaB predominantly making up the remaining filament. The two flagellins display different properties with FlaA being the more rigid of the two.

It has previously been observed that *S. putrefaciens* can 'corkscrew' its flagella around itself in highly viscous environments (see figure 3.2.1) [156]. It had been postulated that this arrangement of the two flagellins is necessary for this 'corkscrew' behaviour and holography was used to investigate how a genetic manipulation of the flagellin arrangements may alter swimming motility.
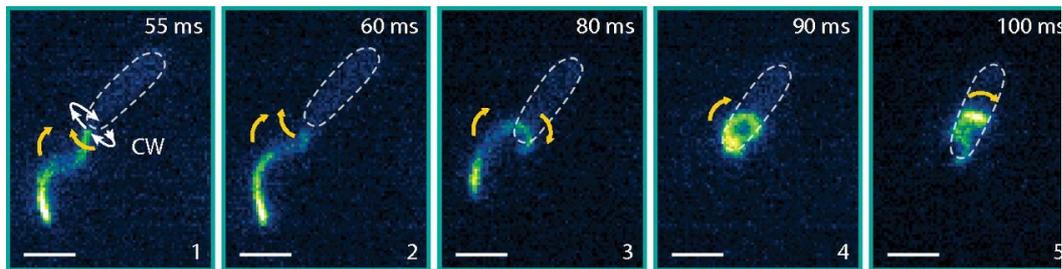
FIGURE 3.1. Fluorescently labelled flagella states at various times. Cells are in a medium of 20% Ficoll 400 to increase viscosity and cell body is indicated by a dotted ellipsoid. Yellow arrows indicate the movement of the flagellar filament. Figure is adapted from [156].

3.2.2 Data collection

To investigate the effect of the flagellins' arrangement, 4 strains were investigated. The first, the wild type (WT) was the standard CN-32 *S. putrefacians* strain with FlaA first (protruding from the cell body) followed by FlaB. Also investigated were strains that had been genetically altered to only produce either FlaA (FlaA-only) or FlaB (FlaB-only). The final strain had been genetically altered to switch the locations and ratios of the two flagellin (FlaBA). The flagella of this strain first produced a short length of the less rigid FlaB followed by a longer length of FlaA. All four of these strains were analysed in standard media and in high viscosity media to investigate whether a particular flagella confirmation was advantageous in a highly viscous environment.

To grow the saturated cultures of the strains provided by the collaborators, a crystal of frozen stock culture was incubated in 10ml of LB overnight at 30° shaking at 150rpm. An exponential culture was then grown by inoculating 10ml of lactate medium (LM) with 10μl of the saturated culture and incubating at 30° shaking at 150rpm for 5 hours or until $OD_{600} = 0.6$. Three biological replicates for all the different strains were grown on three separate days and six samples were used from each of the cultures.

To image, three of the six samples from the exponential culture were diluted $1:1000$ fresh LM (viscosity = 1cP [157] and the other three were diluted at the same ratio into LM with 15% (wt vol^{-1} - equivalently a viscosity of 10cP [157]) Ficoll 400 to investigate viscosity. Each of the samples was loaded into a regular chamber slide that was sealed with nail varnish after loading. The samples were images immediately after loading on the standard holography set-up in chapter 1 using the 642nm laser. Movies were

recorded for 60s at 50Hz with an AOI of 1024×1024 px.

3.2.3 Results

The holographic data was processed as described previously to extract the tracks of the cells in each of the samples. For all four strains, between 1340 and 4887 tracks were found in both the regular and high viscosity media giving substantial population sizes. From the track data, three different parameters were identified for comparison. The first of these was the instantaneous speed. The instantaneous velocity at each point of each track was found using a forward difference method. The results for each of the strains in both media types are shown in figure 3.2.3 c,d. Here, as in the other plots of figure 3.2.3, relative statistics are shown so that different sample sizes may be compared.

In the regular media, the four strains have similar profiles with a similar top speed and two sub-populations around similar points. The slower of these two had congruent profiles for all strains except the FlaBA strain in which case the peak was much broader indicating a greater range of speeds and an increase in the average speed of the FlaBA slower sub-population peak. The position of the faster sub-population peak was different for all strains. For the high velocity media, this two-population trend persisted but the total average speed was lower for all strains. Unlike in the regular media where WT had the maximum speeds, in the high viscosity media, the FlaA-only strain appeared to have an advantage [153]. This is interesting since the flagella of the FlaA-only strain were found to have a smaller helical radius and aligns with the previous theory that having a smaller helix diameter aids swimming in elevated viscosity [158].

The second parameter was the length of runs in each of the samples. To correctly determine the length of a run, the run had to be 'book-ended' by reorientation events and so those reorientation events needed to be identified. The angle between the direction vectors of the instantaneous velocities at each proximate point is calculated, $\theta(t)$, where t is time. A peak search algorithm was used to find the maxima in the $d\theta/dt$ curve and these were taken as the loci of reorientation events provided that the angle change was $> 5°s^{-1}$. Figure 3.3 shows an example track along with its $d\theta/dt$ curve and identified reorientation events circled. Figure 3.2.3 a,b show the distribution of run lengths for the 4 strains in the two types of media. In the normal media, the strains all had similar profiles with a maximum run length of approximately 20s. In the higher viscosity, other than a slight shift towards longer runs, little difference was observed except in the FlaBA

strain in which there was a distinct lack of the longer runs.

Once a reorientation event had been identified, the total tumble angle of the event was found by determining the angle between the swimming direction 0.25s before and after the event. Figure 3.2.3 e,f shows the distributions of tumble angles for each reorientation event that was identified. In the regular media, all strains show a distribution of reorientation angles with all but FlaBA showing very similar profiles. In the high viscosity media, the WT and FlaBA retained a broadly similar profile but the FlaA-only and FlaB-only mutants had an increased proportion of a high angle tumbles.

3.2.4 Discussion

In the regular media, 3 of the strains displayed similar profiles but the FlaBA strain had an increased instantaneous speed on average. When this is taken with the much decreased run length of FlaBA in the high viscosity media, it suggests that the specific structure of the flagellins in *S.putrefaciens* may be a balance to ensure cells can adapts to various environments. The FlaBA mutants also exhibit a distinctly different tumble angle profiles to the other mutants in both the types of media. In the tumble profiles, high angles indicate 'run-reverse' motility where the cell is less effectively sampling the environment, without external instabilities (ie. Brownian motion). On the other hand, small turning angles suggest the cell is not reversing but not tumbling effectively either. This type of swimming would give a greater directional persistence. Results in the literature suggest that the bending characteristics of the flagellar filaments and hook are important in the reorientation of bacteria that swim with a run-reverse-flick motility [159**?** , 160]. This suggests that the rigid proximal FlaA segment of WT *S. putrefaciens* likely aids directional changes in normal viscosity while the proximal FlaB segment in the FlaBA mutant suppresses reorientation. The increased number of small reorientation angles seen in the FlaBA mutant also suggests that the motor direction switching time is shorter than in the WT. This is seen more at higher viscosities which may be explained by differences in load for this arrangement of flagellar filament [161, 162].

It is also interesting to note that in the high viscosity media, there was an increase of cells that were in the slow population of instantaneous velocities for the WT and FlaB-only mutants. Looking at individual trajectories suggested that the cells were dropping in speed, switching direction and continuing at a lower speed before switching direction and returning to a greater speed. This effect was not seen on the other strains
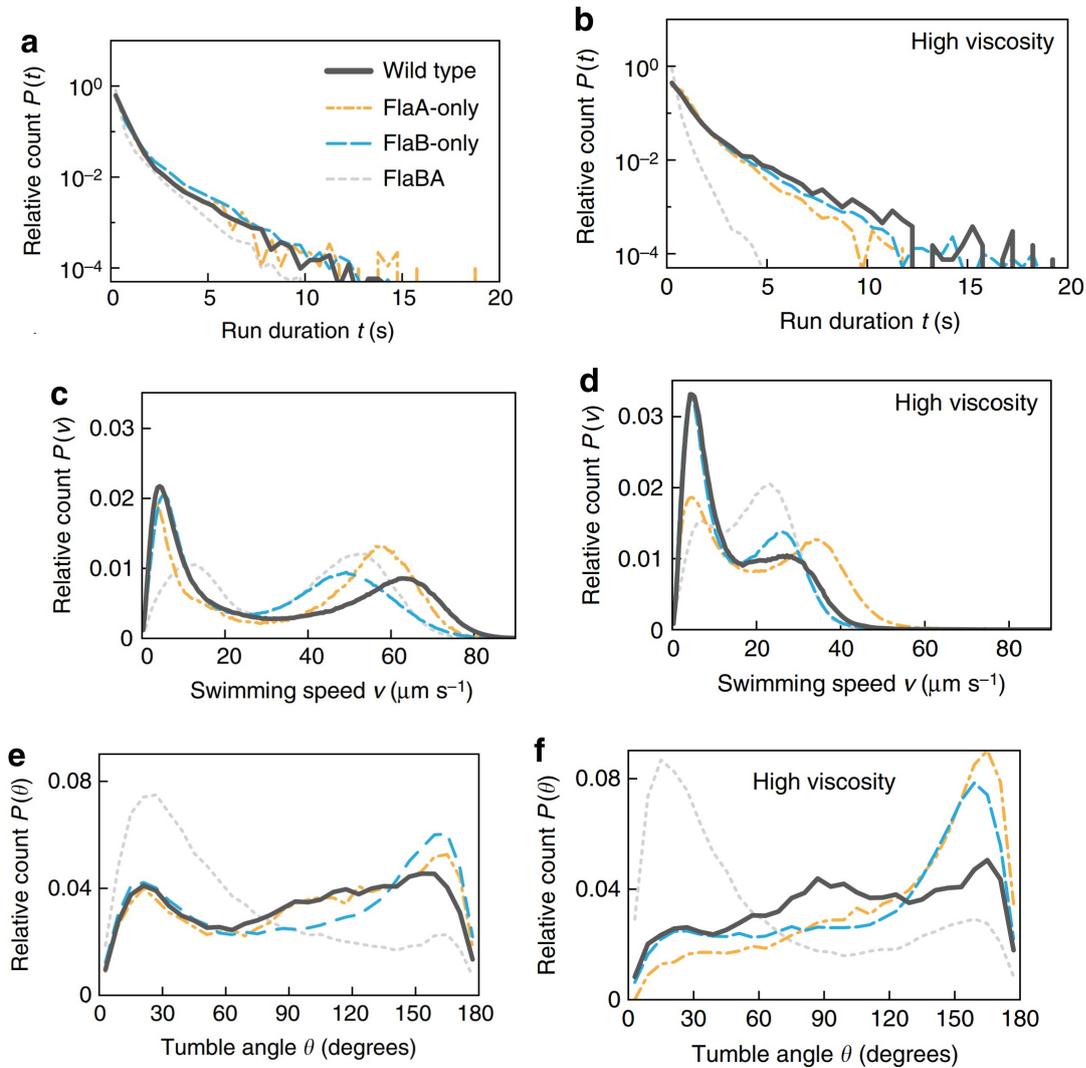
FIGURE 3.2. The free-swimming motility of the 4 strains of *S .putrefaciens*. a,b) show the run duration between reorientation events for the strains in regular and high viscosity media respectively. c,d) show the instantaneous speeds of strains in regular and high viscosity media respectively. e,f) shows the distributions of tumble angles for each reorientation event identified. Figure is adapted from [153].
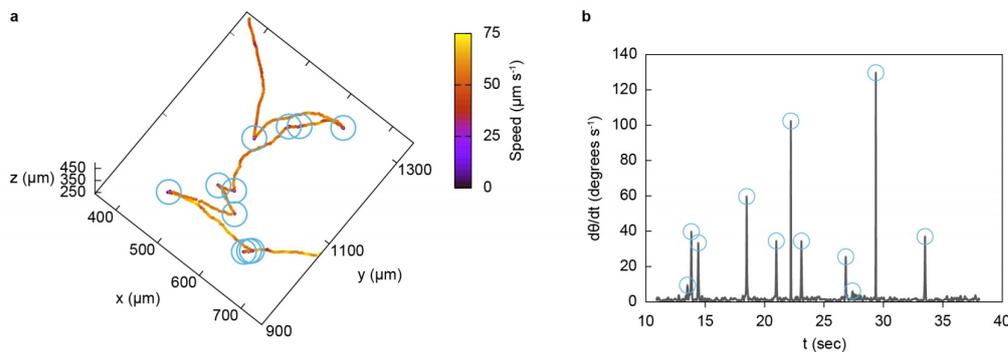
FIGURE 3.3. a) shows an example track of WT in regular media from a birds-eye view. The colour indicates the instantaneous speed of the track and the blue circles identify reorientation events. b) shows the $d\theta/dt$ profile of the same track with the reorientation event that have been identified circled again in blue. Figure adapted from [153]

and was attributed to cells undergoing the 'corkscrew' motility. This suggests that the more rigid FlaA is not flexible enough to wrap around the body and a long length of FlaB is needed for that phenomenon. Taken together with the tumble data, this suggests that the purpose of FlaA near the body is to stabilise but its short length is a balance between stability and ability to 'corkscrew' in highly viscous environments. Furthermore, collaborator analysis on the length of the FlaA filament revealed a wide distribution of lengths within a population. This diversity would ensure that the population as a whole is competitive in a variety of environments.

This work paints an interesting picture of the effect of flagellin arrangement on the motility of cells. It has begun to explain some of the mechanisms but leaves more to be answered. In particular, since a substantial portion of flagellated bacteria can produce multiple flagellins, it would be interesting to understand how different cope with similar problems. It would be an interesting future study to understand which flagellins are produced by the bacteria at various stages of surface attachment/ early biofilm formation stages. The localisation of a primary flagellar filament at the base of the flagella has been reported in other bacterial species not just *S. putrefaciens* [163, 164] which suggests that arrangement of flagellar filaments may also be important in the swimming of these species. Again, all work other than holographic data collection was completed in conjunction with collaborators.

3.3 Two-colour holographic microscopy

3.3.1 Motivation

Earlier in this chapter, the extraction of tracks from holographic data was discussed. One of the key elements in this reconstruction method is using the intensity gradients of the reconstructed stacks to identify the z-coordinate of each object in a frame. This method works well if the objects imaged have similar refractive index but can be much less reliable if a highly scattering object is near a object that scatters less. Detailed here is work undertaken to test the effectiveness of a two-colour holographic set-up to overcome this issue. Information on the set-up and further uses are given in [154].

3.3.2 Data collection

The 2-colour set-up is shown in figure 3.4 where the light is from two lasers. a wavelength division multiplexer is used to ensure the two light sources follow the same incident path to the sample. To test the ability of the set up to identify objects with different scattering properties, the sample chosen was a mix of *E. coli* cells (comparatively low scattering) and 0.5μm diameter polystyrene beads (comparatively high scattering). The strain HCB1 *E. coli* cells were grown first to saturation in LB then to exponential in TB following the protocol to grow *P.aeruginosa* in chapter 1. Once the cells had reached an $OD_{600} = 0.2$ the sample to be imaged was made of the exponential culture diluted $1:100$ with fresh TB. The sample was inoculated into a regular chamber slide and the chamber was sealed after inoculation. A $20\times$ lens was used and the focal plane was approximately 50μm below the chamber. Movies of 1000 frames were collected at 100fps and saved as uncompressed .avi files.

3.3.3 Data pre-processing

The frames recorded are composed of two images of the AOI side by side since the images from the red and green sources arrive separately on the camera. After these two images were separated into red and green submovies, they had to be mapped onto one another. First each of the submovies was then processed much the same as the single colour holography discussed previously in this chapter. The difference in the way the two colour data was treated came after the threshold had been applied to the projected stack giving bright points where an object had been identified. Figure 3.5 shows how the threshold-applied projected stack for the two channels are slightly different. The de-
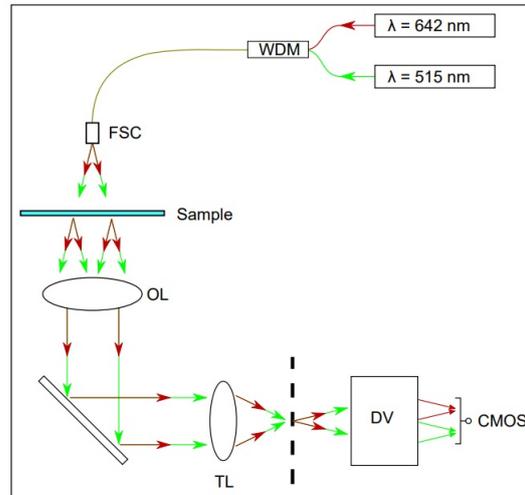
FIGURE 3.4. A schematic showing the two-colour holographic configuration. The two wavelengths are coupled using a wavelength division multiplexer (WDM) and pass through the sample via a free-space coupler (FSC). The light then passes through the objective lens (OL) and the tube lens (TL) to the DuelView (DV) that images the microscope image plane (dotted line) onto the CMOS camera. Figure taken directly from [154].

tails of the method used to map the images appropriately can be found in the article [154].

Once the mapping had been applied, the movies were cropped to 256×256 to speed up the FFT operations. As in the one colour holography, the Rayleigh-Sommerfeld back propagation method was used to obtain the intensity gradient $I_{grad}(x, y, z; t)$ for each frame of each of the two submovies. These arrays for each of the channels were multipled to produced the joint arrays. From these the remaining steps of the holographic reconstruction detailed previously are followed to obtain the tracks. This resulted in a reduction in the noise associated with refractive index variation as detailed in [**? **].

3.3.4 Results

Figure 3.6a shows an example track of a swimming cell found using the two-colour method. While this track does not appear vastly different to the tracks determined using the single colour holography technique previously, the efficiency of the two-colour technique can be seen by analysing the noise of the two methods. To do this, the deviations of the raw track from the smoothed track were investigated. Here the smoothing method
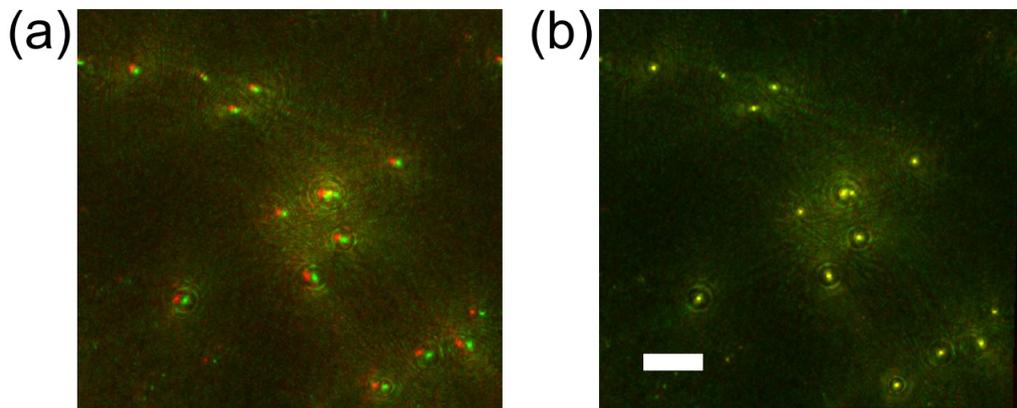
FIGURE 3.5. The projected stacks for an example sample of polystyrene beads and *E. coli* cells. a) shows a superposition of the projected stacks for the red and green channels after a suitable filter had been applied. The green image is displaced for the red and distorted slightly. b) shows a superposition of the same images after the appropriate mapping had been applied. The scale bar indicates 30μm. Figure taken directly from [**?**].

was the same as detailed in the single colour holography method previously. Figure 3.6b shows the z-positions of the raw track (markers) along with the smoothed data (lines) when using the red submovie only, the green submovie only and when using both. The markers of the two-colour data align much more closely with the smoothed data than those of either of the single colours.

Figure 3.6 c-e show the residuals when the splined smoothed data is taken from the raw track data for the red only and two colour sets. While the improvement in the x and y directions from using the two colour system is minimal, there is a vast improvement in the improvement in the accuracy of the z co-ordinate. Further work in the article evaluated the advantage of using the two colour to image a single cell with varying refractive indices by simultaneously imaging the cell body and flagellum of the parasitic species *Leishmania mexicana*.

3.3.5 Discussion

This work demonstrates that using two colours of illumination in the holographic set-up can decrease the uncertainty in an objects vertical position. This is particularly useful when imaging object's with an inhomogeneous refractive index. Later in this thesis, the
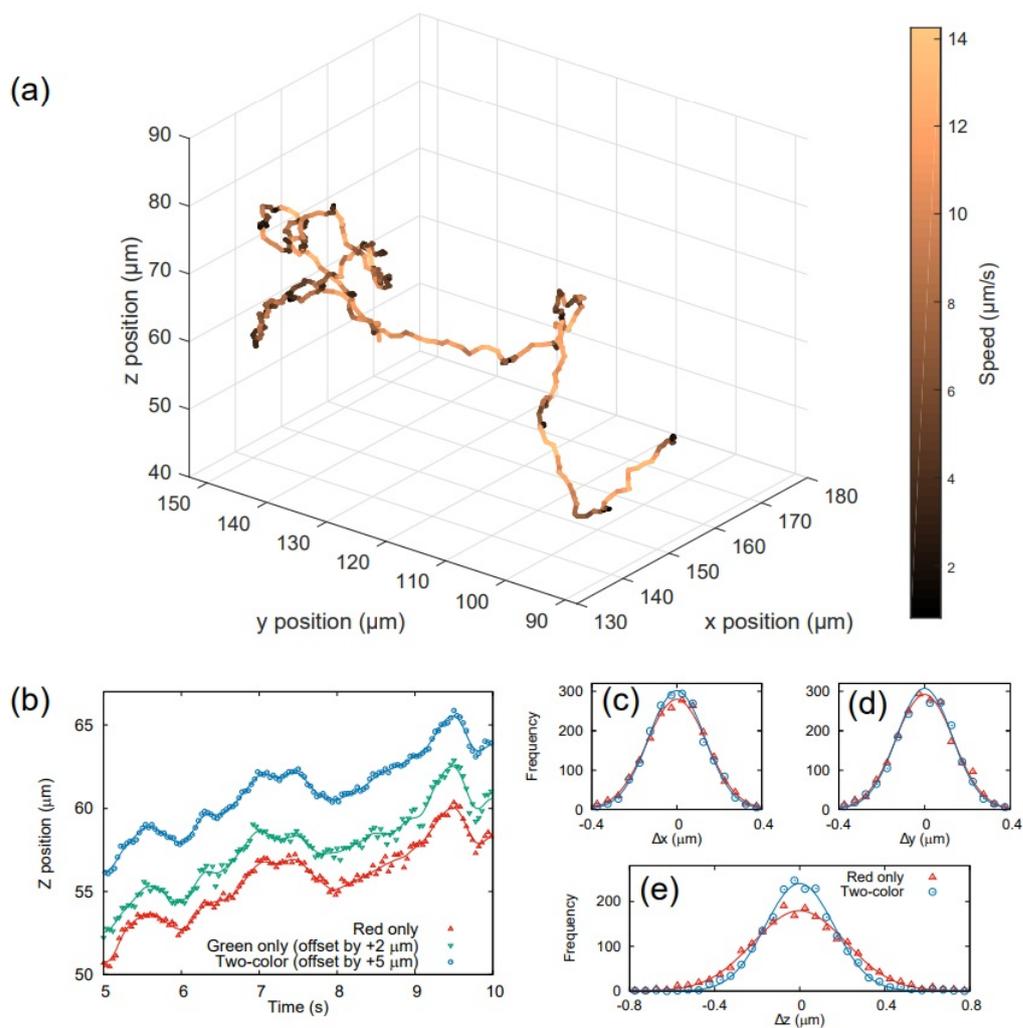
FIGURE 3.6. a) is a 3D plot of a swimming bacterial track from the mix of polystyrene beads and *E. coli* cells found using the two-colour holographic configuration. The track is colour coded according to speed. b)shows the raw track z co-ordinates (markers) along with the smoothed z co-ordinates for 5s of the track plotted in 3.6a. The results for the track obtained using the red only submovie, the green only submovie and the two colour data is shown. The green and two-colour data are offset vertically for clarity. c-e) show histograms of the residuals when the spline smoothed data is removed from the red and two-colour track data. Figure taken directly from [**?**].

motion of tracer beads near stuck cells is investigated using holographic microscopy and, since this is a mix of objects, the two colour system was considered. However, as only the motion of the beads is of interest and the cells are very dilute, it was decided that the experiment was effectively concerned only with beads and therefore a sample with a homogeneous refractive index. It was therefore decided that the benefits of the two colour system were outweighed by the added complexity of the image processing and so the regular holographic arrangement was used.

3.4   Chapter conclusions

In this chapter, holographic microscopy was used to investigate the effect of viscosity and flagellin arrangement on the swimming of *S. putrefacians*. Here it was determined that the more rigid FlaA flagellin helps to stabilise the flagellum and allows the cell to remain motile and effectively perform chemotaxis in various environments.

Finally, a two-colour holographic set-up was used to effectively image a sample containing *E. coli* cells and polystyrene beads with different refractive indices. Here analysis of tracks showed that using the two-colour configuration significantly reduces the uncertainty in the z-position of an object when a mixture of refractive indices is within the sample.

4

FIELD AROUND INDIVIDUAL CELLS ON A SURFACE

"Confidence is what you have before you understand the problem."

Woody Allen

4.1 Introduction

Conventional wisdom in the literature of biofilm formation, states that cell motility is down-regulated in biofilms [37] . However, there are observations of motile-surface attached bacteria so there is some length of time for which bacteria are on the surface but still moving their flagella.

Cells are thought to sense the surface before committing to irreversible attachment [37, 165] and the working theory currently is a form of mechanosensing, in that the increased load on the flagellum near the surface triggers a signalling pathway that leads to further attachment [166]. In *P. aeruginosa*, this signalling pathway is yet to be identified but signalling systems for mechanosensing in other bacterial species have been identified [167–169]. In chapter 2, analysis of 3D swimming PA01 cells showed that cells exposed to a lactam analogue swim slower and increase the rate of flagellar reversals. The literature suggested that this effect could be due to the lactam interrupting the cAMP signalling pathway [170]. In this chapter, surface-attached bacteria with moving

flagella are investigated. A novel use of holographic microscopy is shown to image the flow around surface-attached cells with a moving flagellum, whilst florescence microscopy is used to image the flagella themselves. The aim is to identify whether the lactam impacts the motility of cells that are body-attached to a surface with a free flagellum.

4.2 How can cells be surface attached and produce a field?

4.2.1 How do cells attach to a surface?

In chapter one, the multiple methods of bacterial surface-attachment were discussed. Cells are known to attach via their flagella and via their cell body, sometimes using appendages called pili. It is also well documented that in biofilm-forming cells, these surface-attachment events are either reversible (leading to the cell eventually leaving the surface) or irreversible (the precursor to biofilm formation). There has been some investigation into the motility of surface-attached cells but this has tended to focus on cells for which the cell body itself moves [171, 172]. This is for the obvious reason that, with standard bright field microscopy, the flagella are not visible and so a cell with a stationary cell body appears immobile. In this chapter, tracer beads are used to investigate surface-attached cells with active flagella but a stationary cell body. The aim is to understand the implication of this phenomenon on the formation of biofilms. This first investigation focuses on the method of the cells' surface-attachment. The aim is to determine whether a significant proportion of cells maintain a motile flagellum while the cell body is stationary. Is there a time-dependence to the method of surface-attachment? Does the lactam analogue alter the method of cells' surface-attachment?

4.2.2 Data collection

4.2.2.1 Sample preparation

Three exponential cultures of PA01 were grown from three different saturated cultures on two separate days, following the standard protocols (see chapter 1). Six different samples were made, two each from the three different exponential cultures to control for biological variability. Samples 1 and 2 were from the first exponential culture, 3 and 4 from the second and 5 and 6 from the third. Samples 1,3, and 5 were made by diluting 100μl of exponential culture into 1ml of MB. 10μl of 0.13μm bead stock was

added and the sample shaken gently to mix. These samples were used to investigate a time dependence on the surface attached motility of cells. Sample 2, 4 and 6 were similarly made but with 0.37ml of MB replaced by the same amount of 1500μM lactam stock solution (so that the sample is 20% lactam stock solution). These samples were used to investigate the effect of the lactam analogue on the motility of surface attached cells. The samples were imaged in the extra thin chamber slides for increased likelihood of surface attachment. All samples were imaged as soon as they were put in the chamber slides.

4.2.2.2   Imaging set-up

Samples were imaged using the standard bright field set up with a 60x oil immersion lens. The 60x is the smallest magnification (therefore biggest area and so most cells) for which the beads were easily visible. The microscope was focused approximately $10\mu m$ below the coverslip. This meant that the cell body was visible along with beads slightly above the boundary. Starting immediately after sample loading, a 1000 frame video was recorded at 100fps at one minute intervals. In total, 30 videos were recorded per sample. The area of interest (AOI) was set to 1024 by 1024 px which was the maximum for this set-up. Recording was stopped after 30 minutes because the sealed chambers meant oxygen was limited and so after this time the cells appeared less motile. Videos were saved uncompressed and analysed in ImageJ.

4.2.3   Data analysis

For each of the videos, the first step in the analysis process was to identify all surface-attached cells present in the first frame of the video. This was simply done by eye since it is easy to distinguish between cells and beads on the surface by eye. Next the number of flagella-attached motile cells were counted. These were easy to identify because the cell body is seen to spin (see figure 4.1). Only spinning cells present for the whole length of the video were recorded in this count but the number of cells that were spinning and detach, or attach and began spinning were recorded separately.
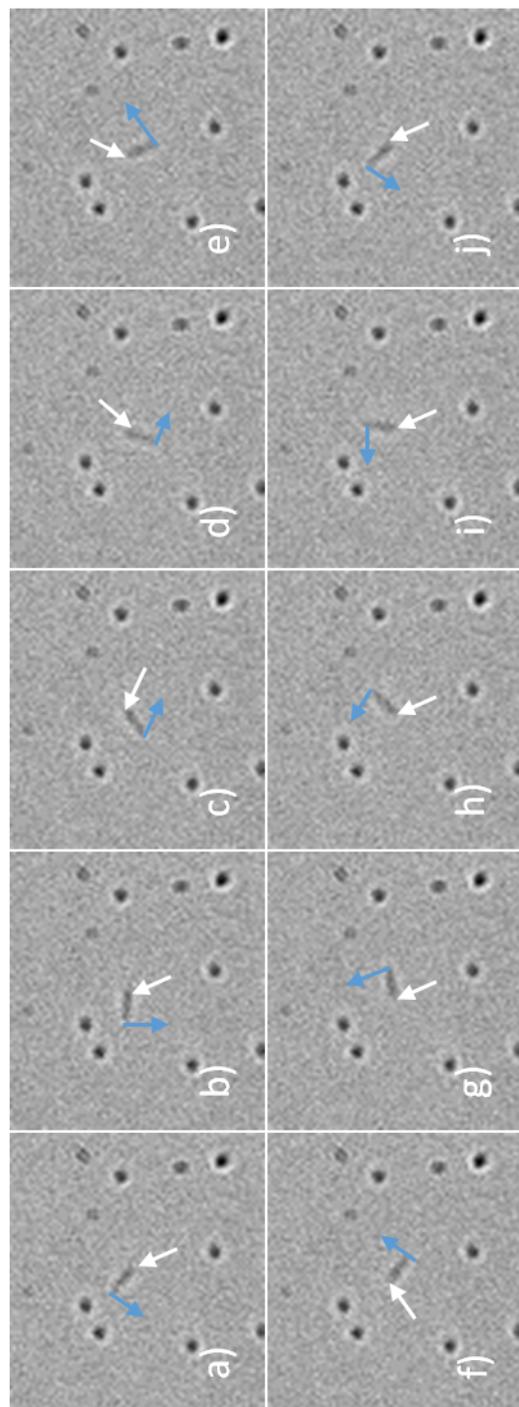
FIGURE 4.1.

Images a) - j) are progressive frames of a video of a motile, surface-attached cell that was classified as flagella-attached because the cell body spins. The frames are taken at 0.05s intervals. The white arrows show the tether point of the cell - ie. the end that the flagellum is attached. The blue arrows show the tangential direction of rotation for each frame.

Motile, body-attached cells were more difficult to identify. Since the flagella were invisible in this imaging, motility could only be determined by watching the cell advect a tracer bead. This is seen as evidence of the cell pumping the fluid around it using its motile flagellum. This pumping is easy to distinguish from Brownian motion of the bead because it is a much faster motion and more directed (see figure 4.2). However, in some cases, no bead came near to the stuck cell in the time of the recording. In this case, the cell was recorded as non-motile so it is possible that the number of body-attached cells is under-reported. Cells that remained attached (did not start to spin) throughout the whole video were recorded as motile and body-attached if they were seen to advect a bead at any point of the recording. Any cells seen to transition between spinning and pumping or vice versa were not included in this count but were recorded separately.
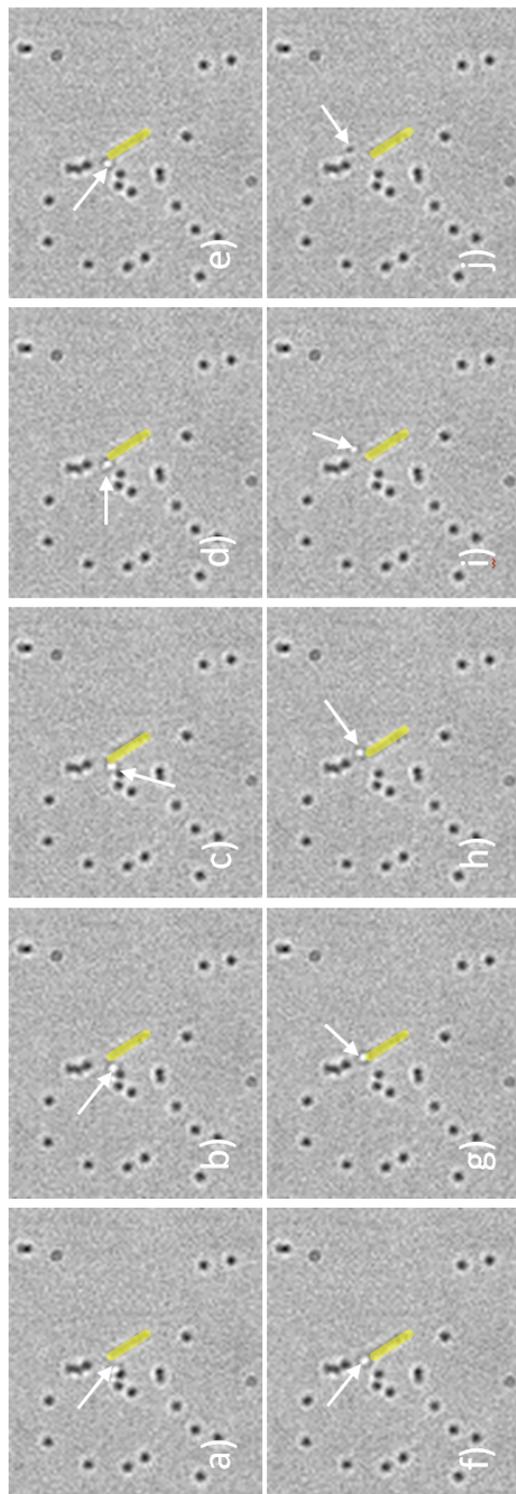
FIGURE 4.2.

Images a) - j) are progressive frames of a video of a surface-attached cell with a moving flagellum that was classified as body-attached, because the cell is fixed but a bead is pumped by the cell. The frames are taken at 0.01s intervals. The cell body is highlighted in yellow to show it remains fixed. The white arrows indicate the bead being pumped. The field of the cell is overcoming the random Brownian motion.

4.2.4 Results

4.2.4.1 Time-dependent motility of surface-attached cells

For each time and each sample, the proportion of motile cells identified as pumping (or body-attached) was recorded. The average across the four samples is plotted in figure 4.3. Error bars indicate the standard error across the samples. This is found by dividing the standard deviation by the square root of the number of samples.

Figure 4.3 shows a steady proportion of these body-attached cells initially, with the proportion dropping after approximately 23 minutes. It should be remembered that, since the chambers are small and sealed, there was limited oxygen and nutrients in the chamber. These results may, therefore suggest that cells are less likely to be body-attached and motile as the environment becomes harsher. Since the sample-to-sample variation is large within this data, perhaps a more useful analysis is the overall proportion of body-attached motile cells. The mean proportion of motile cells identified as pumping (body-attached) is $60 \pm 12\%$. Therefore, despite the high variation between samples, a significant proportion of motile, surface-attached cells are attached via their body with a free flagellum. These cells are often over-looked in other studies of surface motility because the flagellum is invisible using standard bright-field microscopy.

4.2.4.2 Effect of lactam analogue on surface attached motility state

Samples 2, 4 and 6 were used to investigate whether the lactam analogue alters the motility states of surface-attached cells. Here, only the time average states are investigated. For the non-lactam samples, $60 \pm 12\%$ of motile, surface-attached cells were observed to be body attached, while the samples containing the lactam analogue, had $62 \pm 7\%$. Again, the standard error is used here to give the variation of the mean. The striking similarity of these values suggests that the lactam analogue has no effect on the motility state of surface attached cells.

4.2.4.3 Transition between motility states

It is also interesting to investigate whether flagella-attached cells can transition into body-attached and vice versa. It was fairly uncommon to observe a transition event and across all the control samples, 30 transitions between the spinning/pumping states were observed. Of these, 57% were cells that were initially spinning and began pumping and
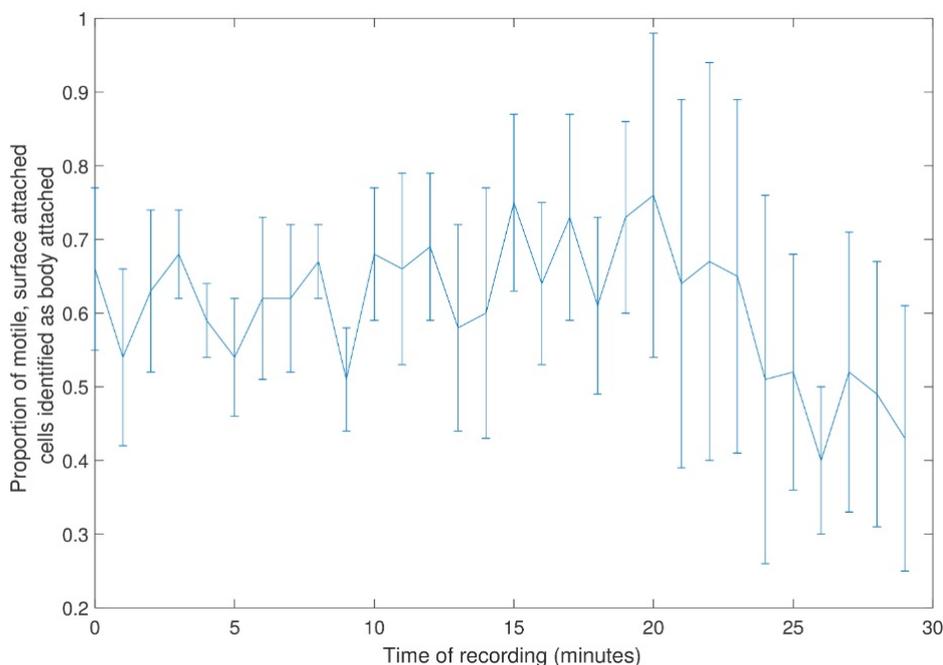
FIGURE 4.3.
The time dependent proportion of surface-attached motile cells identified as pumping (ie. body-attached). Data is the average proportion of pumping cell across all three samples and the standard error is shown using error bars.

43% were in the opposite direction. Within the lactam sample, the respective percentages were 48% and 52% from 24 transitions. These transition events were not common enough to build up reliable data on whether the lactam analogue alters the rate/direction of transitions. However, since all the samples showed a similar number of transitions in each direction, this suggests that neither spinning nor pumping are intrinsically the irreversibly-attached stage of biofilm formation described in the literature.

4.2.4.4 Motility of cells detaching

A more informative test of whether the modes of surface-attached motility are reversible or irreversible is to investigate detachment events. To collect statistics on detaching events, all motility states are included but only cells that were seen to detach in the recording were included. This means that the statistics under-estimate the number of events because cells that detached between videos were not counted. Cells that detach between recordings are not included because it is not possible to determine which motility state they were in directly before detachment. Across all times and all six samples, 38

detaching events were identified. Of these 38 events, 100% were cells that were in the spinning (flagella-attached) motility state before detaching from the surface.

4.2.4.5   Motility of cells attaching

The detachment data hints towards a link between the motility state and likelihood of detachment. Using the same videos, it is also possible to investigate whether the motility state is linked to attachment. Just as in in the detachment investigation, the motility of cells that were observed to attach were counted. Any cells that attached between recordings were not included since it is impossible to determine what motility state the cells exhibited directly upon attaching to the surface. Across all times and all six samples, 42 attachment events were identified with all cells attaching and showing spinning motility when they became attached.

Considering this, along with the detachment data, it suggests that flagella-attachment is the method that most cells first attach the surface but it is also the motility state in which they are most likely to detach. Perhaps cells primarily attach to the surface via the flagellum then they can either detach or transition into body attached. Then perhaps, once body-attached they either transition back to flagella-attached or remain body-attached and eventually become irreversibly attached by some mechanism such as pili. This could suggest that body-attachment is a transition stage between the reversible and irreversible stages of attachment. If this is the case and body-attachment is a later stage, it means it is the more relevant stage for biofilm formation investigations.

4.2.5   Discussion

Although this data begins to hint at some interesting results, it should be remembered that these cells were imaged in MB. The justification for this choice of media is that any fluorescence imaging must be in MB and so it allowed for comparison of results. However, the results may be seen as less biologically relevant since cells are unlikely to 'want' to remain in a nutrient poor area, and are therefore less likely to act as they would during the early stages of biofilm formation. Chen *et al* determined that, as expected, PA01 biofilms grew better in nutrient rich environments [173] and therefore, an extension of this investigation would be to determine if cell motility in more nutrient-rich media is the same as here. Another consideration is that, by investigating just the proportion of visibly motile cells, any effect of cell density is ignored. Finally, only samples of only a single type of bacteria were investigated. This means that, although the results may give

an idea of of motility states during surface-attachment transitions, a more detailed study would be needed to make solid conclusions as to whether the results seen are generic to all bacterial species.

The above is not an exhaustive study and is not without its limitations. However, for the purpose of this study, it is enough that this experiment means it is possible to conclude that a substantial proportion of cells remain motile while their cell body is entirely fixed to the surface. This state of surface-attached motility has been under-investigated in the literature. The attachment/detachment data above suggests that flagella-attachment is more reversible and that the cells must become body-attached to transition into their irreversibly attached state. This is justification for the investigation into the flow induced by these body-attached cells in the context of biofilm formation.

4.3   3D field around single stuck cell

4.3.1   Motivation

Biofilms form at interfaces, be they surface-fluid or fluid-fluid. In this work, the focus is on biofilms forming at surface-fluid interfaces. Sometimes called semi-infinite environments, the biofilm grows on a surface extending out into the bulk fluid. Therefore, in order to make any conclusions on how bacterial motility might impact biofilm formation, the full 3D flow induced by a surface-attached cell must be determined.

One method of determining a 3D image is by using a bright field microscopy and taking a series of 'z-slices' at various heights through the sample and combining these into a 3D image [174], [175]. However, there is some time delay in imaging the stacks in this way so a dynamic field may not be captured. Flagellar reversals and the phenomenon of polymorphic transitions [176] suggest that any flow due to a surface attached bacterium is not steady. Therefore, this method of imaging may not be the correct choice for capturing the field in this case.

Instead, holographic microscopy is used to image the whole 3D field around a stuck bacterium instantaneously. The shape, magnitude and time-dependence of this field is investigated. The field around stuck cells in both control and lactam analogue samples was imaged to determine whether the lactam alters the field and subsequently, whether this might explain the observed decrease in biofilm formation in the presence of the

lactam analogue.

4.3.2 Data collection

4.3.2.1 Sample preparation

Data was collected over three days using three exponential cultures of PA01 grown from three saturated cultures. For each day, both a control sample and a sample with lactam analogue were prepared. The control was 100μl of exponential culture diluted into 1ml of MB with 10μl of 0.13μm bead stock solution added and the sample shaken gently to mix. The lactam analogue samples were made by replacing 0.37μl of MB with the same amount of lactam analogue stock solution. All samples were imaged in a thin chamber to increase probability of cell attachment and limit noise from beads in the bulk. The chambers were sealed with nail varnish to prevent evaporative drift so the samples were imaged immediately (while there was no risk of oxygen deprivation). As discussed previously, cells were seen to de-energise after approximately 30 minutes in the sealed chambers.

4.3.2.2 Imaging set-up

The standard holographic set-up was used to image the cells. A $60\times$ lens was used to ensure the beads were visible and a red LED was used as the light source. The LED was chosen over the laser since its shorter coherence length meant that a smaller depth of chamber was imaged. This meant that beads far from the cell, and not expected to be affected by the cell's motility, were not imaged. They could not, therefore, contribute to the uncertainty at the reconstruction stage associated with multiple beads with the same $x - y$ position at different heights. Once a motile, body-attached cell was identified, the focal plane was set approximately 5μm below the sample chamber and the AOI was set at 512×512px with the cell approximately central. 2000 frames of video were recorded at 100fps and the recordings were saved uncompressed in .avi format.

4.3.3 Data analysis

4.3.3.1 Data preprocessing

Before, processing this data, each recording was opened in ImageJ to collect some extra data used in the averaging stages later. Once the cell had been confirmed by eye to be motile (a bead had been clearly seen to be advected by the cell), the $x - y$ positions in

pixels of the center of the cell was determined by eye. Using this, the displacement of the cell from the centre of the AOI was determined in pixels. This was then converted to microns using the known magnification value.

For the averaging process, it is also important to ensure that all the cells are orientated the same way. *P. aeruginosa* cells have a single polar flagellum and the orientation of the cell was specified as the angle between the horizontal and the flagellum tether, taken in the clockwise direction (see figure 4.5). The location of the flagellum cannot be definitively determined from the holographic data, in which the flagellum is not visible. However, it was observed by eye that the flow of the beads switched between two different directions over time. Termed 'modes', the first of these saw beads being 'pushed' away from the cell while the second appear to show bead being 'pulled' across the cell body (see figure 4.4). It is postulated that these two flows are due to the flagellum rotating in different directions and changing its position relative to the cell body. For the sake of averaging, the pole of the cell away from which the beads are 'pushed' in mode 1 was assumed to be the flagellum end and the orientation of the cell is determined accordingly.

Aside from the time-averaged field, it is also interesting to analyse the field of the two modes separately. In order to do this, the recordings were analysed by eye and the frames for which the cells were in each of the modes was noted.
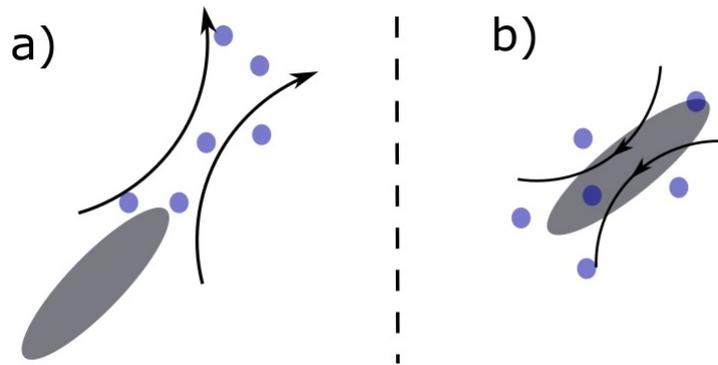
FIGURE 4.4.
a) and b) are two schematics showing the position and direction of the clearest bead flow in modes 1 and 2 respectively. These are thought to correspond to forward and reverse flagella directions.

4.3.3.2 Extracting 3D data

The method used to extract the 3D data from the recordings was the same as in the previous sections where swimming cell trajectories was extracted. In this case, beads were tracked for a minimum of 10 frames (cells in Chapter 2 were tracked for a minimum of 100 frames). The extracted tracks were stored in a file containing information on the corresponding cell's position and orientation.

4.3.3.3 Averaging process

For each of the stuck cells, the time averaged field and the averaged field for each mode was found using the same custom MATLAB code. For each track, the track data is read in as a 7 column array of varying length. The first column is the time (in seconds) with columns $2-4$ and $5-7$ giving the x, y, z positions of the raw and smoothed track respectively. The central difference velocity in each of the three directions is taken by dividing the difference of two subsequent values in columns $5-7$ by the time-step between them. For the purposes of averaging, it is assumed that the instantaneous velocity at the mid-point between two subsequent points in columns $5-7$ is the average velocity of the bead between the points.

All of the tracks associated with each cell are stored in a folder containing the position of the cell and its orientation. These values are read into MATLAB and stored as X_d, Y_d for the displacement of the cell from the centre of the AOI and Θ for the orientation of the cell. The x positions of the mid-point array are shifted to centre over the centre of the AOI by subtracting the sum of X_d and half the width of the AOI in microns. The y positions are similarly shifted using Y_d and the half length of the AOI. The x, y components of the mid-point array and velocities are then rotated by $-\Theta$ using the matrix

$$
\begin{bmatrix}
\cos(-\Theta) & -\sin(-\Theta) \\
\sin(-\Theta) & \cos(-\Theta).
\end{bmatrix}
\tag{4.1}
$$

This transformation places the cell at the origin (center of the AOI) with the flagellar pole of the cell toward the positive x direction (see fig 4.5).
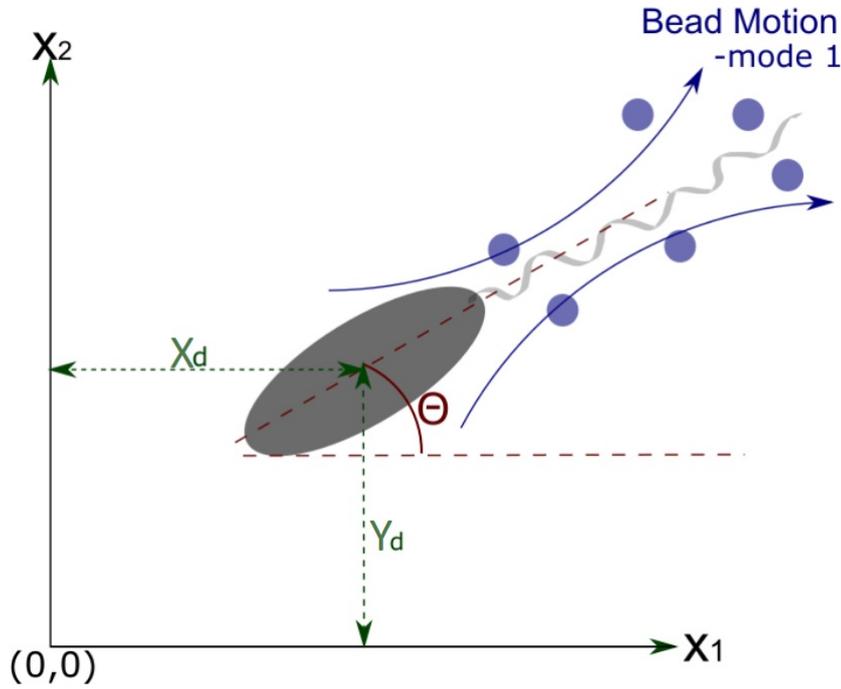
FIGURE 4.5.
The orientation of the cell is determined as the angle between the horizontal and the pole of the cell that beads are pushed away from the cell rather than over it.

To determine the average field, a 3D grid of 'nodes' around the origin is specified. These nodes are simply point in the field at which the flow is evaluated. Motivated by the work in [23] the field is set $20\mu m$ in each direction around the cell. Eight nodes are equally spaced between 0 to $20\mu m$ along the z-axis and fourteen nodes are equally spaced between -20 to $20\mu m$ along the x and y-axes. For each time-point (i) for each track node, a normal distribution (ND(i)) value is calculated such that

$$\text{ND}(i) = e^{\frac{(-((X_{node}-X_{track}(i))^2+(Y_{node}-Y_{track}(i))^2+(Z_{node}-Z_{track}(i))^2))}{2\sigma^2}}, \quad (4.2)$$

where $X_{node}, Y_{node}, Z_{node}$ are the arrays x, y, z giving the positions of the nodes, $X_{track}(i)$, $Y_{track}(i)$, $Z_{track}(i)$ are the shifted x, y, z positions of the ith time-step in the track and $\sigma = 5\mu m$. The σ value is the standard deviation of the normal distribution and, as such, controls how close a bead trajectory must be to a node to contribute to the field. The value of $5\mu m$ for σ was chosen since the field of a cell close to a surface for a swimming cell was found to spread approximately $10\mu m$ from the cell [23]. The normal distribution gives a normal 'weighting' of each time-point of each track on each node depending on the

distance of the track from the node. This value gives an idea of 'certainty' with which the field velocity at each field is known. If the field at a node is determined by many beads passing close to the node, the 'certainty' will be greater than if the field is determined only using bead trajectories far from the node. The sum of all ND(i) for each point of each track is recorded as an array (TND). This indicates the 'certainty' that the velocity at each node is known after all tracks have been processed. The average field around the cell is found by summing up the ith velocities multiplied by the corresponding ND(i) and dividing by TND. The average field of all cells is found by summing up all the individual fields. Modal fields were found using the same code but only summing the contributions from tracks in the appropriate mode.

When investigating the field, only the data at nodes for which the 'certainty' was sufficiently high were used. Therefore, a level of 'credibility' of the velocity values was specified. Two ways of defining the credibility were tested, the Classical credibility (C_C) [177] and the Bühlmann credibility (C_B) [178], where

$$C_C = \sqrt{\frac{TND}{K_1}}, \qquad C_B = \frac{TND}{TND + K}. \tag{4.3}$$

Here, K_1 and K are fit parameters to be determined. For the case of the initial investigation K_1 and K are both set to = 10. The choice of K/K_1 is evaluated later in this section. The Bühlmann credibility asymptotically approaches its maximum of 1.00 while the Classical credibility is filtered such that any value > 1 is set to 1. Only nodes that have a TND sufficiently high that the credibility is = 1 (to 3 s.f) are used in the final analysis of the field. Figure 4.6 shows plots of the two credibility functions. From this figure, it is clear that the TND of a node must be much larger to reach a credibility value of 1 for C_B than C_C. Figure 4.7 shows the two types of credibility for all nodes in the control time-averaged field plotted against the magnitude of velocity determined at each node. Many of the larger velocities correspond to credibilities lower than the threshold, suggesting that the credibility may drastically alter the shape of the field. Inset in figure 4.7 is the difference between the Classical and Bühlmann credibilities at each node. Although there is little difference in the values, the classical credibility is greater than that of the Bülhmann for many of the smaller velocities. Since these smaller velocities are what we expect to be true, to err on the side of caution, the Bühlmann credibility is used from here on to filter the field. Any nodes with a $C_B < 1$ are given a velocity value of NaN.
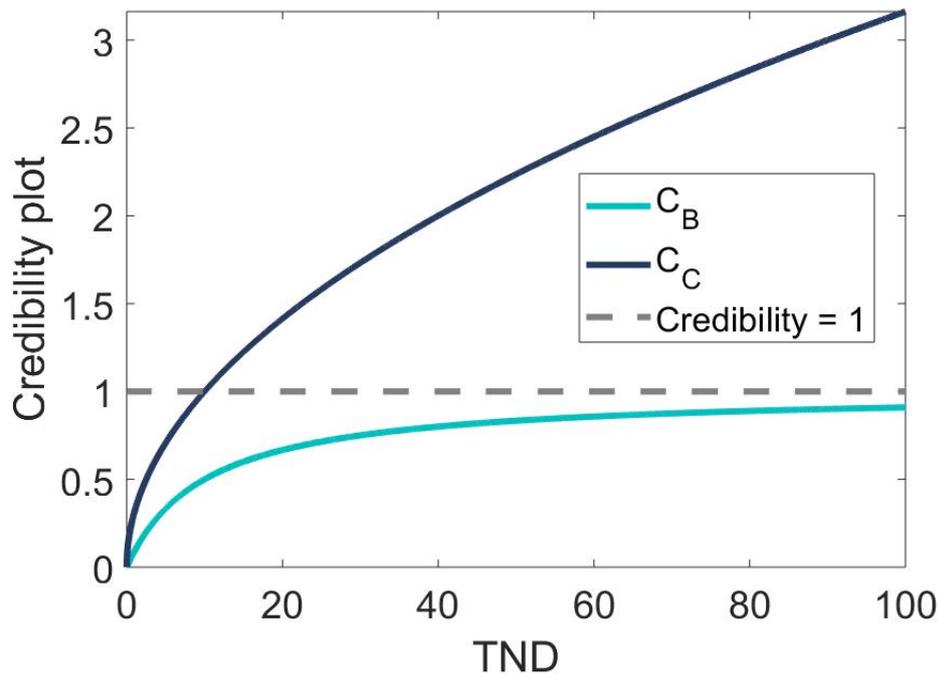
FIGURE 4.6.

The two functions investigated to determine credibility of node data is plotted. Shown is a plot of the Bühlmann credibility function (C_B), Classical credibility function (C_C) and, for reference, the line of credibility = 1 (which is the minimum credibility value of a node used in the following work).
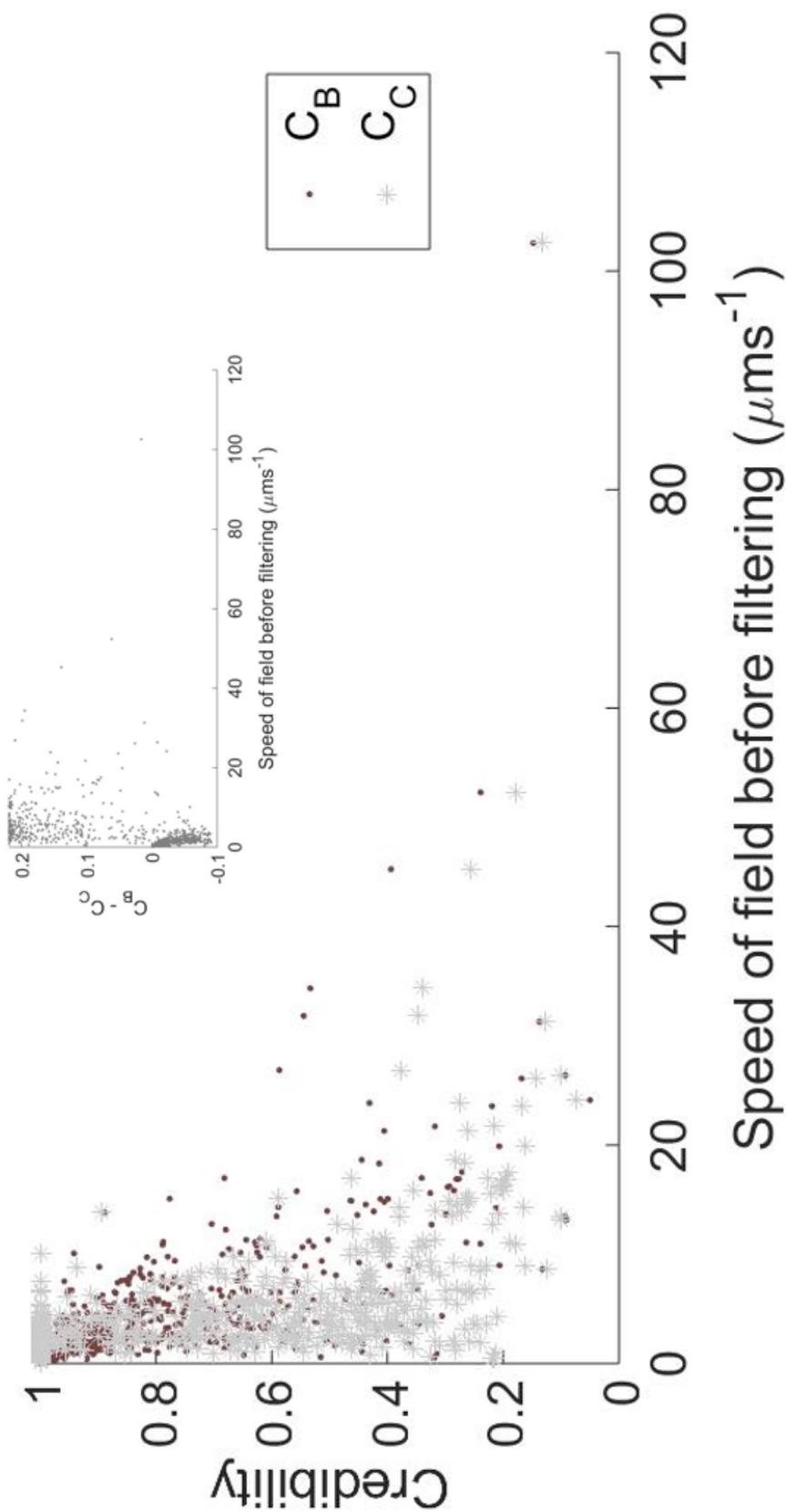
FIGURE 4.7.
The Classical and Bühlmann credibilities determined for each node in the time-averaged control sample field plotted against the speed determined at that node. Inset is the difference between the two types of credibility.

4.3.3.4 Splitting into modes

Once the tracks were obtained, a custom MATLAB code was used to split the tracks into the two different modes. This code takes in the data of which mode the cell was in for each frame and puts the track data into two sub-folders according to the time data in the track.

4.3.4 Results

4.3.4.1 Total time averaged field

To determine the appropriate K value to use in the Bülhmann credibility, the effect on the field of changing K is investigated. Figure 4.8 shows a slice through the plane $y = 0$ of the time-averaged field around all cells in the lactam. For these plots, the original data are the same but only nodes with a Bülhmann credibility is 1 (to 3 s.f) for the various K values are shown. Since the field does not appear to change much from $K = 10$ onward, this $K = 10$ value is chosen as the value from here on.

What is interesting in figure 4.8 is that when $K > 0$ there are few nodes above $z = 15\mu$m for which there is credible data. To check that this is not an artifact of the smoothing process, the bead tracks around a single control cell are plotted in figure 4.9. From this, it is clear that there are more beads near the surface with most being in the $z = 0 - 10\mu$m region. It is unclear whether this phenomenon is due to the beads sedimenting (i.e. they are not neutrally buoyant as assumed), some kind of surface attractant behaviour or as a result of the cell induced flow. Whatever the reason, it explains the lack of credible data for the nodes with a larger z co-ordinate. Some cells have more bead trajectories high in the sample than others but this highlights the need to define a credibility criterion. The cells are made of polystyrene with a density of 1.055 g/cm^3 which suggests they should take over an hour to sediment to the base of the chamber - a much longer time than the imaging timescale. Given this, the low number of beads high in the chamber is likely due to electrostatic potential across the glass of the chamber, a phenomenon commonly observed according to the bead manufacture's website [179].

Figure 4.10 shows a side on view of a selection of tracks around the same single control cell as in figure 4.9. This will be used later to compare to simulated bead trajectories. Also shown in figure 4.10 is the time averaged field determined using only the bead trajectories of the same single cell. The size of the arrows in the flow indicate
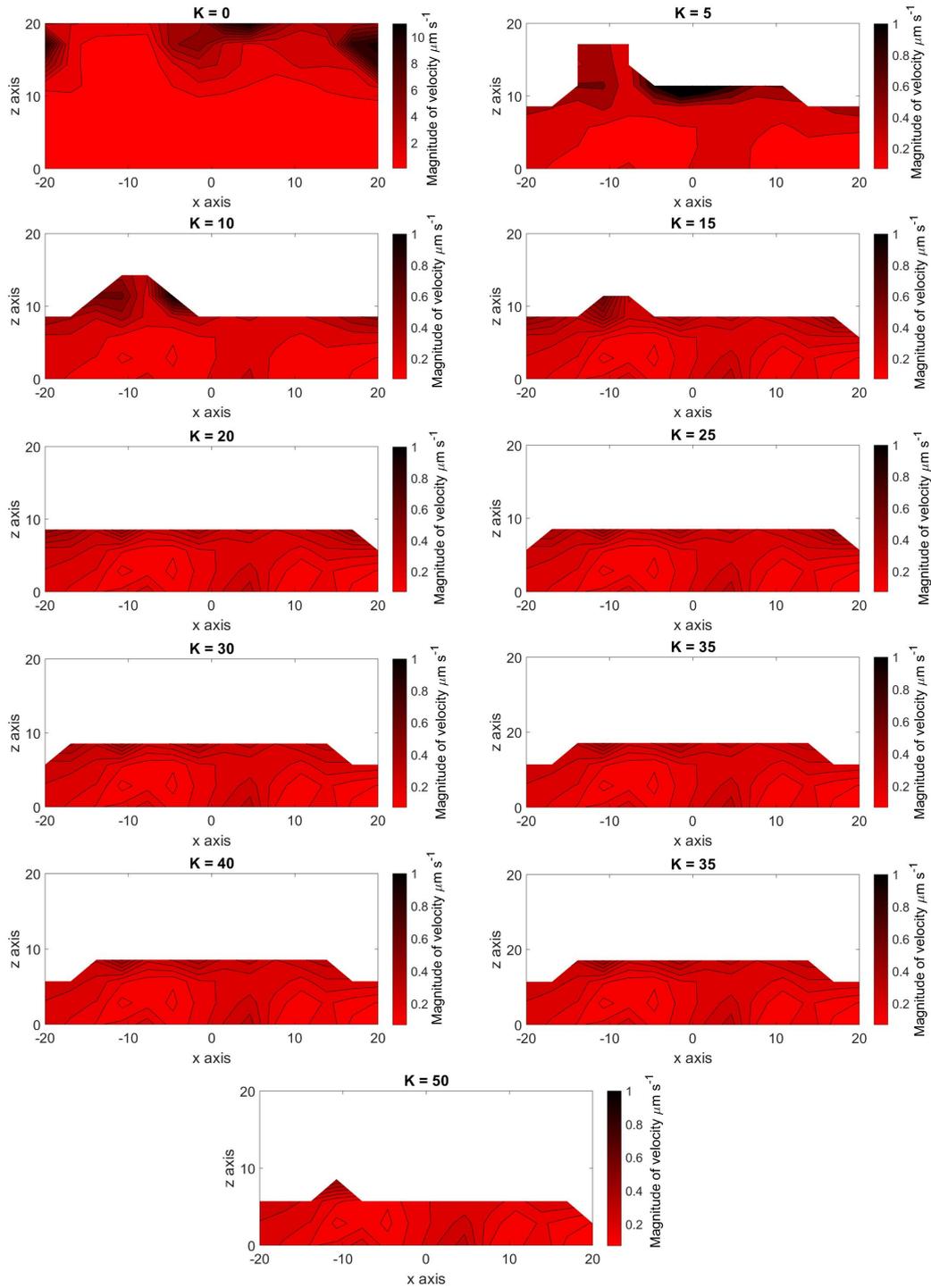
FIGURE 4.8.
A slice through the $x - z$ plane where $y = 0$ of the time averaged field around 20 cells in the control sample, for various values of K in the Bülhmann credibility. Only nodes where the credibility equal to 1 (to 3 s.f) are plotted.
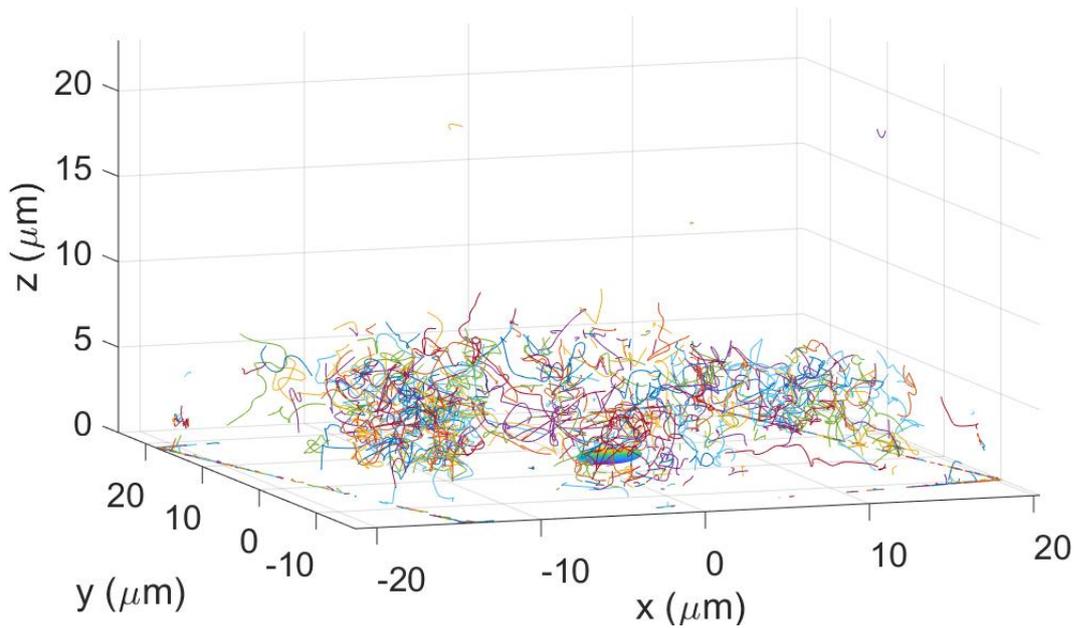
FIGURE 4.9.
The 894 tracks extracted from the recording of a single control cell. Very few tracks are seen above 10μm above the surface. The bead lines on the plane $z = 0$ can be associated with noise on the boundary of AOI and are removed before processing.

the magnitude of the field whilst the colour shows the difference in the summed ND at each node with the maximum summed ND. This means the colour gives an indication of confidence of the flow field with black being the most confident and white least. As expected, nodes high above the surface are known with the least confidence since few bead trajectories are in this region.

To determine the average field around 20 cells, the re-orientated tracks around all the cells are averaged. Figure 4.11 shows the averaged flow fields determined for the control and lactam cells. The two fields are qualitatively different with the control showing a much clearer flow than the lactam.

Another clear difference between the two fields is the size of the flow with the control cells producing a flow approximately twice the magnitude of the lactam cells (see figure 4.12). The mean and standard deviation for the control and lactam samples are
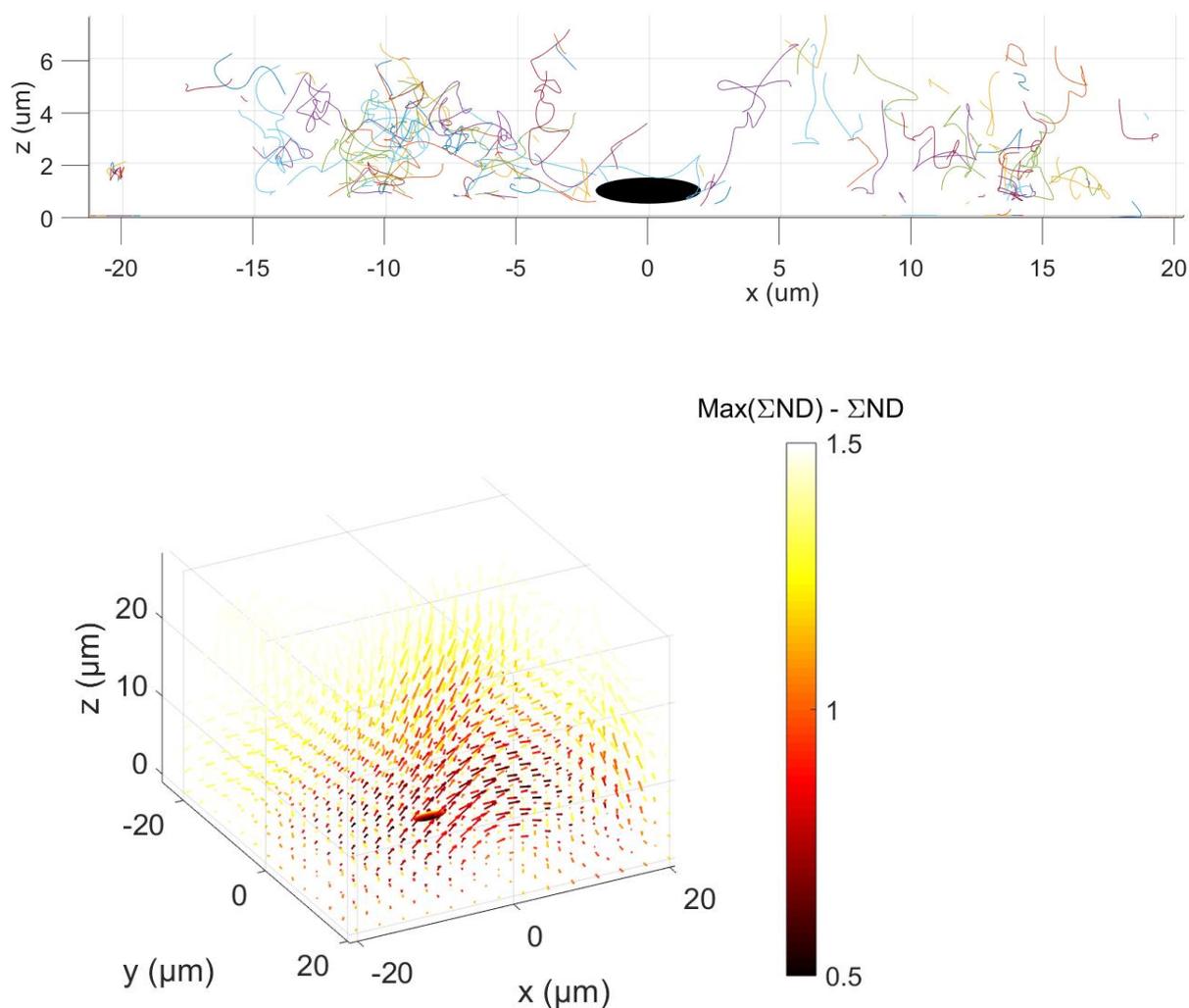
FIGURE 4.10.
On the top A selection of re-orientated tracks around a single cell with the flagellum postulated to be on the 'positive x' pole of the cell (from raw data observation), the cell body is shown (not to scale) for illustration. Below: Field determined using the tracks from the same cell. The colour-bar indicates the difference between the maximum summed ND at any node and the summed ND at each node.

$0.70 \pm 0.01 \mu m s^{-1}$ and $0.29 \pm 0.01 \mu m s^{-1}$ respectively. A two-tailed t-test for these values gives a P-value < 0.0001. Therefore, the drop in velocity seen at the nodes in the lactam field is extremely statistically significant. This indicates that the lactam analogue does alter the motility of surface-attached cells, which could, in turn, suggest that this motility impacts biofilm formation.
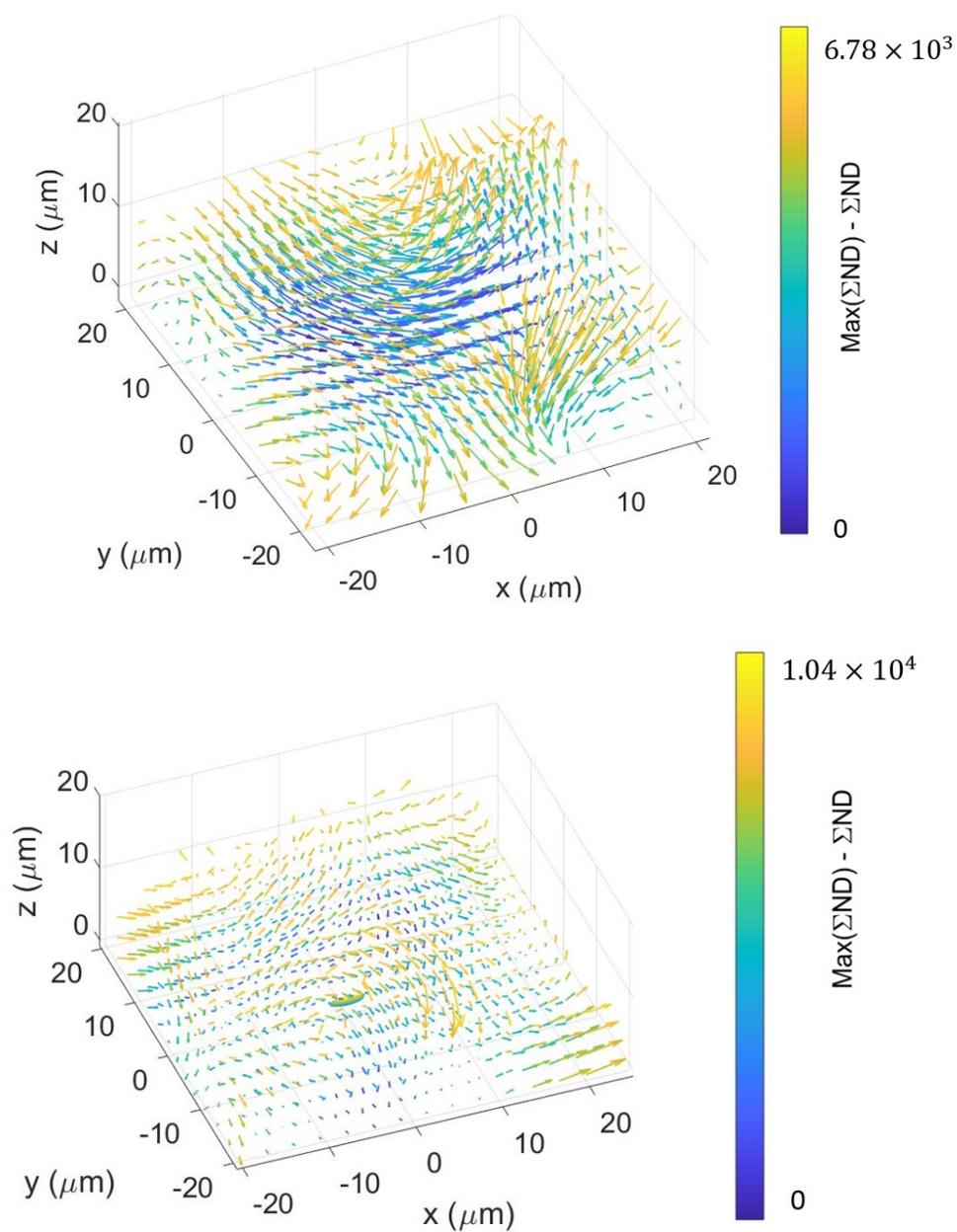
FIGURE 4.11.
From top to bottom: the time averaged flow fields determined for the control and lactam samples respectively. The fields are determined using all bead tracks around the 20 cells in each sample.
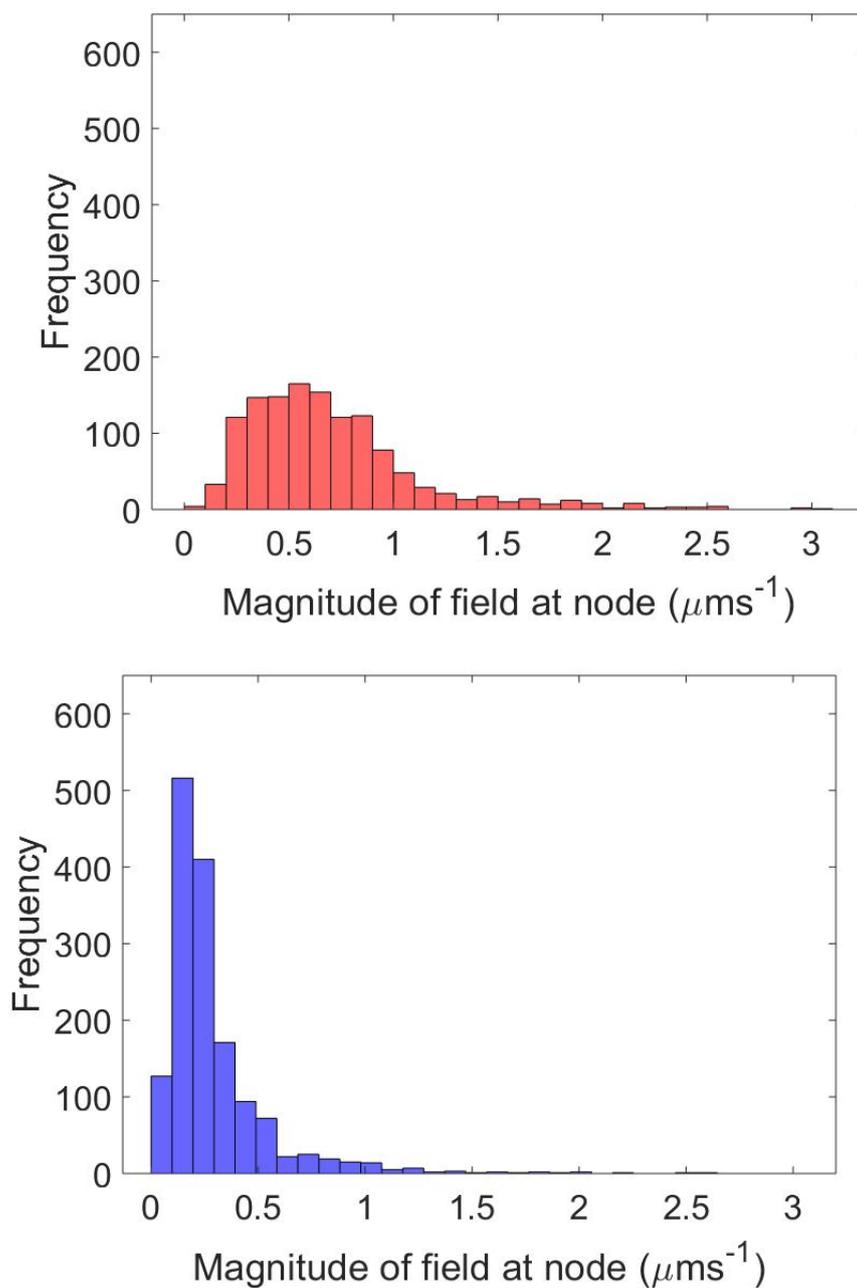
FIGURE 4.12.
From top to bottom: histograms of the magnitude of the flow at node points in the control and lactam time-averaged fields respectively. Only velocities at nodes where the credibility was equals one are used. The mean and standard deviation for the control and lactam samples are $0.70 \pm 0.01 \mu m s^{-1}$ and $0.29 \pm 0.01 \mu m s^{-1}$ respectively. A two-tailed t-test for these values gives a P-value < 0.0001. Therefore, the drop in velocity seen at the nodes in the lactam field is extremely statistically significant.

Although the time-averaged flow fields above indicate an impact of the lactam analogue on motility, the dynamic nature of the flagellum means that time-averaging may not capture the field effectively. As previously noted, two distinct modes of flow were identified which, when averaged together may provide an unclear picture. In the next section, the averaged field of the modal flow is investigated.

4.3.4.2 Modal averaged flow

As previously noted, the bead motion in the raw data was observed to be split into two distinct modes. It is hypothesised that these model align to direction of flagellar reversal. In this section only the bead trajectories determined as being in a particular mode were used to determine the field. Figure 4.13 shows the field determined by averaging all the bead trajectories, around all 20 cells, that were identified as being due to a flagellum in mode 1. In this figure, planes are shown from which cross-sections of the flow were taken and plotted. These cross-sections may be seen in figure 4.14. Here, the size and direction of the arrows are the magnitude and direction of the projection of the vector field at each node onto the plane while the colour shows the magnitude of the field at the node. Where possible, in this thesis, data from mode 1 is shown in green and mode 2 in purple.
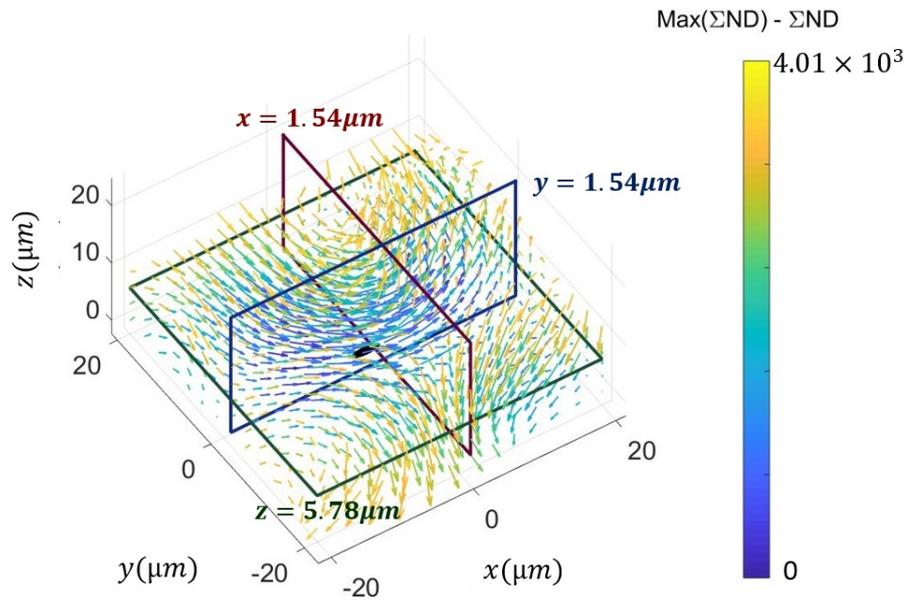
FIGURE 4.13.

The average mode 1 field around the control cells. The planes for which cross sections are taken are indicated. The colour-bar indicates the difference between the sum of the ND values at each node and the maximum of the ND summed.

FIGURE 4.14.
   The cross-sections for the average mode 1 field around the control cells
   projected onto the planes. The planes for which cross sections are taken
   correspond to those in figure 4.13. The $y-z$ plane is taken at $x = 1.54\mu$m,
   the $x-z$ plane at $y = 1.54\mu$m and the $x-y$ plane at $z = 5.78\mu$m.

From figures 4.13 and 4.14 it can be seen that, as expected, the strongest region of
flow is set slightly behind the cell body (ie. in the positive x−direction). There is also a

significant upwards flow away from the surface. The magnitude of the field seen here is lower than expected since some beads were determined by eye to be traveling at approximately $50\mu\mathrm{ms}^{-1}$. The colour scheme chosen here is a combination of green and red to correspond with control cells in mode 1. Similarly, the colour schemes for control cells in mode to are generally purple and red, those in lactam and mode 1/2 are blue and green/purple respectively.

Figure 4.15 shows the magnitude of the field along the lines where two of the planes in figure 4.10 intersect. The error bars show the standard error around the mean value. These values are found by calculating the field for each of the cells individually and determining the standard error at each node. There is a relatively high variance between the different cells, which explains why the size of the field in figure 4.14 is lower than expected.
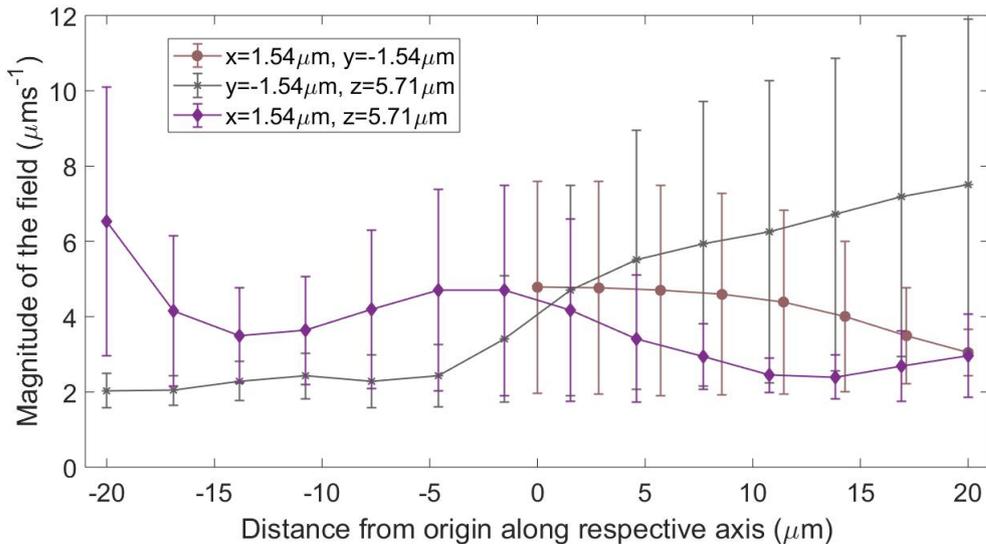
FIGURE 4.15.
The magnitude of the average mode 1 field around the control cells taken on lines through the cell. The error bars give the standard error found by taking the square root of the variance of the magnitude at each node divided by the number of cells contributing data to the node. Cells only contributed to the field at a node if the credibility equals one.

Figures 4.16 and 4.17 show the field and cross-sections in the field, determined from

bead trajectories when the flagella were identified as being in mode 2, respectively. In this case, the constant x and constant y planes chosen were different to those chosen for the mode 1 flows. This is because the planes were chosen to capture the areas of greatest flow, which were different in the two cases. However, the constant z plane is the same for both the mode 1 and mode 2 flows and it is in this cross-section that the difference in the two modal flows in clear. The field projected onto the z-plane in this case is far less clear and directional than in the mode 1 case.

The x and y planes show clear qualitative differences to the mode 1 flow also. Whereas in the mode 1 field the flow had a clear upwards motion away from the surface, the mode 2 field seems to reverse so the flow is towards the surface. This aligns well with the theory that the flagellum has reversed for the two modes and the necessary change in plane choice supports the idea that the flagellum is in a different place.

It should also be noted that the magnitude of the mode 2 field is smaller than that of the mode 1 flow. This suggests that there is greater variation between the flows averaged. This could be between the cells but it could also suggest that the mode 2 flagellum position is less stable than that of mode 1 and so the field varies between cells.
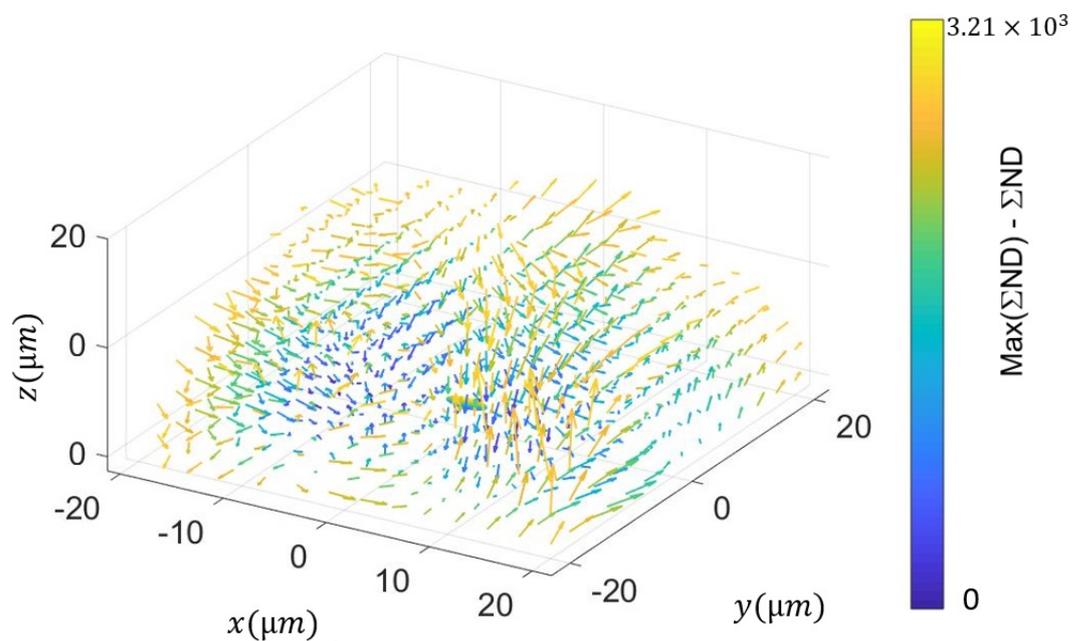
FIGURE 4.16.
    The average mode 2 field around the control cells. The colour-bar indicates
    the difference between the sum of the ND values at each node and the
    maximum of the ND summed.
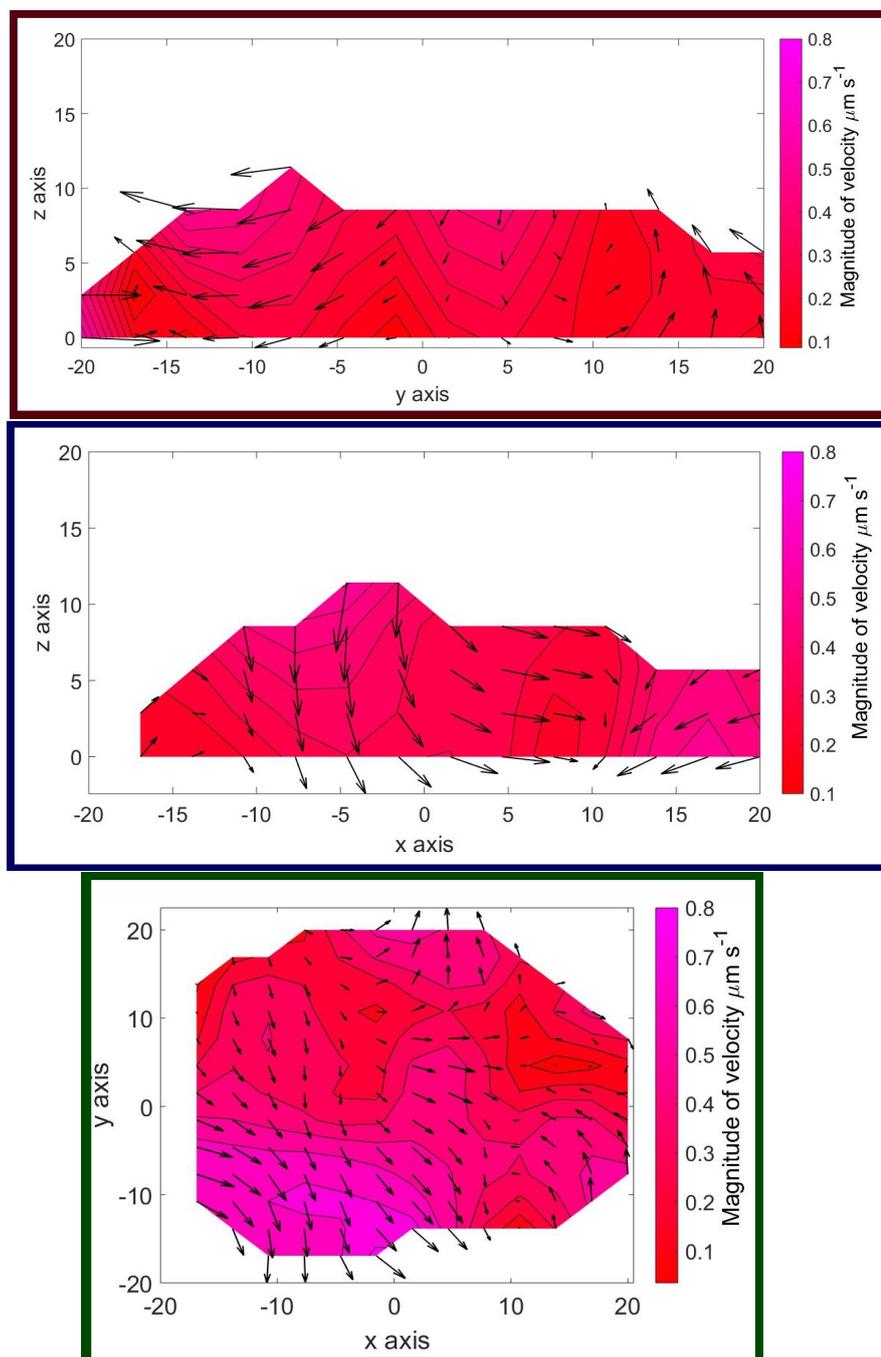
FIGURE 4.17.
The cross-sections for the average mode 2 field around the control cells. The cross-sections are taken at $x = 7.68\mu$m, $y = 7.68\mu$m and $z = 5.78\mu$m.

Figures 4.18 and 4.19 show the cross-sectional projections of the field due to cells in the lactam analogue in mode 1 and mode 2 respectively. The same planes were used as

in the control sample so that a direct comparison may be made. The similarities between the modal fields for the control and lactam samples are striking. Considering the high variation between cells seen in figure 4.15, the averaged fields for the two groups share many common characteristics.

4.4   Flagellar reversal rates of cells on a surface

4.4.1   Motivation

It is known that bacteria vary the reversal rate of their flagellar motor in response to environmental stimulus [180]. In this section, the flagellar reversal rates of surface attached cells are investigated. Here, the reversal rates of cells exposed to the lactam analogue are compared to those in a control media to determine whether the lactam alters the reversal rate of stuck cells.

4.4.2   Data collection

4.4.2.1   Sample preparation

The data for this investigation was a 'by-product' of the pre-processing stage for obtaining the 3D field around a stuck cell. In that section, the mode that the cell was displaying for each frame was recorded, and from this, how often reversal events occurred or the time each cell spent displaying each mode may be determined.

4.4.3   Results

Figure 4.20 displays data on number of reversal events observed per 20s recording in lactam analogue and control samples. The mean number of reversals is 1.65 ± 0.28 and 0.55 ± 0.17 in the lactam and control samples respectively. The error recorded is the standard error, obtained by dividing the standard deviation in values by the square root of the number of values. Even in the relatively small sample size of 20 cells per sample, there does appear to be a difference in the number of reversals in the presence of the lactam analogue. The control sample has fewer reversals per recording and the deviation of the values from the mean value is smaller. This suggests that the lactam analogue may increase the reversal rate of the flagellar motor.
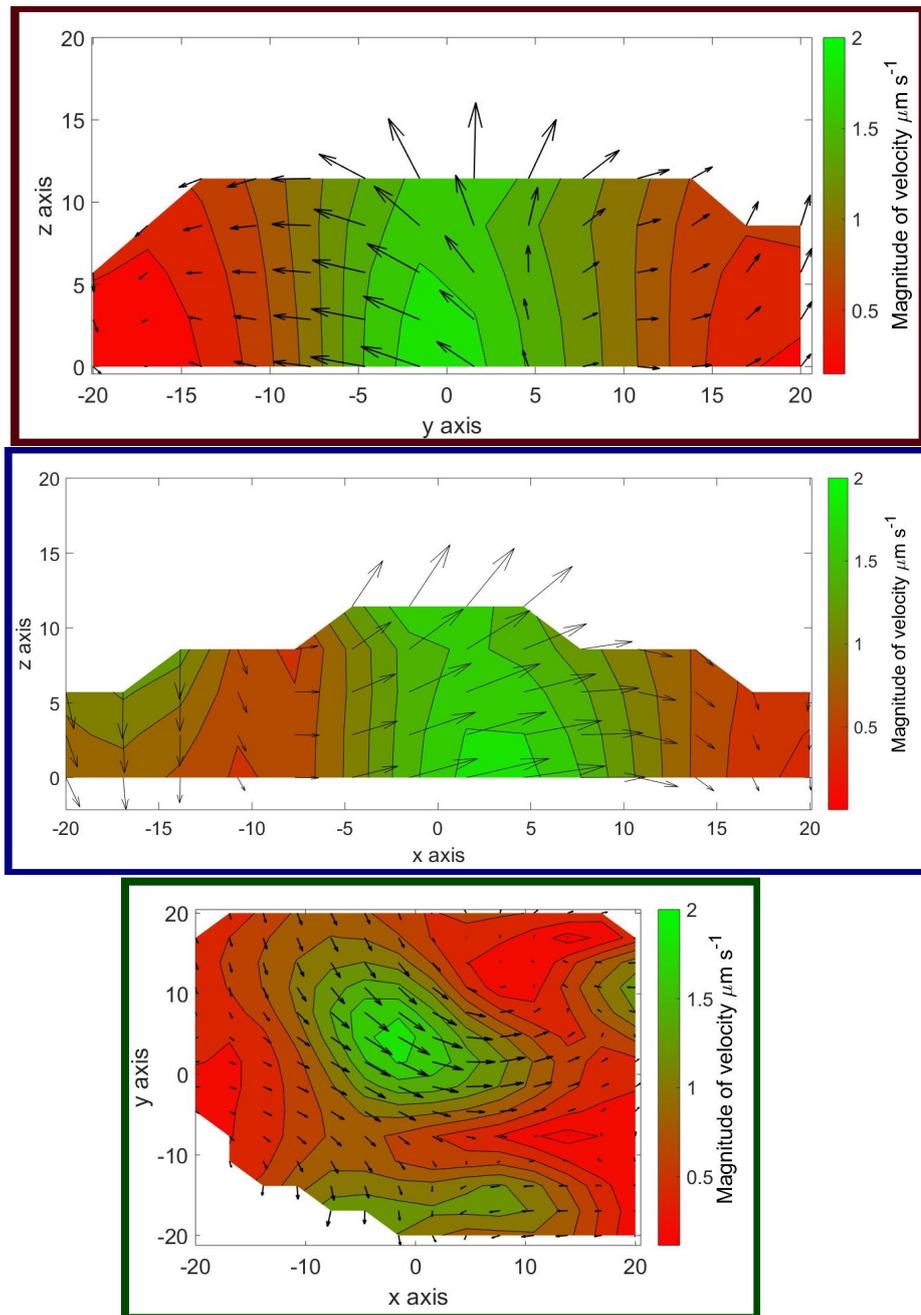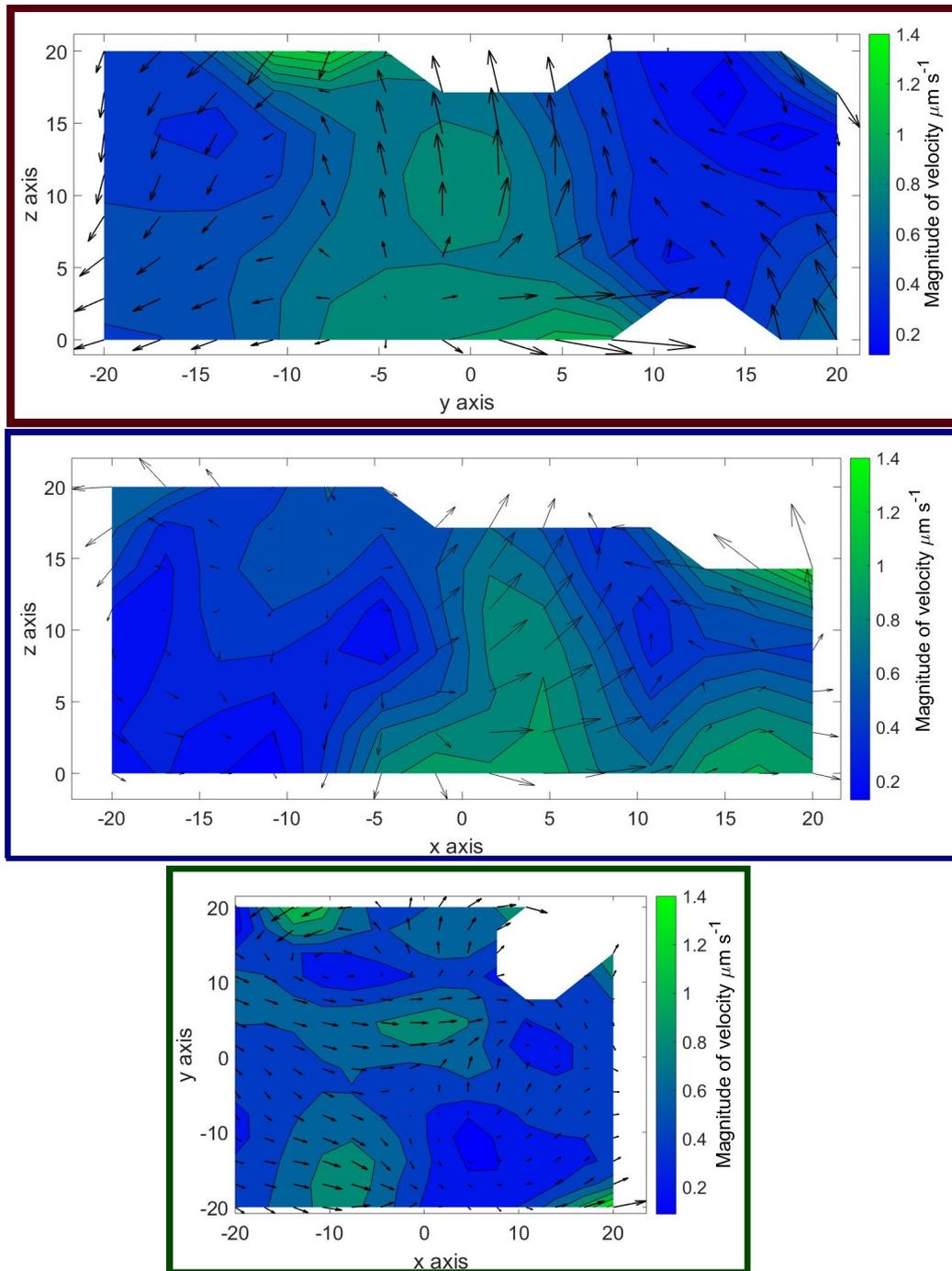
FIGURE 4.18.

The cross-sections for the average mode 1 field around the lactam cells. The planes for which cross sections are taken correspond to those in figure 4.13. The $y-z$ plane is taken at $x = 1.54\mu$m, the $x-z$ plane at $y = 1.54\mu$m and the $x-y$ plane at $z = 5.78\mu$m.
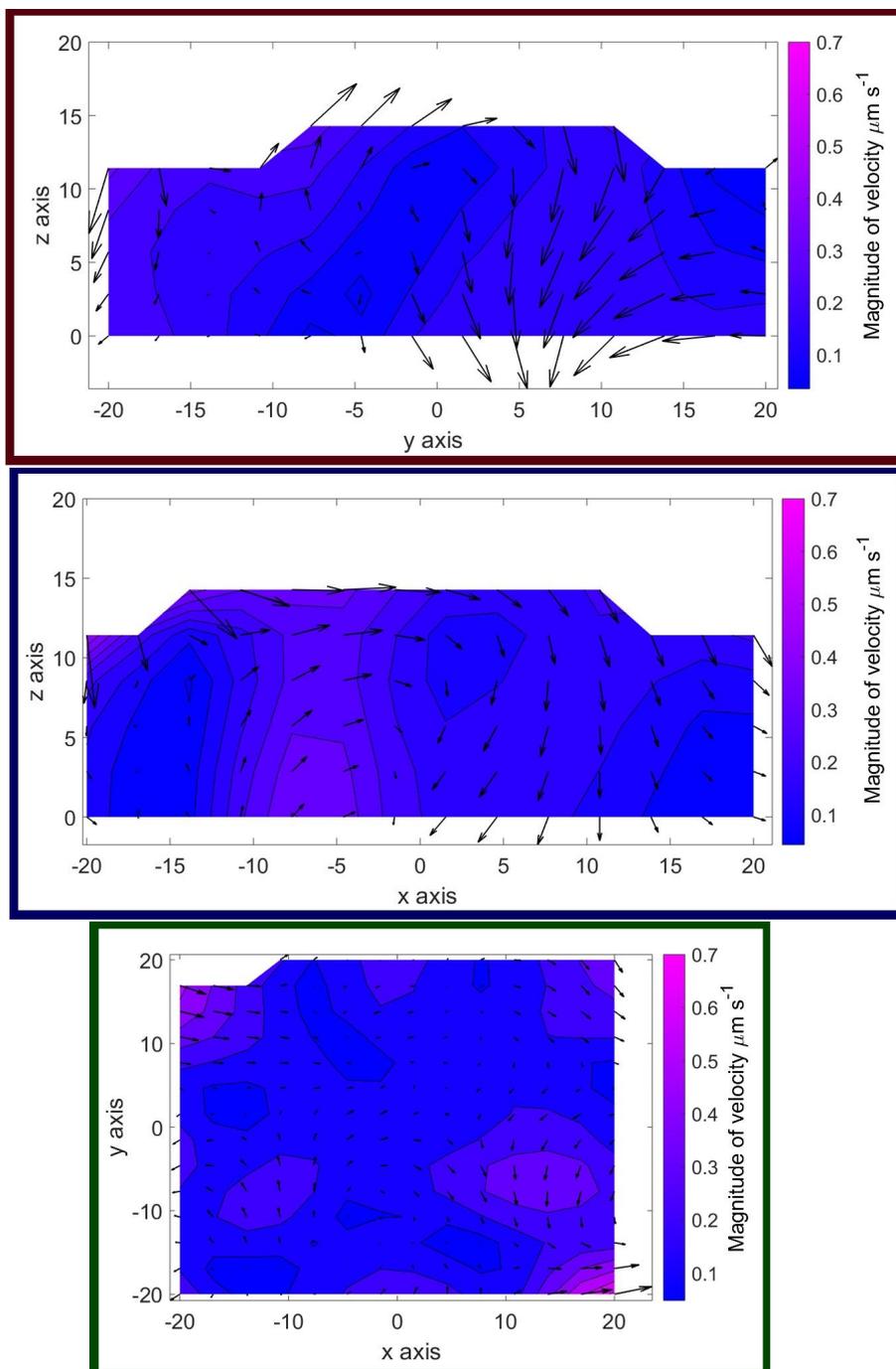
FIGURE 4.19.
    The cross-sections for the average mode 2 field around the lactam cells. The
    cross-sections are taken at $x = 7.68\mu$m, $y = 7.68\mu$m and $z = 5.78\mu$m.
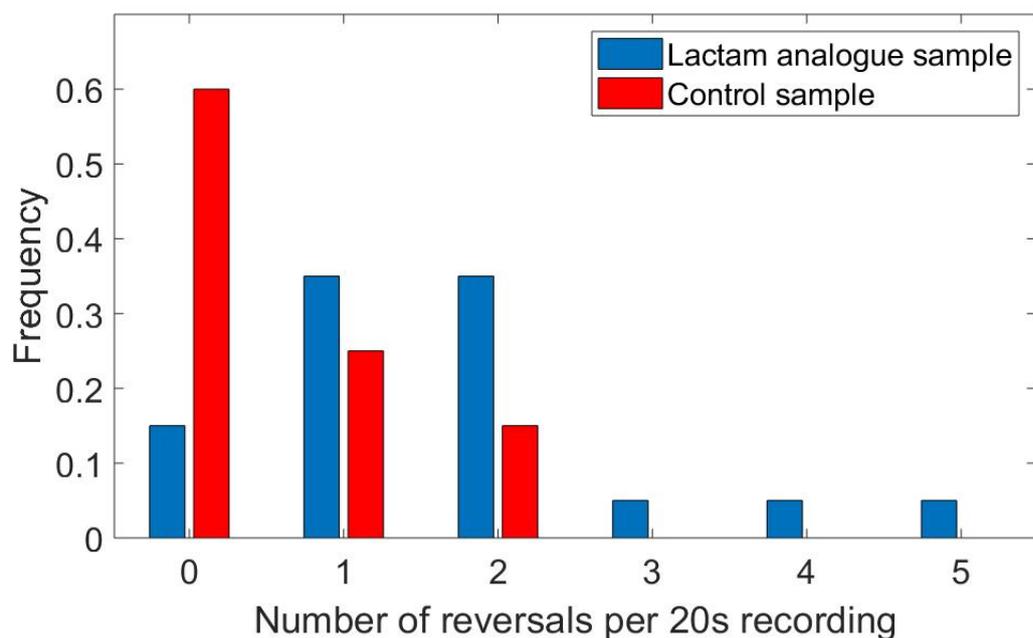
FIGURE 4.20.

The number of times cells were observed to switch between 'mode 1' and 'mode 2' per 20s recording in the lactam analogue/ control samples. These reversal events were seen more frequently in the lactam analogue sample with a greater spread of values also observed in this sample.

Since figure 4.20 suggests that the lactam impacts the number of reversals, it is interesting to investigate whether it also has an effect on the time that the cells spend in the two different modes. Figure 4.21 shows the average time spent in each mode by the two samples. When averaged over the 20 cells for each sample, it appears that the cells in the lactam analogue spend an approximately equal time in each of the two modes while the control set spend more time in mode 1 than in mode 2. This is in contrast to previous observations that *P. aeruginosa* spend an equal amount of time with their flagella in the forward or reverse modes when free-swimming [181]. Coupled with the data from figure 4.20, this suggests that the lactam analogue does impact flagellar motion.
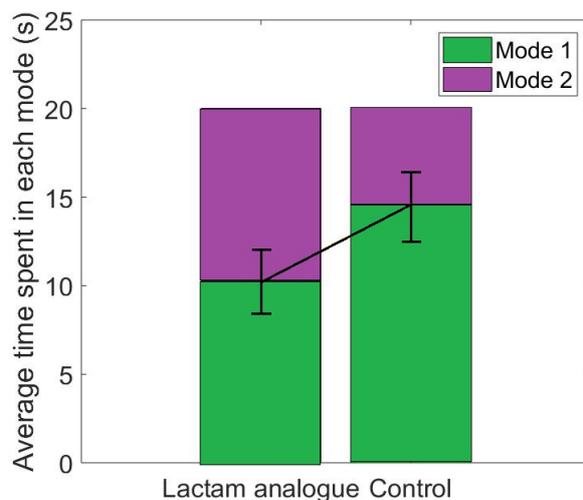
FIGURE 4.21.
The average time in each 20s recording that the cells in either the lactam analogue or control sample spend in 'mode 1' and 'mode 2'.

As it appears that the cells in the lactam analogue spend more time in mode 2 than those in the control sample, it is interesting to investigate the time between reversals in the two different modes. Figure 4.22 shows the normalised frequency of the time between two reversal events. The data shown is only for the cells in lactam since there were an insufficient number of recordings in the control sample with two or more reversal events to collect data. Shown are the data for the two modes separated and the total of the two modes.

The average time spent in mode 1 before reversing is 2.5 ± 0.9 s. This type of event occurred 7 times in the 20 videos of cells and the error is again the standard error. The average time spent in mode 2 before reversing is 4.0 ± 1.1 s based on 9 events. The average of all 16 events is 3.5 ± 0.7 s. In the control sample, this type of event (in either mode) only occurred a total of 3 times giving an average of 9.1 ± 3.5 s between reversals. Although the control sample set is small, this does show that there is a greater time between reversals in the control, which aligns with the data from figure 4.20.

The lactam analogue sample spend longer in mode 2 before reversing than when in mode 1, which is an interesting observation since the control sample spend the majority of time in mode 1.
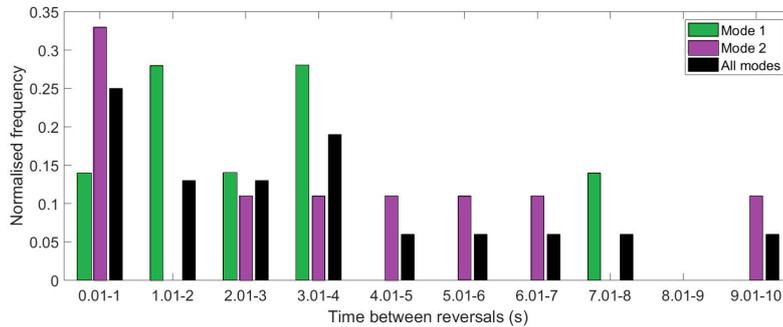
FIGURE 4.22.

The normalized frequency of different times between two reversal events in mode 1 (green), mode 2 (pink) and both modes totaled (black), for cells in the lactam analogue sample.

4.4.4 Discussion

Taking into account the above data, there seems to be a trend of increased reversal events for the cells in the lactam analogue. This corresponds to an alteration in the time spent in each mode for the cells in the lactam. Taken as a whole, this data suggests that the flagellar dynamics of the cells in the lactam analogue are more variable. What is particularly interesting is that the phenomenon seen here may explain the difference between the control and lactam 3D fields obtained in section 4.3. The time-averaged fields of the control and lactam cells were qualitatively different despite the modal fields displaying similarities. The data in this section suggests that the time-averaged fields are different because the lactam and control cells spend different proportions of time in the two modes.

4.5 Imaging flagella

4.5.1 Motivation

For the previous experiments in this chapter, two modes of flow were identified due to a cell attached to a surface via its cell body with a moving flagellum. It has been suggested that these modes are due to the flagellum reversing its direction of rotation and therefore changing its orientation in relation to the cell body. In this section, a preliminary investigation into the flagellar dynamics of cells in the control sample is

undertaken using fluorescence microscopy to directly image the flagellum. The aim is to better understand the flagellar dynamics that result in the two observed modes.

4.5.2 Data Collection

In order to view the flagella of surface-attached cells, cells of PA14 were grown and stained following the standard protocol in chapter 1. Cells were diluted $1:100$ with MB and viewed in a sealed, thin chamber slide. Cells were fluorescently imaged using the set-up detailed in chapter 1. The mercury lamp and $60\times$ magnification were used. Videos of 2000 frames were recorded at 100 fps and saved as uncompressed .avi files.

4.5.3 Results

It was clear from the raw data that the flagellar arrangement of surface attached cells is a lot more complex than previously assumed. Various flagellar dynamics were observed in a single sample of cells. The clearly motile flagella could be broadly separated into two categories: bi-modal and spinning. A preliminary investigation of these two groups is presented below.

4.5.3.1 Bi-modal flagella motion

Cells were categorized as 'bi-modal' if their flagella were seen to transition between two orientations relative to the tether point. This tether point was assumed to be at the end of the flagellum that was seen to maintain a constant position. The bi-modal flagellar motion aligns with the two modes of flow observed in the previous section. However, not all of the cells categorized as bi-modal displayed the same behaviour. One subset of the bi-modal cells had a flagellar helix that maintained an (approximately) constant length whilst in the two modes (see figure 4.23 a-b). For these cells the flagellum alternated between two orientations depending on helical rotation direction. This meant that the flagellum switched between being fixed at two different angles, but the helical length did not visibly change. Since the orientation of the cell body is not known, the relative orientation of the flagellum in these two modes can not be calculated. An attempt was made to image the same cells using bright field after recording the flagellar motion to determine cell body orientation but a significant proportion of the cells did not remain attached to the surface so this was unsuccessful. Instead, the angle between the two flagellar positions is determined using ImageJ. For three cells displaying this motion, an

average of $55 \pm 14°$ difference between the two flagellar orientations has been found.

A second subset of the bi-modal cells still had two distinct flagellar arrangements but the helical length varied between the two (see figure 4.23 c-d). Again the angle between the two flagellar positions for tree cells was determined using ImageJ. The average angle between the two modes was $121 \pm 22°$. Although very preliminary, the difference in the two subsets may help explain the unexpectedly small magnitude of field determined in the early section.
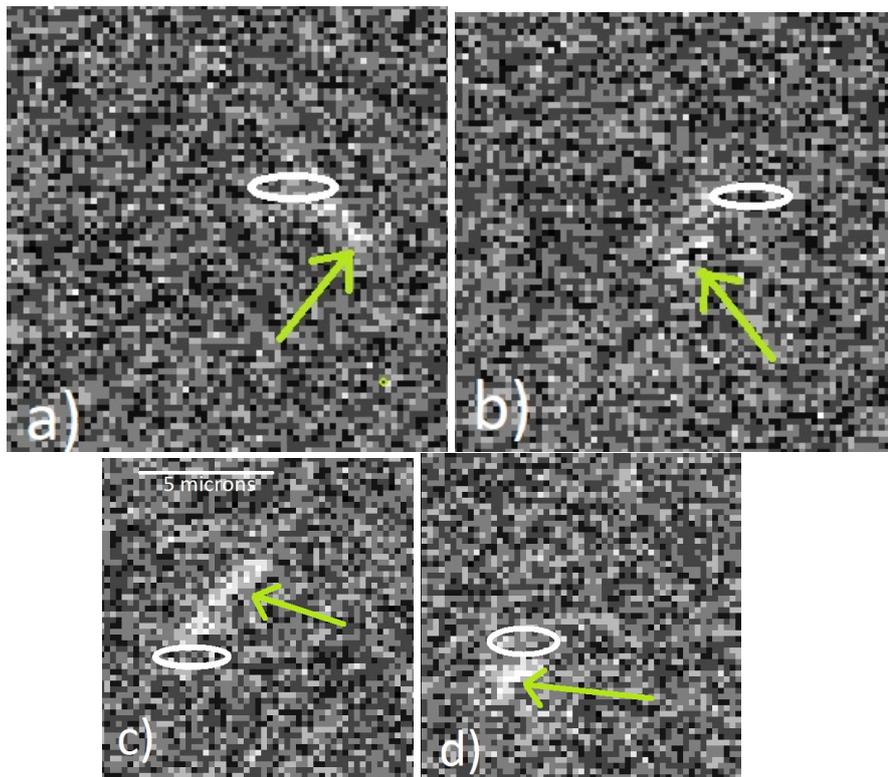
FIGURE 4.23.

The flagellar positions for example cells in the two subsets of the bi-modal cells are indicated by the green arrows. Figures a) and b) are the two modes of the first subset (where the helical length is unchanged). Figures c) and d) show the modes when the helical length changes. An approximate position of the cell body is shown by the white oval at the tethered end of the flagellum. This position was determined from observations of the flagellar motion in the whole movie. For these images, the scale is the same with each pixel representing 0.23μm and the images are different sizes purely due to the choice of area cropped. It should be noted that the flagella are much easier to see in the movie than in the still images due to random pixel noise associated with the low light levels and the flagella were not observed to pass through the region where the cell body is hypothesised to be.

4.5.3.2 Spinning flagella

A proportion of the cells were observed to have flagella that displayed 'spinning' motion. These flagella were seen to circulate around a point and are likely to be the cells that were categorized as flagella-attached in section 4.2.

For these cells, the average time taken for the flagellum to complete one 360° orbit around its tether was investigated. For each cell, the time of three orbits were recorded

and averaged. The data is shown plotted against the number of reversals in flagellar rotation direction observed for the recording in figure 4.24. Error bars are plotted using the standard error calculation and a linear best fit line is shown.

This preliminary data suggests no significant correlation between the number of reversal events observed and the time for an oscillation. The average of all orbit times is 1.08 ± 0.17 s, where again, the error is given as the standard error.
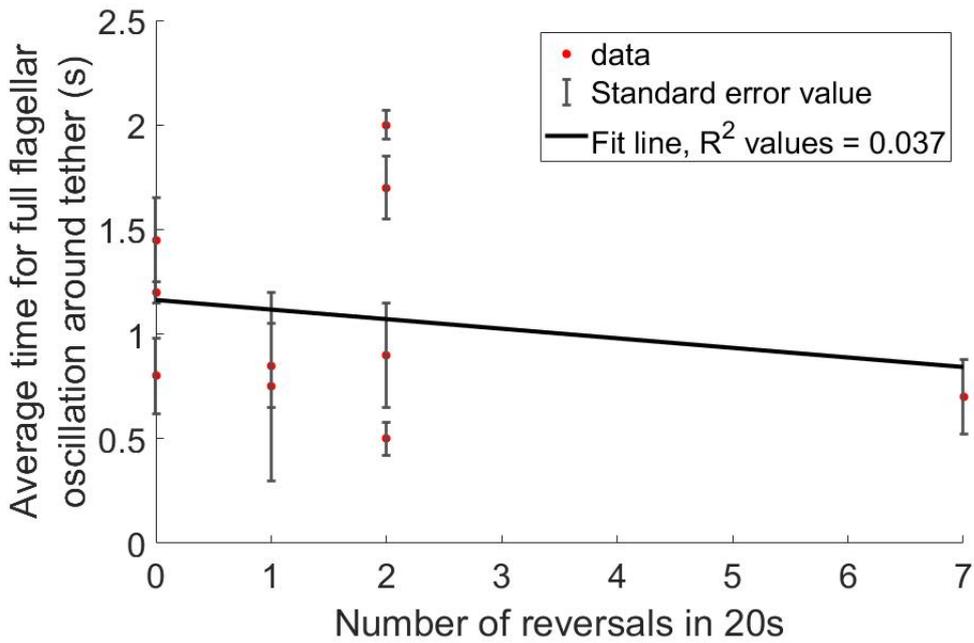
FIGURE 4.24.
The average time taken by a spinning flagellum to complete one full oscillation around its tether. The small R^2 value indicates that there is no correlation between the number of reversals and average time of the oscillation.

4.5.4 Discussion

This investigation into the flagellar dynamics definitely suggests that the flagellar motion of surface-attached cells is far more complex than originally presumed. Apart from the two categories of motility discussed, examples of cells which transition between the categories were observed. In addition, cells were seen to transition between active and inactive flagellar states. There is also some inaccuracy in angle calculations since they were evaluated by eye in ImageJ and there is substantial noise associated with the low

light levels of the experiment. A further consideration is the fact that the cell body is not visible and it is therefore impossible to confirm that the cell body is fully attached to the surface at all times.

4.6   Chapter conclusions

In this chapter the motility of cells attached to a surface has been investigated. The focus is on cells with a cell body attached but a free and motile flagellum. These cells are often overlooked in the literature because they often appear immobile when viewed using standard bright field microscopy. However, using tracer beads, these body-attached cells have been found to make up a significant proportion of moving, surface-attached cells.
An investigation into transitions between types of surface-attached motility has suggested that the body-attached-moving-flagellum mode of motility may be a critical transitional stage of irreversible attachment to a surface, and therefore important in biofilm formation.

In a novel use of DIHM, tracer beads were also used to determine the 3D field around these body-attached cells. The field was found to alternate between two distinct modes which have been associated with flagellar reversals.
The 3D fields of control cells were compared to those of cells exposed to a lactam analogue. The time-averaged field of the lactam cells is qualitatively different to the control but the model fields are strikingly similar. This, taken with the data suggesting that cells in the lactam reverse their flagella more frequently and spend more time in mode 2 than the control cells, suggests that the lactam affects the flagellar motor. The lactam analogue is known to inhibit biofilm formation and this work has shown that it also alters the time-averaged field of body-attached cell. It remains to be seen whether the change in the flow is a means to which the lactam inhibits biofilm formation.

The final work in this chapter was a preliminary investigation into the flagellar dynamics of control cells by fluorescent staining the flagella. This data supported the theory that the two modes seen in the field were due to flagellar reversals and change in position. The information on flagellar orientation will be useful for comparison to model data in later chapters.

MODELLING INDIVIDUAL CELLS ON A SURFACE

"Simplicity is the ultimate sophistication."

Leonardo da Vinci

5.1 Introduction

In this chapter, a simple model for the flow induced by a surface-attached bacterial cell is developed. This model aims to capture the key components of the experimentally derived field whilst remaining computationally inexpensive. In this chapter, the model is presented along with an investigation into its dependence on model parameters. The dynamics of the model flagellum are determined using a set of ordinary differential equations (ODEs) and the long-term solutions are presented. In order to examine the accuracy of the model, the long-term flow of the model is directly compared to the experimentally derived field. Finally, the effect of flagellar reversals on the model flow is determined.

5.2 Singularity model

5.2.1 Motivation

Many geometries involved in the early stages of biofilm formation are incredibly complex and difficult to investigate experimentally. One of the aims of this thesis is to develop a simple computational model of the experimentally-derived field around a single stuck cell. Once the key dependencies of this model have been investigated, the goal is to use the model to investigate the complex, multi-cell systems involved in early stage biofilm formation. By starting with a model for a single stuck cell, the idea is that the effect of cell-induced flow due to multiple cells can be investigated. Furthermore, the effect of chemical additives on these early stage biofilms can be analysed.

5.2.2 Model set-up

The first step in the modelling process is to break down the complex system of the bacterial cell on a boundary into its key components. For this first model, a cell with a single flagellum is modelled simply as an individual flagellum, which is represented by a rigid volume with simple singularity solutions to the Stokes equations placed at C, the centre of the object. Many previous simple flagellar models assume that each flagellum has a constant tilt angle [120, 182, 183]. However, since there is no such constraint in real bacteria, in this model the flagellum is allowed to move around a tether point, D. This is done by imposing a constant motor torque $\boldsymbol{\tau}_m$. The tether point is set at some distance, d, above the boundary in acknowledgement of the fact that the flagellum of a *P. aeruginosa* cell is attached half way up the cell body and to align with a model in the literature where a bacterial cell is attached to a surface via its flagellum and its cell body is allowed to rotate [**?**]. The simulations from the model in [**?**] captured the experimentally observed phenomenon of 'spinning' cell bodies of surface-attached cells. In the work of this thesis, relative to D, the center point is defined by the vector $\mathbf{y} = d\mathbf{k} + l\mathbf{P}$, where l is the length of the tether, $\mathbf{k}$ is the unit vector in the direction $(0, 0, 1)$ and $\mathbf{P}$ is the unit vector indicating the direction of flagellar orientation. In this thesis, the tether length is set as half a flagellar helix length. The direction vector, $\mathbf{P}$, will become useful later for defining singularity directions. The general model set-up can be seen in figure 5.1.

For this simple model, the singularities chosen are the Stokeslet and rotlet to capture
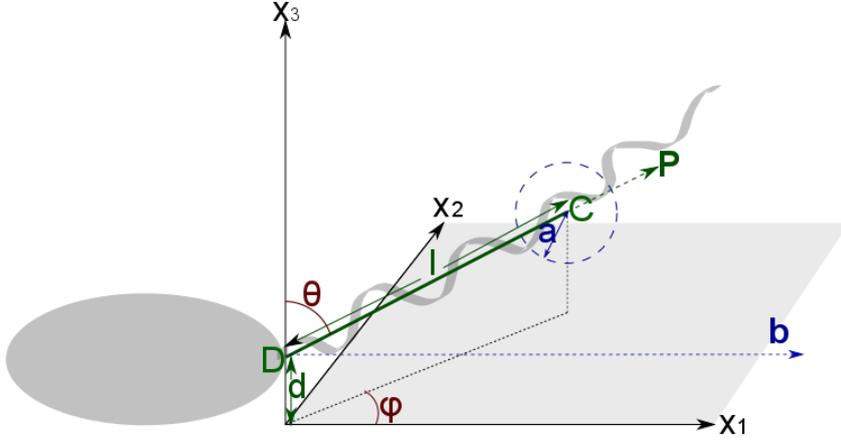
FIGURE 5.1. A schematic of the simplified model set up. The cell is modelled as a sphere, with radius a_s tethered at a distance l, around the point D at a distance d above the boundary. The sphere is able to rotate around its center C. θ and ϕ are the spherical angles denoting the position of the point C. **P** is the unit vector associated with the 'flagellar orientation' and points along the tether line. **b** is the unit vector indicating the 'cell body' direction.

the forcing and rotating components of the helical bacterial flagellum. The total flow due to the singularities along with their images in the no-slip boundary for any number of the model flagella is denoted as **B**. This field has an associated vorticity vector given by $\boldsymbol{\Omega}$ and a rate of strain tensor **E**. It should be noted that since the original flow-producing singularities are inside the flagellar body, for a system of only one flagellum, the original singularities will have no effect on the flagellum's motion. Instead, the flagellum will only move in reaction to the 'image flow' produced when the flow due to the initial singularities encounters the boundary. The 'image flow' for the chosen singularities can be determined by utilising the method of images detailed previously. Then, once this 'image flow' is obtained, the dynamics of the flagellum may be found by considering the torques around the tether point D, as in equation (5.1).

$$\begin{aligned} \boldsymbol{\tau}_D &= \boldsymbol{\tau}_m + \boldsymbol{\tau}_h - \boldsymbol{\tau}_C - (\mathbf{y} - d\mathbf{k}) \times \mathbf{F}_C \\ &= \boldsymbol{\tau}_m + \boldsymbol{\tau}_h - \boldsymbol{\tau}_C - l\mathbf{P} \times \mathbf{F}_C, \end{aligned}$$

(5.1)

where $\boldsymbol{\tau}_D = 0$ is the summed torque at D, $\boldsymbol{\tau}_C$ is the viscous torque at C, $\boldsymbol{\tau}_m$ is the flagellum motor torque, **K** is the unit vector in the direction $(0, 0, 1)$, **y** is the vector denoting the point C relative to the origin and $\mathbf{F}_C$ is the drag force at C.

135

$\boldsymbol{\tau}_h = -k_H \chi \mathbf{e}_\chi$ is the body-hook torque used to model the effect of the the flagella hook and is imposed to prevent the flagellum and body interacting. The variable χ is the angle between the flagellum direction $\mathbf{P}$ and the motor axis direction unit vector $\mathbf{e}_m$. As the bacterial flagellar motor apparatus in embedded in the cell envelope [184] and *P. aeruginosa* cells have polar flagellum, $\mathbf{e}_m = \mathbf{b}$, the body direction, for this model. The unit vector $\mathbf{e}_\chi = (\mathbf{e}_m \times \mathbf{P})/|\mathbf{e}_m \times \mathbf{P}|$ is the direction of increasing χ.

For this model, k_H is a ratio between the bending stiffness of the hook and a product of the hook length and motor torque and is based on the notation of [?]. In [?], the stability in the swimming direction of free swimming cells was investigated using RFT. In their simulations, they varied the flexibility of the flagellar hook by varying k_H and found they could replicate experimentally observed phenomenon such as the 'flick' in run-reverse-flick swimming motility.

The torque at C, $\boldsymbol{\tau}_C$, results from the flow acting on the body and so depends upon the flagellar body shape. The torque on a volume V [185, 186], is given by

$$\tau_{Ci} = -\mu V\left[O_{ij}(v_i - B_i) + \Upsilon_{ij}\left(\omega_j - \frac{1}{2}\Omega_j\right) + Q_{ijk}E_{jk}\right], \tag{5.2}$$

where V is the volume of the body, μ is the viscosity, $\mathbf{v}$ is the object's velocity, $\boldsymbol{\omega}$ is the angular velocity, $\mathbf{O}, \mathbf{Q}$ and $\mathbf{\Upsilon}$ are tensors which contain information about the orientation and geometry of the body. In equation 5.2, the first term inside the square brackets accounts for the torque on the object due to its velocity relative to that of the flow, the second term reflects the viscous torque due to the object's relative rotation compared to the fluid and the final term accounts for the rate of strain within the field.

For this simple model, the flagellum is modelled as a sphere with radius a_s. Giving the flagellum a body acts to prevent the flagellum will intersect the boundary or other flagella and the choice of a sphere allows the formulation to be simplified as $O_{ij} = 0, Q_{ijk} = 0$ for a sphere. Furthermore, $\mathbf{\Upsilon}$ for a sphere is well known [186] such that

$$\Upsilon_{ij} = \alpha_\parallel q_i^1 q_j^1 + \alpha_\perp (q_i^2 q_j^2 + q_i^3 q_j^3) \tag{5.3}$$

where $\mathbf{q}^1, \mathbf{q}^2, \mathbf{q}^3$ are a right-handed orthogonal set of vectors and $\alpha_\parallel$ and $\alpha_\perp$ are shape parameters [?]. The drag force for a sphere is also a well known result [91] so $\mathbf{F}_c = -6\pi\mu a_s(\mathbf{v} - \mathbf{B})$. Hence, balancing torques around D such that $\boldsymbol{\tau}_D = 0$ and substituting the above into (5.1) gives

$$0 = \boldsymbol{\tau}_{mi} + \boldsymbol{\tau}_{hi} - \mu V \left[\Upsilon_{ij}(\omega_j - \frac{1}{2}\Omega_j) + 6\pi\mu a_s l \epsilon_{ijk} P_j(v_k - B_k) \right]. \tag{5.4}$$

As the centre of the object, C, is given by the vector $\mathbf{y} = l\mathbf{P} + \mathbf{D}$, the velocity of the object's centre may be written as $\mathbf{v} = l\dot{\mathbf{P}}$. Therefore, equation (5.4) becomes

$$0 = \boldsymbol{\tau}_{mi} + \boldsymbol{\tau}_{hi} - \mu V \left[\Upsilon_{ij}(\omega_j - \frac{1}{2}\Omega_j) + 6\pi\mu a_s l \epsilon_{ijk} P_j(lP_k - B_k) \right]. \tag{5.5}$$

Simple rearranging of equation (5.5) gives

$$\mu V \Upsilon_{ij}\omega_j = \frac{1}{2}\mu V \Upsilon_{ij}\Omega_j + 6\pi\mu a_s l \epsilon_{ijk} P_j(B_k - l\dot{P}_k) - \tau_{mi} - \tau_{hi}. \tag{5.6}$$

Taking the cross product of equation 5.6 with $\mathbf{P}$, substituting for Υ and using $\boldsymbol{\omega} \times \mathbf{P} = \dot{\mathbf{P}}$ results in

$$\left[\left(\frac{4}{3}\pi\mu a_s^3 \alpha_\perp\right) - \left(6\pi\mu a_s l^2\right) \right]\dot{\mathbf{P}} = \frac{1}{2}\frac{4}{3}\mu\pi a_s^3 \alpha_\perp \boldsymbol{\Omega} \times \mathbf{P} + 6\pi\mu a_s l \left[\mathbf{B} - (\mathbf{P}\cdot\mathbf{B})\mathbf{P} \right] - \tau_{m0}\mathbf{e}_m \times \mathbf{P} + k_H \chi \mathbf{e}_\chi. \tag{5.7}$$

In the above equation, the volume of a sphere has been substituted in so that $V = \frac{4}{3}\pi a_s^3$. The motor and body-hook torques have also been substituted in such that $\boldsymbol{\tau}_m = \tau_{m0}\mathbf{e}_m$ and $\boldsymbol{\tau}_h = -k_H \chi \mathbf{e}_\chi$. τ_{m0} is the size of the motor torque and, for this model, will be directly related to the rotlet strength (discussed in more detail in the next section). The transition from equation 5.6 to equation 5.7 relies on the vector triple product identity $(\mathbf{V}_a \times \mathbf{V}_b) \times \mathbf{V}_c = -\mathbf{V}_a(\mathbf{V}_b \cdot \mathbf{V}_c) + \mathbf{V}_b(\mathbf{V}_a \cdot \mathbf{V}_c)$ where $\mathbf{V}_a$, $\mathbf{V}_b$, $\mathbf{V}_c$ are vectors. It should also be noted that, as $\mathbf{P}$ is a unit vector, $\mathbf{P}\cdot\mathbf{P} = 1$ and $\mathbf{P}\cdot\dot{\mathbf{P}} = 0$. Rearranging equation 5.7 to make $\dot{\mathbf{P}}$ the subject of the equation and simplifying gives

$$\dot{\mathbf{P}} = \frac{a_s^2 \alpha_\perp \boldsymbol{\Omega} \times \mathbf{P}}{(2a_s^2 \alpha_\perp - 9l^2)} + \frac{9l^2}{(2a_s^2 \alpha_\perp - 9l^2)}\left[\mathbf{B} - (\mathbf{P}\cdot\mathbf{B})\mathbf{P} \right] + \frac{3\tau_{m0}}{2a_s\pi\mu(2a_s^2 \alpha_\perp - 9l^2)}\left[\frac{k_H \chi}{\tau_{m0}}\mathbf{e}_\chi \times \mathbf{P} - \mathbf{e}_m \times \mathbf{P} \right]. \tag{5.8}$$

5.2.3 Non-dimensionalisation

In this model, the cells will be almost exclusively attached to the boundary and have the same size. Therefore, the tether height, d, will be constant for most of the situations investigated. This constant property of d makes it a good choice for the non-dimensionalisation of all the lengths in the system. The Stokeslet, giving a velocity field of the flow and, therefore, having units of length/time, gives an appropriate timescale for non-dimesionalisation for a given length scale. At a distance d from the singularity, the first term of the Stokeslet is $\frac{f_0}{8\pi\mu d}$, where f_0 is the magnitude of the Stokeslet. From this,

the characteristic time for this system, T, as $T = \frac{8\pi\mu d^2}{f_0}$ can be obtained. This T may now be used to non-dimensionalise all times such that

$$\tilde{d} = d/d = 1, \quad \tilde{\mathbf{x}} = \mathbf{x}/d, \quad \tilde{l} = l/d, \quad \tilde{a} = a/d, \quad \tilde{\mathbf{r}} = \mathbf{r}/d \qquad (5.9)$$

In the above, a tilde is used to indicate a non-dimensional variable.

In equation 5.8, the third term on the RHS is the only time-dependent term (units of time) and therefore the only term requiring non-dimensionalisation by T. The first term on on the RHS of equation 5.8 is non-dimensional and the second has units of length. This means that, equation 5.8 may be written as

$$\dot{\mathbf{P}} = \alpha\mathbf{\Omega} \times \mathbf{P} + d^{-1}\Gamma\left[\mathbf{B} - (\mathbf{P}\cdot\mathbf{B})\mathbf{P}\right] + \eta T^{-1}\left[\frac{K_h}{\tau_{m0}}\chi\mathbf{e}_\chi \times \mathbf{P} - \mathbf{e}_m \times \mathbf{P}\right], \qquad (5.10)$$

where, $\alpha = a_s^2\alpha_\perp/\zeta$, $\Gamma = 9ld/\zeta$ and $\eta = 12\tau_{m0}d^2/f_0 a_s\zeta$, where $\zeta = (2a_s^2\alpha_\perp + 9l^2)$, $T = 8\pi\mu d^2/f_0$.

Non-dimensionalising lengths with d and times with T, and dropping tildes for clarity, allows equation 5.10 to be transformed into

$$\dot{\mathbf{P}} = \alpha\mathbf{\Omega} \times \mathbf{P} + \Gamma\left[\mathbf{B} - (\mathbf{P}\cdot\mathbf{B})\mathbf{P}\right] + \gamma\chi\mathbf{e}_\chi \times \mathbf{P} - \eta\mathbf{e}_m \times \mathbf{P}, \qquad (5.11)$$

with $\mathbf{B}$ being the field of a Stokeslet and rotlet of magnitude $\beta = \tau_{m0}/f_0 d$ along with their images. $\alpha = ((a_s^2\alpha_\perp/9ld)$ measures the relative effect of the object size on the torque, Γ is the viscous torque on the object centre and $\eta = \beta(4d^2/3a_s l)$ gives the magnitude of the motor torque affecting flagellum orientation. The size of the body-hook torque is controlled by $\gamma = \eta K_h/\tau_{m0}$.

Since the primary motivation for developing this model is to investigate multiple interacting flagella, a final component of the system is applying a Faxén-type correction to prevent the flagella intersecting each other/ the boundary. This correction may also be envisioned as a source dipole and is applied by replacing $\mathbf{B}$ with $\mathbf{B}_f = \left(1 + \frac{a_s^2}{6}\nabla^2\right)\mathbf{B}$.

5.2.4 Obtaining spherical dynamics

$\dot{\mathbf{P}}$ is the velocity in the $\hat{\mathbf{P}}$ direction and, because the sphere is rigidly tethered, with l a constant, $\hat{\mathbf{P}}$ may be written in terms of spherical angles such that

$$\hat{\mathbf{P}} = \begin{pmatrix} \sin\theta\cos\phi \\ \sin\theta\sin\phi \\ \cos\theta \end{pmatrix}. \tag{5.12}$$

Therefore, any velocity in the $\hat{\mathbf{P}}$ direction may be decomposed into components in the $\hat{\boldsymbol{\theta}}$ and $\hat{\boldsymbol{\phi}}$ directions, where

$$\hat{\boldsymbol{\theta}} = \begin{pmatrix} \cos\theta\cos\phi \\ \cos\theta\sin\phi \\ -\sin\theta \end{pmatrix} \tag{5.13}$$

and

$$\hat{\boldsymbol{\phi}} = \begin{pmatrix} -\sin\phi \\ \cos\phi \\ 0 \end{pmatrix}. \tag{5.14}$$

Since $\dot{\mathbf{P}} = \dot{\theta}\hat{\boldsymbol{\theta}} + \dot{\phi}\hat{\boldsymbol{\phi}}\sin\theta$, equations for $\dot{\theta}$ and $\dot{\phi}$ can be obtained by using dot products, such that

$$\dot{\theta} = \dot{\mathbf{P}} \cdot \hat{\boldsymbol{\theta}} \tag{5.15}$$

and

$$\dot{\phi} = \frac{\dot{\mathbf{P}} \cdot \hat{\boldsymbol{\phi}}}{\sin\theta}. \tag{5.16}$$

5.2.5 Realistic values for parameters

As a starting point for investigating the dynamics of the system, realistic values for α, β and γ were obtained. Suitable values for the dimensional variables in the system were determined from the literature. The value for the helical radius (a_s) is obtained from [187] and for a bacterial flagellum is approximately 0.3 μm. The 'stretched' length of the *P. aeruginosa* flagellum is $4.5 - 9$ μm [188]. Therefore, for the purposes of this model, the flagellar length (l) has been set as 5 μm since it is about the correct order of magnitude. *P. aeruginosa* cells are $0.5 - 1.0$ μm in width [8], and for the purpose of this model, it is assumed that the cells have similar height to width. The variable d determines the height at which the model 'flagellum' is tethered above the boundary. This, therefore, is set as 0.5 μm since it is approximately half the cell height. For the non-dimensional

system, the value of $f_0 = 1.6$pN to align with the literature [189].

The parameter $\alpha_\perp$ was found to be 6 following [91] giving $\alpha = 0.024$. Reference [21] used slender-body theory to determine that the ratio of the force to torque of helical flagellar should be $\beta = 1.948$ for *E. coli* cells where the bundle was modelled as a single helix of length 7.5μm. Although [21] was interested in the bundle, as it was modelled as a single helix, the same value for β is used in this work. This means that $T = 1/100$ s and $\eta = 0.0431$. This gives realistic values for α and β leaving just an appropriate value for k_H to be determined. Reference [26] suggested that the hook would be stable for $k_H \geqq 0.5$. Therefore, different k_H values close to 0.5 have been investigated.

Also important is the direction vector that the body-hook torque is centered on. This may be thought of as the motor angle. For all the simulations in this work this angle is set at $\pi/2$ meaning it aligns with the cell body.

5.2.6 Results

5.2.6.1 Time dependent flagellar dynamics

The figures in 5.2 show the dynamics of a single model flagellum over a period of 800 non-dimensional units (or equivalently 8s). Figures 5.2a and b show the initial and final orientations of the flagellum (red arrow) relative to the cell body and the surface ($x - y$ plane) respectively. Also shown are arrows indicating the flow field induced at the final time step and the positions of tracer particles (blue/ green spheres) for the initial and final times. To simplify calculations, the tracers are treated as point particles with no volume so they do not alter the flow in any way. Their location is found by considering the velocity of the field at their location and applying a forward difference technique without any simulated Brownian noise added.

Figure 5.2c show the time-dependence of the flagellar angles over the 800 time units. The flagellum can be seen to settle in a stable orientation after approximately 200 time units. In this stable orientation, the flagellum is slightly displaced from being directly behind the cell body (ie. $\phi > 0$) and is raised slightly from being parallel to the boundary. The fact that the flagellum does not align exactly with the cell body indicates that the flow due to the image system is acting against the body-hook torque. For these simulations, α and β are set as the values given previously and $k_H = 0.5$. The fact that these steady

angles are seen for long times aligns well with the prediction that the hook is stable when $k_H \geq 0.5$ [26].

To further test the suggestion that the value of k_H controls the stability of the flagellar hook, the above simulation was repeated with various values for k_H. Using the starting orientation of both the flagellum and particles was the same as in figure 5.2a, the value of k_H was found to have little effect when it was increased up to a value of 5. This aligns with the work of [26], where it was suggested that for values of $k_H \geq 0.5$, the flagellar hook was stable and so there would be little impact of increasing k_H. With values as small as $k_H = 0.2$, there is again, little difference from the dynamics in 5.2. However, with $k_H \leq 0.1$ the flagellar dynamics change. Figure 5.3a shows the flagellar and particle positions after 800 time units. Although the flagellum appears in a similar place, the particles have been advected differently and the path traced by the flagellar tip (indicated by red circles) is also different than seen in figure 5.2b. When the flagellar angles are investigated (figure 5.3b), the reason for these differences is clear; the flagellum oscillated around the same stable angles as previously. This oscillation appears to be tending towards the steady state for longer times and supports the idea that the flagellar hook is less stable for smaller k_H values.

5.2.6.2 Impact of α, β and γ

The parameter α is directly linked to the radius of the flagellar object in the model and so may be thought of as controlling the object size relative to the tether. Although the data is not shown, an investigation into the impact of varying α aligns with what would be predicted: α impacts the height above the boundary (the theta angle) of the flagellum's long-time orientation. This parameter, therefore impacts the dynamics only when the flagellum is very close to a surface or another flagellum. As the helical radius of the bacterial flagellum is fairly well know, for the rest of the simulations in this thesis, α will not be varied.

The parameter β determines the ratio of Stokeslet and rotlet strengths but in this model it is also directly linked to the strength of the motor torque. Simulations run with various values for β show that β has little impact on the flagellar θ angle, and a large β means that the flagellum has long time dynamics where the flagellum is parallel to the boundary and aligns with the body axis. A small β sees the flagellum still parallel to the boundary but lying left of the cell body (when viewed from behind). These results
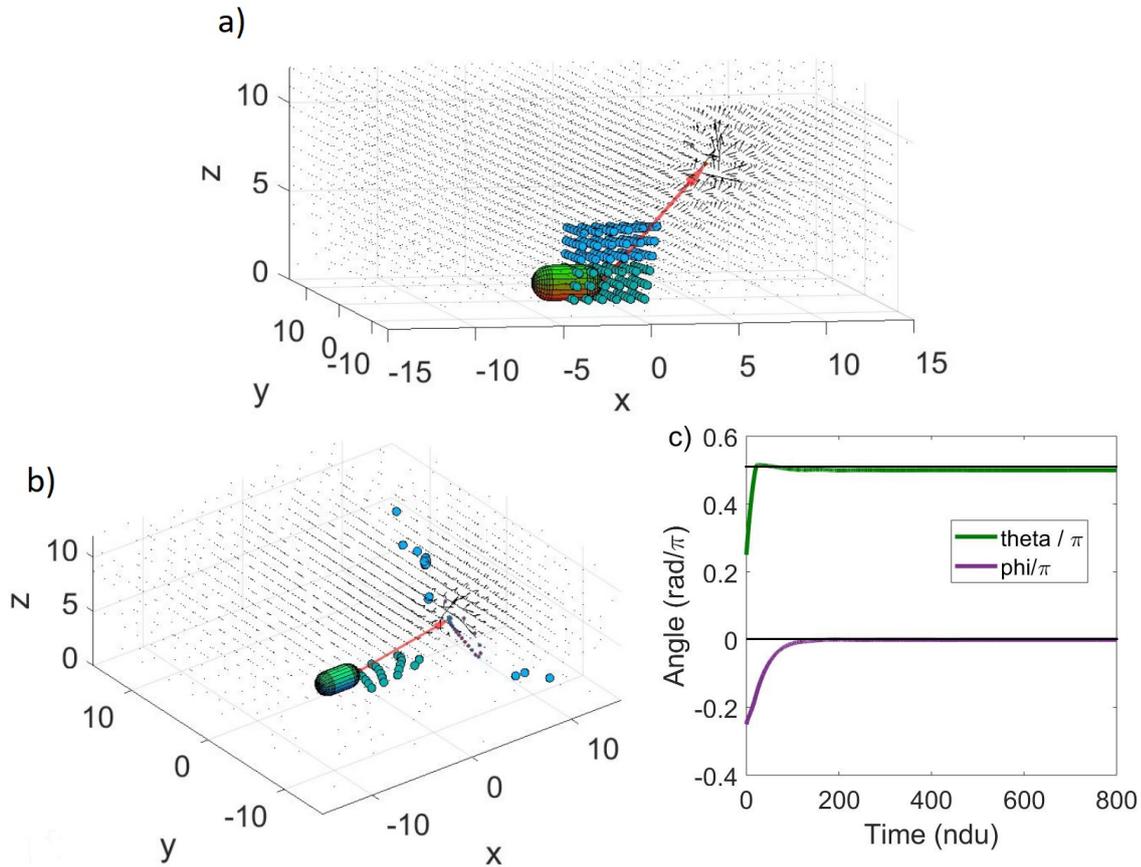
FIGURE 5.2.

    The time dependent dynamics of the single model cell with α and β set to the previously discussed 'realistic' values and $k_H = 0.5$. a) shows the initial configuration with the cell body shown, the flagellar direction indicated with a red arrow and the direction and relative magnitude of the induced flow field shown with black arrows. Also shown is the initial position of tracer particles to indicate the effect of the flow field. b) shows the position of the flagellum and tracer particles after 800 time steps along with the induced field at this time. The red circles show the path followed by the flagellar tip. c) shows the time dependence of the flagellar angles. After approximately 200 time steps, the flagellum settles to a stable orientation. Lines for $\phi = 0$ and $\theta = \pi/2$ are shown for comparison.

a)

b)
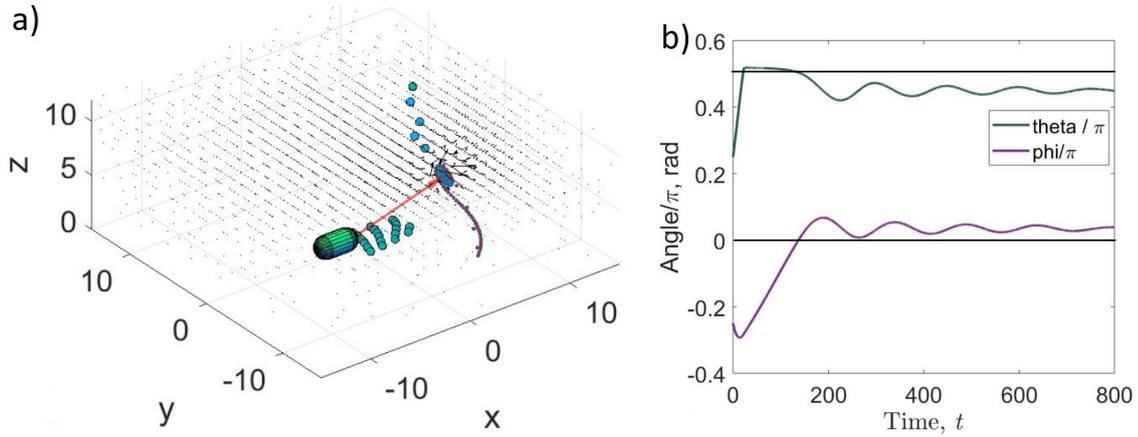
FIGURE 5.3.

The time dependent dynamics of the single model cell with α and β set to the previously discussed 'realistic' values and $k_H = 0.1$. a) shows the position of the flagellum and tracer particles after 800 time units along with the induced field at this time. The red circles show the path followed by the flagellar tip. The direction and relative magnitude of the flow field is shown by black arrows and the cell body is indicated by the ellipsoid. b) shows the time dependency of the flagellar angles. Lines for $\phi = 0$ and $\theta = \pi/2$ are shown for comparison. The flagellum oscillates be appears to tend towards a fixed angle that is further displaced for being directly behind the cell than when $k_H = 0.5$.

can be explained by the fact that a large β means a large motor torque so the body-hook torque term dominates and χ in minimised. A small β means a small motor torque and the effect of the image rotlet dominates. As there is substantial evidence in the literature for the appropriate value of β (see previous section), for the rest of this thesis, $\beta = 1.948$.

The parameter γ controls the size of the body hook torque for a given α, β. Data not shown reveals that changing γ has little impact on θ and, as expected, an artificially large γ means the body-hook term is large compared to the rotlet torque and so the flagellum aligns behind the cell body to give a small χ. A small value of γ means the rotlet dominates and χ is large, with the flagellum lying left of the cell body (when viewed from behind).

5.2.7 Discussion

It should be remembered that the averaging issues producing a smaller-than-expected field for the experimental results would be likely to change the averaged direction of the field at the nodes also. These difficulties in the experimental results further emphasise the usefulness of the model to capture situations that are difficult to analyse experimentally.

One of the key weaknesses of this model is that the helical flagellum is modelled as a tethered sphere. As previously discussed, options to model the full helix are available (SBT, RFT, regularized Stokeslets, etc.) but are far more computationally expensive than this model. However, work to model the flow of a surface-attached cell with a moving flagellum by employing SBT has revealed qualitatively similar results to those seen in this simple model (unpublished work -M.Bees). Another issue with this model is that the cell body is not present. This means that flow and tracer particles can pass through where the cell body should be, giving slightly erroneous tracer dynamics. It also means that, theoretically, the flagellum could pass through where the cell body should be - although this has not been seen unless γ is set very small. The inclusion of the cell body would be a sensible extension to this work and could be modelled using a dipole singularity for example or using BEM as in [109].

The fact that the flagellum is modelled as a tether sphere at a fixed distance from **D** in this model means that polymorphic transitions and bending effects of the flagellum are not captured. This would likely impact both the flagellar and tracer dynamics. Polymorphic transitions are beyond the scope of this thesis but have been modelled in [190, 191]. Understanding the impact of polymorphic transitions on the flow would be an interesting extension to the project and may help to understand some of the averaging issues encountered when experimentally determining the 3D flow in chapter 3.

Despite these over-simplifications to real bacteria, this simple model is in good company. The value of computationally inexpensive models in analysing complex arrangements of bacteria is well acknowledged [120] and this work has the advantage of allowing for varying flagellar orientation in 3D. In chapter 3 it was discussed that a by-eye examination of bead motion predicted that the field was around $50\mu s^{-1}$ very close to the cell, but that this was not reflected in the averaged field at the given node points. Using the 'realistic' parameters in the model produced a field approaching this

magnitude near the $x-y$ plane in the simulation. Taken together, this suggests that, though the model is inherently simplistic, it is useful as a mode of investigating the flow due to motile surface-body-attached cells. Furthermore, it may be considered to more accurately represent the instantaneous flow of such cells than the experimentally determined averaged flow. A direct comparison between simulated and experimental data can be found later in this chapter.

5.3 Effect of reversals on the field

5.3.1 Motivation

Although the simple model developed so far begins to show some interesting dynamics and is useful for comparison to the two 'modes' observed in chapter 3, it is lacking in that it does not account for flagellar reversals. In this section, the direction of the rotlet in the simple model is allowed to change to represent a reversal of the flagellum.

5.3.2 Model set-up

The reversals are built into the model by setting a 'probability of reversal' at each time-step. MATLAB is used to generate a Gaussian random array of numbers between 0 and 1 the same length as the number of time-steps. At each time-step, if the corresponding number in the array is less than the probability of reversal then the rotlet remains in the direction is was for the previous time-step, if the number is greater than the probability of reversal then the rotlet reverses direction. All other aspects of the code used to determine the system's dynamics remain the same as in the previous section.

At this stage, for simplicity, the effect of the cell's current mode in its likelihood to reverse is ignored. Instead, the probability of reversal is found by considering the average number of reversal per 20s from the data in Chapter 3 and dividing that by the number of time-steps. This means that the trial probability of reversing is 0.03s^{-1} for the control sample and 0.08s^{-1} for the sample containing the lactam analogue.

Figure 5.4 displays an example set of simulated data found using the above reversal probabilities. To mirror the experimental data, the number of reversals seen in the model over 20s for 20 cells is shown. Using this modelled data, the mean number of reversal

	Experimental data -20s	Simulated data -20s
Mean number of reversals- lactam	1.68 ±0.28	1.70 ±0.28
Mean number of reversals- control	0.55 ±0.17	0.55 ±0.18

TABLE 5.1. The mean number of reversals in the control/lactam samples seen over 20s is compared to the number seen when reversals are simulated using the control/ lactam rates for the same duration. The standard deviation in the data is also shown. There is no statistically significant difference between the control and simulated results (P-values >0.8). This is an important verification is the trail method of simulating reversals by using a reversal rate.
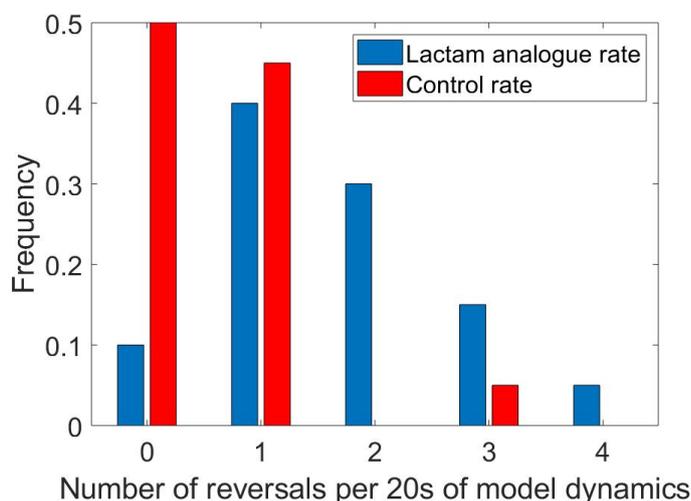
FIGURE 5.4.
An example of the randomly generated number of reversal per 20s data using the lactam analogue and control reversal probabilities.

is 1.70 ± 0.28 and 0.55 ± 0.18 in each 20s of simulation for the lactam analogue and control sets respectively. These mean values correspond well to the experimental data and, although there will always be variation due to the random generation of the data, the overlap in the means suggests that the reversal probability values are appropriate. For comparison, results from the experiments in chapter 3 are shown with simulated results in table 5.3.2.

5.3.3   Results

5.3.3.1   Time dependent flagellar dynamics

Since it has been hypothesised that the lactam analogue may alter the reversal rate of the bacterial flagellum, here the effect of altering reversal rate on flagellar dynamics is investigated. Figure 5.5 shows the results. The paths followed by the flagella (see figure 5.5a,c) do not appear markedly different for the two rates. However, when the flagellar angles are compared (figure 5.5b,d), there is a slight difference in long time flagella dynamics. For this simulation, the initial flagella angles were $\theta = 0.25\pi, \phi = 3.5\pi/2$.
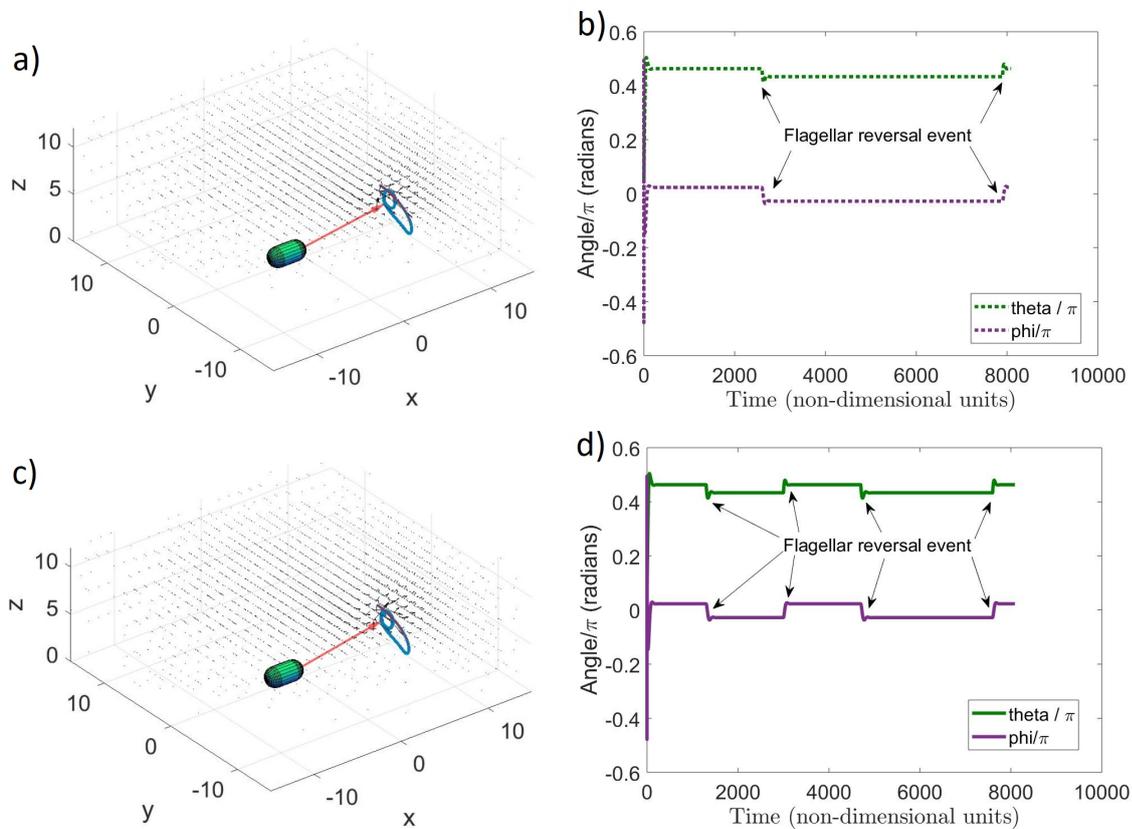
FIGURE 5.5.
    a) and c) show the trajectories of the simulated flagella along with the induce field for the control reversal rate of 0.03s^{-1} and the lactam reversal rate of 0.08s^{-1} respectively. b) and d) show the flagellar angles for the same control and lactam simulated cells respectively.

5.3.3.2 Impact of reversal rates on particle transport

As the reversal rates are not drastically different, the overall dynamics are not dissimilar and the dynamics appear to recover fairly quickly after a reversal event. However, by simply looking at the flagellar dynamics, it is not possible to determine the impact of varying the reversal rates on particle transport within the flow. Therefore, to investigate tracer transport, 8000 tracer particles, originating int a $10 \times 10 \times 10$ ndu grid around D, are followed for 2000 non-dimensional time units as they are advected by the flow. The tracers are treated as point particles that do not disturb the flow, and their trajectories are determined by applying a forward difference method of the induced field on the tracers' previous locations. Brownian motion is also included by applying a random noise term to the positions. This term was determined by using MATLAB random number generator to pick a number from a normal distribution centered on 0 with a standard deviation $= 6Dt/A$. Here D is the diffusion coefficient discussed in chapter 1, t is the time between subsequent tracer positions and A is the notional radius of the particle. It should be noted that this method of determining Brownian motion is commonly used to determine the long-term diffusion of particles in a bulk fluid due to Brownian motion [**?**]. The presence of a surface has been shown to increase the effect of Brownian motion of bacterial cells [192] and Brownian diffusion rate increases with shorter timescales [193]. Therefore, the method of determining Brownian motion in this thesis is likely to underestimate the Brownian term. For this investigation the particle size was set at 20nm since this was around the average size of the *P. aeruginosa* QS molecule 3-oxo-C_{14}-HSL [194].

The main question for this section is whether there is a difference in the size of the field induced by cells with their flagella reversing at different rates. To do this, the distance from the cell at which tracer particles cease acting ballistically (i.e. being advected by the flow) and become purely Brownian for the different reversal rates needs to be determined. Commonly, the mean squared displacement (MSD) of a particle is used to determine whether it is moving purely vie Brownian motion or not [195, 196]. From the MSD data, the diffusion coefficient, D_i, can be determined and compared to the predicted Brownian motion diffusion coefficient for the system [197]. However, as Michalet remarks "it is important to realize that if the molecule is undergoing multiple types of diffusion during the observed trajectory, the extracted value will only be an average one" [197]. Therefore, as it is expected that the particles close the cell with move with a ballistic motion then their movement will gradually become purely Brownian as they move away from the cell, simply calculated the MSD of the particles' trajectories is

not a good choice for this system. Darnton *et al* looking at the transport of particles by a bacterial carpet and overcame the problem of averaging MSD by splitting the particle trajectories into those near and far from cells [198]. However, Darnton *et al* used 2D particle tracking to follow their tracer particles and therefore could not follow particle that passed out of their focal plane. This meant that they could not follow particles as they moved from near the carpet to far away. Conversely, the simulated nature of the data in this thesis means that the particle can be followed throughout the whole trajectory. Therefore, there are more options for investigating the particle transport by the cells in this thesis and much consideration is need to determine the best way of compare the impact of cells on particle motion.

First, the approach of Darnton *et al* is emulated and the MSD of particles near and far from the cell is compared. Figure 5.6 shows mean MSD vs delay time plots for 24000 simulated tracers near to (< 50ndu) and far from (> 200ndu) a simulated cell reversing at the control reversal rate $0.03s^{-1}$. These plots were made using a freely available MATLAB script [199]. The data is from three repeats of 8000 tracers followed for 1000 non-dimensional time units. The data is plotted on a log-log scale as the gradients of such plots can be used to determine whether a particle is advected or purely diffusive [197]. Lines with gradients 1 (purely diffusive) and 2 (purely ballistic) are shown for reference. From these plots, it is clear that, close to the cell, the particles are moving with a more ballistic motion and far from the cell the motion is almost purely diffusive. As would be expected, this clearly shows the impact of the simulated cell and shows that the is little to no impact of the cell > 200ndu from the cell and the motion is Brownian.
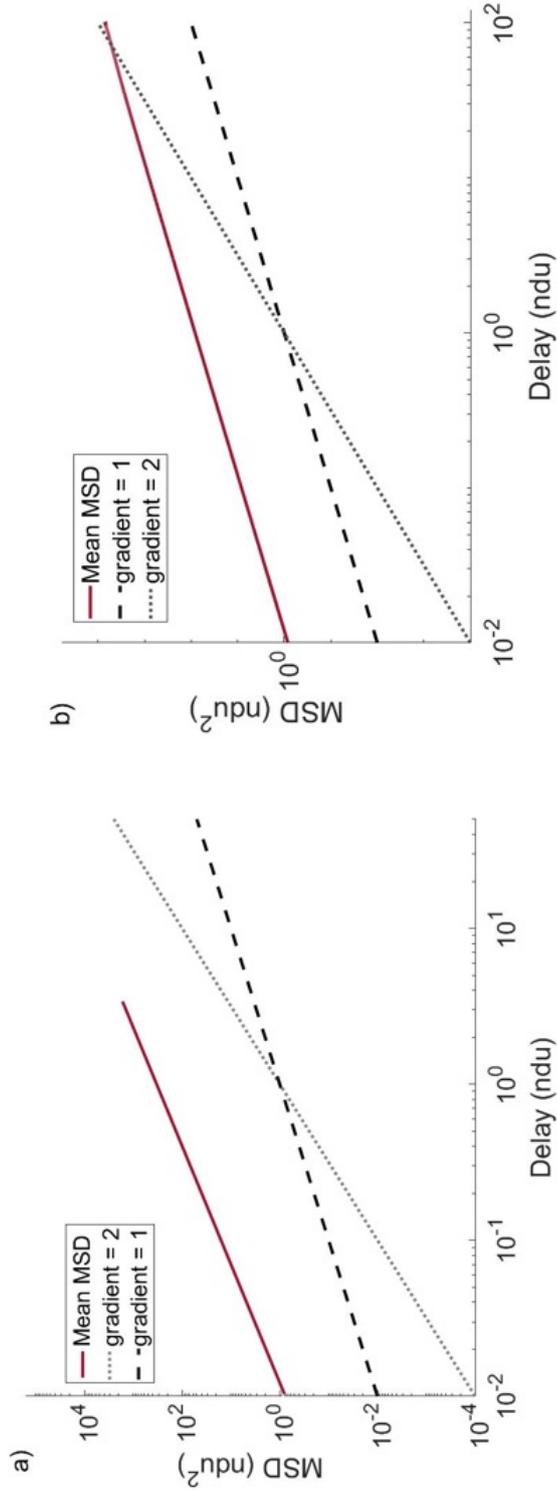
FIGURE 5.6.

Mean MSD vs delay time plots for 24000 simulated tracers a)near to (< 50ndu) and b) far from (> 200ndu) a simulated cell reversing at the control reversal rate $0.03s^{-1}$. The data is from three repeats of 8000 tracers followed for 1000 non-dimensional time units. The data is plotted on a log-log scale as the gradients of such plots can be used to determine whether a particle is advected or purely diffusive [197]. Lines with gradients 1 (purely diffusive) and 2 (purely ballistic) are shown for reference.

However, investigating particle transport in this way requires an *a priori* assumption of what should class as 'near to' or 'far from the cell. Also, by losing the time dependency of the particle trajectories in this way, it is impossible to determine whether certain simulation parameters (such as flagellar reversal rate) impact the distance at which the flow induced by the cell alters the tracers' motion. One hypothesis of this thesis is that cells maintain their motile flagella to transport fluid and that the lactam analogue may impact this transport. To further understand how the distance of tracers from the cell is dependent of time and flagellar reversal rate, figure 5.7 shows the mean distance of the same 24000 particles from the cell at different times, for cells reversing at the control and lactam reversal rates. Error bars indicate the standard deviations in distances from the cell. For both reversal rates, the gradient of the mean distance plot is initially steeper before becoming shallower. This transition indicates where the particle motion transitions from having ballistic contributions from the cell flow to being purely diffusive. The transition occurs at shorter times/ closer to the cell for the control reversal rate resulting in enhanced transport for the lactam simulation.
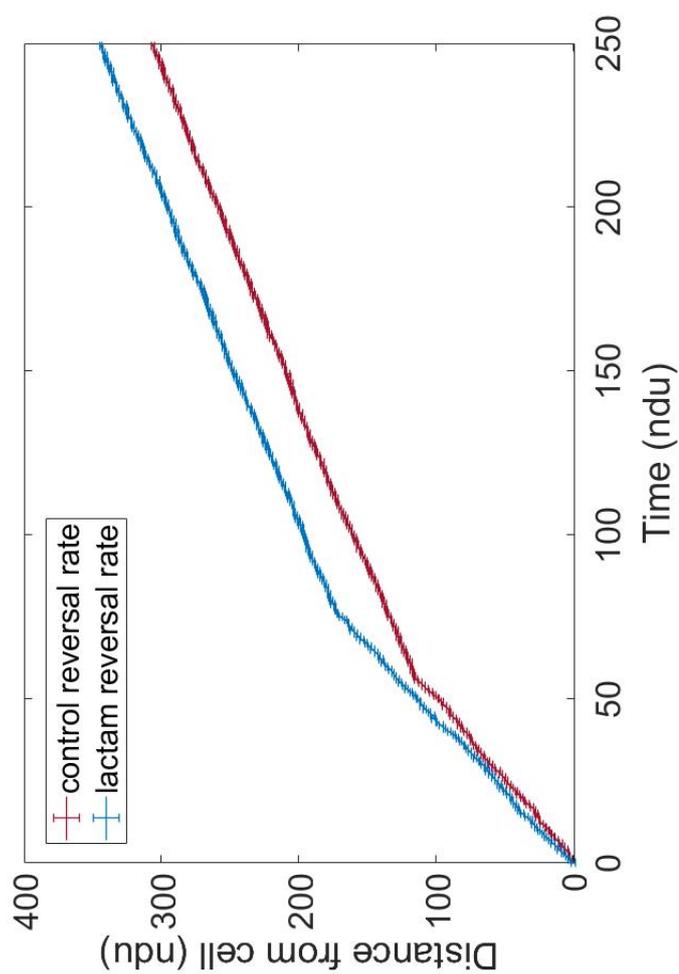
FIGURE 5.7.

The mean distance of 24000 tracer particles from a cell reversing at either the control reversal rate of $0.03s^{-1}$ or the lactam rate of $0.08s^{-1}$. Data is from three repeated simulations of 8000 particle each. Error bars indicate the standard deviations in mean distances from the cell between the three repeats.

5.3.4 Discussion

As discussed above, it is standard in the literature to use particle MSD to investigate the motion of particles. However, the temporally varying nature of the reversing flagella in this simulation mean that MSD has been determine to not be the best way of investigating the system. Instead, the mean distance of particles from the cell is used to compare the impact of varying the reversal rate between the control and lactam rate. The results in this section suggest that, for particles approximately of the size of QSMs, the increased lactam reversal rate enhances transport of particles compare to the reversal rate. It has previously been shown that increased directional changes of cilia motion enhances transport in the brain [200], which aligns well with the results in this section. Furthermore, unregulated motility has been shown to destabilise *P. aeruginosa* biofilm structure [201]. Taken together with the results of this section, an hypothesis of this thesis is that the lactam prevents biofilm formation by preventing the build-up of QSMs (as transport is enhanced) and destabilising biofilm structure by interfering with motility regulation. To test this, it would be interesting to analyse whether cells exposed to the lactam remain motile for longer than control cells.

5.4 Comparison with experiment

5.4.1 Motivation

The model of a single surface-attached bacterial cell with a moving flagellum presented in this chapter has been developed by considering experimentally derived factors (e.g. the fact that the flagellum rotates and is attached at a cell pole etc.). This technique of identifying key properties to be included in the model is often seen in simple model descriptions of bacteria flagella and cilia [119, 202–204]. However, this minimalist approach to modelling such arrangements means that, inevitably, aspects of the system will be excluded. There is a limit to the uses of a model if it does not reflect the real-life system. Therefore, many of the simple models presented in the literature compare results derived from the simulations to those obtained via experiments. To test the simple model introduced in this chapter, in this section the simulated flow induced by the simple model flagellum is compared to the experimentally derived field presented in chapter 4.

5.4.2 Method

To best emulate the experimental set up, the trajectories of simulated tracer particles around a single simulated cell with the flagellum reversing at the control reversal rate are collected. The experimental flow field is the average of 20 cells so the simulation is repeated 20 times and all the particle trajectories are averaged. Again to align with the experiment, the simulated particles were given a diameter or 0.13μm for the purposes of calculating Brownian motion. The AOI for the experimental frames was approximately $120 \times 120\mu$m so the start positions of the 8000 simulated tracer particles was a random $120 \times 120 \times 30\mu$m grid around the simulated cell. The simulation was run for 2000 non-dimensional time unit which equates to 20s (the same length of time of the experimental recordings) and the average flow field was obtained from the tracer trajectories using the same MATLAB code as used to determine the experimentally derived field for the control cells.

5.4.3 Results

Figure 5.8 shows the time-averaged field over the 20 single simulated cells. The arrow sizes indicate the relative magnitude of the velocity field at each node, the cell body location is shown by the ellipsoid and the arrow colour shows the difference between the maximum and summed ND at each node. The colours are scaled so that the maximum and minimum align with those of the time-averaged field of the 20 single cell in the control experimental sample. By eye, a key difference between the experimentally derived field and figure 5.8 is that there are more blue arrows at nodes with high z values, indicating more reliable data in this region. This can be explained by the fact that the simulated particles do not experience the electrostatic surface interaction that was postulated to cause the relatively high density of particle near the surface in the experimental data.
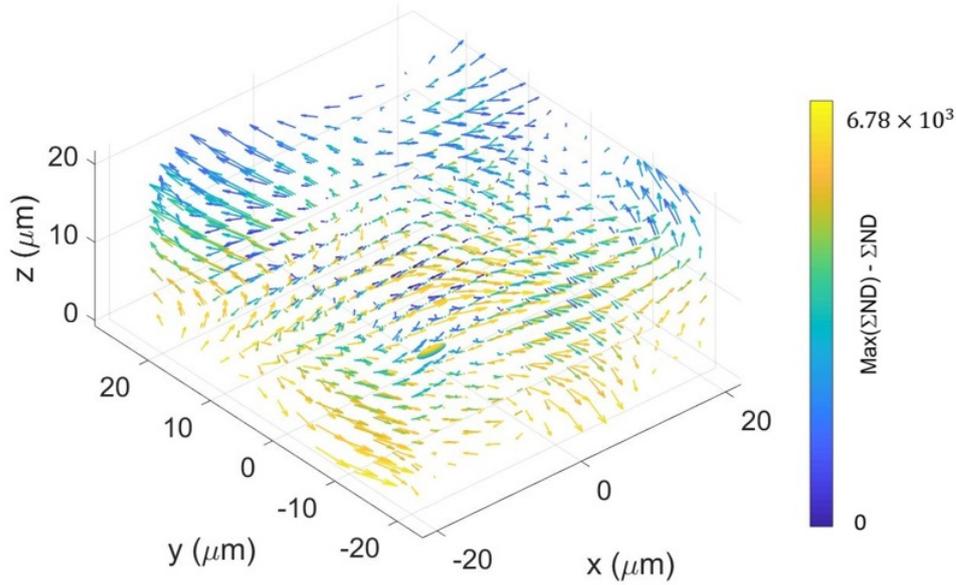
FIGURE 5.8.

The averaged time-averaged velocity field around 20 simulated single cells. The arrow sizes indicate the relative magnitude of the velocity field at each node, the cell body location is shown by the ellipsoid and the arrow colour shows the difference between the maximum and summed ND at each node. The colours are scaled so that the maximum and minimum align with those of the time-averaged field of the 20 single cell in the control experimental sample.

Another by-eye difference between figure 5.8 and the experimentally derived field is that many of the arrows indicating the relative size of the field are larger in the experimental field. As the arrow sizes are relative to the magnitude of the velocity at all the nodes, they are not directly comparable between the two fields. Therefore, to better identify whether the magnitudes of the velocity is different in the simulated and experimental fields, figure 5.9 shows histograms of the magnitude of the velocity at each of the nodes in the simulated and experimental time-averaged fields. As in the experimental field, any nodes with a $C_B < 1$ (3.s.f) are set to NaN. For comparison between simulated and experimental fields, only nodes at which the velocity magnitude $\neq$ NaN for both simulated and experimental were compared. This was a total of 925 nodes. The mean velocity magnitude of the simulated and experimental samples are $1.69 \mu m s^{-1}$ and $1.75 \mu m s^{-1}$ respectively. The standard deviation on the simulated and experimental means are $0.76 \mu m s^{-1}$ and $0.81 \mu m s^{-1}$ respectively. Therefore, a t-test on the 925 nodes compared gives a P-value of 0.1118 suggesting that the difference in distribution of

velocity magnitudes of the fields is not statistically significant.

Figure 5.9 shows that the simulated and experimental time-averaged do not have statistically difference distributions in the velocity magnitude at nodes. However, this does not show the difference in the direction of velocity at each node. Theoretically, the two fields could have the exact same magnitude of velocity at each node but have the fluid moving in significantly different directions. To investigate this, figure 5.10 shows plots of the difference in velocity in the x_1, x_2 and x_3 directions between the experimental and simulated flow fields plotted against the distance of the node point from the centre of the experimental cell body. Also plotted is line of best fit to each of the three data sets obtained using linear R-squared regression method (MATLAB). All three of the fits have R-squared values indicating a poor fit to the data. There is, therefore, no suggestion that the difference in velocities between the experimental and simulated flow fields is dependent on distance from the cell body. The mean difference in the experimental and simulated field at the nodes in the x_1, x_2 and x_3 directions is $-0.0985 \pm 0.0001 \mu m s^{-1}$, $0.0961 \pm 0.0002 \mu m s^{-1}$ and $0.0438 \pm 0.0001 \mu m s^{-1}$ respectively, where the error shown is the standard error (standard deviation / number of nodes). All three of these difference values are $< 10\%$ of the mean magnitude of the field and the maximum deviation at any of the nodes is $0.6145 \mu m s^{-1}$, which is around a third of the mean magnitude of velocity. These results show that there is good agreement between the simulated and experimental fields.

5.4.4 Discussion

In this section, the experimentally derived flow field around a single cell time-averaged over 20s and averaged over 20 cells in the control sample was compared to the corresponding simulated flow field. The good agreement of the two fields suggests that the simple model does effectively capture the flow field induced around a single, surface-attached cell with a moving flagellum. No dependency on the difference in velocity on distance from the centre of the experimental cell body was seen and the differences in velocity in the three directions x_1, x_2 and x_3 was of similar scale, suggesting that the differences in velocity fields did not have a systematic cause. One cause of the differences in the fields could be that the dampening of Brownian motion near surfaces, described by Drescher *et al* [23], is not included in the simulated particle trajectories used to determine the simulated flow field.
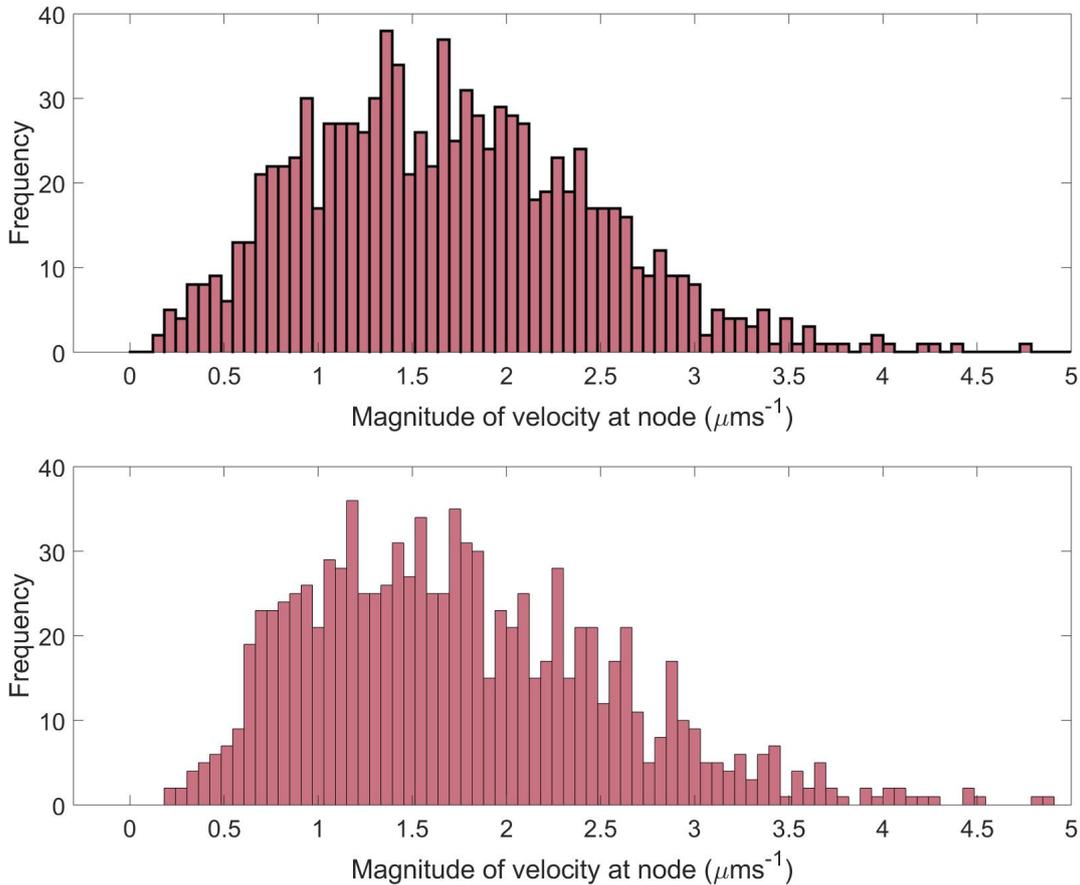
FIGURE 5.9.

Top: Histogram showing the distribution of velocity magnitudes at each node in the average, time-averaged field around 20 simulated individual cells with a flagellar reversal rate of $0.03s^{-1}$ (control reversal rate). Bottom: Histogram showing the distribution of velocity magnitudes at each node in the average, time-averaged field around 20 individual cells in the experimental control sample. The mean velocity magnitude of the simulated and experimental samples are $1.69\mu ms^{-1}$ and $1.75\mu ms^{-1}$ respectively. The standard deviation on the simulated and experimental means are $0.76\mu ms^{-1}$ and $0.81\mu ms^{-1}$ respectively. Therefore, a t-test on the 925 nodes compared gives a P-value of 0.1118 suggesting that the difference in distribution of velocity magnitudes of the fields is not statistically significant.
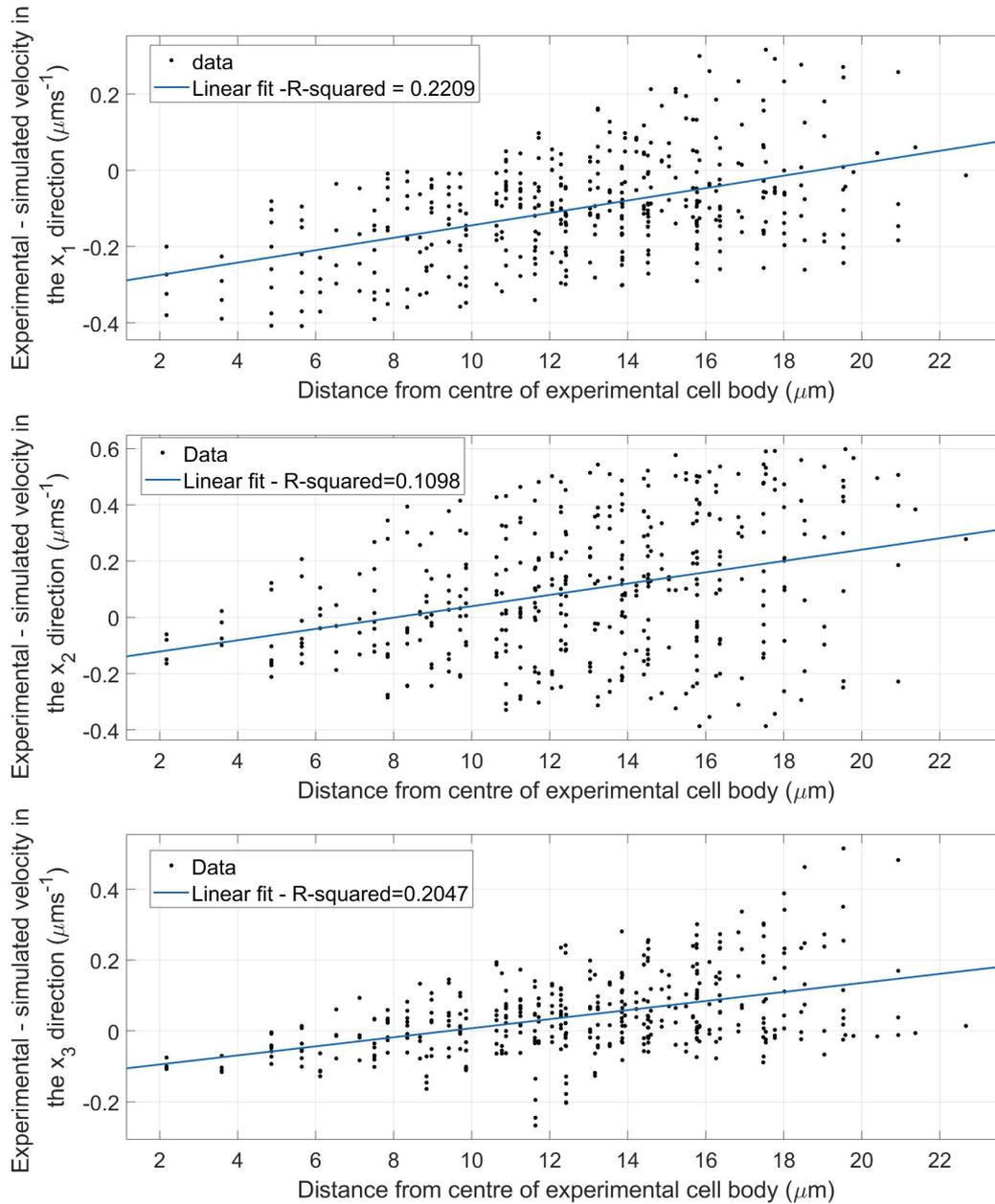
FIGURE 5.10.

From top to bottom: The difference in velocity in the x_1, x_2 and x_3 directions respectively, between the experimental and simulated flow fields plotted against the distance of the node point from the centre of the experimental cell body. Also plotted is line of best fit to each of the three data sets obtained using linear R-squared regression method (MATLAB). All three of the fits have R-squared values indicating a poor fit to the data. There is, therefore, no suggestion that the difference in velocities between the experimental and simulated flow fields is dependent on distance from the cell body.

Furthermore, in chapter 4, it was discussed that a possible electrostatic surface effect could be the cause of an increased density of beads near the surface in the experiment. Such a surface effect was not included in the model and therefore, an accumulation of tracers near the surface was not seen. Including these different effects in the model could be investigated to improve the agreement of the simulated and experimental fields.

5.5   Chapter conclusions

In this chapter, a simple model for a surface-attached cell with a motile flagellum is presented. The flagellum is represented by singularity solutions to the Stokes equations tethered to a no-slip boundary and the effect of the surface is determined by using the method of images. The flagellum is allowed to respond to the induced flow field and the flagellar dynamics of a single flagellum are investigated.

Three key parameters of the non-dimensional model were identified: α representing the size of the flagellar body, β controlling the ratio of Stokeslet to rotlet strengths and k_H determining the rigidity of the flagellar hook. As suitable values for α and β can be found in the literature, standard values for these parameters were used throughout all simulations.

The literature suggests that the value of k_H would have a significant impact on the dynamics of the simulated flagellum and, although studies have presented values for k_H that result in a stable flagellum, there is little experimental data on the rigidity of the flagellar hook in *P. aeruginosa*, although data is available for *E. coli* [205]. In this chapter, the flagellar dynamics of different values of k_H were investigated. For large k_H, the flagellum reaches a stable orientation, which aligns with the suggestion from the literature that a large k_H ensures a stable flagellum. A small k_H induces the flagellum to oscillate around the fixed position again suggesting that k_H is key to the stability of the flagellum.

Using the smallest k_H that produced stable results, the time-averaged induced flow field was compared to the experimental field found in chapter 4. There was good agreement between the two time-averaged fields. Issues with the averaging of the experimental field were the reason for comparing time-averaged rather than instantaneous fields. The model captures the instantaneous flow making it a useful tool in understanding the flow

around a surface-attached cell with a mobile flagellum, which is difficult to determine experimentally.

One thing adding to the complexity of the system is that real flagella are known to reverse their direction of rotation. To reflect the variation in reversal rates for the control and lactam cells seen in chapter 3, the flagellar dynamics of cells with the two reversal rates were investigated using the simulation. This investigation determined that the increased reversal rate when the cells are exposed to lactam enhances the transport of particles. In chapter 6 this is further investigated by studying the effect of reversal rate on the motion of tracers near a bed of simulated flagella.

MODELLING MULTIPLE CELLS ON A SURFACE

"I have complete faith in the continued absurdity of whatever is going on."

Jon Stewart

6.1 Introduction

In chapter 4, the flow induced by a stationary, surface-attached cell with a motile flagellum was investigated experimentally. In chapter 5, a simple model was developed in an attempt to capture this same flow. The primary reason for developing such a simple model was to be able to investigate complex systems that are difficult to study experimentally and too computationally expensive for other models. The focus for this thesis is the implication that the experimentally observed flows may have on biofilm formation. As motility is down-regulated in the later stages of biofilm formation, [?] it is likely that this form of motility will only impact nascent biofilms. Therefore, in this chapter, the simple model is used to investigate the dynamics of small numbers of interacting cells. To investigate any possible effects of the lactam analogue, this model is also used to investigate the impact on flagellar dynamics and simulated tracer particle motion from changing flagellar reversal rates.

6.2 Two cells

6.2.1 Motivation

As one of the earliest stages of biofilm formation is cluster formation (see chapter 1), it is interesting to investigate how close cells have to be to one another to interact according to the simple model developed in chapter 5. It is also important how a nearby cell may impact the flagellar dynamics, and hence the flow field associated with a cell. This of course impacts the motion of particles within the flow. Therefore, here the effect of cell separation on particle distribution is investigated.

In this section the simple model developed in chapter 5 is utilised. Here, flagella of two closely-situated cells react to the flow field associated with their neighbour in conjunction with their own induced image system flow. The results here are presented in non-dimensional units (ndu) but it should be remembered that the non-dimensional characteristic length is 0.5μm and so non-dimensional length units should be multiplied by the characteristic length to obtain the dimensional length. Time is also given in non-dimensional units and 100 equates to 1s.

6.2.2 Results

6.2.2.1 Effect of distance on flagellar dynamics

Here, the dynamics of the two flagella are investigated for 800 time steps and various cell separation distances. A minimum separation of 10 non-dimensional units (ndu) was used since at shorter separations than this the flagella often came too close together causing problems with computation. The two cell bodies were long-axis attached to the surface and orientated so the flagella were pointing towards each other (meaning the b_ϕ angles were 0, π see figure 6.1). Here the start θ angles of the two flagella were both $= \pi/4$ and $\phi = 3.5\pi/2,\ 1.6\pi/2$ for the flagella of cell 1 and 2 respectively. Here, all angles are relative to the lab frame. These different ϕ angles were chosen to prevent the flagella starting too close to each other but after trying a few different initial angles it seems that the initial angles have little impact on the equilibrium configuration.

Figure 6.2 shows the θ and ϕ dynamics of the first cell for various cell separation distances and figure 6.3 shows the same for the second cell. It is interesting that for a cell separation of 10ndu, the dynamics of both cells are very similar to those seen for a single, isolated cell in chapter 5. This may seem counter-intuitive as cells close to each
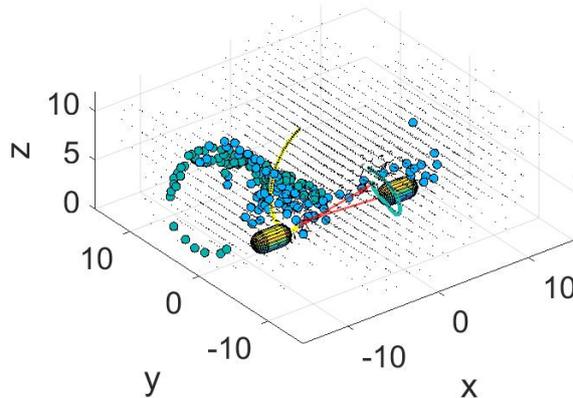
<small>F</small>IGURE 6.1.
The tracer positions and flagellar orientation for the two cell arrangement when the cell separation is 10ndu after 50 time units. Arrangement of the cell bodies are shown and the black arrows indicate the flow field.

other may be expected to have the most impact on each other. However, in this 10ndu arrangement, the centre of each flagella settles into a position close to the tether of the other flagellum. Therefore, the moment of the flow from one flagellum will have very little impact on the tether point torques.

Increasing the separation distance from 10ndu to 15 or 20ndu has the effect of pushing the flagellum of cell 1 closer to the boundary and decreasing its ϕ angle and having the opposite effect on cell 2. This can be explained by the fact that the 'ideal' or isolated cell position for the two flagellum are now between C and D. This means that with increasing separation, the flow due to one flagellum with have an increasing torque at the tether point of the second flagellum. This acts in the opposite direction to the image of the second flagellum and so has almost the effect of increasing the hook torque. For the larger of the two separations, 20ndu, there is a 'wobble in the dynamics before they settle into their stable orientations. This can be explained by the fact that the flagella start with a small θ and the trajectory of an isolated cell is that θ increases. As the two cells are approaching the boundary in this way the become close and so are strongly affected by each other's field until they move far enough apart that they can settle into their stable orientations. This effect is also seen when the separation is 25ndu, but in this case, the two flagella never move far enough away from each other and so the steady state is oscillatory.
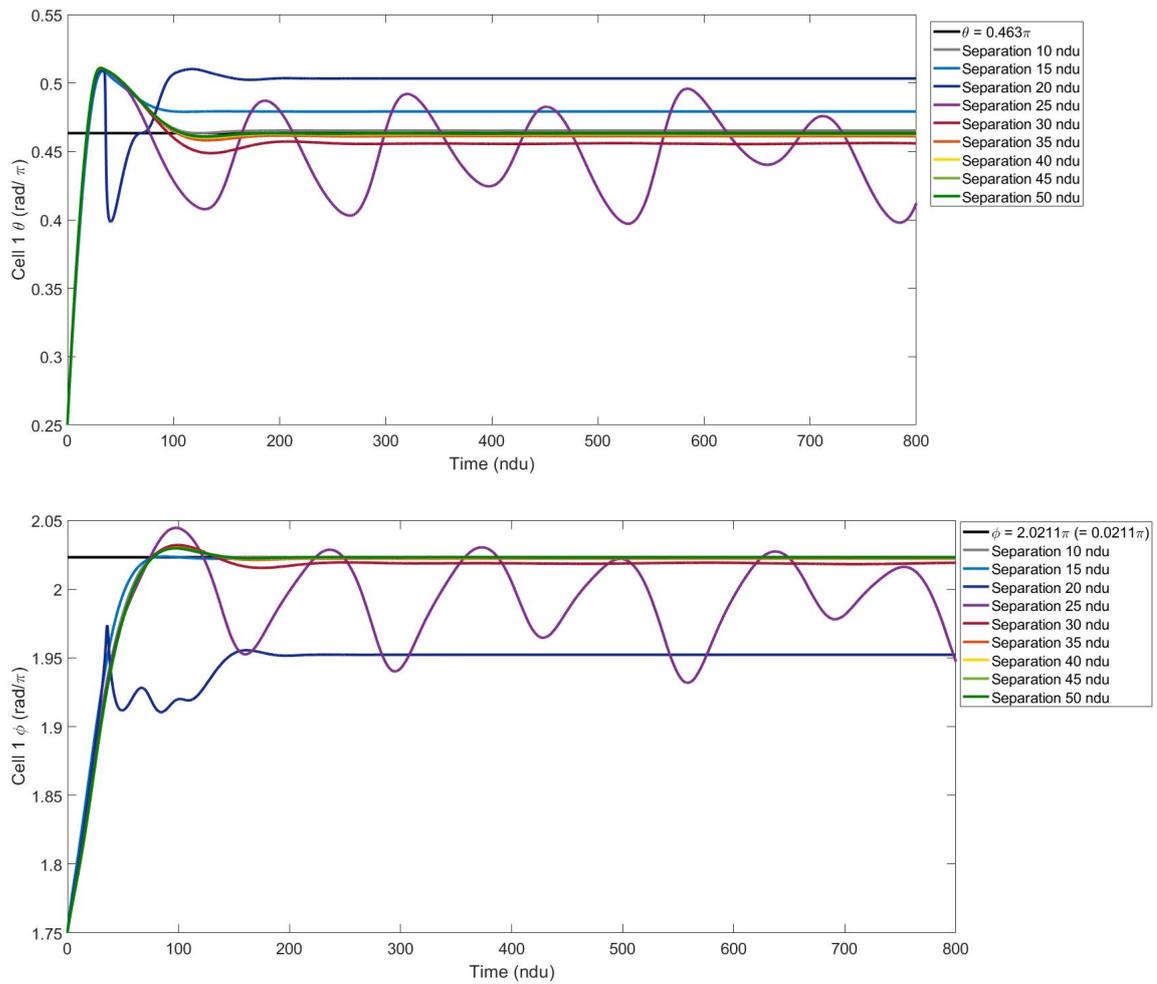
FIGURE 6.2.

Top: the θ angle (angle from the vertical) for the cell 1 over 800 time steps. In this simulation, there are two cells separated by various distances indicated by colour. Bottom: the ϕ angle (angle around the vertical) for the same cell.
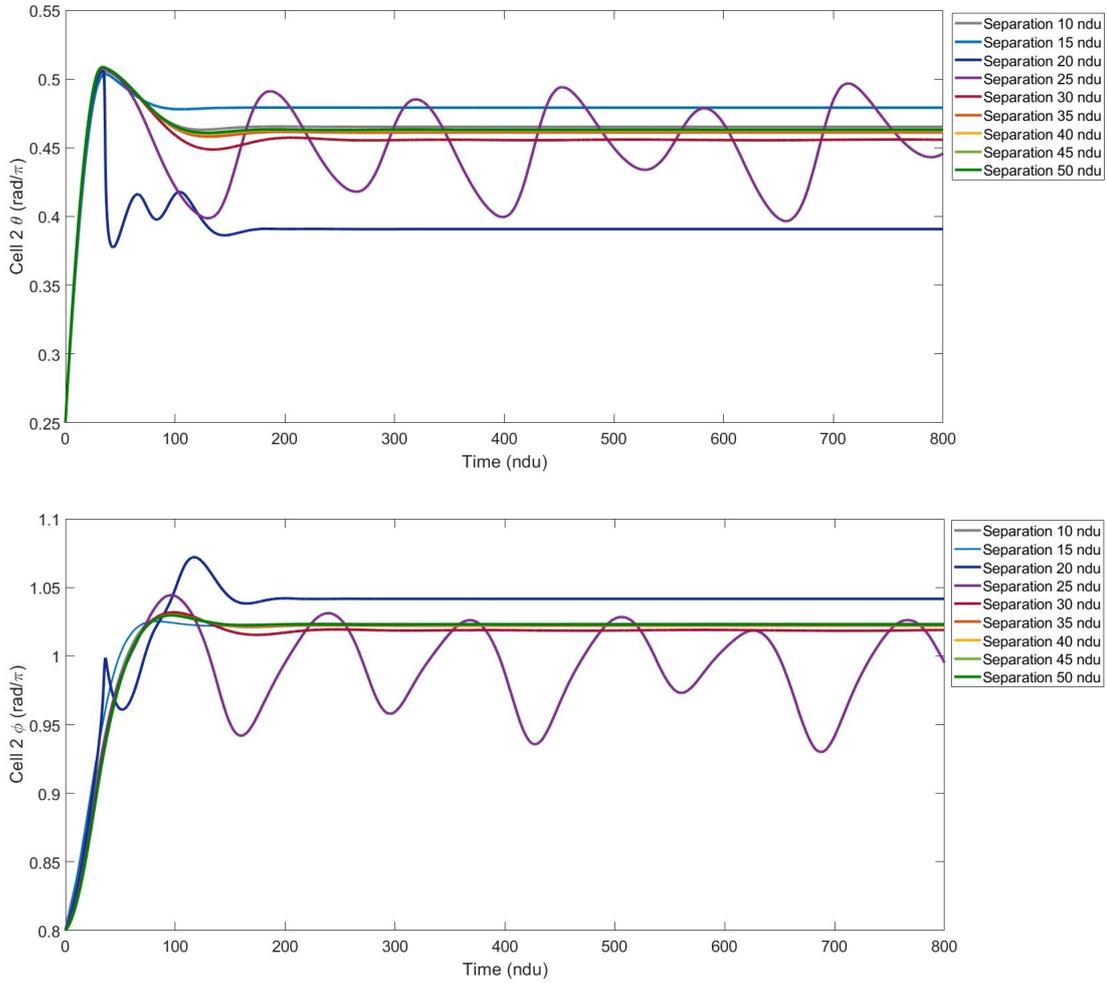
FIGURE 6.3.

Top: the θ angle (angle from the vertical) for the cell 2 over 800 time steps. In this simulation, there are two cells separated by various distances indicated by colour. Bottom: the ϕ angle (angle around the vertical) for the same cell.

Further increasing the cell separation sees the reverse of the trend for 15 and 20ndu separations until at a separation of 50ndu the two cells appear as two isolated cells. This is intuitively because the increased separation means the two cells are exposed to less of the field from each other, (as the Stokeslet term decays as $1/r$).

The flagellar dynamics discussed in this section are for a single arrangement of cells. To investigate the impact of relative cell orientations on dynamics, the above simulations were repeated with the b_ϕ angle for cell 1 being set at $pi/2, \pi$ and $,3\pi/2$. There results

were then compared to those in this section with the b_ϕ angle for cell 1 being 1. The data for these repeats is not shown in this thesis but is discussed below. For the repeats, the flagellar dynamics appeared identical for the different separation values with the two flagella obtaining stable fixed angles within 50 non-dimensional time units. In this way, the separation distance appears to be less important in the determination of the flagellar dynamics than the relative cell orientation. For these repeats the initial flagellar orientation (relative to the cell body) is the same as in the above investigation. An investigation into changing the initial flagellar orientation (data not shown) indicates that, for $k_H = 0.5$, cell body orientation has more of an impact on flagellar dynamics than initial flagellar angles (so long as the initial angles are not causing the flagellum to encounter the 'cell body').

6.2.2.2 Effect of varying k_H

In chapter 5, the parameter k_H was identified as important in determining the flagellar dynamics of a single cell. k_H is defined as the ratio between the bending stiffness of the flagellar hook and a product of the hook length and motor torque. This definition for k_H is based on work by Jabbarzadeh and Fu who determined that for values of $k_H < 0.5$, the flagellum would be unstable [26]. In chapter 5, an investigation into the flagellar dynamics of a single cell with different k_H values aligned with this. In this section the flagellar dynamics of two cells with their flagellum-tethering poles pointing together are investigated for different k_H values. Figures 6.4 and 6.5 show the flagellar dynamics for the two cells over 800 non-dimensional time units for various values of k_H. The two cells are separated by a distance of 10ndu and are orientated as in the previous section, with their flagellum-tethering poles pointing together. As in the single cell simulations, for values of $k_H \geq 0.5$, the flagella achieve long-time stable angles and values of $k_h < 0.5$ result in oscillations of the flagellar angles. The similarity of the results in these graphs with those of a single cell show that the parameter k_H is very important in the determination of flagellar dynamics and is just as important as the flow of nearby cells.

The plots in this section only represent the dynamics for a single cell orientation arrangement. This arrangement was chosen because results in the previous section suggested that this arrangement was the one in which the two flagella were most likely to interact, and, therefore, was the one in which any impact of changing k_H might be the most clear. In order to test this hypothesis, the above simulation was repeated with the b_ϕ angle of cell 1 being either $\pi/2, \pi$ or $3\pi/2$ (data not shown) keeping the relative initial
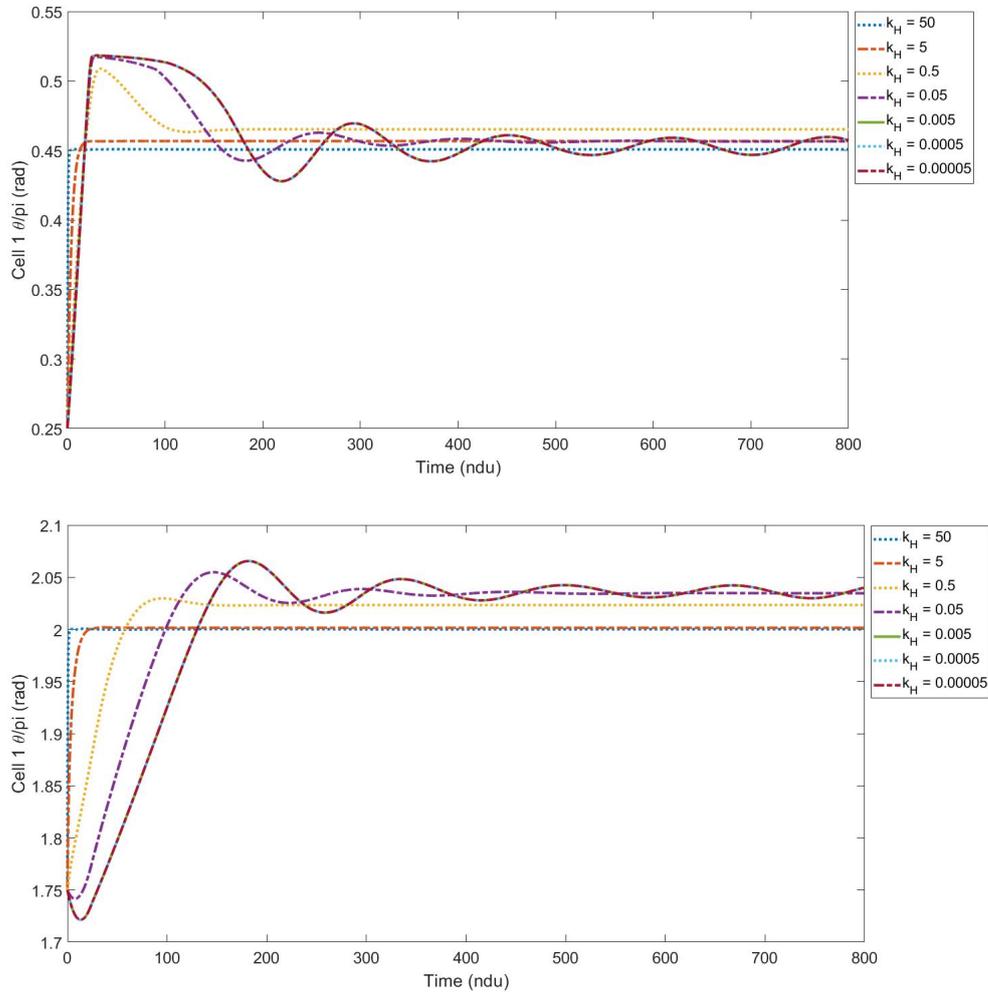
FIGURE 6.4.
From top to bottom, the θ and ϕ flagellar angles for cell 1 in a two cell arrangement over 800 non-dimensional time units. The two cells are 10ndu apart and have their flagellum-tethering poles pointing towards each other. Show are the flagellar dynamics for various k_H values. Values of k_H smaller than 0.5 can be seen to produce oscillating dynamics whilst 0.5 and above obtains stable angles.
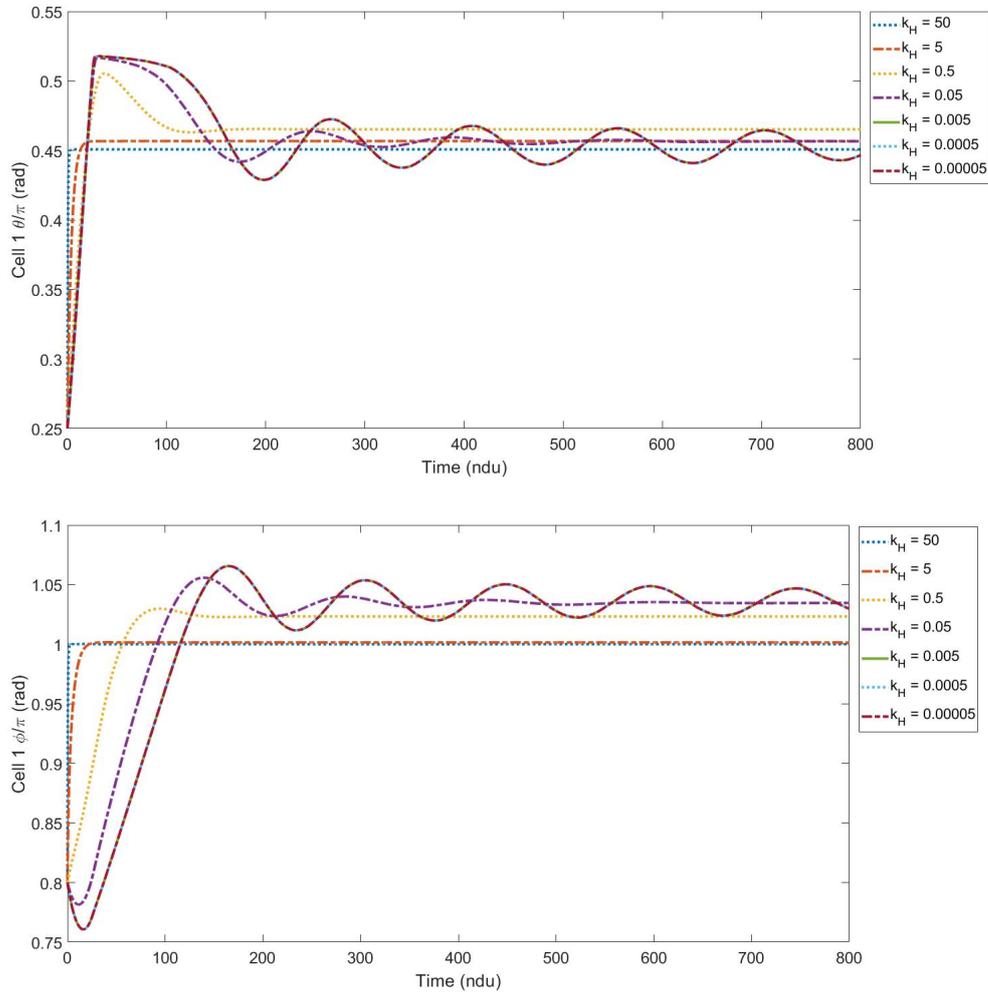
FIGURE 6.5.
From top to bottom, the θ and ϕ flagellar angles for cell 2 in a two cell arrangement over 800 non-dimensional time units. The two cells are 10ndu apart and have their flagellum-tethering poles pointing towards each other. Show are the flagellar dynamics for various k_H values. Values of k_H smaller than 0.5 can be seen to produce oscillating dynamics whilst 0.5 and above obtains stable angles.
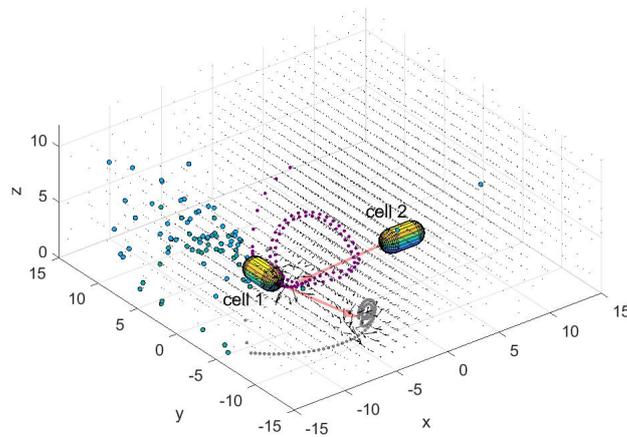
FIGURE 6.6.
  The two cell arrangement where the b_ϕ angle of cell 1 is set at $3\pi/2$ after 800 time units. The positions of the tracers are shown in blue and the black arrows indicate the flow field. The flagella positions are shown with the red arrows and the path followed by the point C for cell 1 and 2 are shown by the grey and purple dots respectively. For this simulation, $k_H = 0.005$ which is lower than the threshold for a stable hook ($K_H = 0.5$), resulting in the oscillating of the flagellar angles seen.

flagella positions and all other parameters the same. In these repeats, changing the value of k_H had the same impact on flagellar dynamics as seen previously in this section. Namely, $k_H \geq 0.5$ resulted in a long-time stable angle of the flagella whilst $k_H > 0.5$ saw oscillations in the angles. Figure 6.6 shows an example arrangement where the b_ϕ angle of cell 1 is set at $3\pi/2$ after 800 time units. The positions of the tracers are shown in blue and the black arrows indicate the flow field. The flagella positions are shown with the red arrows and the path followed by the point C for cell 1 and 2 are shown by the grey and purple dots respectively. For this simulation, $k_H = 0.005$ which is lower than the threshold for a stable hook ($K_H = 0.5$), resulting in the oscillating of the flagellar angles seen. This work suggests that at a cell separation of 10ndu, the value of k_H is more influential on flagellar dynamics than relative cell orientation.

6.3 Three cells

6.3.1 Motivation

The results in the previous section show that cell separation, relative cell orientation and the parameter k_H are all important in determining the flagellar dynamics of a two cell system. A crucial stage in biofilm formation is cluster formation. Moving on from two cells, in this section, the next simplest case of a three cell cluster is investigated. The aim is to begin to understand how nearby cells may impact each others' flagellar dynamics as the clusters begin to grow. To simplify the study, three key cell arrangements are chosen and the cell separation is kept at the smallest of 10ndu - since microscopy images show cells in many cell clusters are within a few microns of their neighbours [60]. The sensitivity of flagellar dynamics on cell arrangement is discussed and the impact of changing k_H is shown. In all the work in this section, the 'realistic' values discussed in chapter 5 were used unless otherwise stated.

6.3.2 Results

6.3.2.1 Flagellum-tethering poles pointing together

As with the two cell case, the first three cell arrangement studied is that of three evenly spaced cells in a triangle with their flagellum-tethering poles pointing together (see top figure in figure 6.7. This is the most symmetric arrangement in which the flagellum are the closest and, as such, is one of the simplest to begin to understand the interacting flagellar dynamics. The lower figure in figure 6.7 shows plots of the θ angle for the flagellum of cell 1 for various values of k_H over 800 non-dimensional time units. The longtime stable θ angle obtained for a single, isolated cell with $k_H = 0.5$ is shown for reference. Only the θ angle of cell 1 is shown as the general pattern repeats for the different cells and for ϕ (i.e. longtime stable fixed angles, oscillations or chaos). The initial θ angles for all the cells are set at $0.25\pi/2$ and the ϕ angles for cell 1,2 and 3 are set at $2.2\pi.2, 2.5\pi/3$ and $2.5\pi/3$ respectively. b_ϕ angles for cells 1,2 and 3 are set at $0, 2\pi/3$ and $-2\pi/3$ respectively. Although the data is not shown, the longtime dynamics were not altered by a change in the initial angles so long as the angles were chosen so as the 'flagellum' did not 'pass through the cell body'. This is a particularly interesting arrangement because it shows that a comparatively simple system can produce dramatically different results depending solely on a change in k_H. As with the single and two cell systems, the flagella obtain longtime fixed angles for $k_h = 50$ and $k_H = 5$. However, when $k_H = 0.5$ or

170

$k_H = 0.05$, oscillations in the flagellar angles are seen. Reducing the k_H slightly to 0.005 sees these oscillations breaking down into chaos. Further reduction of k_H results in the flagella obtaining longtime fixed angles. These results show how dependent on k_H the flagellar dynamics are.

To also try to understand the importance of relative cell orientation on the dynamics of this arrangement, above simulations were repeated but the b_ϕ angle of cell 1 was varied from the 'regular arrangement in figure 6.7 (data not shown). First the b_ϕ was set to π, keeping the initial flagellar angles relative to the cell body constant. This symmetric arrangement resulted in flagellar dynamics similar to those in the single and two cell arrangements. Again, k_H values 0f 0.5 and above resulted in longtime fixed flagellar angles whilst smaller k_H values resulted in oscillations in the angles. However, the dynamics differed from the single cell in a slight difference in the fixed angles obtained and in a slight damping of the oscillations in flagellar angles seen for small k_H values. These deviations can be explained by the flow of neighbouring cells providing further resistance to the body-hook torque and so lessening amplitude of oscillations.

The two arrangements discussed here are useful starting points as their symmetry and regular arrangements make it easier to understand the dependencies of the flagellar dynamics on k_H and cell orientation. However, a major motivation for developing this model was to be able to use it to study real-life scenarios and it is unlikely a real pre-biofilm cluster would form in such a regular pattern. Therefore, the flagellar dynamics of the system was also studied when b_ϕ of cell 1 was given various random values (data not shown). In all cases the initial flagellar angles relative to the cell body were kept the same as in the 'regular' arrangements above. In all such simulations, the flagellar dynamics behaved much the same as in the case of $b_\phi = \pi$ for cell 1, with the only difference being a small variation in the fixed angles and the amount of damping on the oscillations. Varying the initial flagellar angles had very little impact on the longtime dynamics so long as the flagellum did not 'pass through' the cell body location for the initial angle. These results suggest that, although relative orientation of neighbouring cells have a small impact on flagellar dynamics, a qualitative shift in the dynamics is seen when k_H is varied.
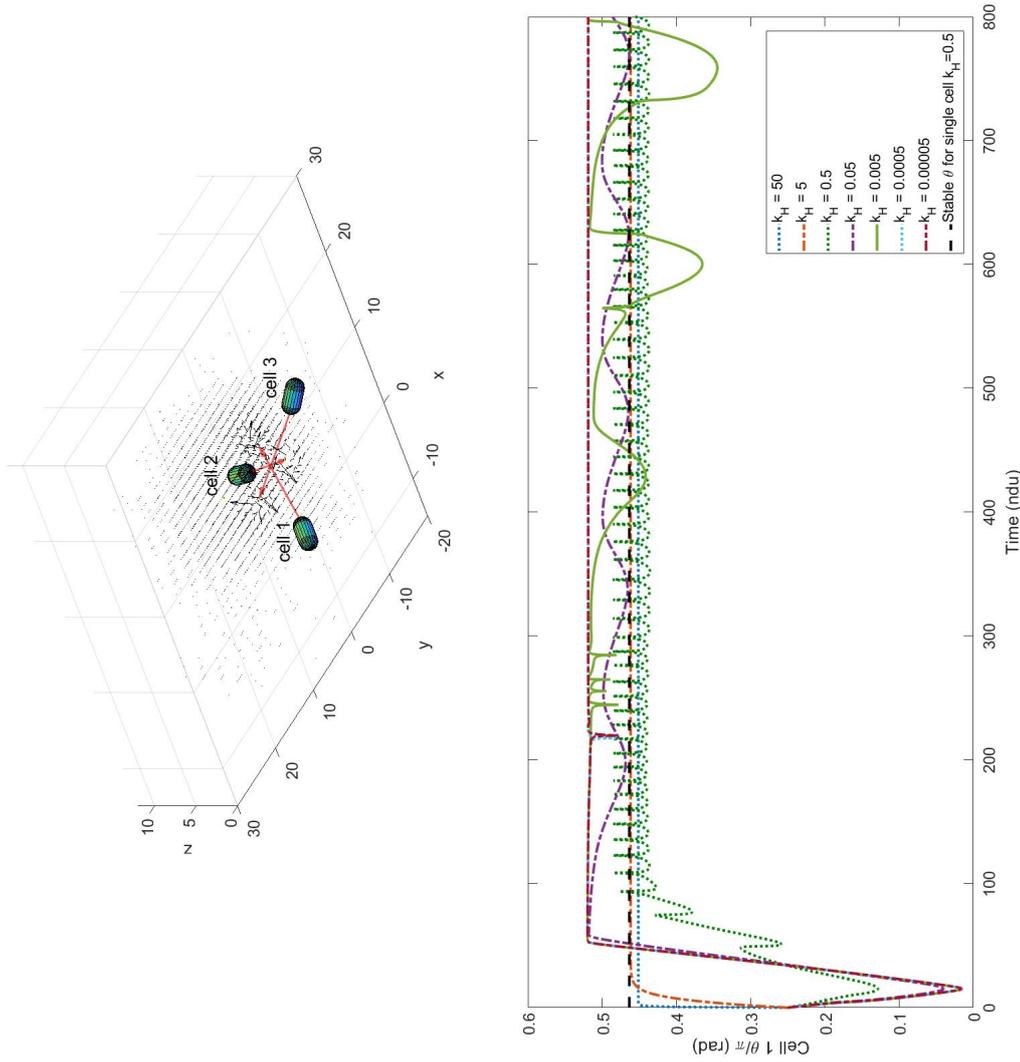
FIGURE 6.7.

Top: an example frame from the simulation of three cells with their flagellum-tethering poles pointing together to show the arrangement. Red arrows show the flagella positions, black arrows show the relative flow velocity. Bottom: the θ angle for the cell 1 flagellum over 800 non-dimensional time units for various values of k_H. Patterns of angle dynamics (i.e. fixed angle, oscillating, chaotic) are repeated for other flagella angles.

6.3.2.2 Flagellum-tethering poles pointing apart

In this section, the dynamics of a three cell system with the cells having their flagellum-tethering poles pointing away from each other are studied. As before, first the dynamics of the 'regular' arrangement are investigated. In this arrangement, the relative initial flagellar angles were kept the same as in the previous subsection but the b_ϕ angles for cells 1,2 and 3 were set at $\pi, -\pi/3$ and $\pi/3$ respectively (see top figure in figure 6.8). Again, only the θ angle for cell 1 over 800 non-dimensional time units and different k_H values is shown as the pattern of dynamics repeats (bottom figure in figure 6.8). In this arrangement, the dynamics follow very similar patterns to those of individual cells with k_H values of 0.5 and above resulting in longtime fixed angles for the flagella and smaller k_H values seeing oscillations. In fact, for $k_H = 0.5$, the fixed angles obtained are the same as those for the single cell. The only difference in the dynamics compared to the single cell is a damping of the oscillations for small k_H. This phenomenon was also seen in the previous subsection and can be attributed to the flow of neighbouring cells providing more resistance to the body-hook torque.

As before, variations on this 'regular' arrangement were also studied by altering the b_ϕ for cell 1 whilst keeping the relative initial flagellar angles constant. In this case, all variations showed very similar, predictable dynamics (data not shown). In all cases, k_H values of 0.5 and above resulted in stable fixed angles the varied only slightly from the single cell case and $k_H > 0.5$ had oscillating flagellar angles that were slightly damped. This apparently minimal dependence on the orientation of cell 1 can be explained by the fact that, whilst the flagellum-tethering poles are separated by 10ndu in all these simulations, the flagella themselves are much further apart and so the impact of their flow on their neighbours is lessened.

6.3.2.3 Cells in a row

The final arrangement studied in this section is that of three cells in a row. All the cells are again separated by 10ndu and all have $b_\phi = 0$ with initial flagella angles of $\theta = \pi/8$ and $\phi = \pi/4$ (see top of figure 6.9). The θ angles for cell 1 over 800 non-dimensional time units and for different k_H values are shown in the the bottom figure in figure 6.9. For this arrangement k_H values of 0.5 and above obtain longtime fixed angles with $k_H = 0.5$ reaching the same longtime angles as in the single cell case with the same k_H. What is different about the dynamics in this case compared to those investigated earlier
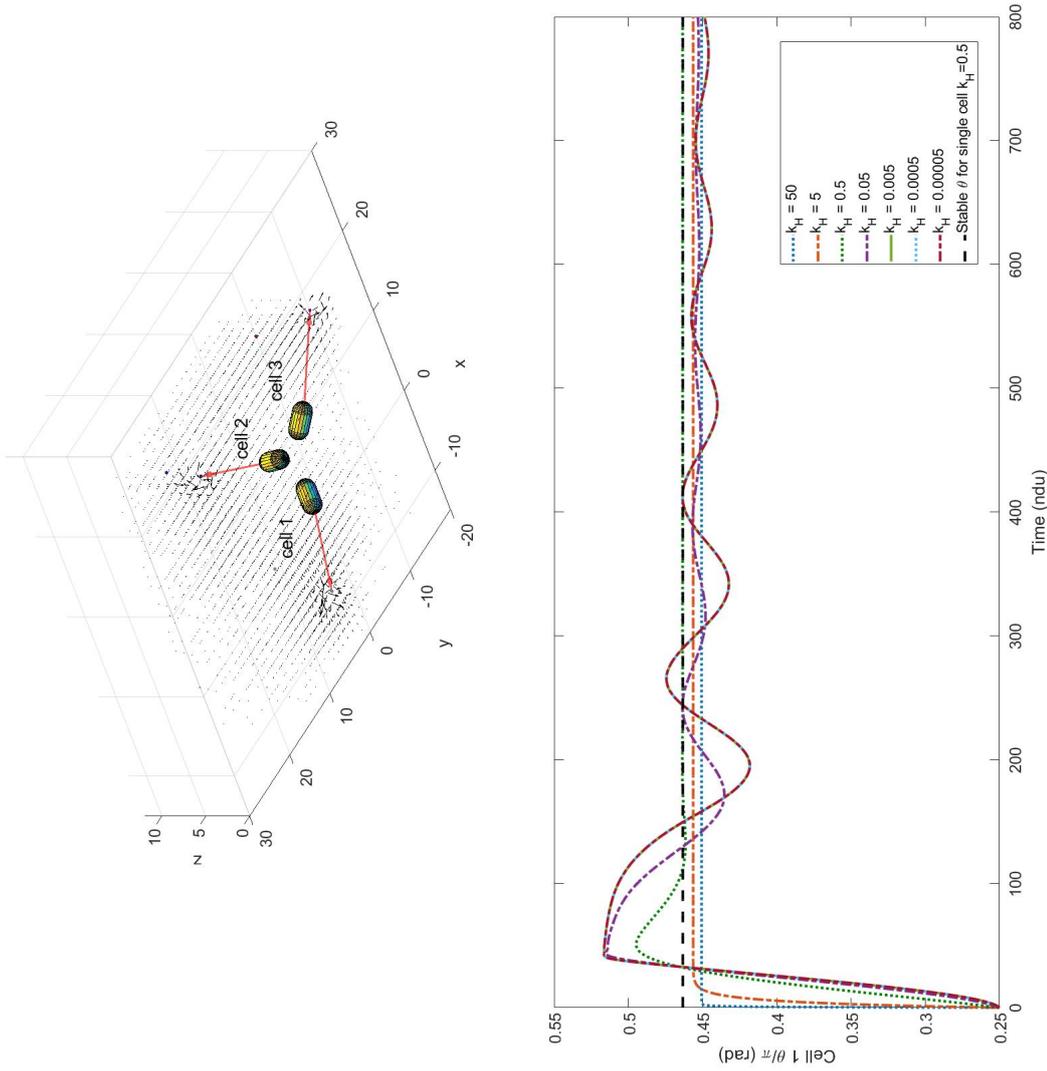
FIGURE 6.8.

Top: an example frame from the simulation of three cells with their flagellum-tethering poles pointing apart to show the arrangement. Red arrows show the flagella positions, black arrows show the relative flow velocity. Bottom: the θ angle for the cell 1 flagellum over 800 non-dimensional time units for various values of k_H. Patterns of angle dynamics (i.e. fixed angle, oscillating, chaotic) are repeated for other flagella angles.

is that smaller k_H, although they do have some oscillation in the flagellar dynamics, approach a fixed angle for after approximately 1400 time units (data not shown). In this arrangement, it appears that the k_H value is less important to the long-time dynamics as the flow induced by neighbouring cells act to stabilise the dynamics.

Again, to study the sensitivity of the system to the relative cell orientation the b_ϕ angle of cell 1 is varied and the simulations repeated (data not shown). In all cases, the dynamics conform to the pattern seen previously with $k_H \geq 0.5$ giving longtime fixed angles and smaller k_H values resulting in oscillations in the flagellar angles. Slightly different fixed angles are seen compared to the single cell which must be expected due to the flagellum being exposed to a slightly different field and therefore the steady states of the dynamical system being slightly different. The amplitude of oscillations when k_H is small is also slightly different to the single cell depending on cell 1 orientation. This can be explained by the flow induced by the neighbouring either acting for or against the body-hook torque. Despite these small variations, it appears that the flagellar dynamics of this arrangement are only qualitatively different when k_H is varied and are less sensitive to relative cell orientation.

6.3.3 Discussion

In this section, the flagellar dynamics of a range of three-cell orientations have been investigated. To simplify the investigation, three different arrangements of cell were studied and the sensitivity of their flagellar dynamics to relative cell orientation and k_H were discussed. These particular arrangements were chosen because many cell arrangements can be considered as slight deviations from these key arrangements. The results in this chapter suggest that, although some small quantitative difference were seen, the dynamics were fairly robust to changes in relative cell orientation apart from in the case of flagellum-tethering poles pointing directly together. The flagellar dynamics were far more dependent on the choice of k_H in these simulations. For all except the case of the flagellum-tethering poles pointing directly together, $k_H = 0.5$ (the value used for most of this thesis) resulted in all the flagella obtaining fixed angles over long time. In 2009, Hesse *et al* fluorescently imaged the flagella of Salmonella typhimurium and *Serratia marcescens* attached to glass [206]. They found that the flagella of neighbouring surface attached cells did interact with each other but did not form flagellar bundles (similar to those of swimming cells) as they might have expected. Instead, the flagella on the whole maintained fixed angles relative to the cell body
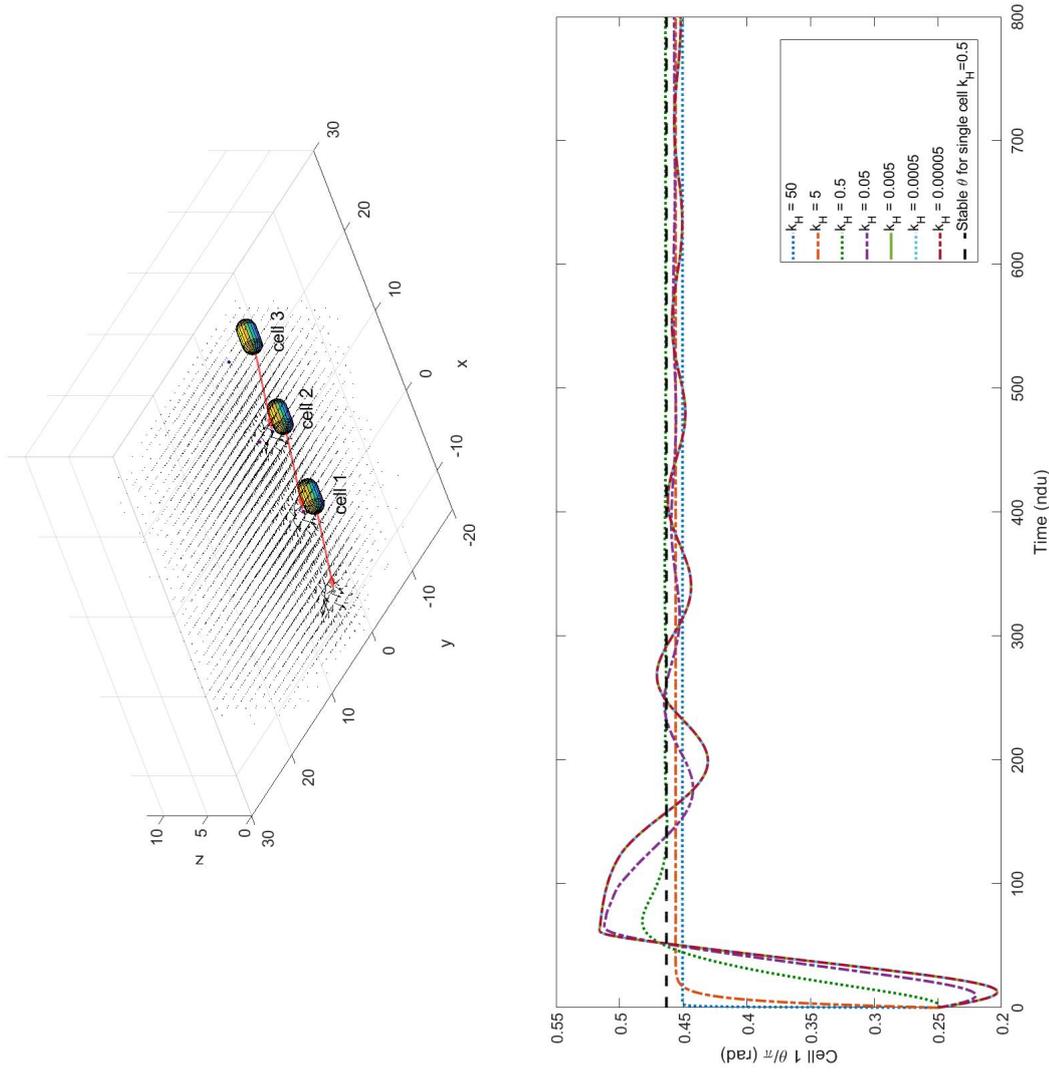
FIGURE 6.9.

Top: an example frame from the simulation of three cells in a row to show the arrangement. Red arrows show the flagella positions, black arrows show the relative flow velocity. Bottom: the θ angle for the cell 1 flagellum over 800 non-dimensional time units for various values of k_H. Patterns of angle dynamics (i.e. fixed angle, oscillating, chaotic) are repeated for other flagella angles.

for periods between polymorphic transitions. Although no data on the actual angles is presented, the qualitative similarities to the results in this section lend confidence to the choice of $k_H = 0.5$ in this thesis. An interesting extension to the work may be to consider whether the polymorphic transitions discussed in [206] can be replicated by introducing reversals and a variable tether length to the simulation.

6.4 Particle transport over cells

6.4.1 Motivation

In the previous section, the effect of cellular arrangement on flagellar and tracer dynamics was investigated. However, in that work, flagellar reversals were not investigated. In 2016, Faubel *et al* discovered that a cilia-based switch in the ventricles of mouse brains could alter the flow of cerebrospinal fluid, and so control the transport of substances [200]. Cilia and flagella are often modelled similarly [? ?] and therefore, [200] suggests that reversals in the flagellar rotation direction of aggregations of surface-attached cells with a moving flagellum may also impact transport of substances in flow. In this section, the effect of flagellar reversal rate and particle size on tracer transport is investigated. This is especially important to understand how the increase in reversal rate when cells are exposed to the lactam analogue may impact the ability of cells to communicate via QSM, encounter nutrients, and interact with planktonic cells.

6.4.2 Data collection

For this work, a cluster consisting of 9 cells are arranged in a rough grid. To better imitate a real life scenario, the cells are not regularly spaced and instead have have body

center co-ordinates, c_x, c_y, at:

$$(c_x, c_y) = \begin{bmatrix} -10.0, & 2.0 \\ 7.0, & 1.5 \\ 2.5, & 0.0 \\ -7.0, & 10.0 \\ 10.0, & 8.0 \\ 0.0, & 7.0 \\ -7.0, & -7.0 \\ 7.0, & -10.0 \\ 0.0, & 5.5 \end{bmatrix}. \tag{6.1}$$

Similarly, a variety of different cell angles are chosen to align with observations of cell clusters. The body angles for the cells in this section were set at (π, $-\pi/2$, $\pi/2.2$, $\pi/3$, π, $-\pi$, $-\pi/3$, $\pi/4$, π) and the initial flagella positions were $\theta = 0.25\pi/4$ for all cells and $\phi = 3.1\pi/2$, $\pi/3$, $\pi/3$, $\pi/3$, $\pi/3$, $3.1\pi/2$, $\pi/3$, $\pi/3$, $\pi/3$. The 8000 tracers, originating from a $20 \times 20 \times 10$ ndu grid centred on $(0, 0, 5.5)$ were followed for 400 time- steps. Figure 6.10 is an example timestep from the simulation to illustrate the body positions.

The tracer grid was specified by using MATLAB meshgrid to evenly arrange the tracers then adding Gaussian noise with a standard deviation of 0.1 to the position. It should be noted that, as the number of tracers in the x, y, and z directions were the same but the grid volume was shallower than it was wide, the tracers are closer in the z direction than in the x and y.

The reversal rates chosen were $10^{-6}, 10^{-5}, 10^{-4}, 10^{-3}, 10^{-2}, 3 \times 10^{-2}, 8 \times 10^{-2}, 10^{-1} 10^{0}, 10^{1}$ s^{-1}. The reversal rates experimentally determined for the lactam and control samples were chosen to understand the impact of this small change in reversal rate on tracer transport. The other reversal rates chosen are orders of magnitude different from those experimentally determined to understand the impact of dramatically changing reversal rate.

6.4.3 Results

To investigate the impact of reversal rate on the dynamics, the particle size was initially kept constant at 10^{-8}m (similar to that of QSMs). The particle size only impacts the
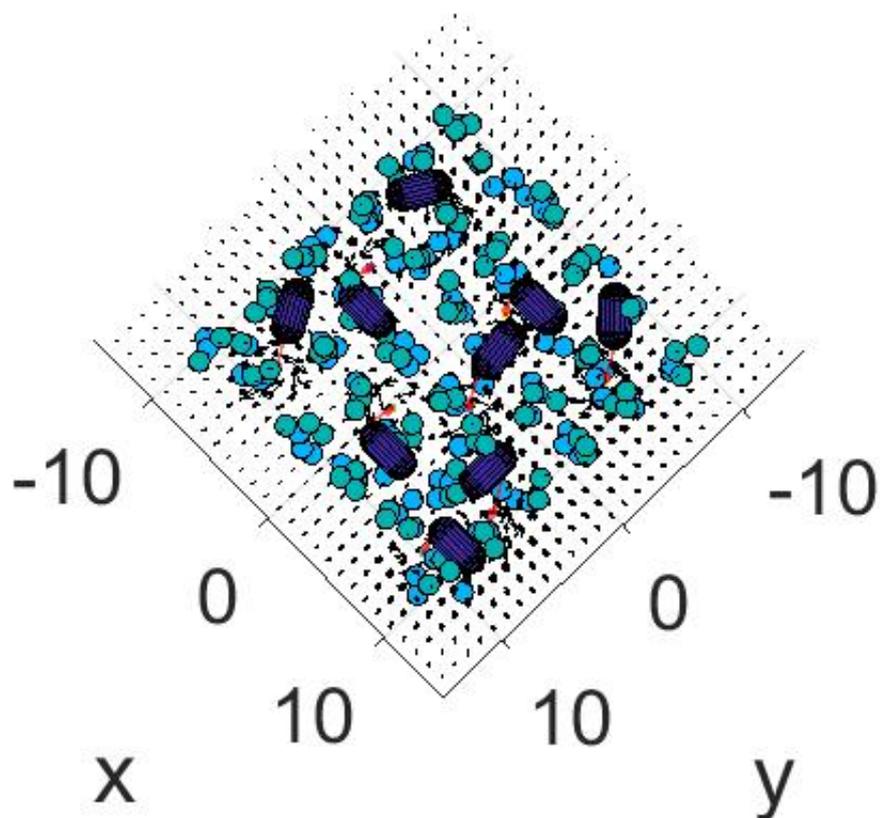
FIGURE 6.10.

An example timestep from the simulation of tracers over a grid of cells. Cell body positions and orientations are shown by spheroids, tracers are shown by blue and green circles. The flagella are shown by red arrows and black arrows show the field. In this case, the tracer size was set at 10^{-8}m, the reversal rate was 0.03s^{-1} and the time step was 10. The same body positions and initial positions for tracers and flagella were used for all subsequent simulations in this section.

particle dynamics in that it controls the size of the Brownian motion term added at each time-step (using the same technique as discussed in chapter 5). Figure 6.11 shows the mean distance of 8000 particles from their start position over a grid of 9 cells with varying flagellar reversal rates over time. Data shown is the mean of 3 repeated simulations and a plot of purely Brownian motion is shown in black. After approximately 100 non-dimensional time units, all the particle vs time plots are similar to the no-cells plot, suggesting that after this diffusion dominates (shaded region). Notably, the lactam reversal rate of $0.08s^{-1}$ transports the particles considerably further than the control of $0.03s^{-1}$.

To investigate whether the lactam consistently enhanced particle transport, the above simulation was repeated with various particle sizes. The different tracer sizes used were $10^{-10}, 10^{-9}, 10^{-8}, 10^{-7}, 10^{-6}$ m (converted to non-dimensional units). These sizes were chosen as the range incorporates the order of magnitude of the Van der Waals Radius of a hydrogen atom [207] and the order of magnitude of a bacterial cell (to understand how planktonic cells may be impacted by surface attached cells). The different sizes impact the Brownian motion applied to the tracers but the particles are still modelled as point particles without a volume and so the despite the different sizes, the particles are all impacted by the induced flow the same.

Figure 6.12 is a heat map showing the mean distance of 8000 simulated particles from their start position after 100 non-dimensional time units for various particle sizes and flagellar reversal rates. Particles are moved by a combination of simulated Brownian motion and the flow induced by a grid of the 9 cells. Colour indicates the log_{10} of the mean distance. Values shown are a mean of 3 repeated simulations. As expected, small particles travel further which is an effect of the simulated Brownian motion term. Particles consistently travel further when the cells are at their lactam reversal rate compared to control.

6.4.4   Discussion

In this section, the impact of flagellar reversal rate and particle size on particle transport has been investigated. For all particle sizes, the lactam reversal rate results in enhanced transport of particles compared to the control reversal rate. As discussed in chapter 5, this results was also seen when particle transport due to individual cells was investigated and aligns with work in the literature that found enhanced transport of particles when cilia reversal direction more frequently [200]. Furthermore, it is interesting to note that
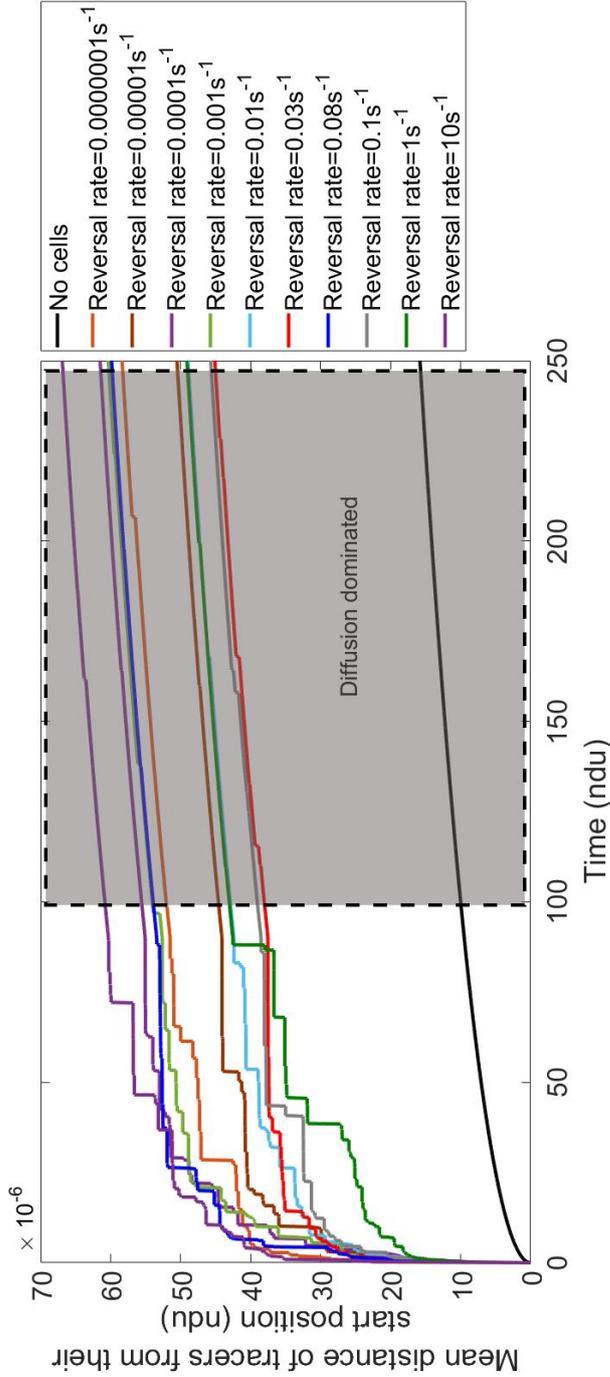
FIGURE 6.11.
The mean distance of 8000 particles from their start position over a grid of 9 cells with varying flagellar reversal rates over time. Particles have a diameters of 10^{-8}m (similar to QSMs) and this particle size is only used to model Brownian motion. Data shown is the mean of 3 repeated simulations and a plot of purely Brownian motion is shown in black. After approximately 100 non-dimensional time units, all the particle vs time plots are similar to the no-cells plot, suggesting that after this diffusion dominates (shaded region). Notably, the lactam reversal rate of $0.08s^{-1}$ transports the particles considerably further than the control of $0.03s^{-1}$.

Particle diameter (m)	0.000001	0.00001	0.0001	0.001	0.01	0.03	0.08	0.1	1	10
1e-10	2.338	2.029	2.731	2.888	2.71	2.538	2.675	2.474	2.557	2.478
1e-09	1.989	1.94	2.072	2.161	1.915	2.064	2.165	2.003	1.988	1.973
1e-08	1.717	1.649	1.745	1.733	1.632	1.58	1.732	1.592	1.634	1.784
1e-07	1.38	1.237	1.311	1.279	1.301	1.23	1.342	1.273	1.245	1.322
1e-06	0.7324	0.6675	0.8085	0.638	0.7284	0.7376	0.8374	0.81	0.7375	0.7805

Flagellar reversal rate (per sec)

Colour scale: 2.8, 2.6, 2.4, 2.2, 2, 1.8, 1.6, 1.4, 1.2, 1, 0.8

Log_{10} of mean particle distance from start after 100 non-dimensional time units.
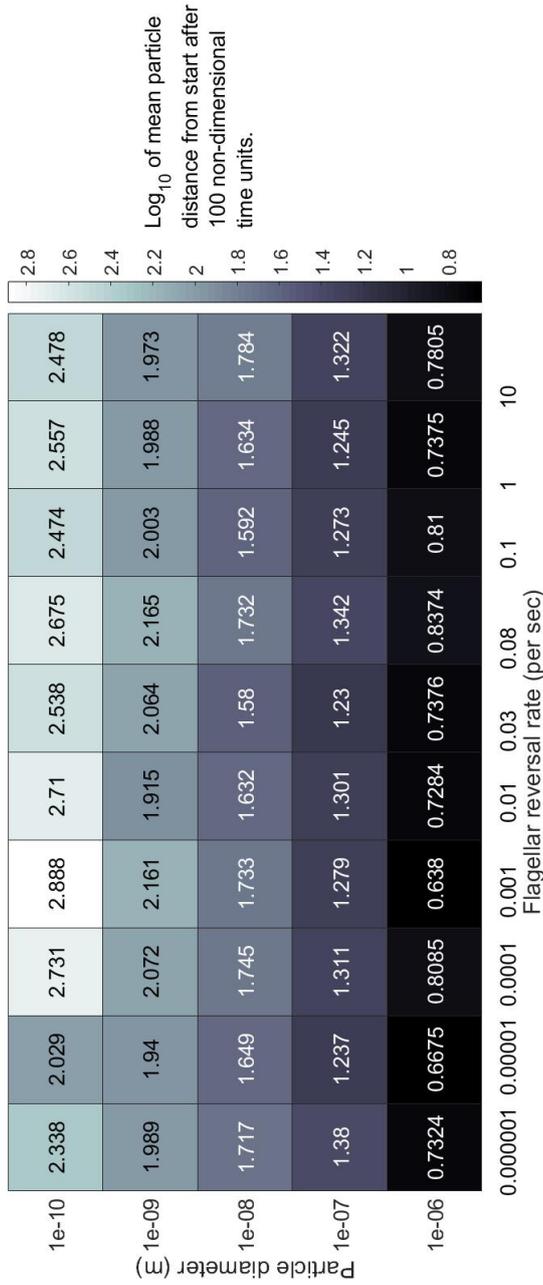
FIGURE 6.12.

Heat map showing the mean distance of 8000 simulated particles from their start position after 100 non-dimensional time units for various particle sizes and flagellar reversal rates. Particles are moved by a combination of simulated Brownian motion and the flow induced by a grid of 9 cells. Colour indicates the log_{10} of the mean distance. Values shown are a mean of 3 repeated simulations. As expected, small particles travel further which is an effect of the simulated Brownian motion term. Particles consistently travel further when the cells are at their lactam reversal rate compared to control.

the distance from the cell at which the particle trajectories become purely diffusive is comparable for one or nine cells.

Also interesting is that these simulated results align well with work in the literature. Darnton *et al* [40] analysed the motion of tracer beads over a bacterial carpet of surface attached cells with motile flagella. They observed clear areas of flow and islands lacking tracers. Although in the carpet there were far more than 9 interacting flagella, similar areas with and without flow are seen in the simple model simulations in this work.

Figure 6.13 shows a view from above the same arrangement of cells as in the previous simulations after 100 time-steps. In this case, the flagellar reversal rate was the control cell rate (0.03 s^{-1}) and the tracer size the QSM molecule size (2×10^{-8} m). The number of tracers was 8000 and islands with no beads can be seen with areas of flow.

6.5   Chapter conclusions

In this chapter, the simple model developed in chapter 5 was used to investigate the effect of various parameters and bacterial arrangements. The flagellar dynamics of two cells at different separation distances were used to investigate the distance at which one surface-attached cell impacts the flagellar dynamics of another. The results from these simulations suggested that there is little impact of a cell greater that 30 ndu away. As 30 ndu converts to 15 μm, this suggests that the flow of a surface-attached cell with a motile flagellum decays within approximately 10 body lengths. This aligns with the fact that the Stokeslet flow in the simple model decays as $1/r$. Investigation of tracer particle motion around two cells showed that a cell separation of 25 ndu resulted in the greatest dispersion of particles.

Simulations of arrangements of three cells showed that the flagellar dynamics of such systems were fairly robust to changes in relative cell orientation apart from in the case of flagellum-tethering poles pointing directly together. The flagellar dynamics were far more dependent on the choice of k_H in these simulations.

Investigations into the dependence of particle motion over a bed of nine cells on particle size and flagellar reversal rate showed that cells reversing at the lactam reversal rate consistently resulted in particles travelling further from their start position compared to control. This aligns with what is seen in the literature and what was observed in chapter
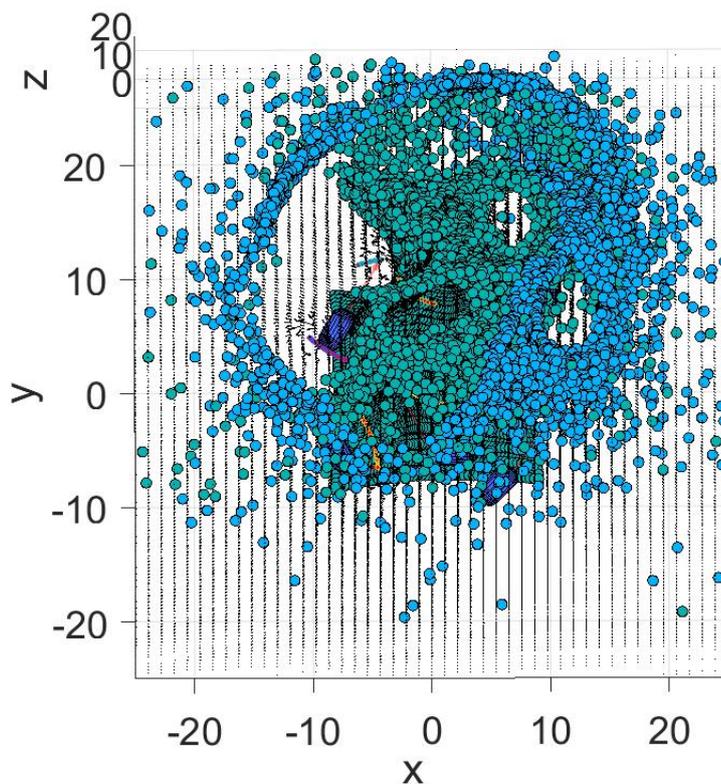
Figure 6.13.

A view from above of tracers above the same arrangement of 9 simulated cells as in the previous section. Here, the tracers originate from the same area but, rather than 216, there are 1000 tracers. The view is after 100 time-steps with the flagellar reversal rate being the control cell rate (0.03 s^{-1} and the tracer size the QSM molecule size (1×10^{-8} m).

5. It is postulated that this enhanced transport reduced the build up of QSMs and thus is a further way in which the lactam analogue inhibits biofilm formation.

MULTI-FLAGELLATED CELLS

"If you're going through hell, keep going."

Winston Churchill

7.1 Motivation

The primary strength of the simple model developed in this thesis is its use in investigating complex systems of surface associated flagella. In chapter 6, simulations of multiple interacting flagella produced interesting dynamics with one of the key conclusions from the work being that the cell orientations relative to each other are important. In this section, the flagellar orientations of multi-flagellated cells are experimentally investigated in order to compare with numerical results.

7.2 Data collection

Previous experiments in this thesis have focused primarily on polar-flagellated *P. aeruginosa* cells. However, to investigate multiple interacting flagella, peritrichously-flagellated *E. coli* are instead used for this experiment to ensure that interacting flagella are tethered close together. The cells were grown in the antibiotic cephalexin to elongate them. Cephalexin is a β-lactam antibiotic that acts on the cell separation machinery, preventing

them from dividing properly and so as the cells grow they elongate [208]. Cephalexin has previously been used to investigate the effect of cell length on motility [209], and therefore the protocol for its application to *E. coli* is well documented. The cells were initially grown following the standard procedure to grow a saturated culture in LB (see chapter 1). Then, cells were transferred to TB and incubated for a total of 300 minutes. To investigate the effect of cephalexin, 60μg/ml of cephalexin was added to the cell culture medium. All samples were incubated for the same total time, but the moment of antibiotic addition was varied within this to control cell length, as detailed below.

7.3 Results

7.3.1 Cell growth in cephalexin

For each of the samples grown as above, 0.05μl of the sample was imaged in a extra thin sample chamber (see chapter 2) using bright field imaging and a 60x lens. For each duration of cephalexin exposure, three biological repeats were used and for each repeat three 512×512 px still images were taken of areas in the middle of the sample. In all cases the focal plane was set just below the coverslip so that cells on the surface were clearly visible and to ensure a similar part of each sample was imaged. ImageJ object recognition was then used to determine the number of cells in the image for each of the frames. Figure 7.1 shows the average number of cells at each incubation time averaged over all the repeats. The error bars show the standard deviation of the number of cells identified in each frame and, as expected, the longer the cells were incubated in cephalexin, the fewer cells were seen (because division is restricted and so there are fewer, each of which are longer).

Of importance for this project is the length of cells after incubation in the cephalexin. Using the same still images taken to determine the number of cells, the length of cells was investigated. ImageJ was used to measure the length of cells and only cells attached to the coverslip surface were measured to ensure a direct comparison between samples. The 3D curved nature of the longer cells lead to a difficulty in measuring the length and so three repeats of the length were taken with the average of the three recorded. It is likely that the length of the longer cells is under-reported. Figure 7.1 shows the proportion of cells at each cephalexin incubation time that had various lengths. The

results confirm what might have been expected: the general trend is an increase in cell length with an increase in the cephalexin incubation time. Also with an increase in cephalexin incubation, there is an increase in the variance of cell lengths. This can be explained by biological variation in the growth rate of cells [210].

7.3.2   Flagella of elongated cells

To study the effect of multiple interacting flagella, a 2 ml sample was taken from each of the three biological repeats of samples incubated for 300 minutes in cephalexin. These were used to stain the cells' flagella with a fluorescent dye using the protocol detailed in chapter 1. The sample was viewed using extra thin chamber slides using the fluorescence microscopy set-up detailed in chapter 1. Surface attached cells were measured (again the average of three measurements was taken) and the number of flagella bundles visible along with the bundle angle to the cell body. The 'flagella bundles' may have been one flagellum but the resolution and frame rate made it difficult to determine precisely the number of flagella in a bundle (see figure 7.2). Only cells that appeared to have fully intact flagella were used. ImageJ was used to identify the acute angle between the flagella bundle and the cell body only if the flagella bundle maintained a fixed angle for at least 10 s. Some of the cells with short flagella possessed only one coherent bundle that maintained a fixed angle for a sufficient time.

Figure 7.3 shows a plot of the cell lengths against the average angle of the flagellar bundles to the cell body. The colours in the scatter plots indicate the number of fixed flagella bundles that were observed and the error bars indicate the standard deviation in the cell body length measurements and the standard deviation of flagellar bundle angles to the body. Any non-stationary flagellar bundles were not included in the number but, were seen to decrease with cell length. Although the standard deviation in the angles of the flagellar bundles is consistently relatively large, there is a decrease in angle with an increase in flagella length. As would be expected, the number of flagellar bundles increased with cell length.
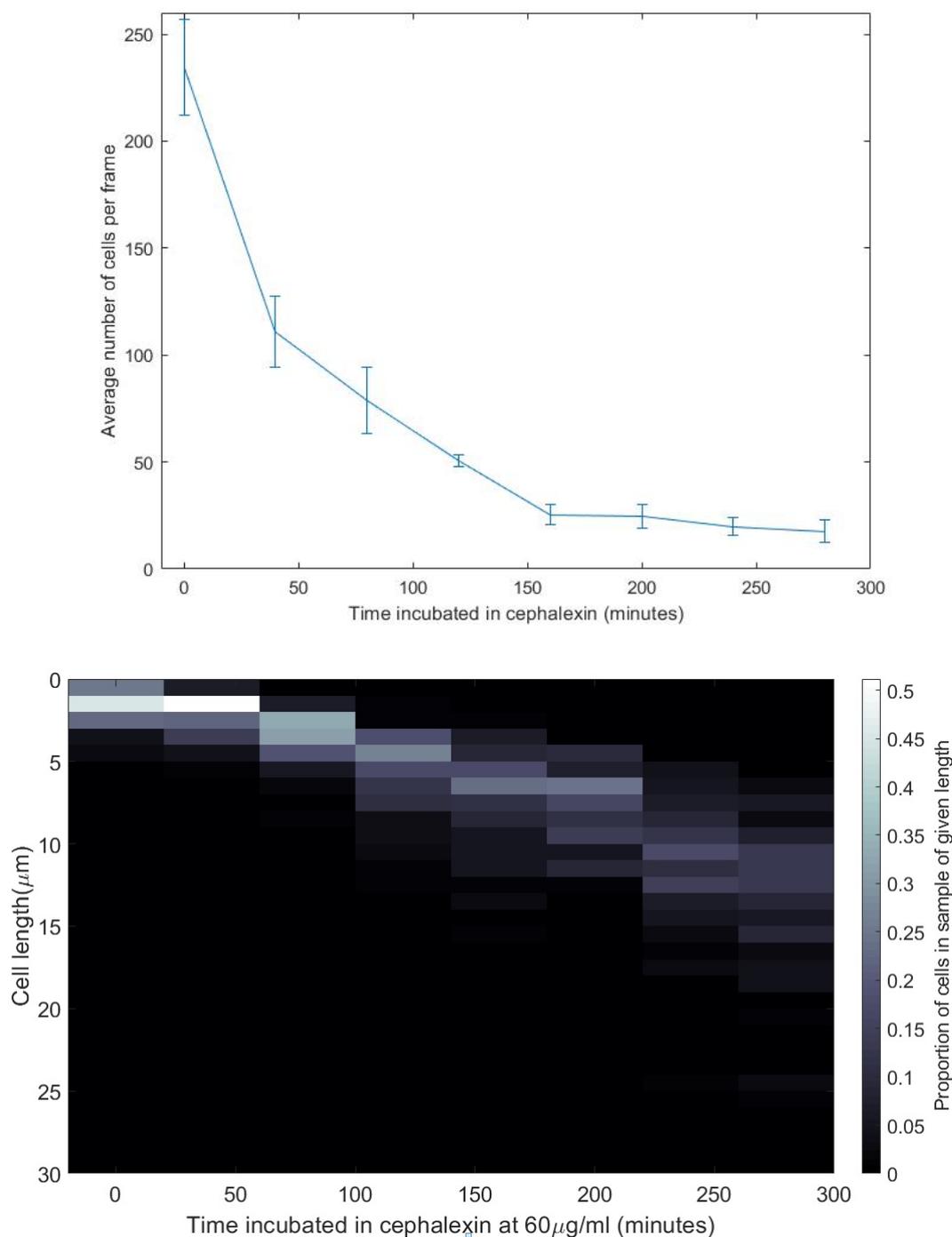
FIGURE 7.1.
   Top: The effect of various times of exposure to cephalexin on the number
   of cells. Error bars indicate the standard deviation between the number of
   cells in each of the sample frames. Bottom: The proportion of cells at various
   lengths after various lengths of time incubated in cephalexin. All samples
   were incubated for a total of 300 minutes with the cephalexin added after
   time, indicated on the horizontal axis.

188
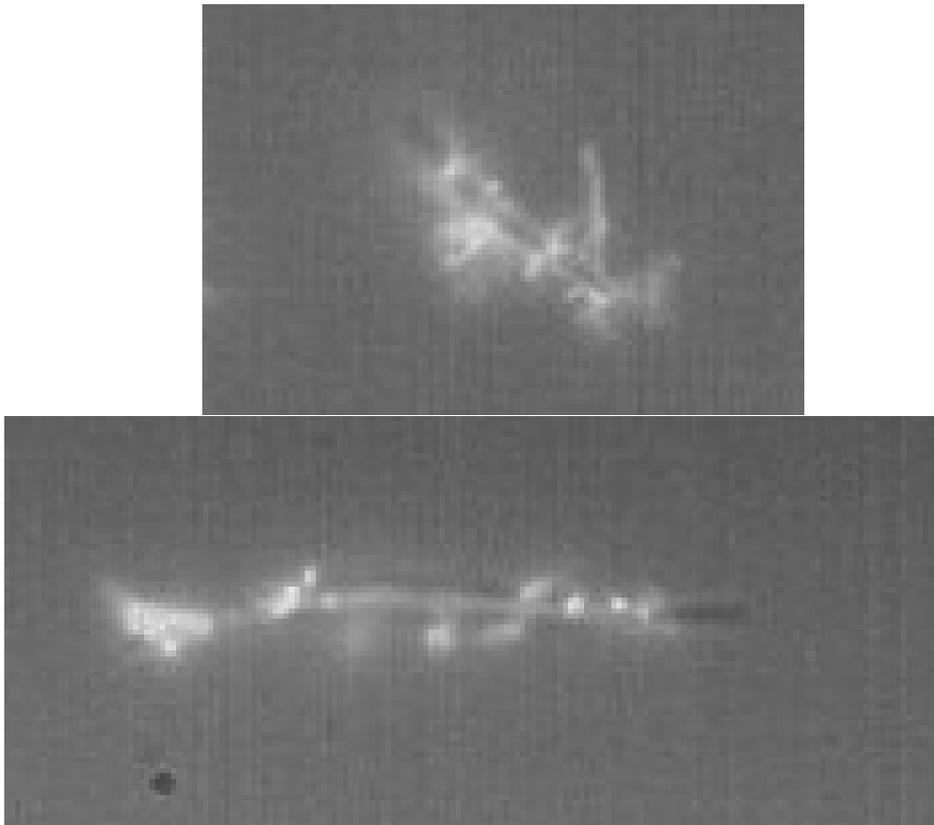
FIGURE 7.2.

From top to bottom: An example of a surface-attached cell that has been exposed to cephalexin for 300 minutes and has had its flagella stained with Alexa Fluor 647 maleimide dye. An example of a similar cell that has had some flagella sheared off - likely as a result of the staining process.

7.3.3 Simulated multi-flagellated cells

In order to further investigate the experimental results above, a multi-flagellated cell is simulated by placing a set number of simulated flagella in two parallel rows. Six cells of varying lengths from figure 7.3 were chosen to replicate (indicated by arrows). The simulated cells were given the same number of flagella bundles as were seen in the experiment and were spread in an irregular pattern around the cell body. The simulations were run for 800 time-steps as the simulated flagella were seen to settle into a steady state after this time.

For the flagella, the initial θ angle was always set at 0.25π but the ϕ angle was varied. All simulation parameters were the same as those in chapter 5 with the cell bodies orientated towards the centre of the bodies. Figure 7.4 shows an example of a
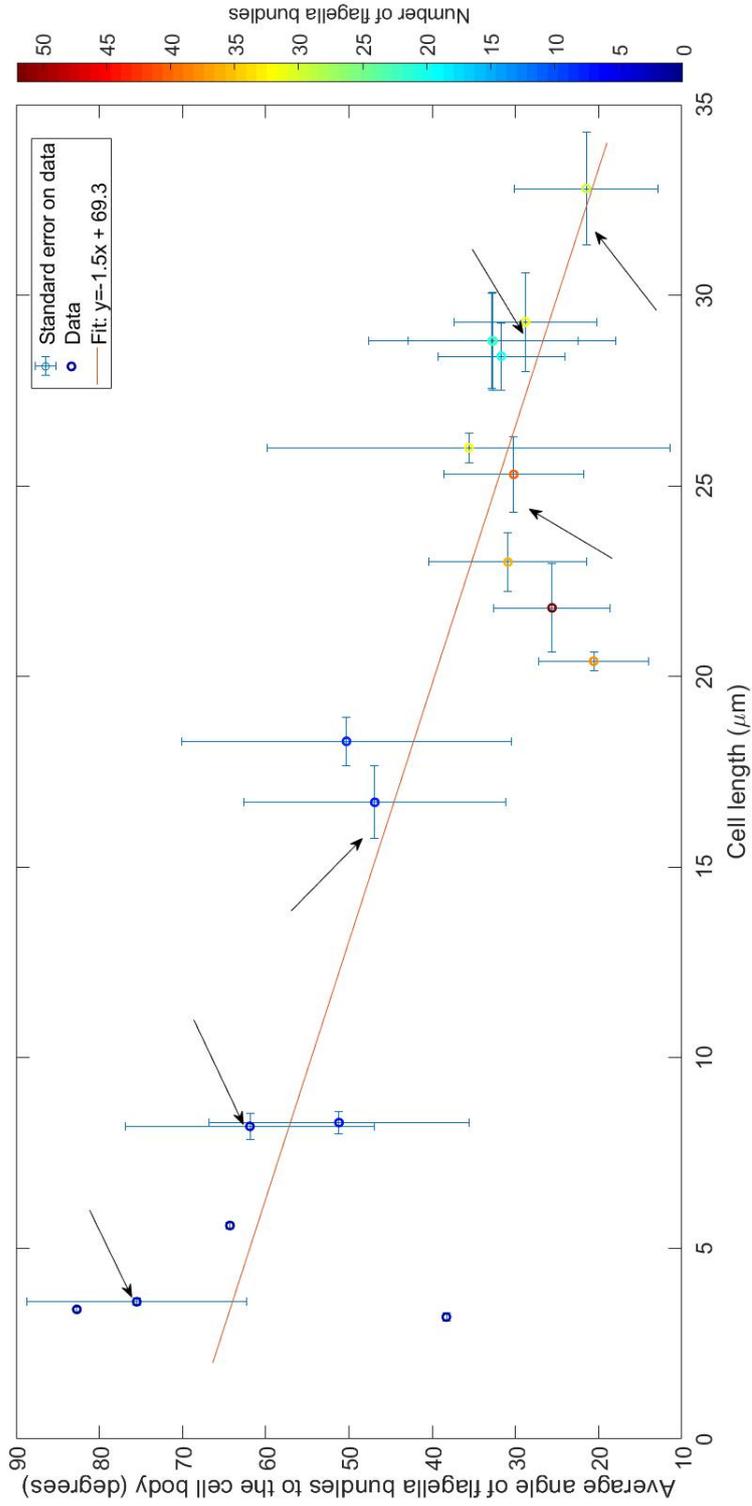
FIGURE 7.3.
The average angles between a cell's flagellar bundles and its cell body are plotted against the length of the cell body. Error bars in the horizontal and vertical directions represent the standard deviation in the measurements for the cell length and the angle each flagella bundle makes to the cell body, respectively. The colour of the scatter point indicates the number of flagella bundles identified for each cell.

simulated multi-flagellated cell. It is interesting to note that some of the flagella appear short because they are hidden by the cell body. This could perhaps explain the increased number of 'sheared' flagella seen for the longer cells in experiments.

To best align with the experimental data, the final flagellar orientations from the simulation were viewed from below and the angle tool in ImageJ was used to determine the angle of the flagella to the cell body. Again, to align with experiment, any flagella that had not obtained a fixed orientation by the end of the simulation were not considered. The number of flagella that did not reach a fixed orientation was no more than 2/3 per cell independent of cell length/ number of simulated flagella. Figure 7.5 shows the average angle of the flagella to the cell body for the various cell lengths. The error bars indicate the standard deviation on the mean and it can be seen that there is a large spread of angles for all cell lengths. Also shown are the linear fits to both the simulated and experimental data (both of which were obtained using the MATLAB polyfit least squares function). There is a general trend for decreasing flagella-body angle with increasing cell length. Notably, the 26μm cell shows a lower than average mean flagella-body angle. This cell was observed to have 45 flagella bundles in experiment which is above the mean bundle number for its length. This together with the fit lines suggest that an increased number of flagella - which goes hand in hand with cell body length - results in a decreased mean flagellum-body angle.

7.4   Discussion

One of the main challenges with the experimental component of this work was the rarity with which long cells were surface attached with fully intact flagella. A more detailed investigation would require optimisation of the method to minimise flagella shearing events. A further issue is that the flagellar bundles were recorded in a plane parallel to the boundary, which may miss bundles aligned perpendicular to the boundary. For the longer cell bodies with greater 3D curvature, there was also the issue that the cell often didn't attach to the surface 'flat' and so there were few cells that could be investigated. Even for those cells that did attach to the surface well, some of the flagella may have been obscured by the cell body and so the number of flagella bundles is likely to have been under-recorded.
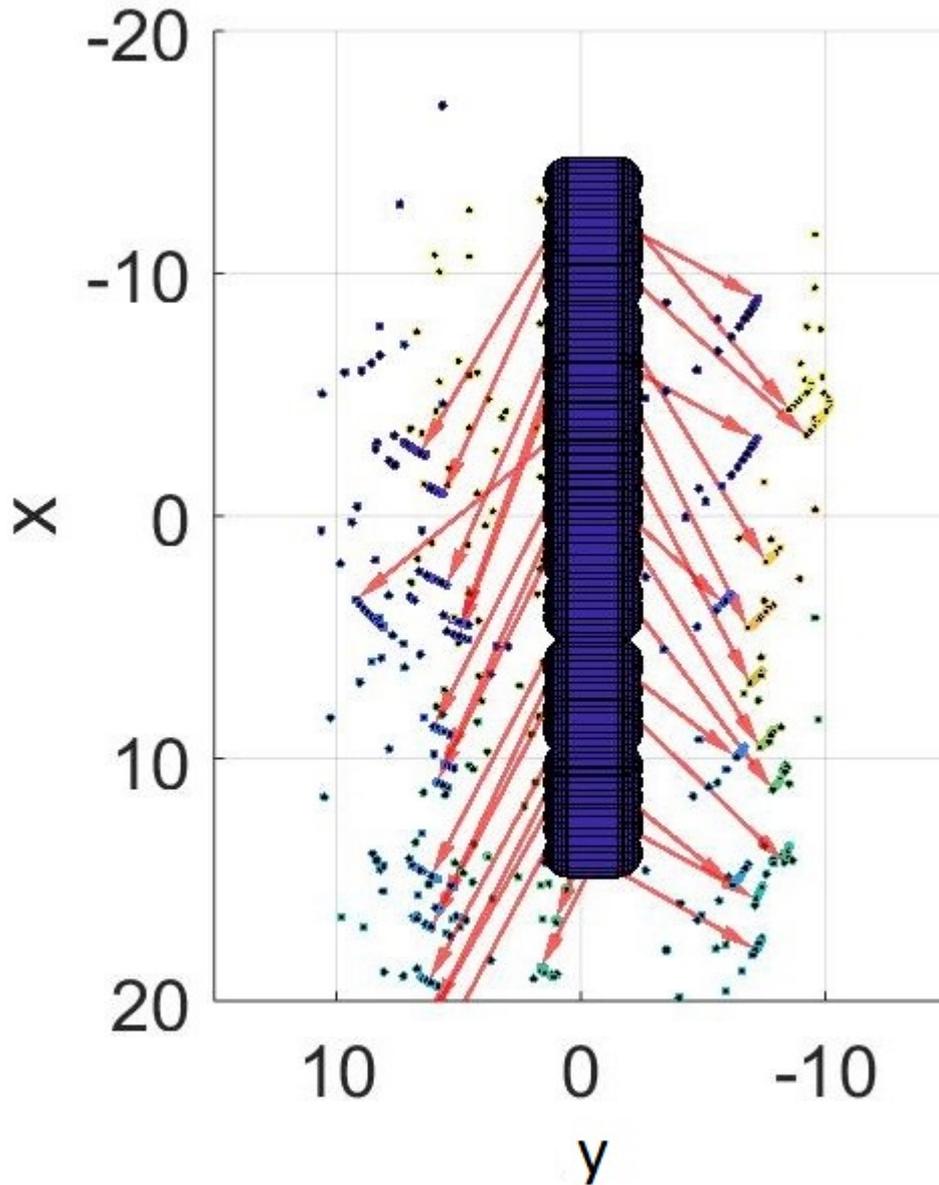
FIGURE 7.4.
    The view from beneath a simulated multi-flagellated cell. In this case, the
    cell body is set at 26μm and the cell has 45 flagella that have been given
    various initial angles. In all cases the body-hook torque acts to align the
    flagellum to be normal to the long cell body.
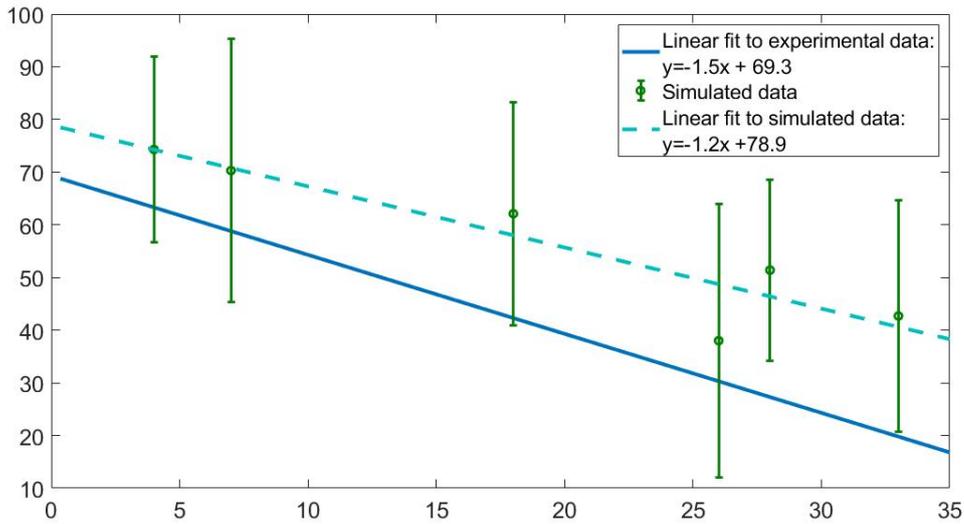
FIGURE 7.5.

The average angle of flagella to the cell body for six multi-flagellated cells of various lengths. For reference, the number of flagella simulated for the 4, 7, 18, 26, 28 and 33μm cells were 5, 7, 10, 45, 19 and 29, respectively. Error bars indicate the standard deviation while the dashed line shows the linear fit to the six data points. Also shown for comparison is the linear fit to the experimental data in figure 7.3.

On the simulation side, an obvious discrepancy with the real life situation is that the flagellar bundles, which may have consisted of multiple individual flagella, were modelled by only a single flagellum. While this is certainly a consideration, there is an argument that an entwined flagellar bundle may be thought of as 'large' flagellum. The main difference would be the direction of the mean body-hook torque of the interacting individual flagella in the bundle.

Another important note is that flagellar reversals were not included in these simulations and this would be an obvious extension to the work. Also important is that the simulations were not repeated for various flagellar arrangements and an investigation into this would increase the confidence in these results.

It should also be noted that, in these simulations, the flagella were oriented in parallel rows and the motor angle was set parallel to the boundary. In reality, it is likely that the flagella protrude from all over the peritrichously flagellated body and so the

hook angle would also vary.

The simulated data consistently overestimates the flagellar angle to the cell body compared to the experimental results. This may, in part, be explained by the fact that many of the cells chosen to simulate from the experimental data were above the line of best fit to the experimental data. This was unintentional as the cells chosen were picked arbitrarily and the aim was to simulate cells with a wide range of lengths. However, another possible explanation is that the body-hook torque term in the model is too large. This would mean that there is a larger torque aligning the flagella to an angle perpendicular to the body - and therefore encouraging the flagella to have a larger flagellum-to-body angle.

Despite these over-simplifications of the model, there is clearly a similar trend, between the simulated and experimental data sets, such that the flagella-body angle decreases with increased number of flagella/flagellar bundles. This may be due to the rotlet component of each flagellum 'pushing' their neighbour. This could be tested by reversing the direction of rotation to observe whether the flagella are 'pushed' in the opposite direction.

7.5   Chapter conclusions

In this chapter the simple model has been used to investigate the flagellar arrangement of various lengths of peritrichously flagellated cells. This simulated data has been compared to experimental data and similar trends have been identified. It is interesting to recall that there have been observations of flows circulating around peritritiously flagellated cells trapped at the edge of a thin film [**?**] and that the flagellar arrangement in the simulations of this chapter suggest the flow would be pushed past the cell rather than circulating. This is likely due to the different boundary conditions involved. In the experiments of [**?**], the confinement and asymmetric boundaries result in the flow circulation.

CONCLUSIONS AND FURTHER WORK

"Never miss a good chance to shut up."

Will Rogers

8.1 Conclusions

In this thesis, flows induced around surface-attached cells was investigated as a means to further understand early biofilm formation. As a control, holographic microscopy was used to track free-swimming *P. aeruginosa* cells in 3D when far from, and near to, surfaces. Comparisons between sample sets exposed to a biofilm inhibiting lactam analogue or not revealed the the lactam had a clear impact of the swimming trajectories whether near or far from the surface. Cells exposed to the lactam were seen to reverse their flagellar rotation more frequently and to swim slower. The same holographic microscopy technique was also used to investigate the effect of altering flagellin arrangement on the motility of cells in environments with different viscosities. This work contributed to the conclusion that flagellin arrangement is crucial in allowing certain cells to remain motile in a wide range of viscosities. A novel two-colour holographic microscopy technique was also presented and the data from this work contributed to the conclusion that utilising this two-colour set-up enables a sample with objects that have different optical properties

to be simultaneously tracked in 3D.

Having determined that the lactam analogue had an impact on free-swimming cells, bright field microscopy was used on *P. aeruginosa* to investigate the effect of the lactam on surface attached cells. Tracer beads were used to determine if a flow was present around cells and, using these, motile surface attached cells were separated into two categories (spinning - with a moving cell body - and stuck - where the body is stationary but a flow is seen). Transitions between the two states and between swimming/attached were investigated. This work revealed that bacteria always attach or detach when in the spinning state and that cells readily switched between the two surface-attached state. This is in disagreement with the literature whereby the stuck state is said to be 'irreversibly' attached. Data collected over 30 minutes suggested that the lactam had little impact on the motility state of surface attached cells.

This phenomenon of surface-attached cells maintaining a moving flagellum that induces a flow has not previously been reported and the shape of the flow is unknown. In this thesis, holographic microscopy and tracer beads were used to determine the average flow around 20 surface-attached *P. aeruginosa* cells with a moving flagellum. Gaussian smoothing was used to obtain a field from the bead trajectories and the field was found to have two distinct modes - attributed to reversal of flagellum rotation direction. Exposure of the cells to the lactam analogue was found to change the 3D flow field induced by the cells and this was suggested to be because of an increased flagellar reversal rate in the lactam meaning a smaller time averaged field. This reflects the effect seen in free-swimming investigations and suggest that the lactam may interfere with flagellar control mechanism. For both the control and lactam samples, the averaged field was found to be smaller in magnitude that expected and this was attributed to temporally varying flagellar orientations. In an attempt to understand this, a preliminary investigation into the flagellar orientations was undertaken by fluorescent staining of flagellar filaments.

As the experimental system of even a single cell was so complex, a simple model designed to capture key elements of the flow was presented. In this model, the cell body was ignored and a surface-attached cell with a moving flagellum was modelled as a sphere tethered above a boundary with singularity solutions to the Stokes equations placed inside the sphere to induce the flow. The interaction of the induce flow with the

surface was determined using the method of images and the sphere was allowed to move in response to the flow according to a torque balance at its tether. The key parameters of the model were determined to be α that controlled the radius of the sphere in relation to tether length, β which controlled the ratio of Stokeslet to rotlet strengths, Γ that controlled the motor torque to rotlet strength ratio and k_H which specified the strength of the body-hook torque. The effect of changing these parameters was discussed and appropriate values for them were suggested from the literature.

The simple model for the surface-attached cell was used to investigate the change in reversal rate seen when cells were exposed to the lactam analogue. This work showed that the increase reversal rate when expose to the lactam increased the distance that particles were transported. The suggestion from this is that the lactam prevents the build up of QSMs and so prevents later stages of biofilm formation being triggered.

Arrangements of two and three of this simple model cells showed that cell separation impacted flagellar and tracer dynamics. These systems were found to be highly sensitive to cell orientation and oscillating flagellar dynamics were suggested to enhance diffusion, which aligns with work in the literature that suggests reciprocal swimmers have enhanced diffusion over Brownian motion despite the reversibility of Stokes flow [211].

The simple model was also used to investigate particle transport over an arrangement of nine cells. In this work, flagellar rotation direction reversal rate and notional particle size was varied. Transport was increased with decreased particle size, which aligns with what would be expected from Brownian motion. The impact of the cells' flow was observed up to a distance of approximately ten cell body lengths for QSM size particles.

The final results chapter in this thesis used the simple model to investigate multi-flagellated cells. *E. coli* cells were elongated with cephalexin to produce cells at various lengths with various flagellar bundles. By fluorescent staining the flagella, the angle of the flagellar bundle to the cell body was determined. The simple model was used to simulate a selection of these cells and the flagellar angle to cell body was again investigated. The simulated and experimental data showed similar trends, lending credibility to the model, but the simulation consistently slightly overestimated the cell body- flagella angle. It was suggested that this may be due to the value of the body-hook torque being slightly too large.

The work in this thesis has increased the understanding of fluid dynamics in early stage biofilm formation. The previously unreported flow due to a surface-attached cell with a moving flagellum has been presented and a simple model has been developed to investigate its effects. It is hoped that this work will lead to a method of controlling biofilm formation.

8.2 Future Work

Although the data is this thesis has lead to some interesting conclusions, especially about the effect of reversal rate on particle diffusion, it has raised more questions than it has answered. The simple model presented in this thesis is an incredible tool for investigating complex arrangements of surface-attached cells, but the focus in this work has been on a single set of parameters. The next step should be an investigation into how parameters such as tether length impact the flagellar dynamics. This would be especially interesting as it would mean that the best position for the sphere along the flagellum to be investigated. During this work, the sphere was placed half way along the flagellar helical length but it could be that the experimental field is better captured by placing the sphere at the tip for example. This would also be an interesting study because there is experimental data of the motion of a tracer bead attached to a sheared flagellum [124]. If, in the simple model, the tether length was shortened, this would almost exactly replicate this experimental set-up. From this, parameters such as k_H could be better fit by direct comparison to experimental data.

In this thesis, the motor torque axis was always taken to align with the cell body but this is not necessarily the case. In [156], experimental observations were well replicated when the motor torque was taken to have components both parallel, and perpendicular, to the cell body. It would be an interesting extension to this work to investigate particle transport with different motor torque axes. Further extensions to the model might include modelling the cell body or changing the shape of the object from a sphere to a spheroid, for example. Another element not addressed in this model was a background flow. Many biofilms develop in flow environments and it would be interesting to observed whether the cell-induced flow acts to isolate the surface-attached cells from the background flow so as they are not removed before they have had a chance to irreversibly attach via pili etc. This would be a simple addition to the model as it would only mean

an additional term in the **B** calculation.

In chapter 5, the effect of surface-attached cells on the motion of a cell-sized particle was investigated and it was found that these particles are transported further when the surface-attached cells were reversing their flagella at the lactam rate compared to that of the control. However, the planktonic cells were not actively swimming and it would be interesting to investigate the impact of reversals on swimming cells. Swimming cells far from a boundary are often modelled as dipoles [23] and so this would be a good initial model. Bacteria have been shown to display rheotaxis (respond to shear flow), which causes them to align upstream [212]. This might indicate that flow out from the surface (from surface-attached cells) would cause planktonic bacteria to align towards the surface and so may increase the likelihood of them attaching to the surface and hence increase the chance of biofilm formation. The use of a multi-mode microscope similar to the one used in [**?**] might be used to simultaneously collect holography and Total Internal Reflection Microscopy (TIRM) data. This might be used to follow the trajectory of a swimming cell over surface-attached cells and would allow the orientation of the swimming cell near the surface to be determined. This experimental data could then be compared to simulated data to determine whether the dipole is an appropriate model for the swimming cell in this configuration. The same multi-mode microscope might also be used to image tracer beads and surface-attached cell flagellum simultaneously. This would allow the trajectories of beads when the flagellar are in certain positions to be averages and might help to determine why the experimentally derived field in chapter 3 was smaller than expected.

8.3 Wider Context

As discussed above, one of the key extensions to this work would be to investigate the effect of varying different parameters. Varying parameters such as tether length and sphere radius would allow the model to be used to look as different species of bacteria. Furthermore, there is no reason why the investigation should be limited to bacteria, a simple variation in parameters would allow cilia to modelled and the results of such an investigation could be directly compared to the results from more computationally expensive models [213]. There is also new evidence that algal cells attach to surfaces [214] and the model could be adapted to investigate flow involvement in this initial attachment. A further adaptation would be to model the hydrodynamics of coral polyps

and how they create a flow in order to gather nutrients [215]. This is especially important in the light of global coral reef decline in recent decades.

The flow, reported in this thesis, due to surface-attached cells with a moving flagellum may also help to explain why some surfaces display anti-microbial properties. Using a high-throughput array testing technique, [216] identified a polymer coating for a surface that was remarkably resistant to biofilm formation. The polymer was found to have no toxic effect on the cells and it not thought to be repelling planktonic cells via charge etc. It could be that the polymer is interacting with the cells' flagella and so the cells do not induce the flow seen in this thesis and this impacts biofilm formation.

The identification of a flow induced by surface-attached cells with a motile flagellum and the development of the simple model to capture the flow are key steps forward in the understanding of how fluid dynamics impact nascent biofilms.

LIST OF NOTATIONS

- A - Particle radius

- AI - Auto-inducer

- AOI - Area of interest

- A_{ref} - Reference wave amplitude

- A_{scat} - Scattered wave amplitude

- A_1 - Steepness of Reorient Probability curve

- A_2 - Center of Reorient Probability curve

- **B** - Flow field

- BEM - Boundary Element Method

- c_x, c_y - Body-centre co-ordinate

- **C** - Object centre

- C_D - Sphere drag coefficient

- CA - Cellular Automaton

- C_B - Bühlmann Credibility

- C_C - Classical Credibility

- CCW - Counter Clockwise

- CW - Clockwise

- d - tether distance above the boundary

- **d** - Directional derivative

- D - Stokes doublet strength magnitude

- **D** - Tether point

- Di - Diffusion coefficient

- DIHM - Direct Inline Holographic Microscopy

- DV - Duel View

- $\mathbf{e}_m$ - Motor axis

- $\mathbf{e}_\chi$ - Direction of increasing χ

- E - Source doublet strength magnitude

- $\mathbf{E}$ - Flow field rate of strain tensor

- EM - Extra-cellular Matrix

- EPS - Extra-cellular Polymeric Substance

- $\mathbf{f}$ - External forces

- F - Stokeslet strength magnitude

- $\mathbf{F}_C$ - Viscous drag force at $\mathbf{C}$

- FFT - Fast Fourier Transform

- FSC - Free Space Coupler

- h - Height above plane

- IbM - Individual-based Model

- k_B - Boltzmann constant

- k_H - Ratio between bending stiffness of hook and a product of hook length and motor torque

- K - Bühlmann fit parameter

- K_1 - Classical fit parameter

- l - tether length

- L - Characteristic length

- m - Mass

- MSD - Mean Squared Displacement

- ND - Normal Distribution

- ndu - non-dimensional units

- OL - Objective Lens

- $\mathbf{P}$ - Stokeslet direction

- Pr - Pressure

- Pe - Peclét number

- $P_{reorient}$ - Probability of reorientation event

- QS - Quorum Sensing

- QSI - Quorum Sensing Inhibitor

- QSM - Quorum Sensing Molecule

- $\mathbf{r}$ - Distance from singularity

- $\mathbf{R}$ - Distance from image singularity

- Re - Reynolds number

- RFT - Resistive Force Theory

- SBT - Slender Body Theory

- t - Time

- t_r - Relaxation time (Brownian)

- T_A - Absolute temperature

- TL - Tube Lens

- TND - Total Normal Distribution

- $\mathbf{u}^d$ - Source doublet flow

- $\mathbf{u}^r$ - Rotlet flow

- $\mathbf{u}^{r*}$ - Rotlet image flow

- $\mathbf{u}^s$ - Stokeslet flow

- $\mathbf{u}^{s*}$ - Stokeslet image flow

- $\mathbf{u}^{sd}$ - Stokes doublet flow

- U - Characteristic velocity

- U_c - Characteristic flow velocity

- U_p - Particle speed

- U_0 - Transverse amplitude profile

- $\mathbf{v}$ - Fluid velocity

- WDM -Wavelength Division Multiplexer

- WT - Wild-Type

- x_i, x_j, x_k - Orthogonal co-ordinate system

- Δx_s - Step size

- $\dot{x}$ - Velocity

- $X(\dot{x})$ - Probability of reorient due to speed

- X_d, Y_d - Displacement of cell from centre of AOI

- $X_{node}, Y_{node}, Z_{node}$ - Node location for 3D flow

- $X_{track}, Y_{track}, Z_{track}$ - Shifted bead track co-ordinate

- z_f - Distance from focal plane

- ι - Focal plane

- λ - Wavelength

- μ - Dynamic viscosity

- μ_c - Mean speed of cells in control

- μ_l - Mean speed of cells in lactam

- Ω - Rotlet strength magnitude

- $\boldsymbol{\Omega}$ - Flow field vorticity

- Θ - Cell body orientation taken anti-clockwise from horizontal

- ρ - Density

- σ - Standard deviation of normal distribution for 3D experimental flow smoothing

- σ_c - Standard deviation of speed in control

- σ_l - Standard deviation of speed in lactam

- τ_C - Torque at $\mathbf{C}$

- τ_D - Torque at $\mathbf{D}$

- τ_h - Body-hook torque

- τ_m - Motor torque

- ξ - Angle between proximal velocity vectors

- $\Xi(\xi)$ - Probability of reorient due to angle

- - angle between body-hook alignment and body alignment

- $\hat{\zeta}_0$ - Polarization

MEDIA PROTOCOLS

B.1 Lysogeny broth (LB) protocol

Equipment required

- Nitrile gloves

- Lab coat

- Safety glasses

- 2L beaker

- 4× 500ml sterile media flasks

- ml sensitive measuring cylinder

- Precision balance + sterile weigh boats

- pH meter

- Filter steriliser

- Magnetic stirrer and warmer plate

Chemicals required

- Tryptone

- Yeast Extract

- Sodium Chloride ($NaCl$)

- Sodium Hydroxide ($NaOH$)

- Deionised water (DI)

Protocol

1. Dissolve 10g of tryptone, 5g of yeast extract and 10g of $NaCl$ in 950ml of DI water using a magnetic stirrer and warmer plate.

2. Adjust pH to 7.0 using $NaOH$.

3. Bring volume up to 1L using DI water.

4. Autoclave to sterilise and store correctly labeled in the 4 500ml sterile media flasks at room temperature.

B.2   Tryptone broth (TB) protocol

Equipment required

- Nitrile gloves

- Lab coat

- Safety glasses

- 2L beaker

- 4× 500ml sterile media flasks

- ml sensitive measuring cylinder

- Precision balance + sterile weigh boats

- pH meter

- Filter steriliser

- Magnetic stirrer and warmer plate

Chemicals required

- Tryptone

- Sodium Chloride ($NaCl$)

- Sodium Hydroxide ($NaOH$)

- Deionised water (DI)

Protocol

1. Dissolve 10g of tryptone and 5g of $NaCl$ in 900ml of DI water using a magnetic stirrer and warmer plate.

2. Adjust pH to 7.0 using $NaOH$.

3. Bring volume up to 1L using DI water.

4. Autoclave to sterilise and store correctly labeled in the 4 500ml sterile media flasks at room temperature.

B.3   Motility buffer (MB) protocol

<u>Equipment required</u>

- Nitrile gloves

- Lab coat

- Safety glasses

- 2L beaker

- 4× 500ml beakers

- 6× 500ml sterile media flasks

- 2× 250ml sterile media flasks

- ml sensitive measuring cylinder

- Precision balance + sterile weigh boats

- pH meter

- Filter steriliser

- Magnetic stirrer and warmer plate

<u>Chemicals required</u>

- Potassium Phosphate (KPO_4)

- Ethylenediaminetetraacetic acid disodium dihydrate ($Na_2EDTA.2H_2O$)

- Sodium Chloride ($NaCl$)

- Sodium Hydroxide ($NaOH$)

- Hydrochloric acid (HCL).

- Deionised water (DI)

<u>Protocol</u>

1. Make a 250ml stock solution of 1M potassium phosphate monobasic (KH_2PO_4) by dissolving 34.0225g of KH_2PO_4 in 250ml of DI water using a magnetic stirrer and warmer plate. Store correctly labeled in sterile 500ml media flask.

2. Make a 250ml stock solution of 1M potassium phosphate dibasic (K_2HPO_4) by dissolving 43.545g of K_2HPO_4 in 250ml of DI water using a magnetic stirrer and warmer plate. Store correctly labeled in sterile 500ml media flask.

3. Make a 100ml stock solution of 1M potassium phosphate (KPO_4) by adding 61ml of 1M K_2HPO_4 to 39ml of 1M KH_2PO_4. Sterilise by autoclaving and store correctly labelled at room temperature in a sterile 250ml media flask.

4. Make a 100ml stock solution of 0.5M EDTA by dissolving 18.61g of $Na_2EDTA.2H_2O$ in 100ml of DI. Make pH to 8.0 with $NaOH$. (EDTA will dissolve when pH is 8.0). Sterilize by autoclaving and store correctly labelled at room temperature.

5. Make 1L of MB by adding 10ml 0f 1M KPO_4, 0.2ml of 0.5M EDTA and 3.915g of $NaCl$. Adjust pH to 7.0 by adding HCL or $NaOH$. Add H_2O to a total volume of 1L. Filter to sterilise and store correctly labeled in 4 500ml sterile media flasks at room temperature.

B.4 Lactate medium (LM) protocol

Equipment required

- Nitrile gloves

- Lab coat

- Safety glasses

- 2L beaker

- 4× 500ml sterile media flasks

- ml sensitive measuring cylinder

- Precision balance + sterile weigh boats

- pH meter

- Filter steriliser

- Magnetic stirrer and warmer plate

Chemicals required

- 4-(4-hydroxyethyl)-1-piperazineethanesulfonic acid (HEPES)

- Yeast Extract

- Sodium Chloride ($NaCl$)

- Potassium Hydroxide (KOH)

- Peptone

- Lactic acid (85%)

- Deionised water (DI)

Protocol

1. Dissolve 2.835g of HEPES, 0.2g of yeast extract, 0.1g of peptone, 1.1ml of lactic acid and 5.845g of $NaCl$ in 900ml of DI water using a magnetic stirrer and warmer plate.

2. Adjust pH to 7.5 using KOH.

3. Bring volume up to 1L using DI water.

4. Autoclave to sterilise and store correctly labeled in the 4 500ml sterile media flasks at room temperature.

BIBLIOGRAPHY

[1] P D Schloss and J Handelsman. Status of the Microbial Census. *Microbiology and molecular biology reviews*, 68(4):686–691, 2004.

[2] C. Nicolella, M.C.M. van Loosdrecht, and J.J. Heijnen. Wastewater treatment with particulate biofilm reactors. *Journal of Biotechnology*, 80(1):1–33, jun 2000.

[3] Zhi-Wu Wang and Shulin Chen. Potential of biofilm-based biofuel production. *Applied Microbiology and Biotechnology*, 83(1):1–18, may 2009.

[4] E D. van Hullebusch, H. Zandvoort, and P N.L. Lens. Metal immobilisation by biofilms: Mechanisms and analytical tools. *Reviews in Environmental Science and Bio/Technology*, 2(1):9–33, 2003.

[5] M A. Cooley, C Whittall, and M S. Rolph. Pseudomonas signal molecule 3-oxo-C12-homoserine lactone interferes with binding of rosiglitazone to human PPARγ. *Microbes and Infection*, 12(3):231–237, mar 2010.

[6] M. P. Schultz, J. A. Bendick, E. R. Holm, and W. M. Hertel. Economic impact of biofouling on a naval surface ship. *Biofouling*, 27(1):87–98, jan 2011.

[7] T J. Mitchell. The pathogenesis of streptococcal infections: from Tooth decay to meningitis. *Nature Reviews Microbiology*, 1(3):219–230, dec 2003.

[8] N A. Bhawsar and M Singh. Isolation And Characterization Of Pseudomonas aeruginosa From Waste Soybean Oil As Biosurfactants Which Enhances Biodegradation Of Industrial Waste With Special Reference To Kosmi Dam, Betul District, (M.P.). *International Journal of Advanced Research*, 2(6):778–783, 2014.

[9] J W Costerton, Z Lewandowski, D DeBeer, D Caldwell, D Korber, and G James. Biofilms, the customized microniche. *Journal of bacteriology*, 176(8):2137–42, apr 1994.

[10] M. Alexander, B R. Bloom, A. Hopwood, R. Hull, B H. Iglewski, A I. Laskin, S G. Oliver, M. Schaechter, W C. Summers, and J. Lederberg. *Encyclopedia of Microbiology, Four-Volume Set*. Elsevier, 2000.

[11] K Botzenhart and G Döring. *Ecology and Epidemiology of Pseudomonas aeruginosa*. Springer, Boston, MA, 1993.

[12] B. Fick. *Pseudomonas aeruginosa, the opportunist : pathogenesis and disease*. CRC Press, 1993.

[13] G R Johnson and R H Olsen. Multiple pathways for toluene degradation in Burkholderia sp. strain JS150. *Applied and environmental microbiology*, 63(10):4047–52, oct 1997.

[14] C Gessard. On the Blue and Green Coloration that Appears on Bandages. *Clinical Infectious Diseases*, 6(Supplement_3):S775–S776, sep 1984.

[15] R Henry. Etymologia:Pseudomonas. *Emerging Infectious Diseases*, 18(8):1241–1241, aug 2012.

[16] N J. Palleroni. ThePseudomonas Story. *Environmental Microbiology*, 12(6):1377–1383, jun 2010.

[17] O.F. Müller. *Vermium terrestrium et fuviailium*. 1773.

[18] J Bruzaud, J Tarrade, A Coudreuse, A Canette, J Herry, E Taffin de Givenchy, T Darmanin, F Guittard, M Guilbaud, and M Bellon-Fontaine. Flagella but not type IV pili are involved in the initial adhesion of Pseudomonas aeruginosa PAO1 to hydrophobic or superhydrophobic surfaces. *Colloids and Surfaces B: Biointerfaces*, 131:59–66, jul 2015.

[19] J Zaburdaev H Taktikos, V Stark. How the motility pattern of bacteria affects their dispersal and chemotaxis. *PLoS ONE*, 8(12), 2013.

[20] G M Barbara and J G Mitchell. Bacterial tracking of motile algae. *FEMS Microbiology Ecology*, 44(1):79–87, may 2003.

[21] E Lauga, W R DiLuzio, G M Whitesides, and H A Stone. Swimming in circles: motion of bacteria near solid boundaries. *Biophysical journal*, 90(2):400–12, jan 2006.

[22] J Elgeti, R G Winkler, and G Gompper. Physics of microswimmers‚Äîsingle particle motion and collective behavior: a review. *Reports on Progress in Physics*, 78(5):056601, may 2015.

[23] K Drescher, R E. Goldstein, N Michel, M Polin, and I Tuval. Direct Measurement of the Flow Field around Swimming Microorganisms. *Physical Review Letters*, 105(16):168101, oct 2010.

[24] J S. Guasto, K A. Johnson, and J. P. Gollub. Oscillatory Flows Induced by Microorganisms Swimming in Two Dimensions. *Physical Review Letters*, 105(16):168102, oct 2010.

[25] K Son, D R. Brumley, and R Stocker. Live from under the lens: exploring microbial motility with dynamic imaging and microfluidics. *Nature Reviews Microbiology*, 13(12):761–775, dec 2015.

[26] M Jabbarzadeh and H C Fu. Dynamic instability in the hook-flagellum system that triggers bacterial flicks. *Physical Review E*, 97(1):012402, jan 2018.

[27] Saverio E Spagnolie and Eric Lauga. Hydrodynamics of self-propulsion near a boundary: predictions and accuracy of far-field approximations. *J. Fluid Mech*, 700:105–147, 2012.

[28] J. R. Blake and A. T. Chwang. Fundamental singularities of viscous flow. *Journal of Engineering Mathematics*, 8(1):23–29, jan 1974.

[29] R Cortez and D Varela. A general system of images for regularized Stokeslets and other elements near a plane wall. *Journal of Computational Physics*, 285:41–54, mar 2015.

[30] J Ainley, S Durkin, R Embid, P Boindala, and R Cortez. The method of images for regularized Stokeslets. 2008.

[31] M A-S Vigeant, R M Ford, M Wagner, and L K Tamm. Reversible and irreversible adhesion of motile Escherichia coli cells analyzed by total internal reflection aqueous fluorescence microscopy. *Applied and environmental microbiology*, 68(6):2794–801, jun 2002.

[32] Guanglai Li, Lick-Kong Tam, and Jay X Tang. Amplified effect of Brownian motion in bacterial near-surface swimming. *Proceedings of the National Academy of Sciences of the United States of America*, 105(47):18355–9, nov 2008.

[33] P D. Frymier and R M. Ford. Analysis of bacterial swimming speed approaching a solid‚Äìliquid interface. *AIChE Journal*, 43(5):1341–1347, may 1997.

[34] P D Frymier, R M Ford, H C Berg, and P T Cummings. Three-dimensional tracking of motile bacteria near a solid planar surface. *Proceedings of the National Academy of Sciences of the United States of America*, 92(13):6195–9, jun 1995.

[35] H C Berg and L Turner. Chemotaxis of bacteria in glass capillary arrays. Escherichia coli, motility, microchannel plate, and light scattering. *Biophysical journal*, 58(4):919–30, oct 1990.

[36] K Drescher, J Dunkel, L H Cisneros, S Ganguly, and R E Goldstein. Fluid dynamics and noise in bacterial cell-cell and cell-surface scattering. *Proceedings of the National Academy of Sciences of the United States of America*, 108(27):10940–5, jul 2011.

[37] G A. O'Toole and R Kolter. Flagellar and twitching motility are necessary for Pseudomonas aeruginosa biofilm development. *Molecular Microbiology*, 30(2):295–304, oct 1998.

[38] A M Spormann. Gliding motility in bacteria: insights from studies of Myxococcus xanthus. *Microbiology and molecular biology reviews : MMBR*, 63(3):621–41, sep 1999.

[39] L H. Cisneros, J O. Kessler, R Ortiz, R Cortez, and M A. Bees. Unexpected Bipolar Flagellar Arrangements and Long-Range Flows Driven by Bacteria near Solid Boundaries. *Physical Review Letters*, 101(16):168102, oct 2008.

[40] N Darnton, L Turner, K Breuer, and H C. Berg. Moving Fluid with Bacterial Carpets. *Biophysical Journal*, 86(3):1863–1870, mar 2004.

[41] R Saini, S Saini, and S Sharma. Biofilm: A dental microbial infection. *Journal of natural science, biology, and medicine*, 2(1):71–5, jan 2011.

[42] K Sauer, A H Rickard, and D G Davies. Biofilms and Biocomplexity. *Microbe*, 2(7):347–353, 2007.

[43] G Feng, Y Cheng, S-Y Wang, D A Borca-Tasciuc, R W Worobo, and C I Moraru. Bacterial attachment and biofilm formation on surfaces are reduced by small-diameter nanoscale pores: how small is small enough? *NPJ biofilms and microbiomes*, 1:15022, 2015.

[44] R L. Scharff. Economic Burden from Health Losses Due to Foodborne Illness in the United States. *Journal of Food Protection*, 75(1):123–131, jan 2012.

[45] J D Bryers. Medical biofilms. *Biotechnology and bioengineering*, 100(1):1–18, may 2008.

[46] K. Smith and I. S. Hunter. Efficacy of common hospital biocides with biofilms of multi-drug resistant clinical isolates. *Journal of Medical Microbiology*, 57(8):966–973, aug 2008.

[47] A Cydzik-Kwiatkowska and M Zielińska. Bacterial communities in full-scale wastewater treatment systems. *World journal of microbiology & biotechnology*, 32(4):66, apr 2016.

[48] C Rodriguez-Navarro, F Jroundi, M Schiro, E Ruiz-Agudo, and M T González-Muñoz. Influence of substrate mineralogy on bacterial mineralization of calcium carbonate: implications for stone conservation. *Applied and environmental microbiology*, 78(11):4017–29, jun 2012.

[49] H Liu and B E Logan. Electricity Generation Using an Air-Cathode Single Chamber Microbial Fuel Cell in the Presence and Absence of a Proton Exchange Membrane. 2004.

[50] V S R K Maddula, E A Pierson, and L S Pierson. Altering the ratio of phenazines in Pseudomonas chlororaphis (aureofaciens) strain 30-84: effects on biofilm formation and pathogen inhibition. *Journal of bacteriology*, 190(8):2759–66, apr 2008.

[51] M R. Cruz, C E. Graham, B C. Gagliano, M C. Lorenz, and D A. Garsin. Enterococcus faecalis Inhibits Hyphal Morphogenesis and Virulence of Candida albicans. *Infection and Immunity*, 81(1):189–200, jan 2013.

[52] I Kuiper, E L. Lagendijk, R Pickford, J P. Derrick, G E. M. Lamers, J E. Thomas-Oates, B J. J. Lugtenberg, and G V. Bloemberg. Characterization of two Pseudomonas putida lipopeptide biosurfactants, putisolvin I and II, which inhibit biofilm formation and break down existing biofilms. *Molecular Microbiology*, 51(1):97–113, nov 2003.

[53] G Ramage, S P Saville, B L Wickes, and J L López-Ribot. Inhibition of Candida albicans biofilm formation by farnesol, a quorum-sensing molecule. *Applied and environmental microbiology*, 68(11):5459–63, nov 2002.

[54] J C A Janssens, H Steenackers, S Robijns, E Gellens, J Levin, H Zhao, K Hermans, D De Coster, T L Verhoeven, K Marchal, J Vanderleyden, D E De Vos, and S C J De Keersmaecker. Brominated furanones inhibit biofilm formation by Salmonella enterica serovar Typhimurium. *Applied and environmental microbiology*, 74(21):6639–48, nov 2008.

[55] C Fuqua, S C. Winans, and E. P Greenberg. Census and consensus in bacterial ecosystems: The LuxR-LuxI Family of Quorum-Sensing Transcriptional Regulators. *Annual Review of Microbiology*, 50(1):727–751, oct 1996.

[56] M B. Miller and B L. Bassler. Quorum Sensing in Bacteria. *Annual Review of Microbiology*, 55(1):165–199, oct 2001.

[57] A Delago, A Mandabi, and M M. Meijler. Natural Quorum Sensing Inhibitors - Small Molecules, Big Messages. *Israel Journal of Chemistry*, 56(5):310–320, may 2016.

[58] D G Davies, M R Parsek, J P Pearson, B H Iglewski, J W Costerton, and E P Greenberg. The involvement of cell-to-cell signals in the development of a bacterial biofilm. *Science (New York, N.Y.)*, 280(5361):295–8, apr 1998.

[59] C Alfiniyah, M A Bees, and Wood. Pulse generation in the quorum machinery of Pseudomonas aeruginosa. *Bulletin of Mathematical Biology*, pages 1360–1389.

[60] K Sauer, A K Camper, G D Ehrlich, J W Costerton, and D G Davies. Pseudomonas aeruginosa displays multiple phenotypes during development as a biofilm. *Journal of bacteriology*, 184(4):1140–54, feb 2002.

[61] K P Rumbaugh, J A Griswold, B H Iglewski, and A N Hamood. Contribution of quorum sensing to the virulence of Pseudomonas aeruginosa in burn wound infections. *Infection and immunity*, 67(11):5854–62, nov 1999.

[62] A Siryaporn, S L Kuchma, G A O'Toole, and Z Gitai. Surface attachment induces Pseudomonas aeruginosa virulence. *Proceedings of the National Academy of Sciences of the United States of America*, 111(47):16860–5, nov 2014.

[63] P S Stewart and J W Costerton. Antibiotic resistance of bacteria in biofilms. *Lancet (London, England)*, 358(9276):135–8, jul 2001.

[64] H-C Flemming, T R Neu, and D J Wozniak. The EPS matrix: the "house of biofilm cells". *Journal of bacteriology*, 189(22):7945–7, nov 2007.

[65] H-C Flemming and J Wingender. The biofilm matrix. 2010.

[66] C C. C. R. de Carvalho. Marine Biofilms: A Successful Microbial Strategy With Economic Implications. *Frontiers in Marine Science*, 5:126, apr 2018.

[67] S S Socransky and A D Haffajee. Dental biofilms: difficult therapeutic targets. *Periodontology 2000*, 28:12–55, 2002.

[68] T C Montie, D Doyle-Huntzinger, R C Craven, and I A Holder. Loss of virulence associated with absence of flagellum in an isogenic mutant of Pseudomonas aeruginosa in the burned-mouse model. *Infection and immunity*, 38(3):1296–8, dec 1982.

[69] L A De Weger, C I van der Vlugt, A H Wijfjes, P A Bakker, B Schippers, and B Lugtenberg. Flagella of a plant-growth-stimulating Pseudomonas fluorescens strain are required for colonization of potato roots. *Journal of bacteriology*, 169(6):2769–73, jun 1987.

[70] C C Grant, M E Konkel, W Cieplak, L S Tompkins, and L S Tompkins. Role of flagella in adherence, internalization, and translocation of Campylobacter jejuni in nonpolarized and polarized epithelial cell cultures. *Infection and immunity*, 61(5):1764–71, may 1993.

[71] D R Korber, J R Lawrence, and D E Caldwell. Effect of Motility on Surface Colonization and Reproductive Success of Pseudomonas fluorescens in Dual-Dilution Continuous Culture and Batch Culture Systems. *Applied and environmental microbiology*, 60(5):1421–9, may 1994.

[72] R De Nys, P D Steinberg, P Willemsen, S A Dworjanyn, C L Gabelish, and R J King. Broad spectrum effects of secondary metabolites from the red alga *delisea pulchra* in antifouling assays. *Biofouling*, 8(4):259–271, may 1995.

[73] Global report. ANTIMICROBIAL RESISTANCE Global Report on Surveillance. Technical report.

[74] B E. Rittmann and P L. McCarty. Model of steady-state-biofilm kinetics. *Biotechnology and Bioengineering*, 22(11):2343–2357, nov 1980.

[75] O. Wanner and W. Gujer. A multispecies biofilm model. *Biotechnology and Bioengineering*, 28(3):314–328, mar 1986.

[76]   B M. Peyton and W. G. Characklis. A statistical analysis of the effect of substrate utilization and shear stress on the kinetics of biofilm detachment. *Biotechnology and Bioengineering*, 41(7):728–735, mar 1993.

[77]   B E. Rittmann and P L. McCarty. Model of steady-state-biofilm kinetics. *Biotechnology and Bioengineering*, 24(10):2291–2291, oct 1982.

[78]   D. Rodriguez, A. Carpio, and B. Einarsson. A cellular automata model for biofilm growth. pages 409–421, may 2014.

[79]   S. Skoneczny. Cellular automata-based modelling and simulation of biofilm structure on multi-core computers. *Water Science and Technology*, 72(11):2071–2081, dec 2015.

[80]   Y Tang and A J. Valocchi. An improved cellular automaton method to model multispecies biofilms. *Water Research*, 47(15):5729–5742, oct 2013.

[81]   S Wolfram. Cellular automata as models of complexity. *Nature*, 311:419–424, 1984.

[82]   D.G. Green. Cellular automata models in biology. *Mathematical and Computer Modelling*, 13(6):69–74, jan 1990.

[83]   S W Hermanowicz. A simple 2D biofilm model yields a variety of morphological features. *Mathematical Biosciences*, 169(1):1–14, jan 2001.

[84]   H J. Eberl, D F. Parker, and M C. M. Van Loosdrecht. A New Deterministic Spatio-Temporal Continuum Model for Biofilm Development. *Journal of Theoretical Medicine*, 3(3):161–175, 2001.

[85]   C.S. Laspidou, A. Kungolos, and P. Samaras. Cellular-automata and individual-based approaches for the modeling of biofilm structures: Pros and cons. *Desalination*, 250(1):390–394, jan 2010.

[86]   A R. Standaert, F Poschet, A H. Geeraerd, F V. Uylbak, J-U Kreft, and J F. Van Impe. A Novel Class of Predictive Microbial Grown Models: Implementation in an Individual-Based Framework. *IFAC Proceedings Volumes*, 37(3):183–188, mar 2004.

[87]   A.J. Verhulst, A.M. Cappuyns, E. Van Derlinden, K. Bernaerts, and J.F.M. Van Impe. Individual-based Modelling of Non-motile Bacterial Colony Formation In

Structured Foods: A Comparative Study. *IFAC Proceedings Volumes*, 43(6):329–334, jan 2010.

[88]   Q Wang and T Zhang. Review of mathematical models for biofilms. *Solid State Communications*, 150(21-22):1009–1022, jun 2010.

[89]   D C Yang, K M Blair, and N R Salama. Staying in Shape: the Impact of Cell Shape on Bacterial Survival in Diverse Environments. *Microbiology and molecular biology reviews : MMBR*, 80(1):187–203, mar 2016.

[90]   J-U Kreft, C Picioreanu, M C. M. van Loosdrecht, and J W. T. Wimpenny. Individual-based modelling of biofilms. *Microbiology*, 147(11):2897–2912, nov 2001.

[91]   S. Kim and S J. Karrila. *Microhydrodynamics : principles and selected applications*. Butterworth-Heinemann, 1991.

[92]   M Haw. The Restlessness of Matter and Life. In *Middle World*, pages 181–188. Palgrave Macmillan US, New York, 2007.

[93]   E. Guazzelli, J F. Morris, and S. Pic. *A physical introduction to suspension dynamics*. Cambridge University Press, 2012.

[94]   D B Dusenbery. Minimum size limit for useful locomotion by free-swimming microbes. *Proceedings of the National Academy of Sciences of the United States of America*, 94(20):10949–54, sep 1997.

[95]   J R Blake. A note on the image system for a stokeslet in a no-slip boundary. *Proc. Gamb. Phil. Soc*, 70(303):70–32, 1971.

[96]   G. Taylor. Analysis of the Swimming of Microscopic Organisms. *Proceedings of the Royal Society A: Mathematical, Physical and Engineering Sciences*, 209(1099):447–461, nov 1951.

[97]   T D Montenegro-Johnson and E Lauga. Optimal swimming of a sheet. *PHYSICAL REVIEW E*, 89(060701), 2014.

[98]   J. Gray and G. J. Hancock. The Propulsion of Sea-Urchin Spermatozoa. *Journal of Experimental Biology*, 32(4), 1955.

[99]   J J Blum and J Lubliner. Biophysics of Flagellar Motility. *Annual Review of Biophysics and Bioengineering*, 2(1):181–219, jun 1973.

[100] C J Brokaw. Non-sinusoidal bending waves of sperm flagella. *J. Exp. Biol*, 43:155–169, 1965.

[101] C J Brokaw. Bending moments in free-swimming flagella. *J. Exp. Biol*, 3:445–464, 1970.

[102] R E Johnson and C J Brokaw. Flagellar hydrodynamics. A comparison between resistive-force theory and slender-body theory. *Biophysical journal*, 25(1):113–27, jan 1979.

[103] G. J. Hancock. The Self-Propulsion of Microscopic Organisms through Liquids. *Proceedings of the Royal Society A: Mathematical, Physical and Engineering Sciences*, 217(1128):96–121, mar 1953.

[104] J B. Keller and S I. Rubinow. Slender-body theory for slow viscous flow. *Journal of Fluid Mechanics*, 75(04):705, jun 1976.

[105] R E. Johnson. An improved slender-body theory for Stokes flow. *Journal of Fluid Mechanics*, 99(02):411, jul 1980.

[106] J P Hernandez-Ortiz, P T Underhill, and M D Graham. Dynamics of confined suspensions of swimming particles. *Journal of Physics: Condensed Matter*, 21(20):204107, may 2009.

[107] M Phan-Thien, Nhan, Tran-Cong, T, Ramia. A boundary-element Analysis of Flagellar Propulsion. *Journal of Fluid Mechanics*, 184(1):533–549, 1987.

[108] T Goto, S Masuda, K Terada, and Y Takano. Comparison between Observation and Boundary Element Analysis of Bacterium Swimming Motion. *JSME International Journal Series C*, 44(4):958–963, 2001.

[109] H. Shum, E. A. Gaffney, and D. J. Smith. Modelling bacterial behaviour close to a no-slip plane boundary: the influence of bacterial geometry. *Proceedings of the Royal Society A: Mathematical, Physical and Engineering Sciences*, 466(2118):1725–1748, jun 2010.

[110] B Liu, K S. Breuer, and T R. Powers. Helical swimming in Stokes flow using a novel boundary-element method. *Physics of Fluids*, 25(6):061902, jun 2013.

[111] R Cortez. The Method of Regularized Stokeslets. *SIAM Journal on Scientific Computing*, 23(4):1204–1225, jan 2001.

[112] A. J. Reynolds. The swimming of minute organisms. *Journal of Fluid Mechanics*, 23(02):241, oct 1965.

[113] D. F. Katz, J. R. Blake, and S. L. Paveri-Fontana. On the movement of slender bodies near plane boundaries at low Reynolds number. *Journal of Fluid Mechanics*, 72(03):529, dec 1975.

[114] M K Jawed and P M Reis. Dynamics of a flexible helical filament rotating in a viscous fluid near a rigid boundary. *PHYSICAL REVIEW FLUIDS*, 2(034101), 2017.

[115] E. Barta and N. Liron. Slender Body Interactions for Low Reynolds Numbers‚ÄîPart I: Body-Wall Interactions. *SIAM Journal on Applied Mathematics*, 48(5):992–1008, oct 1988.

[116] M Ramia, D L Tullock, and N Phan-Thien. The role of hydrodynamic interaction in the locomotion of microorganisms. *Biophysical journal*, 65(2):755–78, aug 1993.

[117] D Giacché, T Ishikawa, and T Yamaguchi. Hydrodynamic entrapment of bacteria swimming near a solid surface. *Physical Review E*, 82(5):056309, nov 2010.

[118] J D. Martindale and H C. Fu. Autonomously responsive pumping by a bacterial flagellar forest: A mean-field approach. *Physical Review E*, 96(3):033107, sep 2017.

[119] N. Uchida and R. Golestanian. Synchronization in a carpet of hydrodynamically coupled rotors with random intrinsic frequency. *EPL (Europhysics Letters)*, 89(5):50011, mar 2010.

[120] A Buchmann, L J. Fauci, K Leiderman, E Strawbridge, and L Zhao. Mixing and pumping by pairs of helices in a viscous fluid. *Physical Review E*, 97(2):023101, feb 2018.

[121] H.C. Berg and E.M. Purcell. Physics of chemoreception. *Biophysical Journal*, 20(2):193–219, nov 1977.

[122] A E Labauve and M J Wargo. Growth and Laboratory Maintenance of Pseudomonas aeruginosa.

[123] C D Amsler, M Cho, and P Matsumura. Multiple factors underlying the maximum motility of Escherichia coli as cultures enter post-exponential growth. *Journal of bacteriology*, 175(19):6238–44, oct 1993.

[124] L Turner, W S Ryu, and H C Berg. Real-time imaging of fluorescent flagellar filaments. *Journal of bacteriology*, 182(10):2793–801, may 2000.

[125] B Amos. Lessons from the history of light microscopy. *Nature Cell Biology*, 2(8):E151–E152, aug 2000.

[126] V Ilardi. *Renaissance vision from spectacles to telescopes*. American Philosophical Society, 2007.

[127] B Schmidt, O, Wilms, K-H, Lingelbach. The Visby Lenses. *Optometry and Vision Science*, 1(76):624–630, 1999.

[128] O Hollricher and W Ibach. High-Resolution Optical and Confocal Microscopy. pages 1–20. Springer, Berlin, Heidelberg, 2010.

[129] A Hecht, E,and Zając. *Optics*. 1974.

[130] K. L. Thornton, R. C. Findlay, P. B. Walrad, and L. G. Wilson. Investigating the Swimming of Microbial Pathogens Using Digital Holography. pages 17–32. 2016.

[131] D Gabor. A New Microscopic Princple. *Nature*, 161(May 15):777–778, 1948.

[132] H-W Fink. Mono-atomic tips for scanning tunneling microscopy. pages 87–92. Springer, Dordrecht, 1986.

[133] H-W Fink. Point source for ions and electrons. *Physica Scripta*, 38(2):260–263, aug 1988.

[134] W Stocker, H-W Fink, and R Morin. Low-energy electron and ion projection microscopy. *Ultramicroscopy*, 31(4):379–384, dec 1989.

[135] H-W Fink, W Stocker, and H Schmid. Holography with low-energy electrons. *Physical Review Letters*, 65(10):1204–1206, sep 1990.

[136] J Garcia-Sucerquia, W Xu, S K. Jericho, P Klages, M H. Jericho, and H. J Kreuzer. Digital in-line holographic microscopy. *Applied Optics*, 45(5):836, feb 2006.

[137] F C Cheong, B J Krishnatreya, and D G. Grier. Strategies for three-dimensional particle tracking with holographic video microscopy. *Optics Express*, 18(13):13563, jun 2010.

[138] M Renz. Fluorescence microscopy-A historical and technical perspective. *Cytometry Part A*, 83(9):767–779, sep 2013.

[139] Janssen K. Vangindertael J, Camach R, Sempels W, Mizuno H, Dedecker P. An introduction to optical super-resolution microscopy for the adverrnturous biologist. *Methods and Applications in Fluorescence*, 6, 2018.

[140] J Couch Bashforth, F, A. *An Attempt to Test the Theories of Capillary Action*. 1883.

[141] S-H Lee and D G. Grier. Holographic microscopy of holographically trapped three-dimensional structures. *Optics Express*, 15(4):1505, feb 2007.

[142] L Wilson and R Zhang. 3D Localization of weak scatterers in digital holographic microscopy using Rayleigh-Sommerfeld back-propagation. *Optics Express*, 20(15):16735, jul 2012.

[143] K Engel. *Real-time volume graphics*. A K Peters, 2006.

[144] J Sheng, E Malkiel, and J Katz. Digital holographic microscope for measuring three-dimensional particle distributions and motions. *Applied Optics*, 45(16):3893, jun 2006.

[145] H. Qian, M.P. Sheetz, and E.L. Elson. Single particle tracking. Analysis of diffusion and flow in two-dimensional systems. *Biophysical Journal*, 60(4):910–921, oct 1991.

[146] C Qian, C C Wong, S Swarup, and K-H Chiam. Bacterial tethering analysis reveals a "run-reverse-turn" mechanism forPseudomonas species motility. *Applied and environmental microbiology*, 79(15):4734–43, aug 2013.

[147] J A. K. Suykens. *Advances in learning theory : methods, models, and applications*. IOS Press, 2003.

[148] H C Berg and E M Purcell. Physics of Chemoreception. Technical report.

[149] D. Ren, J.J. Sims, and T.K. Wood. Inhibition of biofilm formation and swarming of Bacillus subtilis by (5Z)-4-bromo-5-(bromomethylene)-3-butyl-2(5H)-furanone. *Letters in Applied Microbiology*, 34(4):293–299, apr 2002.

[150] C de la Fuente-Núñez, V Korolik, M Bains, U Nguyen, E B M Breidenstein, S Horsman, S Lewenza, L Burrows, and R E W Hancock. Inhibition of bacterial

biofilm formation and swarming motility by a small synthetic cationic peptide. *Antimicrobial agents and chemotherapy*, 56(5):2696–704, may 2012.

[151] A Glessner, R S. Smith, B H. Iglewski, and J B. Robinson. Roles of Pseudomonas aeruginosa las andrhl Quorum-Sensing Systems in Control of Twitching Motility. *Journal of Bacteriology*, 181(5):1623–1629, mar 1999.

[152] Q Yang and T Defoirdt. Quorum sensing positively regulates flagellar motility in pathogenic <i>V</i> <i>ibrio harveyi</i>. *Environmental Microbiology*, 17(4):960–968, apr 2015.

[153] MJ Kühn, F K Schmidt, N E Farthing, F M Rossmann, B Helm, L G Wilson, B Eckhardt, and K M Thormann. Spatial arrangement of several flagellins within bacterial flagella improves motility in different environments. *Nature communications*, 9(1):5369, 2018.

[154] N E. Farthing, R C. Findlay, J F. Jikeli, P B. Walrad, M A. Bees, and L G. Wilson. Simultaneous two-color imaging in digital holographic microscopy. *Optics Express*, 25(23):28489, nov 2017.

[155] H H. Hau and JA. Gralnick. Ecology and Biotechnology of the Genus Shewanella, url = http://www.ncbi.nlm.nih.gov/pubmed/18035608 http://www.annualreviews.org/doi/10.1146/annurev.micro.61.080706.093257, volume = 61, year = 2007. *Annual Review of Microbiology*, (1):237–258, oct.

[156] M J. Kühn, F K. Schmidt, B Eckhardt, and K M. Thormann. Bacteria exploit a polymorphic instability of the flagellar filament to escape from traps. *Proceedings of the National Academy of Sciences*, 114(24):6340–6345, jun 2017.

[157] R Rashid, S M L Chee, M Raghunath, and T Wohland. Macromolecular crowding gives rise to microviscosity, anomalous diffusion and accelerated actin polymerization. *Physical Biology*, 12(3):034001, apr 2015.

[158] W R Schneider and R N Doetsch. Effect of viscosity on bacterial motility. *Journal of bacteriology*, 117(2):696–701, feb 1974.

[159] S. Bubendorfer, M. Koltai, F. Rossmann, V. Sourjik, and K. M. Thormann. Secondary bacterial flagellar system improves bacterial spreading by increasing the directional persistence of swimming. *Proceedings of the National Academy of Sciences*, 111(31):11485–11490, aug 2014.

[160] L. Xie, T. Altindal, S. Chattopadhyay, and X.-L. Wu. Bacterial flagellum as a propeller and as a rudder for efficient chemotaxis. *Proceedings of the National Academy of Sciences*, 108(6):2246–2251, feb 2011.

[161] J Yuan, K A. Fahrner, and H C. Berg. Switching of the Bacterial Flagellar Motor Near Zero Load. *Journal of Molecular Biology*, 390(3):394–400, jul 2009.

[162] F Bai, T Minamino, Z Wu, K Namba, and J Xing. Coupling between Switching Regulation and Torque Generation in Bacterial Flagellar Motor. *Physical Review Letters*, 108(17):178105, apr 2012.

[163] A. Driks, R. Bryan, L. Shapiro, and D.J. DeRosier. The organization of the Caulobacter crescentus flagellar filament. *Journal of Molecular Biology*, 206(4):627–636, apr 1989.

[164] M Kostrzynska, J D Betts, J W Austin, and T J Trust. Identification, characterization, and spatial localization of two flagellin species in Helicobacter pylori flagella. *Journal of Bacteriology*, 173(3):937–946, feb 1991.

[165] J C Conrad. Physics of bacterial near-surface motility using flagella and type IV pili: implications for biofilm formation. *Research in Microbiologoy*, 163:619–629, 2012.

[166] P. P. Lele, B. G. Hosu, and H. C. Berg. Dynamics of mechanosensing in the bacterial flagellar motor. *Proceedings of the National Academy of Sciences*, 110(29):11839–11844, jul 2013.

[167] R Belas, M Simon, and M Silverman. Regulation of lateral flagella gene transcription in Vibrio parahaemolyticus. *Journal of Bacteriology*, 167(1):210–218, jul 1986.

[168] R. Belas and R. Suvanasuthi. The Ability of Proteus mirabilis To Sense Surfaces and Regulate Virulence Gene Expression Involves FliL, a Flagellar Basal Body Protein. *Journal of Bacteriology*, 187(19):6789–6803, oct 2005.

[169] G Li, P J B Brown, J X Tang, J Xu, E M Quardokus, C Fuqua, and Y V Brun. Surface contact stimulates the just-in-time deployment of bacterial adhesins. *Molecular microbiology*, 83(1):41–51, jan 2012.

[170] M Schniederberend, J F Johnston, E Shine, C Shen, R Jain, T Emonet, and B I Kazmierczak. Modulation of Flagellar Rotation in Surface-Attached Bacteria: A Circuit for Rapid Surface-Sensing.

[171] M J. McBride. Bacterial Gliding Motility: Multiple Mechanisms for Cell Movement over Surfaces. *Annual Review of Microbiology*, 55(1):49–75, oct 2001.

[172] R M. Harshey. Bacterial Motility on a Surface: Many Ways to a Common Goal. *Annual Review of Microbiology*, 57(1):249–273, oct 2003.

[173] X Chen, S R Suwarno, T H Chong, D McDougald, S Kjelleberg, A G. Cohen, Yand Fane, and S A. Rice. Dynamics of biofilm formation under different nutrient levels and the effect on biofouling of a reverse osmosis membrane system. *Biofouling*, 29(3):319–330, mar 2013.

[174] W E. Ortyn, D J. Perry, V Venkatachalam, L Liang, B E. Hall, K Frost, and D A. Basiji. Extended depth of field imaging for high speed cell analysis. *Cytometry Part A*, 71A(4):215–231, apr 2007.

[175] M. Zeder and J. Pernthaler. Multispot live-image autofocusing for high-throughput microscopy of fluorescently stained bacteria. *Cytometry Part A*, 75A(9):781–788, sep 2009.

[176] R M. Macnab and M K Ornston. Normal-to-curly flagellar transitions and their role in bacterial tumbling. Stabilization of an alternative quaternary structure by mechanical force. *Journal of Molecular Biology*, 112(1):1–30, may 1977.

[177] W S. Jewell. Model Variations in Credibility Theory., 1974.

[178] H Bühlmann. Experience Rating and Credibility. *ASTIN Bulletin*, 4(03):199–207, jul 1967.

[179] ThermoFischer. Latex Bead Technical Overview.

[180] G H. Wadhams and J P. Armitage. Making sense of it all: bacterial chemotaxis. *Nature Reviews Molecular Cell Biology*, 5(12):1024–1037, dec 2004.

[181] S M. Vater, S Weiße, S Maleschlijski, C Lotz, F Koschitzki, T Schwartz, U Obst, and A Rosenhahn. Swimming Behavior of Pseudomonas aeruginosa Studied by Holographic 3D Tracking. *PLoS ONE*, 9(1):e87765, jan 2014.

[182] G-J Li and A M. Ardekani. Hydrodynamic interaction of microswimmers near a wall. *Physical Review E*, 90(1):013010, jul 2014.

[183] J. D. Martindale, M. Jabbarzadeh, and H. C. Fu. Choice of computational method for swimming and pumping with nonslender helical filaments at low Reynolds number. *Physics of Fluids*, 28(2):021901, feb 2016.

[184] Y Sowa and R M. Berry. Bacterial flagellar motor. *Quarterly Reviews of Biophysics*, 41(02):103–132, may 2008.

[185] G. B. Jeffery. The Motion of Ellipsoidal Particles Immersed in a Viscous Fluid. *Proceedings of the Royal Society A: Mathematical, Physical and Engineering Sciences*, 102(715):161–179, nov 1922.

[186] J. M. Rallison. The effects of Brownian rotations in a dilute suspension of rigid particles of arbitrary shape. *Journal of Fluid Mechanics*, 84(02):237, jan 1978.

[187] M Kim and T R. Powers. Hydrodynamic interactions between rotating helices. *Physical Review E*, 69(6):061910, jun 2004.

[188] N Dasgupta, S K. Arora, and R Ramphal. The Flagellar System of Pseudomonas aeruginosa. In *Pseudomonas*, pages 675–698. Springer US, Boston, MA, 2004.

[189] N C Darnton, L Turner, S Rojevsky, and H C Berg. On Torque and Tumbling in Swimming Escherichia coli ‚Ä† Downloaded from. *JOURNAL OF BACTERIOLOGY*, 189(5):1756–1764, 2007.

[190] R Vogel and H Stark. Rotation-Induced Polymorphic Transitions in Bacterial Flagella. *Physical Review Letters*, 110(15):158104, apr 2013.

[191] S V. Srigiriraju and T R. Powers. Model for polymorphic transitions in bacterial flagella. *Physical Review E*, 73(1):011902, jan 2006.

[192] Guanglai Li, Lick-Kong Tam, and Jay X Tang. Amplified effect of Brownian motion in bacterial near-surface swimming. Technical report, 2008.

[193] P N Segre, O P Behrend, and P N Pusey. Short-time Brownian motion in colloidal suspensions: Experiment and simulation. Technical Report 5, 1995.

[194] B.M. Davis, J.L. Richens, and P. O'Shea. Label-Free Critical Micelle Concentration Determination of Bacterial Quorum Sensing Molecules. *Biophysical Journal*, 101(1):245–254, jul 2011.

[195] J Fung and V N. Manoharan. Holographic measurements of anisotropic three-dimensional diffusion of colloidal clusters. *Physical Review E*, 88(2):020302, aug 2013.

[196] T H Besseling, M Hermes, A Kuijk, B de Nijs, T-S Deng, M Dijkstra, A Imhof, and A van Blaaderen. Determination of the positions and orientations of concentrated rod-like colloids from 3D microscopy data. *Journal of Physics: Condensed Matter*, 27(19):194109, may 2015.

[197] X Michalet. Mean square displacement analysis of single-particle trajectories with localization error: Brownian motion in an isotropic medium. *Physical review. E, Statistical, nonlinear, and soft matter physics*, 82(4 Pt 1):041914, oct 2010.

[198] N Darnton, L Turner, K Breuer, and H C Berg. Moving fluid with bacterial carpets. *Biophysical journal*, 86(3):1863–70, mar 2004.

[199] N Tarantino, J-Y Tinevez, B Crowell, E Fand Boisson, R Henriques, M Mhlanga, F Agou, A Israël, and E Laplantine. TNF and IL-1 exhibit distinct ubiquitin requirements for inducing NEMO-IKK supramolecular structures. *The Journal of cell biology*, 204(2):231–45, jan 2014.

[200] R Faubel, C Westendorf, E Bodenschatz, and G Eichele. Cilia-based flow network in the brain ventricles. *Science (New York, N.Y.)*, 353(6295):176–8, jul 2016.

[201] M Klausen, A Heydorn, P Ragas, L Lambertsen, A Aaes-Jørgensen, S Molin, and T Tolker-Nielsen. Biofilm formation by Pseudomonas aeruginosa wild type, flagella and type IV pili mutants. *Molecular Microbiology*, 48(6):1511–1524, 2003.

[202] N Uchida, R Golestanian, and R R. Bennett. Synchronization and Collective Dynamics of Flagella and Cilia as Hydrodynamically Coupled Oscillators. *Journal of the Physical Society of Japan*, 86(10):101007, oct 2017.

[203] S Gueron, K Levit-Gurevich, N Liron, and J J Blum. Cilia internal mechanism and metachronal coordination as the result of hydrodynamical coupling. *Proceedings of the National Academy of Sciences of the United States of America*, 94(12):6001–6, jun 1997.

[204] Y W Kim and R R. Netz. Pumping Fluids with Periodically Beating Grafted Elastic Filaments. *Physical Review Letters*, 96(15):158101, apr 2006.

227

[205] M T Brown, B C Steel, C Silvestrin, D A Wilkinson, N J Delalez, C N Lumb, B Obara, J P Armitage, and R M Berry. Flagellar Hook Flexibility Is Essential for Bundle Formation in Swimming Escherichia coli Cells. 2012.

[206] MJ Hesse, WR, Kim. Visualization of flagellar interactions on bacterial carpets. *Journal of Microscopy*, 233:302–308, 2009.

[207] S. S. Batsanov. Van der Waals Radii of Elements. *Inorganic Materials*, 37(9):871–885, 2001.

[208] N. Maki, JK. E. Gestwicki, E. M. Lake, L. L. Kiessling, and J. Adler. Motility and Chemotaxis of Filamentous Cells of <i>Escherichia coli</i>. *Journal of Bacteriology*, 182(15):4337–4342, aug 2000.

[209] Ò Guadayol, K L. Thornton, and S Humphries. Cell morphology governs directional control in swimming bacteria. *Scientific Reports*, 7(1):2061, dec 2017.

[210] Y Tanouchi, A Pai, H Park, Sg Huang, R Stamatov, N E. Buchler, and L You. A noisy linear map underlies oscillations in cell size and gene expression in bacteria. *Nature*, 523(7560):357–360, jul 2015.

[211] E Lauga. Enhanced Diffusion by Reciprocal Swimming. *Physical Review Letters*, 106(17):178101, apr 2011.

[212] T Kaya and H Koser. Direct upstream motility in Escherichia coli. *Biophysical journal*, 102(7):1514–23, apr 2012.

[213] D J. Smith. A boundary element regularised Stokeslet method applied to cilia and flagella-driven flow. aug 2010.

[214] Y Vadeboncoeur and M E. Power. Attached Algae: The Cryptic Base of Inverted Trophic Pyramids in Freshwaters. *Annual Review of Ecology, Evolution, and Systematics*, 48(1):255–279, nov 2017.

[215] N Chindapol, J A. Kaandorp, C Cronemberger, T Mass, and A Genin. Modelling Growth and Form of the Scleractinian Coral Pocillopora verrucosa and the Influence of Hydrodynamics. *PLoS Computational Biology*, 9(1):e1002849, jan 2013.

[216] A L Hook, D G Anderson, R Langer, P Williams, M C Davies, and M R Alexander. High throughput methods applied in biomaterial development and discovery. 2009.

228